5-2-2016

Rational Design and Enabling of High Performance Nano-arrays for Environmental Catalysis

Zheng Ren
University of Connecticut, frankren1988@gmail.com

Rational Design and Enabling of High Performance Nano-arrays for Environmental Catalysis

Zheng Ren, Ph.D.

University of Connecticut, 2016

Monolithic catalysts represent an important catalyst configuration which is widely used in industry. However, several issues associated with catalyst preparation such as low materials utilization efficiency, difficulty in microstructure control and lack of structure-property correlation have made it challenging for rational monolithic catalysts design to achieve their optimum performance. Besides, more and more stringent regulation has been imposed upon the automotive emission and developing high performance catalyst has therefore become an inevitable task. In this dissertation, we will first introduce the concept and showcase the fabrication of nano-array catalyst featuring high catalyst utilization efficiency. The monolithic nano-array catalysts exhibit high performance low temperature CO/NO/hydrocarbon oxidation. Detailed discussion will be focused on the rational catalytic activity adjustment by tunable nano-array geometry and composition. Catalytic reaction mechanism, selective doping effects and catalyst stability are further investigated by in-situ spectroscopy in tandem with the density functional theory calculation. Other applications of monolithic catalyst in the nano-array configuration have been demonstrated such as photocatalytic water treatment and water purification. With the demonstrated fabrication at industrial relevant scale, the adjustable catalytic activity and the identified reaction mechanisms, monolithic nano-array catalyst is believed to enable rational catalyst design for environmental applications ranging from automotive emission control to water treatment.

Rational Design and Enabling of High Performance Nano-arrays for Environmental Catalysis

Zheng Ren

B. S., Beihang University, 2010

A Dissertation

Submitted in Partial Fulfillment of the

Requirement for the Degree of Doctor of Philosophy

At the

University of Connecticut

2016

APPROVAL PAGE

Doctor of Philosophy Dissertation

Rational Design and Enabling of High Performance Nano-arrays for Environmental Catalysis

Presented by

Zheng Ren, B.S.

Major Advisor _____

Dr. Pu-Xian Gao

Associate Advisor _____

Dr. Steven L. Suib

Associate Advisor _____

Dr. Ramamurthy Ramprasad

Associate Advisor _____

Dr. Yu Lei

Associate Advisor _____

Dr. Avinash M. Dongare

University of Connecticut
2016

This humble work is dedicated to my beloved parents Keping Ren and Lian Xu for their all-enduring and selfless love

Acknowledgement

I would like to first thank my PhD advisor Dr. Pu-Xian Gao for his mentoring, support and encouragement during my graduate research. His working ethics, wisdom and passion about research have always been a great source of inspiration for me. I sincerely appreciate all the opportunities he gave, conference presentations, invited reviews and proposal drafting, to help me learn and become a better researcher. I also would like to thank Dr. Suib, Dr. Ramprasad, Dr. Lei and Dr. Dongare for serving my advisory committee and providing valuable input and suggestions for my dissertation.

Working in the Nanomaterials Science and Engineering Laboratory has been a terrific and unforgettable journey. I am very fortunate to have worked with my excellent colleagues Dr. Yanbing Guo, Dr. Haiyong Gao, Dr. Caihong Liu, Dr. Zhonghua Zhang, Dr. Wenxiang Tang, Dr. Son Hoang, Dr. Shoucheng Du, Dr. Paresh Shimpi, Dr. Weijie Cai, Dr. Gregory Wrobel, Dr. Kuo-ting Liao, Wen Xiao, Hui-Jan Lin, Sarah Glod, Sibo Wang, Sanka Piyadasa, Mingwan Zhang, Bo Zhang, Xinxu Lu, Junfei Weng. Without your help and support I would not have finished this dissertation. My special thanks also go to Drs. Lichun Zhang, Roger Ristau, Jack Gromek, Heng Zhang, Laura Pinatti and Gary Lavigne for their training on the electron microscopy and spectroscopy facilities at Institute of Materials Science.

It is also a great pleasure for me to have collaborated with many talented researchers at and outside University of Connecticut. I would like to thank Dr. Yongtao Meng, Wenqiao Song, Venkatesh Botu for their collaboration and inspiring discussion on the catalysis project. I am also grateful for the opportunity to have worked with Dr. Zili Wu at Oak Ridge National Laboratory for the in-situ spectroscopy study of heterogeneous catalysis. It is enjoyable to work with all of you and publish great work together.

Finally I would like to express my faithful appreciation to my parents and my grandparents for their enduring and selfless love, my girlfriend Yuan and all my dearest friends for always being there for me. Without you I could have never become who I am today.

Table of contents

List of Figures and Tables

Chapter 1

Introduction

1.1. Background

1.1.1. Challenges of catalysis for environmental applications

Carbon monoxide, nitrogen oxide and hydrocarbon generated from automotive vehicles and power plants are responsible for several severe environmental problems such as acidic rain, photochemical smog and green house effect. In recent years more and more stringent regulations have been imposed upon the emission of automotive vehicles and developing high performance catalyst has therefore become an inevitable task in order to meet the increasingly strict requirements. As monolithic structure represents an important configuration of reactors in many applications such as fine chemical processing, environmental catalysis and clean energy combustion,[1-9] ceramic monolith made of cordierite ($2MgO \cdot 2Al_2O_3 \cdot 5SiO_2$) is one of the major types of monoliths used as catalytic reactors for automotive emission control,[3,10-12] diesel particulate filter (DPF),[13-15] indoor air purification[16] and water filtration[17-19] due to its low thermal expansion coefficient, high thermal shock resistance, relatively high porosity, low weight but good mechanical durability.[3,20]

Equipped on our cars we have a catalytic converter which transforms exhaust emissions like nitrogen oxide, hydrocarbon and carbon monoxide into nontoxic tail pipe emissions. As shown in Figure 1.1, the catalytic converter consists of oxygen sensor, heat shield, the major body and the insulating packaging. The major body of the catalytic converter is a ceramic cordierite coated with the catalysts. Al_2O_3, CeO_2 and sometimes ZrO_2-CeO_2 solid solutions are typically used as the oxide support for the catalyst while the catalytic active materials are mainly Pt group metals

such as Pt, Pd and Rh. In a typical catalytic process, the catalytic converters convert nitrogen oxides (both NO and NO_2) into nitrogen (N_2), hydrocarbon (HC) and carbon monoxide (CO) into carbon dioxide (CO_2) and water vapor (H_2O).

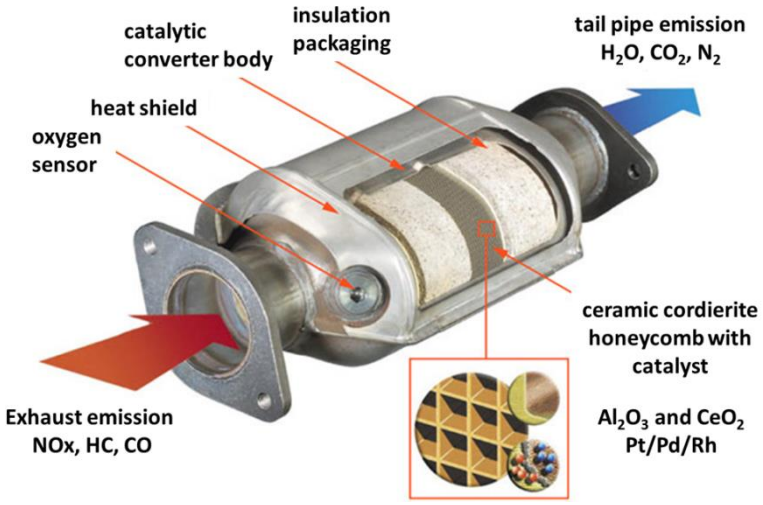

Figure 1.1. Typical configuration of catalytic converters on automotive vehicles for exhaust emission after-treatment and regulation.

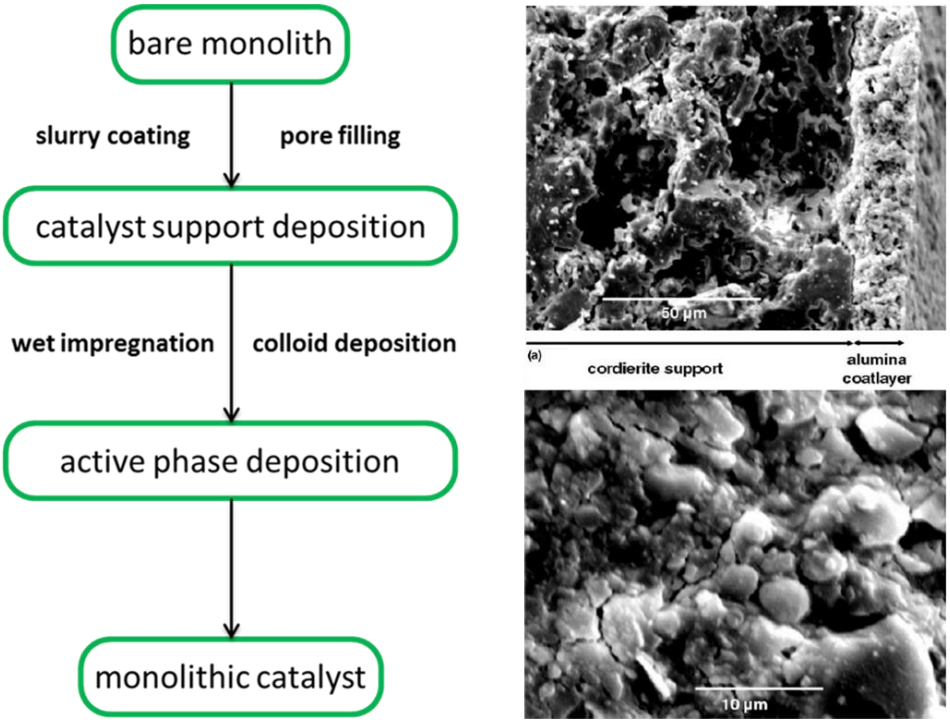

Figure 1.2. An overview of wash-coat fabrication process for monolithic catalysts and the microstructure characterization of the wash-coated catalysts.

Despite all the benefits the monolith configuration is able to provide, challenges remain for preparation of monolithic catalysts. Typically the catalyst preparation requires a uniform coating on the monolithic substrate of either ready-made catalysts (e.g. zeolites) which do not need specific catalytic supports or both support and catalytic active materials.[21] For example, wash-coating of Al_2O_3, SiO_2 or carbon as the catalyst support is usually the first step of the monolithic catalyst fabrication followed by the dispersion of active noble metal (Pt, Rh or Pd) nanoparticles. As demonstrated in Figure 1.2, two typical strategies, pore-filling and slip-casting, are widely used for this wash coating procedure. The pore filling refers to the filling of pores in the monolith ceramics with support materials by colloidal coating which features strong interaction between the support and the substrate. Although mono-dispersed Al_2O_3 or SiO_2 colloidal suspension is easily to be prepared by wet chemical synthesis and the pore-filling process ensures the good adherence since the support materials is confined in the pores, the loading amount is very limited given the relatively small pore volume and low surface area of the cordierite monolith.[3] The slip-casting strategy, also known as slurry coating, is usually employed to increase the materials loading. Since the layer is thicker and most of the materials are not confined to the pores, the adherence to the monolith must be enhanced by adding binders. Such slurry coating sacrifices the catalyst utilization efficiency as a consequence of large amount of catalyst loading. It also adds complexity to the materials processing by the addition of binders because the viscosity of the slurry needs to be carefully controlled and any wrongly prepared slurry precursor will lead to poor adherence to the substrate. In addition, a number of repeated coating procedures are often required to ensure a uniform coverage. For the noble metal nanoparticles deposition, it can be achieved by wet impregnation where noble metal precursors

are introduced to the monolith and noble metal loadings are achieved by thermal treatment that transforms the precursors into noble metals. Alternatively, the noble metals can be loaded by colloidal deposition where the as-prepared noble metals nanoparticles are deposited to the oxide support with a relative weight loading percentage of 1 %. The typical morphology and microstructure of this wash-coated monolithic catalyst after fabrication can be observed in Figure 1.2. From the cross-sectional SEM image, the oxide support layer of Al_2O_3 is over 20 microns thick and the microstructure is not well defined. Generally speaking, the traditional monolithic catalyst configuration faces several challenges. Firstly, the significant amount of materials loading imposes great pressure on the noble metal supply which makes the catalytic converters rather expensive for automotive emission control. Secondly, the less-than-ideal wash-coating process usually does not ensure uniform catalyst deposition with precisely and optimally controlled microstructures, therefore compromises the materials utilization efficiency. Lastly, the random structural arrangement of the wash-coated materials renders difficulty to well correlate catalyst structure, porosity, orientation and the relevant gas-solid interactions with catalyst performance and it is thus no easy task for the rational catalyst design.

1.1.2. Hierarchical assembly of nanostructures

Since the discovery of carbon nanotube back in 1991, the past two decades have witnessed the fast development in nanotechnology with numerous nanostructures synthesized and unique properties discovered.[22-24] The representative nanoscale architectures include nanoparticles, one-dimensional nanowires and two dimensional nanosheets. With the size comparable to the wavelengths of electrons and photons, the nanostructures usually demonstrate unique physical properties governed by quantum mechanics, which are far different from those of the bulk materials. For example, the band gap of quantum dots can be tuned by simply size variation.[22]

One-dimensional metal nanostructures are able to exhibit semiconducting behavior while semiconducting Si nanowire can become insulating[25]. These newly discovered physical properties associated with nanostructures of controlled geometry have opened up exciting opportunities for new materials design and potentially revolutionize current device manufacturing. However, it is necessary to achieve the large-scale assembly and scale-up of these nanoscale units to realize the practical utilization of nanostructures. As the core essence of nanomaterials chemistry, the bottom-up paradigm which aims at designing and arranging materials at the submicron or nanoscale dimension provides an important guidance.[26]

In recent years, hierarchical nanostructures composed of either geometric complexity or multiple constituents have drawn great interest.[27-31] Basically, the hierarchical structures can be categorized into either the structures with nanoscale building blocks extended into more than one dimensions or the structures with multiple components. In the first scenario, the accomplished hierarchy of nanoscale building blocks represents the successful materials manipulation and helps reveal important scientific understanding at an unprecedented length scale. The complexity in extended dimensions brings about advantages such as high surface area that is important in water treatment[32] and large scale ordered arrangement for electronic device manufacturing[33]. For instance, three dimensional urchin-like ZnS hierarchical spheres demonstrated enhanced photocatalytic activity owing to its enhanced light harvesting and high surface to volume ratio.[34] ZnO nanowires were successfully integrated into ordered two dimensional arrays with interesting gas sensing[35] and photo-detecting property.[36] As mentioned above, however, the materials hierarchy can be more than geometric arrangement. Different combination of dissimilar units will lead to multiple functionalities and makes the hierarchical materials exhibit complex property.[37,38] The development of such hierarchical nanostructures is an important task in

advanced nanotechnology to realize better materials performance by rational combination of multiple components.

Among all the synthetic strategies to develop hierarchical nanostructures, self-assembly represents an interesting and efficient approach to construct hierarchical nanostructures with controlled geometry and morphology. For example, propeller-shaped hierarchical structure has been successfully achieved by a solid vapor deposition to extend single crystalline ZnO nanorod into three dimensions.[39] The growth morphology depends on local temperature, surface diffusion and vapor supply. As illustrated in Figure 1.3, a triangle-shaped morphology is achieved in the relatively low temperature region where there is insufficient vapor supply and slower surface diffusion. In regions of higher temperature, uniform and longer blades are formed due to faster vapor diffusion and higher surface mobility. Other hierarchical geometries have been achieved for ZnO nanostructures through vapor phase deposition such as nanosprings[40], nanorings[41,42] and nanohelix[43].

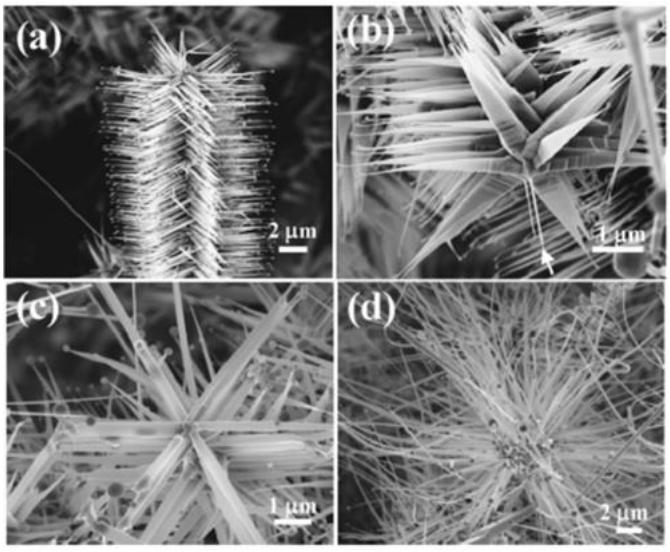

Figure 1.3. ZnO nanopropeller synthesized by vapor deposition.

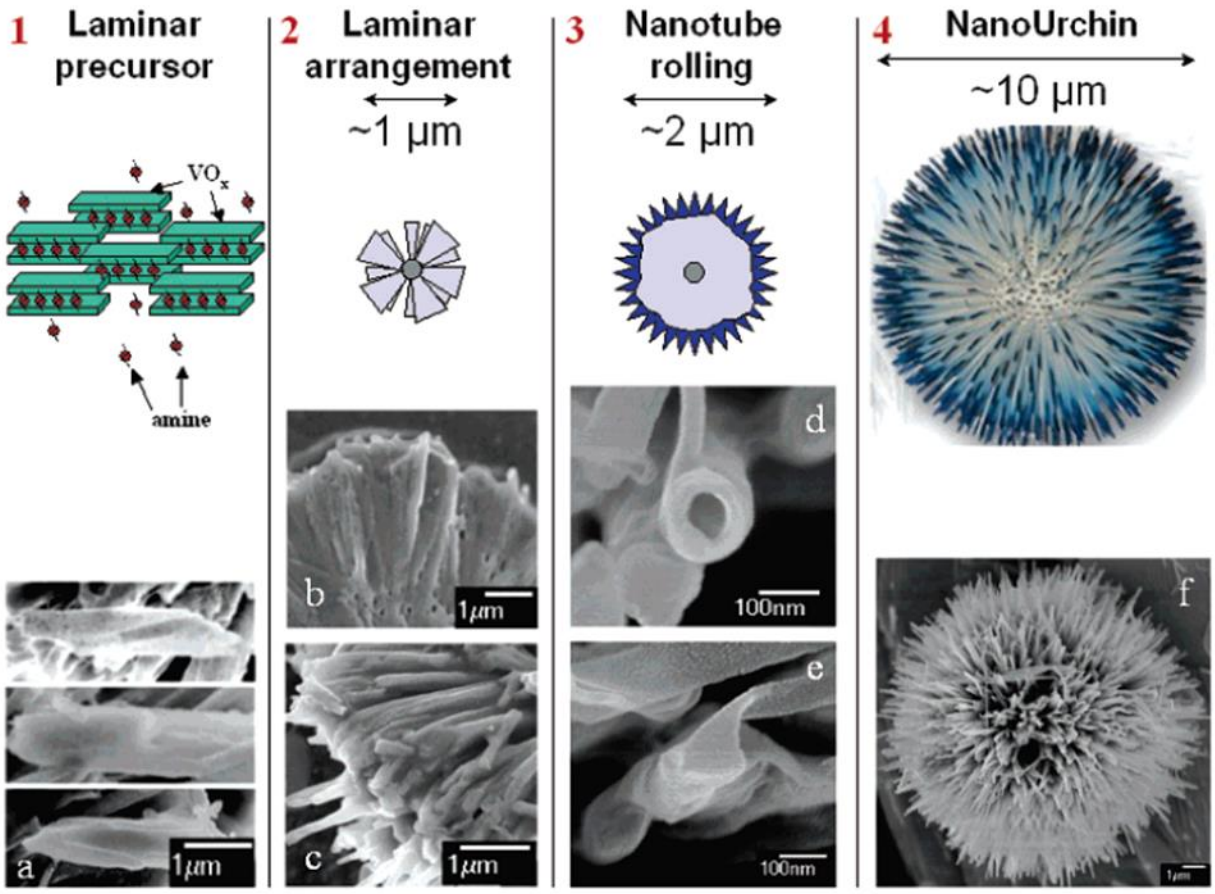

Figure 1.4. Schematic illustration of the morphology evolution and the growth mechanism of vanadium oxide nano-urchin.

Another apt example of self-assembled hierarchical nanostructures is urchin structures of high surface area. The self-assembled urchin-like structure was first reported in the vanadium oxide system, which consists of spherically arranged nanotube radial arrays.[44] Typically, the formation of urchin-like structures is driven by the minimization of interfacial energy between one dimensional nanoscale building blocks. In the vanadium oxide system, for example, anisotropic laminar structures were first formed and self-assembled into spherical aggregates in a radially oriented fashion guided by amine molecules.[44] Each laminar units constituting the spherical aggregates underwent a rolling procedure in the presence of amine and nanotubes with micrometers in length came into shape with minimized the surface energy. The length of the

nanotubes was elongated as the hydrothermal reaction proceeded to achieve the final urchin geometry. The morphology evolution and growth mechanism have been demonstrated in Figure 1.4. Similarly, in the hydrothermal preparation of In_2O_3,[45] individual nanowires appeared in the early stage and arranged into urchin architecture to reduce the surface energy. Such two-step growth mechanism, which involves formation of anisotropic building blocks followed by self-assembly driven by surface energy minimization, has been widely considered to interpret most urchin-structure development.

1.2. Dissertation objectives

In this dissertation research, we would like to utilize the developed synthetic strategy of hierarchical nanostructures featuring high surface area, well-defined geometry and decent catalytic activity to bring a new type of monolithic catalysts, nanostructure array (nano-array) based monolithic catalysts, so-called "Nano-array catalyst", to environmental applications. Specifically, we would fabricate a new type of monolithic catalyst on a large scale based on nano-arrays configuration with all the above-mentioned featured merits in order to potentially enhance the catalytic activity for low temperature emission control, promote the catalyst utilization efficiency and provide valuable guidance toward rational catalyst design by tailoring the catalytic materials structure correlated to the catalytic property. Specifically, six tasks are focused to:

1) Fabricate monolithic nano-array catalyst with well defined geometry and reduced materials loading and compare the catalytic CO oxidation performance with wash-coat catalyst.
2) Achieve fabrication of monolithic nano-array catalyst at industrial relevant scale and develop high performance NO oxidation catalyst.

3) Adjust low temperature catalytic hydrocarbon oxidation performance by rational catalyst design via transition metal doping.
4) Investigate the transition metal doping effects and reaction mechanism by in-situ spectroscopy to develop high performance hydrocarbon oxidation catalyst.
5) Study the thermal stability of transition metal doped nano-array catalyst.
6) Demonstrate nano-array catalyst for other environmental applications.

1.3. Methods and techniques

1.3.1. Synthesis of monolithic nano-array catalysts

The synthesis of several oxide nanostructures will be investigated by wet chemical strategy based on hydrothermal synthesis.

TiO_2: Nanostructured brookite TiO_2 was synthesized by hydrothermal treatment of aqueous titanium trichloride ($TiCl_3$) solutions with saturated sodium chloride (NaCl). Typically, 20 ml of the precursor solution including 3 g of $TiCl_3$ and 10 g of DI-water saturated with NaCl was placed in a Teflon-lined autoclave. Either honeycomb cordierite ceramic (or stainless steel) monoliths were then used as substrates and immersed in the solutions. The autoclaves were then heated to 220 ^{o}C and maintained for 18 hours.

ZnO: The monolith cordierite was first cleaned by DI water and ethanol and then surface-modified with 20 mM zinc acetate ethanol solution for several times to form a seed layer on channel walls. The dip-coated substrate was then annealed at 350 °C for 5 hours to make (001) face of ZnO crystal better oriented. Equal molar zinc nitrate hexahydrate ($Zn(NO_3)_2.6H_2O$) and hexamethylenetetramine ($C_6H_{12}N_4$, HMT) (25 mM) were dissolved in 200 mL DI water as

precursor. The annealed dip-coated substrate was then put in the prepared precursor solution at 70-80 °C for 6 hours.

CeO_2: Firstly, ZnO nanorod array with (001) preferential orientation was prepared. After 2hr incubation growth of ZnO nanorod arrays at 75 °C, cerium nitrate hexahydrate ($Ce(NO_3)_3 \cdot 6H_2O$,125 mM) was then added into the solution, in order to obtain the core/shell-type ZnO/CeO_2 nanorod arrays. Afterward, ZnO/CeO_2 nanorod arrays were immersed in a dilute hydrochloric acid solution (0.05 M) for 40 s at room temperature and then rinsed with DI water to remove residual contaminants such as compounds containing Zn^{2+}or Cl^- in the CeO_2 nanotube arrays. The length of CeO_2 nanotubes is controlled by the length of ZnO template.

Co_3O_4: Briefly, 5 mL 0.5 M cobalt chloride/acetate/nitrate and 5 mL 6 M urea solution were mixed under ultrasonic bath until the solution becomes transparent. The pre-cleaned cordierite substrate was then immersed into the as-prepared solution and sonicated for another 15 minutes before put into water bath (90 °C) for 24 hrs. Then the substrate after growth was rinsed by DI water several times and was slowly annealed at 300 °C for 4 hrs.

Pt/metal oxides nano-arrays: Pt nanoparticle colloid was first synthesized by ethylene glycol (EG) method under inert atmosphere (Ar or N_2). A glycol solution of NaOH (50 mL, 0.5 M) was added into a glycol solution of $H_2PtCl_6.6H_2O$ (1.0 g, 1.93 mmol in 50 mL) with stirring to obtain a transparent yellow platinum hydroxide or oxide colloidal solution which was then heated at 160 °C for 3 hours under inert gas flow. For deposition, the as-prepared Pt colloid (Pt/cordierite=0.1wt%) was diluted by adding ethanol or acetone as solvent. Cordierite monolith substrates with nanostructure array were then immersed into the dilute Pt colloid solution for 24 hours with magnetic stirring. Finally, the sample was dried at 80 °C in air.

1.3.2. Structure characterization and catalytic performance test

The catalyst structure characterization will be performed by a field emission scanning electron microscope (FE-SEM, JEOL 6335F) and a high resolution transmission electron microscope (HRTEM, JEOL JEM-2010, 200 kV). The element distribution was investigated by scanning transmission electron microscopy (STEM) based on the energy dispersive X-ray spectrometry (EDS). The BET surface area is characterized by Quantachrome NOVA 1000 Gas Sorption Analyzer and Micromeritics ASAP 2020 physisorption analyzer. The temperature-programmed desorption of O_2 (O_2-TPD) as well as the temperature-programmed reduction by H_2 (H_2-TPR) was conducted in a tube furnace equipped with a gas analyzer MKS coupled with a quadruple mass selective detector. The temperature was controlled by WATLOW F4 controller. Several other spectrometers including Raman, XPS and DRIFTS (diffuse reflectance infrared Fourier transformation spectroscopy) will be used for the in-situ study of catalyst during reactions.

A BenchCAT reactor (Altamira Instruments) and a home-made gas-line system will be used for catalytic CO/hydrocarbon/NO oxidation test. Mass spectrometer, Agilent Micro-GC and FT-IR are equipped for the gas species analysis in the product stream. Catalytic performance test will be carried out in a temperature range of 20–800°C with the space velocity of ~50,000/h.

In-situ/Operando spectroscopy investigation is conducted to understand the reaction pathways and associated reaction kinetics and mechanisms involved in the low temperature catalytic oxidation reactions. Diffuse Reflectance Infrared Fourier Transform spectroscopy (DRIFTS) is employed to characterize the chemical species on the catalyst surface to extract dynamic evolution of surface species in order to understand reaction mechanisms. Raman scattering spectra are recorded by a triple Raman spectrometer (Princeton Instrument Acton Trivista 555) equipped with a customized ellipsoidal mirror and a fiber optics bundle. Edge filters are used in

front of the fiber optics bundle to block the laser irradiation ($\lambda_{ex.}$ = 532 nm) and a UV-enhanced liquid nitrogen cooled CCD detector is responsible for the signal detection and monitoring. Cyclohexane will be employed as a standard for all the Raman shifts calibration. X-ray photoelectron spectroscopy (XPS) is performed with Kratos Analytical (Axis Ultra DLD) equipped with monochromatic Al Ka source operating at 1486.7eV. The signal is filtered with a hemispherical analyzer (pass energy 160eV for survey spectra and 20eV for narrow high resolution scan). The C 1s photoelectron line at 284.6eV is used as an internal standard for the correction of the charging effect in all samples.

In the photocatalytic water treatment, a Luzchem ring illuminator equipped with UVA light (356 nm, 220 W) will be used and the concentration change of RhB was recorded by UV-vis-NIR absorption spectroscopy (PerkinElmer) to investigate the efficiency of photodegradation.

1.4. Organizations of this dissertation

As stated previously, this dissertation will be focused on the synthesis, scalable fabrication, and catalyst performance evaluation and reaction mechanisms investigation of nano-array catalysts. Therefore, the dissertation is arranged and divided as follows.

Chapter 1 Introduction: we will introduce the technological background of environmental catalysis and illustrate the key challenges associated with the catalyst synthesis and application in industry. In meantime, a brief overview of hierarchical nanostructures design will be provided to summarize the recent development of nanomaterials chemistry and discuss the feature merits enabled by nanostructures that could be potentially utilized in catalytic materials design. The major objectives of this dissertation research will be summarized. The methods and techniques

for the materials design, synthesis, characterization, performance evaluation and fundamental science investigation will be illustrated and discussed.

Chapter 2 Synthesis of monolithic metal oxide/Pt nano-array catalyst: In this chapter we will demonstrate the successful synthesis of monolithic nano-array catalyst by assembly of various nanowires onto the three dimensional commercialized honeycomb substrates (typical catalyst support) with confined channels. The nano-array configuration features a reduction of catalyst loading by 10 to 40 times without sacrificing the catalytic activity. This new type of monolithic catalyst also exhibits decent thermal stability and mechanical robustness under both high temperature and high flow flux which are very important characteristics in terms of practical applications. The well-defined geometry of nano-arrays has enabled the rational adjustment of catalytic activity based on the structure-property relations. By changing the aspect ratio of ZnO nanowires during the wet chemical synthesis, the catalytic activity of ZnO/Pt nano-array catalyst can be easily adjusted due to the tailored interaction between ZnO polar surface and the Pt nanoparticles.

Chapter 3 Fabrication of monolithic Co_3O_4 nano-array catalyst for high performance nitric oxide (NO) oxidation: Starting this chapter we will stick with the concept of "Nano-array catalyst" and look for promising candidates for some important low temperature oxidation reactions in automotive emission control technology. Much research work will be focused on Co_3O_4 which has been believed to act as a high performance catalyst for a series of oxidation reactions at low temperature. In this chapter, we will discuss the catalytic conversion of nitric oxide (NO) to nitric dioxide (NO_2) which is an important step in nitrogen oxide (NOx) treatment in environmental applications such as automotive emission after-treatment. The ordered Co_3O_4 nano-arrays will be deposited onto the three dimensional ceramic cordierite monoliths by

controlled self-assembly in hydrothermal synthesis. High performance NO to NO_2 conversion has been achieved with conversion efficiency of 80% at temperature as low as 275 °C. The surface Co^{3+} has been identified as the active sites to be responsible for the activity.

Chapter 4 Large-scale nano-array manufacturing and transition metals doping of Co_3O_4 nano-array for low temperature hydrocarbon and CO oxidation: We will for the first time demonstrate the scalable manufacturing of Co_3O_4 based monolithic nano-array catalyst. The successful uniform deposition of Co_3O_4 nanowire arrays onto a large commercial cordierite substrate (4 inches in diameter and 2 inches in length) represents an important progress of nano-array catalyst toward practical applications. This prototype product can be directly equipped on vehicles as catalytic converters for on-board testing. The scale-up of Co_3O_4 nano-array catalyst is enabled by external energy input through magnetic stirring which generates an oscillating pressure drop between both ends of the cordierite channels facilitating the mass transfer in the solution during the synthesis. In the mean time, transition metals have been introduced to the Co_3O_4 lattice to adjust the catalytic performance toward methane oxidation and CO oxidation. Theoretical calculation based on density functional theory as well as spectroscopy study extract in-depth understanding of how dopant elements affect the chemisorption behavior on catalyst surface. This chapter also demonstrates the feasibility of rational design of catalyst with controlled activity through chemical composition manipulation.

Chapter 5 In-situ spectroscopy investigations upon transition metal doping effects, reaction mechanism and thermal stability of monolithic Co_3O_4 nano-array based catalyst: Ni doping has been discovered to greatly enhance the reaction kinetics and catalytic activity of hydrocarbon oxidation using Co_3O_4 nano-array catalysts. In addition to the enhanced methane oxidation performance as discussed in Chapter 4, the Ni doped Co_3O_4 nano-array catalyst demonstrates

better activity of propane oxidation. In this chapter, in-situ spectroscopy of diffuse reflectance infrared Fourier transform spectroscopy (DRIFTS) has been employed to study the reaction pathways and catalytic reaction mechanisms by probing the dynamic evolution of intermediate species on the catalyst surface. It has been discovered that the Ni doping is going to promote the formation of less thermally stable carbonates which facilitates the CO_2 formation. Isotope exchange experiments are conducted to explore and validate the reaction pathways that follow Mars-van Krevelen mechanism where surface lattice oxygen is the active sites. In the mean time, Raman spectroscopy and X-ray diffraction further reveal the thermal stability of the Ni doped Co_3O_4 nano-array catalyst which is important for practical applications.

Chapter 6 Other applications of nano-array integrated functional catalysts – photocatalytic water treatment: Starting this chapter we will explore possibilities of utilizing nano-array configured catalysts for other environmental applications. Photocatalytic degradation of organics in water has become an important technology for waste water treatment. We successfully transplanted the concept of nano-array catalyst and developed a unique photocatalyst consisting of multiple functional units to serve as a recyclable photocatalyst for organic dye degradation under UV illumination. The photocatalyst is created to have a koosh ball structure with different functional units integrated: magnetic cores, transparent insulating layer and semiconductor nano-array shells. The controlled reducing/oxidizing atmosphere, the magnetic property can be adjusted by the controlled phase transitions of magnetic core while the defects state of the semiconductor nano-array shells can be tuned to exhibit different photocatalytic activity. This type of integrated nano-array catalyst with multiple components and functionalities represents a high performance functional nanostructure for environmental applications.

Chapter 7 Other applications of nano-array integrated functional catalysts –water purification: In this chapter we demonstrate another example of water treatment by toxic dye removal using nano-array catalysts. TiO_2 nano-arrays have been successfully integrated onto the three dimensional cordierite ceramic substrates. After deposition of TiO_2 Nano-arrays, the surface area of the cordierite honeycomb substrate has been greatly increased and it is feasible to use it as a small continuous flow fix-bed reactor to remove organic dyes in the water.

1.5. References

[1] Cybulski, A.; Moulijn, J. A. *Catalysis Reviews* **1994**, *36*, 179.

[2] Irandoust, S.; Andersson, B. *Catalysis Reviews* **1988**, *30*, 341.

[3] Williams, J. L. *Catalysis Today* **2001**, *69*, 3.

[4] Boger, T.; Heibel, A. K.; Sorensen, C. M. *Industrial & Engineering Chemistry Research* **2004**, *43*, 4602.

[5] Tomašić, V.; Jović, F. *Applied Catalysis A: General* **2006**, *311*, 112.

[6] Geus, J. W.; van Giezen, J. C. *Catalysis Today* **1999**, *47*, 169.

[7] Zamaro, J. M.; Ulla, M. A.; Miró, E. E. *Chemical Engineering Journal* **2005**, *106*, 25.

[8] Nijhuis, T. A.; Kreutzer, M. T.; Romijn, A. C. J.; Kapteijn, F.; Moulijn, J. A. *Chemical Engineering Science* **2001**, *56*, 823.

[9] Casanovas, A.; de Leitenburg, C.; Trovarelli, A.; Llorca, J. *Catalysis Today* **2008**, *138*, 187.

[10] Twigg, M. V. *Applied Catalysis B: Environmental* **2007**, *70*, 2.

[11] Heck, R. M.; Farrauto, R. J. *Applied Catalysis A: General* **2001**, *221*, 443.

[12] Heck, R. M.; Gulati, S.; Farrauto, R. J. *Chemical Engineering Journal* **2001**, *82*, 149.

[13] Adler, J. *International Journal of Applied Ceramic Technology* **2005**, *2*, 429.

[14] Yang, J.; Stewart, M.; Maupin, G.; Herling, D.; Zelenyuk, A. *Chemical Engineering Science* **2009**, *64*, 1625.

[15] Park, J.-K.; Park, J.-H.; Park, J.-W.; Kim, H.-S.; Jeong, Y.-I. *Separation and Purification Technology* **2007**, *55*, 321.

[16] Yao, Y.; Ochiai, T.; Ishiguro, H.; Nakano, R.; Kubota, Y. *Applied Catalysis B: Environmental* **2011**, *106*, 592.

[17] Park, J.; Lee, J.; Lee, S. *Journal of Porous Materials* **2002**, *9*, 203.

[18] Dong, Y.; Liu, X.; Ma, Q.; Meng, G. *Journal of Membrane Science* **2006**, *285*, 173.

[19] Zhou, L.; Wang, T.; Nguyen, Q. T.; Li, J.; Long, Y.; Ping, Z. *Separation and Purification Technology* **2005**, *44*, 266.

[20] Shigapov, A. N.; Graham, G. W.; McCabe, R. W.; Paputa Peck, M.; Kiel Plummer Jr, H. *Applied Catalysis A: General* **1999**, *182*, 137.

[21] Nijhuis, T. A.; Beers, A. E. W.; Vergunst, T.; Hoek, I.; Kapteijn, F.; Moulijn, J. A. *Catalysis Reviews* **2001**, *43*, 345.

[22] Alivisatos, A.P., *Science*, **1996**, *271*, 933-937.

[23] Hu, J., Odom, T. W. and Lieber, C.M., *Accounts of Chemical Research*, **1999**, *32*, 435-445.

[24] Smith, A. M. and Nie, S., *Accounts of Chemical Research*, **2009**, *43*, 190-200.

[25] Xia, Y., Yang, P., Sun, Y., Wu, Y., Mayers, B., Gates, B., Yin, Y., Kim, F. and Yan, H., *Advanced Materials*, **2003**, *15*, 353-389.

[26] Lu, W., Lieber, C. M., *Nature Materials*, **2007**, *6*, 841-850.

[27] Gao P., Wang, Z. L., *The Journal of Physical Chemistry B*, **2002**, *106*, 12653-12658.

[28] Whang, D., Jin, S., Wu, Y. and Lieber, C. M., *Nano Letters*, **2003**, *3*, 1255-1259.

[29] Lao, J. Y., Wen L. G., and Ren, Z. F., *Nano Letters*, **2002**, *2*, 1287-1291.

[30] Gao, P. X., Shimpi, P., Gao, H., Liu, C., Guo, Y., Cai, W., Liao, K. T., Wrobel, G., Zhang, Z., Ren, Z. and Lin, H. J., *International Journal of Molecular Sciences*, **2012**, *13*, 7393-7423.

[31] Ding, Y. S., Shen, X. F., Gomez, S., Luo, H., Aindow, M. and Suib, S. L., *Advanced Functional Materials*, **2006**, *16*, 549-555.

[32] Savage, N., Diallo, M., *J. Nanopart .Res*, **2005**, *7*, 331-342.

[33] Huang, Y., Lieber, C. M, *Pure and Applied Chemistry*, **2004**, *76*, 2051-2068.

[34] Liu, J., Guo, Z., Wang, W., Huang, Q., Zhu, K. and Chen, X., *Nanoscale*, **2011**, *3*, 1470-1473.

[35] Wang, J. X., Sun, X. W., Yang, Y., Huang, H., Lee, Y. C., Tan, O. K. and Vayssieres, L., *Nanotechnology*, **2006**, *17*, 4995.

[36] Soci, C., Zhang, A., Xiang, B., Dayeh, S. A., Aplin, D., Park, J., Bao, X. Y., Lo, Y. H. and Wang, D., *Nano Letters*, **2007**, *7*, 1003-1009.

[37] Sen, S., Kanitkar, P., Sharma, A., Muthe, K. P., Rath, A., Deshpande, S. K., Kaur, M., Aiyer, R. C., Gupta S. K. and Yakhmi, J. V., *Sensors and Actuators B: Chemical*, **2010**, *147*, 453-460.

[38] Liu, J., Jiang, J., Cheng, C., Li, H., Zhang, J., Gong, H. and Fan, H. J., *Advanced Materials*, **2011**, *23*, 2076-2081.

[39] Gao, P. X. and Wang, Z. L., *Applied Physics Letters*, **2004**, *84*, 2883-2885.

[40] Gao, P. X. and Wang, Z. L., *Small*, **2005**, *1*, 945-949.

[41] Kong, X. Y. and Wang, Z. L., *Nano Letters*, **2003**, *3*, 1625-1631.

[42] Hughes, W. L. and Wang, Z. L., *Applied Physics Letters*, **2005**, *86*, 043106-043103.

[43] Gao, P. X., Ding, Y., Mai, W., Hughes, W. L., Lao, C. and Wang, Z. L., *Science*, **2005**, *309*, 1700-1704.

[44] O'Dwyer, C., Navas, D., Lavayen, V., Benavente, E., Santa Ana, M. A., González, G., Newcomb, S. B. and Sotomayor Torres, C. M., *Chemistry of Materials*, **2006**, *18*, 3016-3022.

[45] Chen, L. Y., Liang, Y., and Zhang, Z. D., *European Journal of Inorganic Chemistry*, **2009**, *2009*, 903-909.

Chapter 2

Synthesis of monolithic metal oxide/Pt nano-array catalyst

2.1. Introduction

Heterogeneous catalytic processes are among the major solutions for enhancing materials utilization efficiency, decreasing raw materials consumption and therefore materials cost in chemical industries, fuel cell, and fuel production and for efficiently eliminating or reducing pollutant emissions[1-9]. Discovery and design of cost-effective, efficient, and multifunctional heterogeneous catalysts stands as one of the major challenges facing today's scientists and engineers[10]. As one of the more important catalyst configurations, monolithic catalytic devices such as catalysts, filters, and reactors, are generally more efficient and cost-effective compared with powder or pellet ones, as a result of a few outstanding merits including low pressure drop, high geometric surface area, efficient mass-transfer and relatively low catalyst usage[1-11]. Consequently, they have been important devices as either dedicated or alternative solutions in catalytic combustion, chemical production, separation and purification, and environmental pollutant treatment such as water purification, vehicle and industrial exhaust emissions treatment[12,13]. However, three main issues remain challenging for the research and development of monolithic catalytic devices: (i) The inevitable use of precious metals (Pt, Rh and Pd) in some applications such as exhaust treatment makes them expensive and limited supply; (ii) Empirical wash-coated powder form catalysts lack the well-defined structural and geometrical configurations, which severely compromises the catalytic performance and materials utilization efficiency; (iii) Current understanding of the relationship between practical industrial catalysts' performance and the origin of catalytic activity, i.e., atomic and nanoscopic surfaces and

interfaces in the comprised individual micro-and nanostructures, is quite limited[14]. On the other hand, although various nanostructure (such as nanoparticles, nanowires) based powder-form catalysts have shown promising potential as efficient catalysts[14-18], nanostructure based monolithic catalysts have been rarely investigated due to the lack of effective integration strategy. Herein, through general nanostructure array (nano-array) integration approach (Figure. 1a) we have addressed or significantly mitigated the above mentioned issues. Given its great importance in both practical application (e.g., exhaust pollutant treatment, fuel cell) and fundamental research[19-21], CO oxidation reaction was performed as a probe reaction over the 3D configurated nano-array based monolithic catalysts. Specifically, by using a low-cost, green and robust hydrothermal process, crystalline nano-arrays of support metal oxides such as ZnO, TiO_2, CeO_2, and Co_3O_4 have been directly grown onto commercial honeycomb monolithic substrates, which have greatly enhanced the devices' surface area, the array-surface Pt nanoparticle dispersion and active site population, and demonstrated strong nanostructure-substrate adhesion and tunable nanostructure shape and size. In the meantime, efficient gas diffusion and catalytic reaction have been enabled in these nano-arrays due to the ordered macroporous channels of the array structures. As a result, with 10–40 times less mass loading in both Pt and support metal oxides than classical wash-coated powder-form ones, these monolithic catalysts

2.2. Experimental Design

The chemicals used, including zinc acetate dihydrate ($Zn(CH_3COO)_2 \cdot 2H_2O$), zinc nitrate hexahydrate ($Zn(NO_3)_2 \cdot 6H_2O$), cobalt chloride hexahydrate ($CoCl_2.6H_2O$) , cerium nitrate ($Ce(NO_3)_3$), sodium chloride (NaCl), lanthanum nitrate hexahydrate ($La(NO_3)_3 \cdot 6H_2O$), strontium nitrate ($Sr(NO_3)_2$), cobalt nitrate ($Co(NO_3)_3$), ethoxyethanol, polyvinylpyrrolidone (Mw 55000, 1.1gram), urea and diethanolamine, were purchased from Fisher Scientific.

Hexamethylenetetramine (HMT, 99%) was bought from Acros. The dilute solution of $TiCl_3$ (0.15 M) was supplied by Spectrum Chemical MFG. Corp. All chemicals were used as received without further purification. The cordierite and stainless steel monolith substrates were provided by Honda Research Institute (Columbus, OH) and Corning Inc. (Corning, NY). The cordierite monolith is of 1mm×1mm square channels and 100 μm in wall thickness, with a diameter in a range of one to a few inches. And the stainless steel monolith is 1 inch wide and 1-3 inches high.

2.2.1. Growth of TiO_2 nanorod array

Aligned single-crystalline brookite TiO_2 nanorod arrays were grown on ceramic honeycomb substrate by a low-temperature hydrothermal approach, which are very suitable for inexpensive mass production. Nanostructured brookite TiO_2 was synthesized by hydrothermal treatment of aqueous titanium trichloride ($TiCl_3$) solutions with saturated sodium chloride (NaCl). Typically, 20 ml of the precursor solution including 3 g of $TiCl_3$ and 10 g of DI-water saturated with NaCl was placed in a Teflon-lined autoclave. Either honeycomb cordierite ceramic (or stainless steel) monoliths were then used as substrates and immersed in the solutions. The autoclaves were then heated to 220 ^{o}C and maintained for 18 h. After the autoclave was cooled to room temperature, the honeycomb cordierite monoliths were rinsed thoroughly with deionized (DI) water and allowed to dry on a hot plate at 80 ^{o}C.

2.2.2. Growth of ZnO nanorod and nanowire array

ZnO nanorod array monolith catalysts were fabricated using the modified methods elsewhere.[22] The monolith cordierite was first cleaned by DI water and ethanol in ultrasonic bath and then surface-modified (via dip-coating) with 20 mM zinc acetate ethanol solution for several times to form a seed layer on channel walls. The dip-coated substrate was then annealed at 350 °C for 5 hours to make (002) face of ZnO crystal better oriented. After ZnO seed coating, ZnO nanorod

growth was conducted by a classic hydrothermal process. Equal molar zinc nitrate hexahydrate ($Zn(NO_3)_2.6H_2O$) and hexamethylenetetramine ($C_6H_{12}N_4$, HMT) (25 mM) were dissolved in 200 mL DI water as precursor. The annealed dip-coated substrate was then put in the prepared precursor solution at 70-80 °C for 6 hours. The grown ZnO nanorods were rinsed in DI water and sonicated in ethanol for 10 minutes. Finally, the sample was dried at 80 °C in air for further characterization. The length of ZnO nanorods is tuned from 1-5 μm by repeated growth.

2.2.3. Growth of CeO_2 nanotube array

CeO_2 nanotubes array was fabricated by ZnO templated growth.[23] Firstly, ZnO nanorod array with (002) preferential orientation was prepared as earlier description on ZnO nanowire array growth. After 2hr incubation growth of ZnO nanorod arrays at 75 ^oC, cerium nitrate hexahydrate ($Ce(NO_3)_3 \cdot 6H_2O$,125 mM) was then added into the solution, in order to obtain the core/shell-type ZnO/CeO_2 nanorod arrays. Afterward, ZnO/CeO_2 nanorod arrays were immersed in a dilute hydrochloric acid solution (0.05 M) for 40 s at room temperature and then rinsed with DI water to remove residual contaminants such as compounds containing Zn^{2+} or Cl^- in the CeO_2 nanotube arrays. Furthermore, for comparison with the as-grown nanostructure arrays, uncoated ZnO nanorod arrays were also prepared under exactly the same conditions. The length of CeO_2 nanotubes is controlled by the length of ZnO template.

2.2.4. Growth of Co_3O_4 nanowire array

The uniform Co_3O_4 nanowire arrays were obtained from calcinations of hydrothermally prepared cobalt chloride hydroxide carbonate ($Co(CO_3)_{0.35}Cl_{0.2}(OH)_{1.1} \cdot 1.74H_2O$).[24] Briefly, 5 mL 0.5 M $CoCl_2 \cdot 6\ H_2O$ and 5 mL 6 M urea solution were mixed under ultrasonic bath until the solution becomes transparent. The pre-cleaned cordierite substrate was then immersed into the as-

prepared solution and sonicated for another 15 minutes before put into water bath (90 ^{o}C) for 24 hrs. Then the substrate after growth was rinsed by DI water several times and was slowly annealed at 300 ^{o}C for 4 hrs.

2.2.5. Synthesis of Pt/metal oxide (MO) nano-array catalysts

The Pt/MO nanorod array catalysts were prepared using the colloidal deposition method.[25] Firstly, unprotected Pt nanoparticle colloid was synthesized by ethylene glycol (EG) method as described in literature. Typically, all operations were carried out under inert atmosphere (Ar or N_2). In a typical preparation, a glycol solution of NaOH (50 mL, 0.5 M) was added into a glycol solution of $H_2PtCl_6.6H_2O$ (1.0 g, 1.93 mmol in 50 mL) with stirring to obtain a transparent yellow platinum hydroxide or oxide colloidal solution which was then heated at 160 °C for 3 h, with an Ar flow passing through the reaction system to take away water and organic by products. A transparent dark-brown homogeneous colloidal solution of the Pt metal nanocluster (Pt: 3.76 g/L glycol, 19.3 mmol/L) was obtained without any precipitates. For deposition, the as-prepared Pt colloid (Pt/cordierite=0.1wt%) was diluted by adding ethanol or acetone as solvent to 15-20 mL in different volume. Cordierite monolith substrates with nanostructure array were then immersed into the dilute Pt colloid solution for 24hours with magnetic stirring. Finally, the sample was dried at 80 ^{o}C in air, and Pt/MO nano-array monolithic catalysts were ready to use.

2.2.6. Synthesis of ZnO/CeO_2 nano-array catalysts

ZnO/CeO_2 decorated and core-shell nano-array catalysts were prepared by the same process of CeO_2 nanotube array without etching of ZnO template. ZnO/CeO_2 decorated or core-shell nanostructure can be controlled via CeO_2 deposition time and cycles.

2.2.7. Synthesis of ZnO/(La,Sr)CoO_3 (LSCO), ZnO/LSCO/Pt nano-array catalysts

The ZnO/LSCO, ZnO/LSCO/Pt nano-array catalysts were prepared by the similar procedure as ZnO/CeO_2 nano-array catalysts. Firstly, ZnO nanorod array with (002) preferential orientation was uniformly grown on cordierite monolith. Then, by dip coating the colloidal precursor we developed,[36] $(La,Sr)CoO_3$ or $(La,Sr)CoO_3$/Pt layers could be uniformly coated on ZnO nanorod surface throughout the whole substrate. Finally the substrate was annealed at 550 ^oC for 10 hours to ensure good crystallinity and adhesion of the coating.

2.2.8. Quantitative analysis of materials usage and catalytic performance in nano-array monolithic catalysts

Estimated Mass of Pt and metal oxide in each catalysts

We estimated the mass of metal oxide nanostructure array on cordierite monolith substrate by simply weighting method: $\mathbf{M(MO)=M_1-M_0}$

$\mathbf{M_0}$ is the mass of blank monolith before metal oxide nanostructure growth;

$\mathbf{M_1}$ is the mass of monolith substrate after metal oxide nanostructure growth;

Mass of Pt was quantified by using statistic TEM EDS element ratio analysis results as reference:

M(Pt)=wt%(Pt/MO)×M(MO)

Wt%(Pt/MO) were obtained from statistic results of TEM EDXS analysis.

(i) Co_3O_4 porous nanowires array on cordierite monolith:

By measuring the mass difference before and after Co_3O_4 porous nanowires array loading, Co_3O_4 porous nanowires loaded on cordierite monolithic catalysts take 10% weight (statistic results) in the monolithic catalysts. The sample we used for catalytic performance test is about 38.3 mg. Then the mass of Co_3O_4 porous nanowires array is about 3.83mg.

Pt loading was controlled with Pt: Co_3O_4 weight ratio of 1% by controlling the total amount of Pt colloidal solution as 1wt% of Co_3O_4 nano-array on monolith. Moreover, TEM EDXS results also confirmed the 1% weight ratio between Pt and Co_3O_4. As a result, Pt loaded on Co_3O_4 porous nanowires array should be no more than 0.0383 mg.

(ii) ZnO nanorods array on cordierite monolith:

The weight percentage of seed nanoparticles with respect to total mass of the dip-coated substrate was determined by weighting method to be (1.57±0.06)%. To reduce the influence of substrate destroy during the growing process, we measure the weight loss after etching of ZnO by using 50 mM HCl solution for 1 min. The weight percentage of deposited ZnO NR arrays with respect to total mass of the grown substrate was determined to be (3.8±0.2)%. Pt/ZnO nanorods array monolithic catalyst we used in our test is 37.17 mg in mass. Then, the amount of ZnO nanorods on it is about 1.484 mg.

The same amount of Pt colloidal solution and loading procedure as Pt/Co_3O_4 loading were used for Pt/ZnO preparation. By TEM EDX analysis, the average weight ratio between Pt and ZnO is 2% (from statistical results), then the mass of Pt in ZnO nano-array monolithic catalysts is about 0.030 mg.

(iii) CeO_2 nanotubes array on cordierite monolith:

The mass of CeO_2 nanotubes loading on cordierite monolith was estimated according to the weight ratio of ZnO:CeO_2 in the composite nanostructure array from SEM EDXS analysis. The average weight ratio of ZnO:CeO_2 is about 3.53:1. As we know, the 1um ZnO nanorods loading amount is about 4% of the total monolith catalysts. So the loading of CeO_2 on cordierite monolith is about 1% of the whole monolith catalysts.

Pt/CeO_2 nanotubes array monolithic catalyst we used in our test is 31.7 mg in mass. Then, the amount of CeO_2 nanotubes on it is about 0.317 mg.

We use the same amount of Pt and the same procedure for Pt/CeO_2 catalysts preparation as for Pt/ZnO. TEM EDX analysis results show that the average weight ratio between Pt and CeO_2 is 10% (from statistical results), so the mass of Pt in the monolithic catalysts is about 0.0317 mg.

(iv) TiO_2 nanorods array on cordierite monolith:

The mass of TiO_2 nanorods loading on cordierite monolith was estimated according to the law of mass conservation. Assuming that all Ti precursor 100% converted to TiO_2, The total mass of TiO_2 should be 250 mg. Actually, not all of the TiO_2 were loaded on the monolith substrate. There are TiO_2 precipitates on the bottom of the reactor. We collect, dry and weight the precipitates. It is about 203.5 mg in mass. There are 46.5 mg TiO_2 on 3.06 g cordierite monolith. Then, we got that there were 0.4463 mg TiO_2 nanorods array loading on 29.4 mg monolithic catalysts, which we used for the CO oxidation tests.

The same amount of Pt and the same procedure as the above three catalysts were used for Pt/ TiO_2 nano-array catalysts synthesis. As the statistic results of weight ratio between Pt and TiO_2 is 8% (from statistical results from TEM analysis), the mass of Pt in the monolithic catalysts is about 0.0357 mg.

2.2.9. Catalyst evaluation

A BenchCAT reactor (Altamira Instruments) was used for CO oxidation tests. Dycor Dymaxion mass spectrometer and Agilent Micro GC were used for the gas species analysis in the product stream. Oxidation study was carried out in a temperature range of 20–500 °C using 5 sccm of 10% CO/N_2, 5 sccm of O_2, and 40 sccm of argon, i.e., 1% CO, 10% O_2, 9% N_2, and 80% Ar.

2.3. Results and Discussion

2.3.1. Morphology and Structure of Various Nanostructure Arrays

Figure 2.1b shows the photograph of image for four types of nano-array based monolithic catalysts including ZnO, TiO_2, CeO_2 and Co_3O_4. Scanning electron microscope (SEM) top-view images of ZnO nanowire array rooted cordierite monolith channels are shown in Figure 2.1c at low magnification. The as-synthesized Co_3O_4 nanowires (~10 μm long) in Figure 1d-e exhibited a high uniformity as well as well aligned and densely packed array characteristics. The closer view electron micrographs in Figure 2.1f–m revealed the well-defined structural and morphological characteristics of the grown metal oxide nano-arrays on monolith substrates. For instance, Figure 2.1f (SEM) and 2.1j (TEM) identified the ZnO nanowire arrays with good uniformity and coverage, single crystallinity, a diameter of ~60 nm and [0001] growth direction. Table 2.1 summarizes the physical, chemical, and structural characteristics of the as-grown metal oxide nano-arrays.

Material	Array Morphology	Diameter (nm)/ Length (μm)	Wall thickness or pore size (nm)	Structure/ Crystallinity	Growth direction	d-spacing (nm) /crystal plane	Images (Figure 2)
ZnO	nanorod/ nanowire	50-150/ 1 – 5	--	Wurtzite/ Single crystal	[0001]	0.52/{0001} 0.28/{01-10}	b, e, i
TiO_2	nanorod	50 -130/ 0.5-1	--	Brookite/ Single crystal	[001]	0.35/{120} 0.51/{001}	f, j
CeO_2	nanotube	70-200/ 1-5	10-20	Fluorite/ Polycrystal	--	0.31/{111}	g, k
Co_3O_4	Porous nanowire	100 -200/ 1 – 12	20 (10-50)	Spinel/ Polycrystal	--	0.46/{111} 0.28/{220}	c, d, h, l

Table 2.1. Structure characteristics of grown nano-arrays on bare monolith substrates.

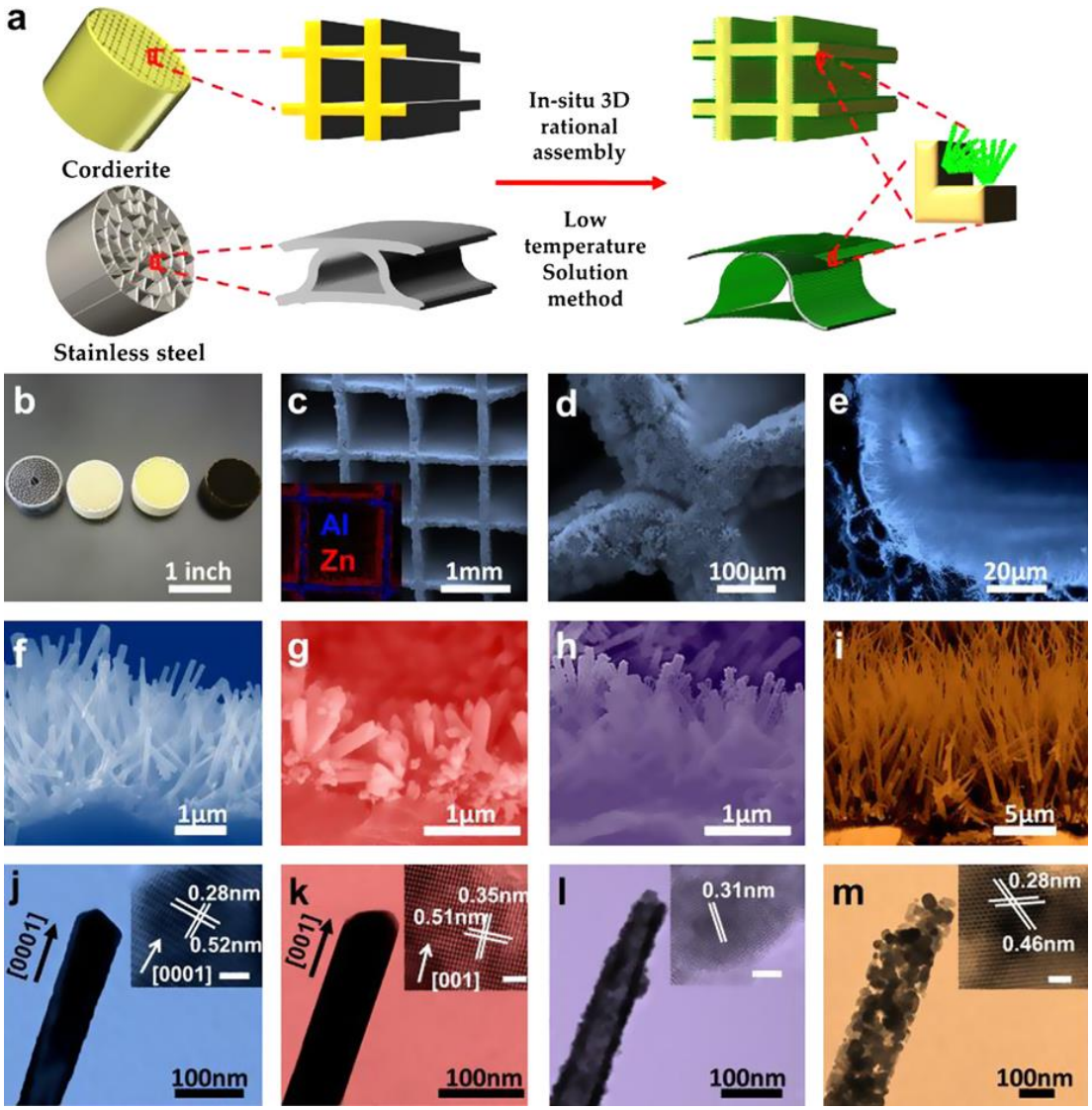

Figure 2.1. a) Schematic illustration for the 3D integration of nano-arrays onto the monolithic cordierite and stainless steel substrate by a hydrothermal approach; b) Photographs of monolithic nano-array catalysts with various nano-arrays deposited; c) low magnification SEM image of ZnO nano-array catalyst with inset showing the element distribution; d-e) low magnification top and cross-sectional SEM images of nano-arrays; f-i) cross-sectional SEM images of f) ZnO nanowire arrays; g) TiO_2 nanorod arrays; h) CeO_2 nanotube arrays; i) Co_3O_4 nanowire arrays; j-m) corresponding TEM characterization of nano-arrays shown in f-i).

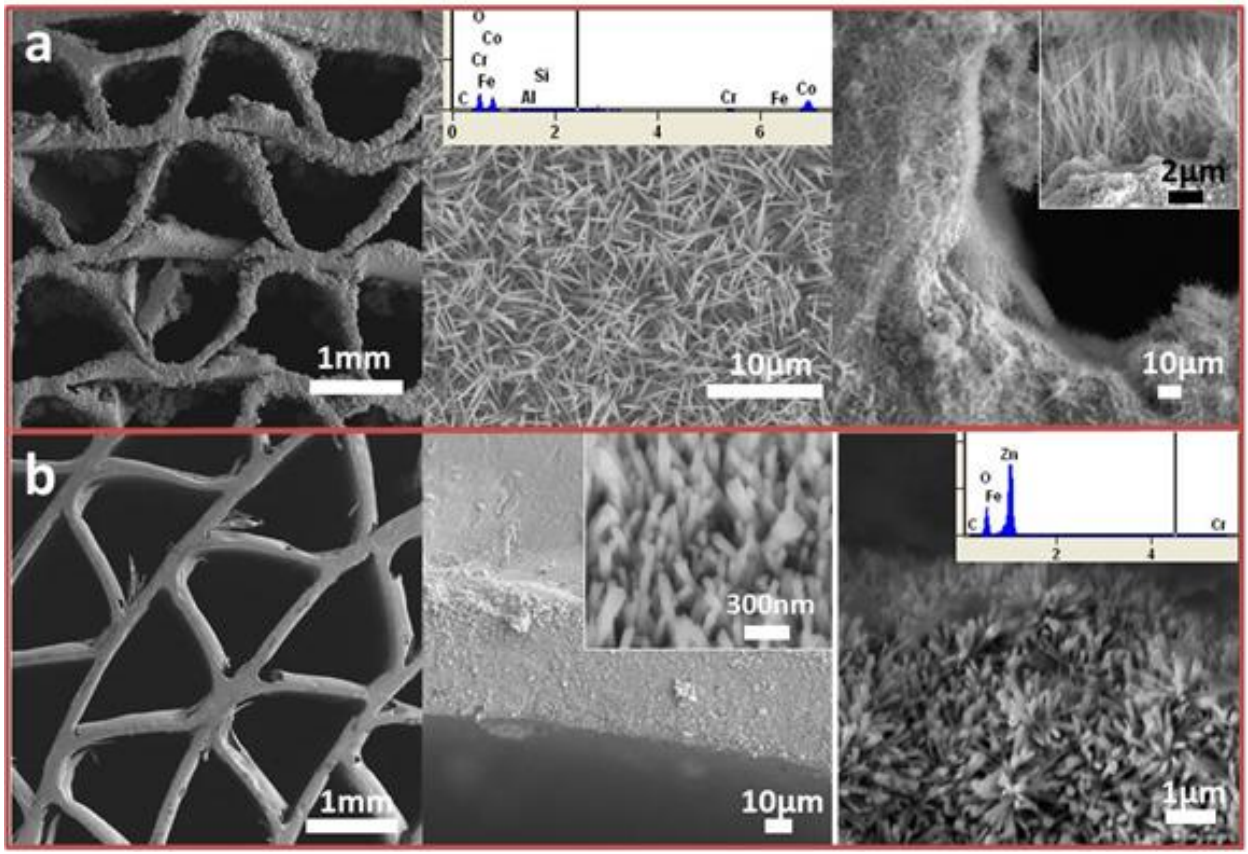

Figure 2.2. SEM and EDS elemental analyses of single-component nanostructure array grown on stainless steel monoliths: a) Co_3O_4 porous nanowire array; b) ZnO nanorod array.

Figure 2.2 shows the uniform deposition of nano-array catalyst onto the stainless steel substrates by the same low temperature hydrothermal synthesis which further indicates the wet chemical synthesis we developed is a generic strategy to fabricate monolithic Nano-array catalyst on various monolithic substrates.

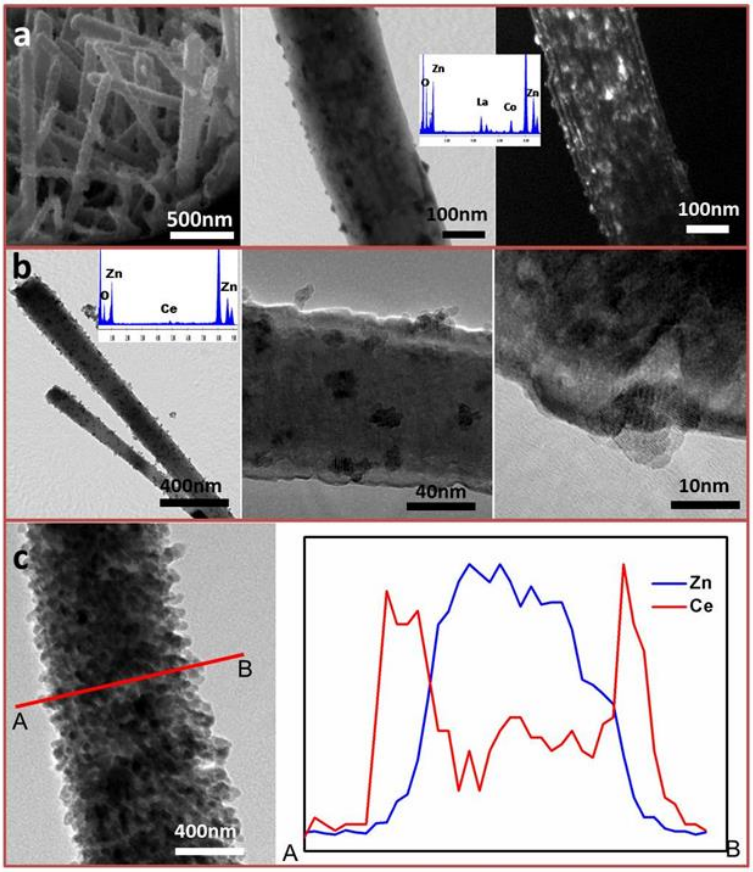

Figure 2.3. Electron microscopy images and spectra of metal oxide-metal oxide binary nanostructure array on monolith: a, ZnO/LSCO decorated nanorods. b, ZnO/CeO_2 decorated nanorods. c, TEM image and corresponding EDS line analysis on ZnO/CeO_2 core-shell nanorod.

The nano-array with well defined geometry also enables the hierarchical complexity with multiple components incorporated for added functionality. In Figure 2.3, the composite nano-arrays featuring ZnO nanorod as the core and CeO_2 or perovskite (La,Sr)CoO_3(LSCO) as the shells have been demonstrated. The added CeO_2 or perovskite serve as the catalytic active sites which utilizes the merits of ZnO nano-array support to enable high surface area and better catalyst dispersion. Specifically, Figure 2.3a shows uniform coverage of LSCO layer upon ZnO nanorod leading to a rough surface. Both dark-field TEM images and EDS spectrum reveals and confirms the deposition of LSCO. Similar sol-gel process can be used to coat a uniform layer of

CeO_2 nanoparticles on the ZnO nanorod surface. The TEM characterization in Figure 2.3b and elemental line scan across these composite nanowires in Figure 2.3c shows the CeO_2 nanoparticles are well dispersed on ZnO nanorods.

2.3.2. Catalytic CO oxidation performance of metal oxide/Pt Nano-arrays

Fig. 2.4a–d displayed the individual ZnO, TiO_2, CeO_2, and Co_3O_4 nanostructures loaded with well-dispersed 2nm Pt nanoparticles on their well-defined crystal surfaces with the inset lattice images clearly identifying the exposed Pt (111) atomic planes. The X-ray diffraction characterization in Figure 2.5 further confirms the crystalline nature of both the support oxides and the loaded Pt nanoparticles. The light-off temperatures (where 50% of CO conversion is achieved) for CO oxidation of Pt-loaded CeO_2, ZnO, Co_3O_4, and TiO_2 nano-array monolithic catalysts are 193 °C, 260 °C, 195 °C, and 258 °C, respectively, and the 100% CO conversion was achieved below 300 °C (Figure. 2.4e). The better CO oxidation performance in Pt/CeO_2 nanotube and Pt/Co_3O_4 porous nanowire array is due to the promotion effect of Co_3O_4 and CeO_2 nanostructure support to Pt nanoparticle. In both Pt-loaded Co_3O_4 and CeO_2 catalytic systems, CO molecules mainly adsorb on the Pt sites, whereas O_2 could be more favorably adsorbed and activated on the cerium or cobalt sites, which may effectively improve the O_2 adsorption on supported catalysts and thus increase the catalytic activity. Besides, metal-metal oxide interactions may help enhance the catalytic activity as well. In Pt/ZnO and Pt/TiO_2 nanorod array monolithic catalysts, similar CO catalytic oxidation performance was achieved, which follows a Langmuir-Hinshelwood mechanism that both CO and O_2 adsorb on the Pt surface itself. Figure 2.4f shows the ZnO, Co_3O_4 and TiO_2 nano-array supported Pt monolithic catalysts all displayed a very stable 100% CO conversion to CO_2 at T_{100} throughout the 24 h. In Pt/CeO_2 nano-array catalysts, 100% CO conversion only sustained the initial 6h. The catalytic activity degradation is

caused by its relatively lower thermal and mechanical stability. During the isothermal CO oxidation test, the amount of Pt/CeO_2 activity site decrease along with the decrease of surface area caused by sintering effect, in which process CeO_2 nanotubes aggregated to each other leading to the destroy of origin aligned array structure. SEM characterization on the Pt/CeO_2 nanotube array catalysts sample after CO oxidation and catalytic stability test proved that serious damage of nanotube array structure had happened to the catalysts and left a Pt/CeO_2 film on the surface of cordierite monolith channel which may lead to the decrease of catalytic activity.

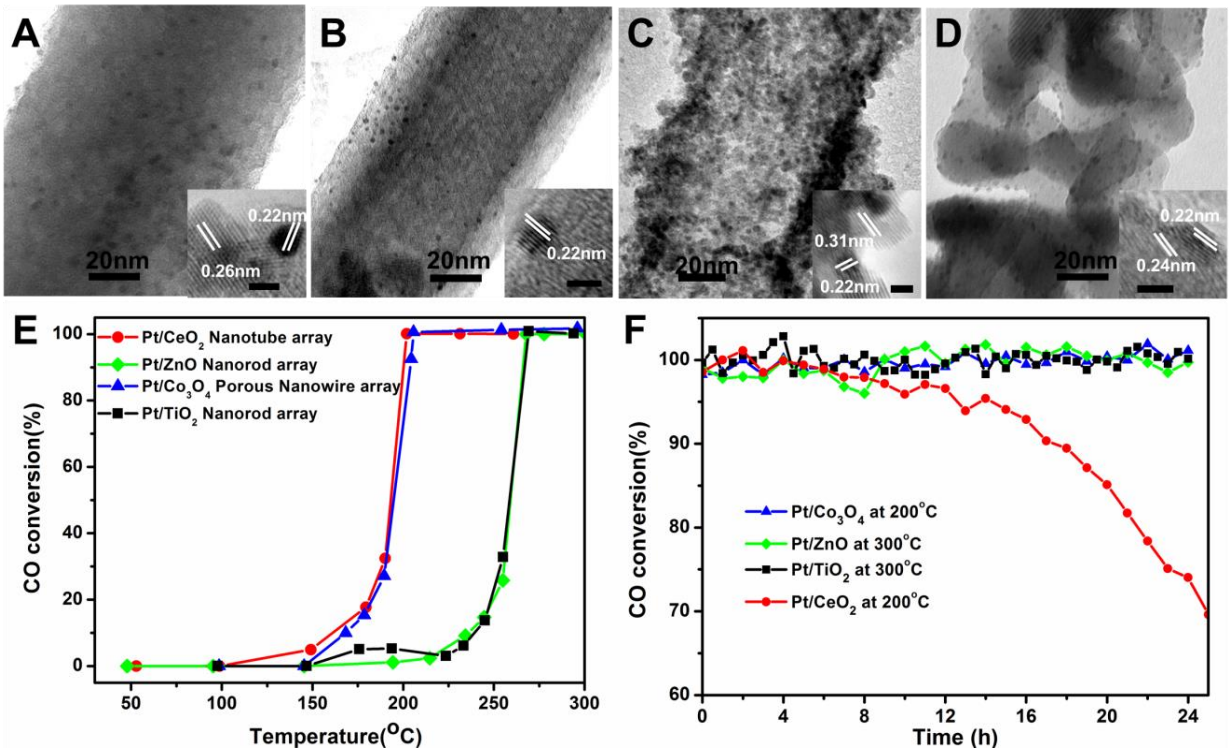

Figure 2.4. CO oxidation over Pt-loaded metal oxide nano-array based monolithic catalysts. Low magnification TEM images of individual metal oxide nanostructure loaded with Pt nanoparticles and its high magnification HRTEM lattice image (inset): (**A**) ZnO nanorod, (**B**) TiO_2 nanorod, (**C**) CeO_2 nanotube, and (**D**) Co_3O_4 nanowire. Scale bars in all the insets are 2 nm. (**E**) CO oxidation conversion as a function of temperature over Pt-loaded (CeO_2, ZnO, Co_3O_4, and TiO_2) nano-array monolithic catalysts. (**F**) Catalytic stability of Pt-loaded (CeO_2, ZnO, Co_3O_4, and TiO_2) nano-array monolithic catalysts.

Compared with the metal oxides nano-arrays on monolithic cordierites, the deposited Pt nanoparticles enhance the catalytic performance toward CO oxidation by pushing the temperatures of complete CO conversion to CO_2 to the lower temperature. Specifically, the 100% CO conversion temperatures are 225 °C, 300 °C, 330 °C and 370 °C for Co_3O_4, TiO_2, CeO_2 and ZnO nano-arrays respectively which are 35 °C higher than Co_3O_4/Pt, 40 °C higher than TiO_2/Pt, 180 °C higher than CeO_2/Pt and 110 °C higher than ZnO/Pt.

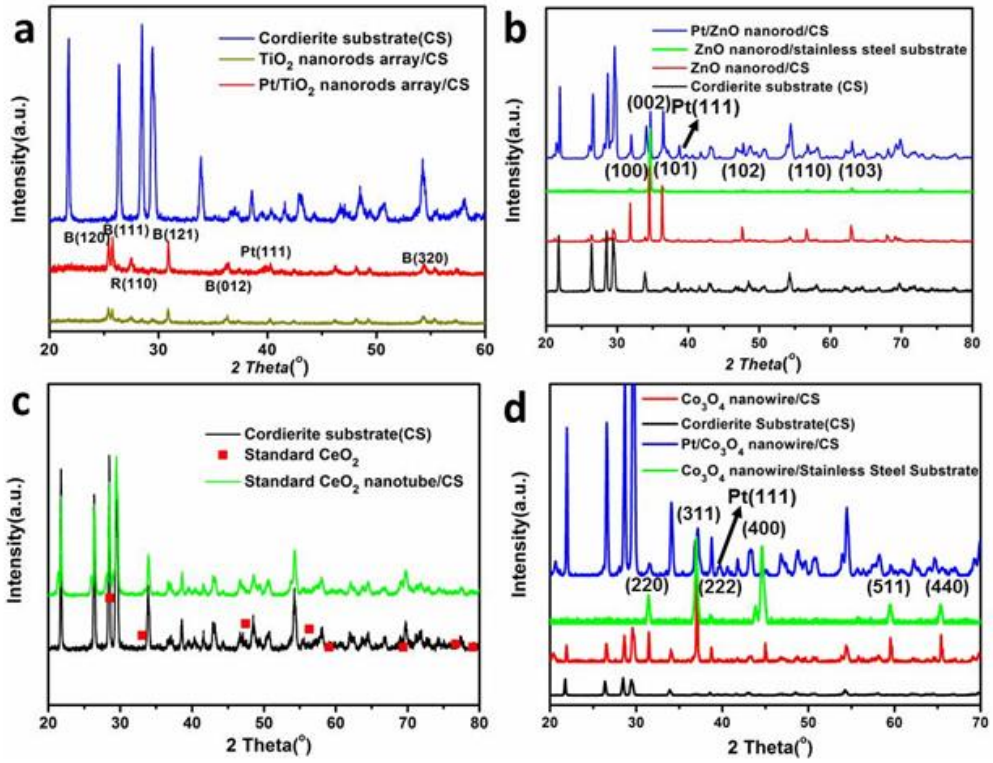

Figure 2.5. XRD spectra of metal-oxide nanorod array on cordierite monolith substrates: a) TiO_2 and Pt/TiO_2 nanorod arrays; b) ZnO and Pt/ZnO nanorod/nanowire arrays; c) CeO_2 nanotube arrays; d) Co_3O_4 and Pt/ Co_3O_4 porous nanowire arrays.

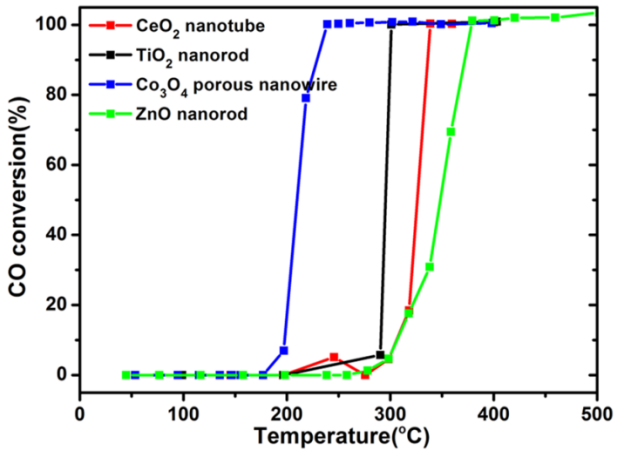

Figure 2.6. CO oxidation of metal oxide nano-arrays on cordierite monolith. CO oxidation conversion efficiency as a function of reaction temperature over CeO_2 nanotube array(red), ZnO nanorod array(green), Co_3O_4 porous nanowire array(blue) and TiO_2 nanorod array(black).

A big advantage of nano-array catalyst over conventional wash-coated powder catalyst is their high materials utilization efficiency of both oxides support and catalytic active noble metal nanoparticles.[29-40] As shown in Figure 2.7, the calculated density of oxide supports used in nano-array configured monolithic catalysts ranges from 6 to 80 g/L which is smaller than that of conventional wash-coated powder catalysts (120-260 g/L). The use of noble metal can be reduced to less than 1 g/L for nano-array catalysts. The thickness of catalyst coating in monolithic nano-array catalyst is less than 10 μm. By comparison to the conventional wash-coated powder catalysts with similar performance, the nano-array configuration has enabled an order of magnitude reduction (10-40 times) in terms of the materials utilization in catalytic reactions which holds great promise for cost-effective design and fabrication of high performance monolithic catalysts.

Catalyst	T_{10} (°C)	T_{50} (°C)	T_{50} (°C)	Mass of loading (Pt/MO, mg/mg)*	Pt loading (g/L)	Metal Oxide loading (g/L)
Pt/ZnO	230	260	267	0.030/1.418	0.49	23.2
Pt/CeO_2	165	193	201	0.0317/0.317	0.74	7.4
Pt/Co_3O_4	168	195	205	0.038/3.83	0.88	88
Pt/TiO_2	245	258	269	0.0357/0.4463	0.52	6.5

Table 2.2. Catalytic performance and materials loading of different metal oxide nano-array monolithic catalysts.

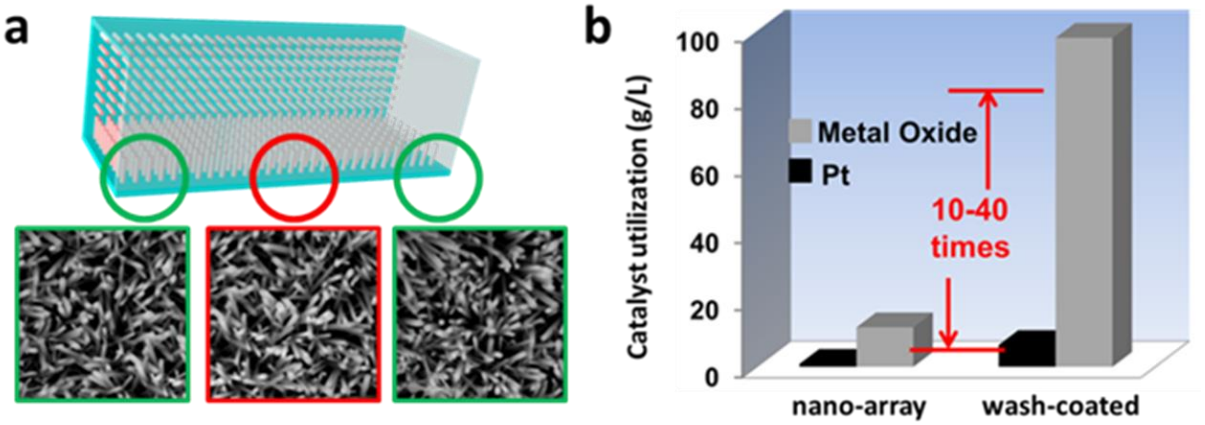

catalyst	oxide support (g/L)	noble metals (g/L)	catalyst thickness (μm)	reference
nano-arrays catalyst	6.5-80	0.4-0.8	1-10	This work
classical washcoat powder catalyst	120-260	1.8-20	20-100	literature

Figure 2.7. a) Illustration of the nano-array within the channels of the monolithic substrate; b) histograms comparison and the table summary of catalyst utilization efficiency for different monolithic catalyst configurations.

Catalyst	Mass (metal oxide, mg)	Mass (Pt, mg)	Flow rate (ml/min)	Space velocity (h^{-1})	CO percentage (vol.%)	T_{50}(°C)	Reference
Pt/Cordierite	N/A	0.25	50	N/A	3% CO in air	223	*(41)*
Pt/Cordierite	N/A	6	50	N/A	3% CO in air	195	*(41)*
Pt/γ-Al_2O_3	72	14	500	30,000	1% CO in air	180	*(42)*
Pt/γ-Al_2O_3	260	0.52	2000	39,000	0.1% CO, 10% O_2/N_2	159-188	*(43)*

Table 2.3. Catalysts usage and 50% conversion temperature of some typical Pt monolithic catalysts reported in literature.

Catalyst	Mass (metal oxide, mg)	Mass (Pt, mg)	Flow rate (ml/min)	Space velocity (h^{-1})	CO percentage (Vol.)	T_{100}(°C)	Reference
Pt/TiO_2	77	0.77	154	120,000 ml/g.h	1 % CO in air	210	*(44)*
Pt/ZnO-Al_2O_3	ZnO:3.76 Al_2O_3:95	2.08	50	N/A	2 % CO/He; air	225	*(45)*
Pt/ZnO	49.5	0.5	100	96,000	0.5 % CO; 10 % O_2/Ar	160	*(46)*
Pt/CeO_2	9	3.5	50	N/A	1 % CO; 20 % O_2 in He	223 (mixture)	*(47)*

Table 2.4. Catalysts usage and 100% conversion temperature of some typical supported Pt powder catalysts reported in literature.

The high activity in these nano-array monolithic catalysts may be originated from three major factors: i) An optimum metal loading and dispersion is achieved in our nano-array monolithic catalysts compared to powder-form monolithic catalysts; ii) The ~1-10 μm high nano-array enables a much better utilization efficiency of the available active sites and promotes CO gas exposure to the nanostructure surfaces by a much shorter diffusion length; and iii) The well-defined nanostructure platform interfaced with the decorated Pt nanoparticles may contribute to more effective charge transport and thus enhanced reaction efficiency.

2.3.3. Morphology of nano-array catalysts after CO oxidation

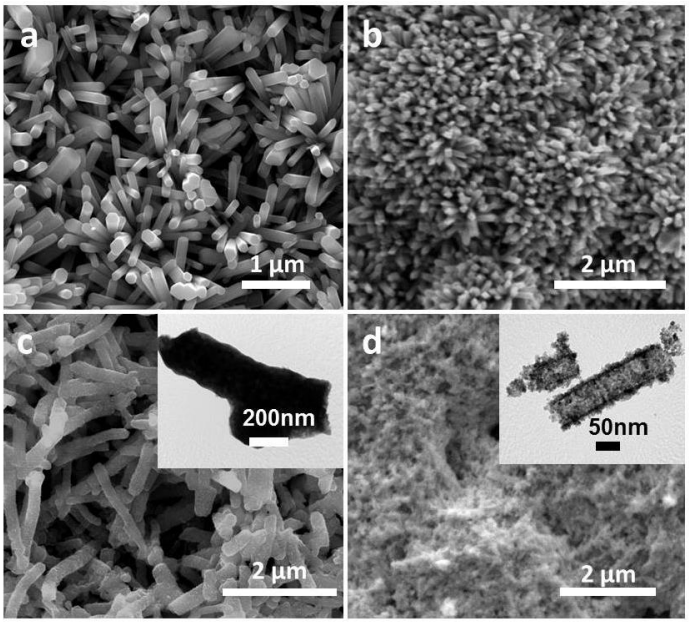

Figure 2.8. SEM and TEM images of nanostructure array catalysts after CO oxidation light-off and catalytic stability test: a, Pt/ZnO nanorods array catalysts. b, Pt/TiO_2 nanorods array catalysts. c, Pt/Co_3O_4 porous nanowire array catalysts; inset: corresponding TEM image. d, Pt/CeO_2 nanotubes array catalysts; inset: corresponding TEM image.

We characterized the structure of nanostructure array catalysts after CO oxidation light-off and stability tests. From the SEM images (Figures 2.8), we can find out that crystalline Pt/ZnO and Pt/TiO_2 nanorods array catalysts retained the array structure very well after 3 times repeat run of CO oxidation light-off test and 300 ^oC 24 hours CO oxidation stability test. However, serious array structure damage was observed on both Pt/Co_3O_4 porous nanowire array catalysts and Pt/CeO_2 nanotube array catalysts in Figure 2.8c and Figure 2.8d, respectively. As shown in inset TEM images, Pt/Co_3O_4 porous nanowire has turned into solid nanorod structure while Pt/CeO_2 nanotube structure still reserved. In summary, after CO oxidation and stability test, Pt/CeO_2 nanotube array monolithic catalysts lost its array structure as a whole but reserve the nanotube structure. Both the array structure and porous nanowire structure were damaged for Pt/Co_3O_4 porous nanowire during the same process. However, CO oxidation performance of Pt/Co_3O_4

porous nanowire did not decrease during stability test, but Pt/CeO_2 nanotube array decreased ~30%, which suggests that in polycrystalline phase, Pt/Co_3O_4 is not as morphology sensitive as Pt/CeO_2 for CO oxidation reaction. The results also hold the potential that the activity of as-prepared nanostructure array catalysts can be effectively improved by tuning the morphology and crystal structure.

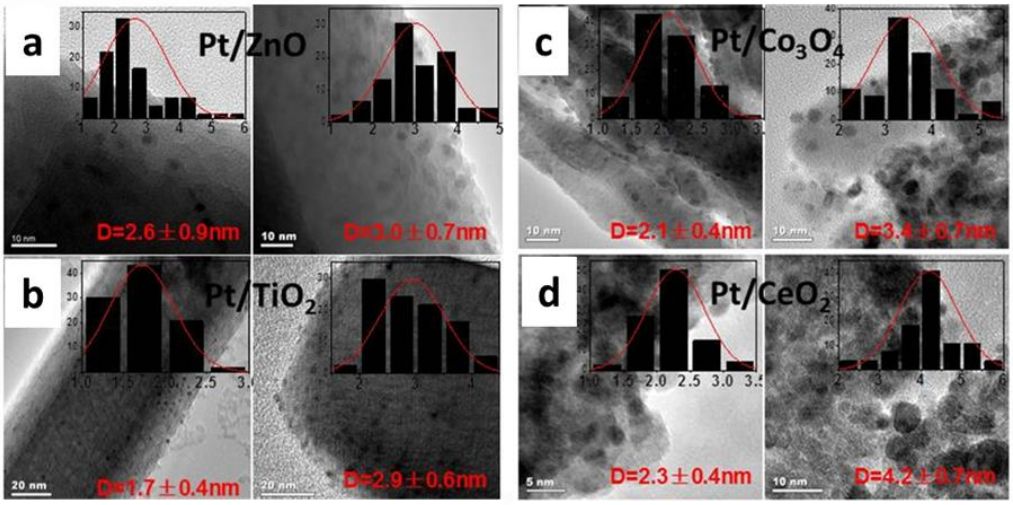

Figure 2.9. TEM images of nanostructure array catalysts before (left) and after (right) CO oxidation light-off and catalytic stability test: a, Pt/ZnO nanorods array catalysts. b, Pt/TiO_2 nanorods array catalysts. c, Pt/Co_3O_4 porous nanowire array catalysts. d, Pt/CeO_2 nanotubes array catalysts. Axis of inset spectra: Particle diameter (nm). The diameter range was determined by covering up 70% of nanoparticles.

Pt particle morphology and size distribution change on metal oxide nanostructure array before and after CO oxidation were also characterized by HRTEM. Interestingly, Pt nanoparticles preserve small size and good distribution on metal oxide nanostructure surface. It is widely accepted as a particularly crucial issue to stable metal nanoparticles in the size range blow 5 nm. It is also reported that the TTAB-capped Pt on silicon wafer and Pt/MCF exhibited severe aggregation of Pt particles after CO oxidation at 300 ^{o}C, which hampered the quantitative study

of CO oxidation above the ignition temperature regime. However, in our metal oxide supported Pt catalysts system (Figure 2.9), Pt nanoparticles still maintain the particle size smaller than 5 nm after 24 h 300 ^{o}C CO oxidation stability tests, even though there are slightly size increase (from 2 nm to 3-4 nm according to different catalysts system). Moreover, the catalytic activity of metal oxide/Pt nanostructure array catalysts did not decrease (except CeO_2/Pt) after 24 h 300 ^{o}C on stream tests. The metal oxide-Pt interface may play an important role in the stability of as prepared nanostructure array catalysts.

2.3.4. Thermal stability and mechanical robustness of monolithic nano-array catalysts

Thermal and mechanical stability of monolithic catalysts is crucial to various catalytic processes at elevated temperature, such as catalytic combustion, steam reforming, and automobile exhaust after treatment. In vehicular applications, the monoliths are also subjected to excessive mechanical vibrations. To evaluate the thermal and mechanical robustness of nano-array based monolithic catalysts, we conduct a series of time dependent studies on thermo-gravimetry, surface area changes, structure and morphology evolution, and mechano-gravimetry. For the nano-array monoliths based on ZnO, TiO_2, and Co_3O_4, less than 1% mass change was observed after a 100-hour 800 °C isothermal annealing process. The corresponding XRD spectra revealed no phase segregation for ZnO, TiO_2, and Co_3O_4 nano-array monoliths. From inset SEM images, the ZnO and TiO_2 nano-array structures remained intact despite the gradually smoothened edges of the nanorods. In Co_3O_4, the as-prepared porous nanowires with relatively smooth surfaces turned into zigzag periodic and rough nanowires after 24 hours annealing at 800 °C (Figure 2.10c). However, the morphology of Co_3O_4 nanowires did not change further after 24 hours. The pore size distribution changed little with an average 20 nm pore size maintained throughout the

800 °C isothermal process (Figure 2.11), but the pore volume dropped by ~46% after the first 24 hours, indicating the decrease of pore population.

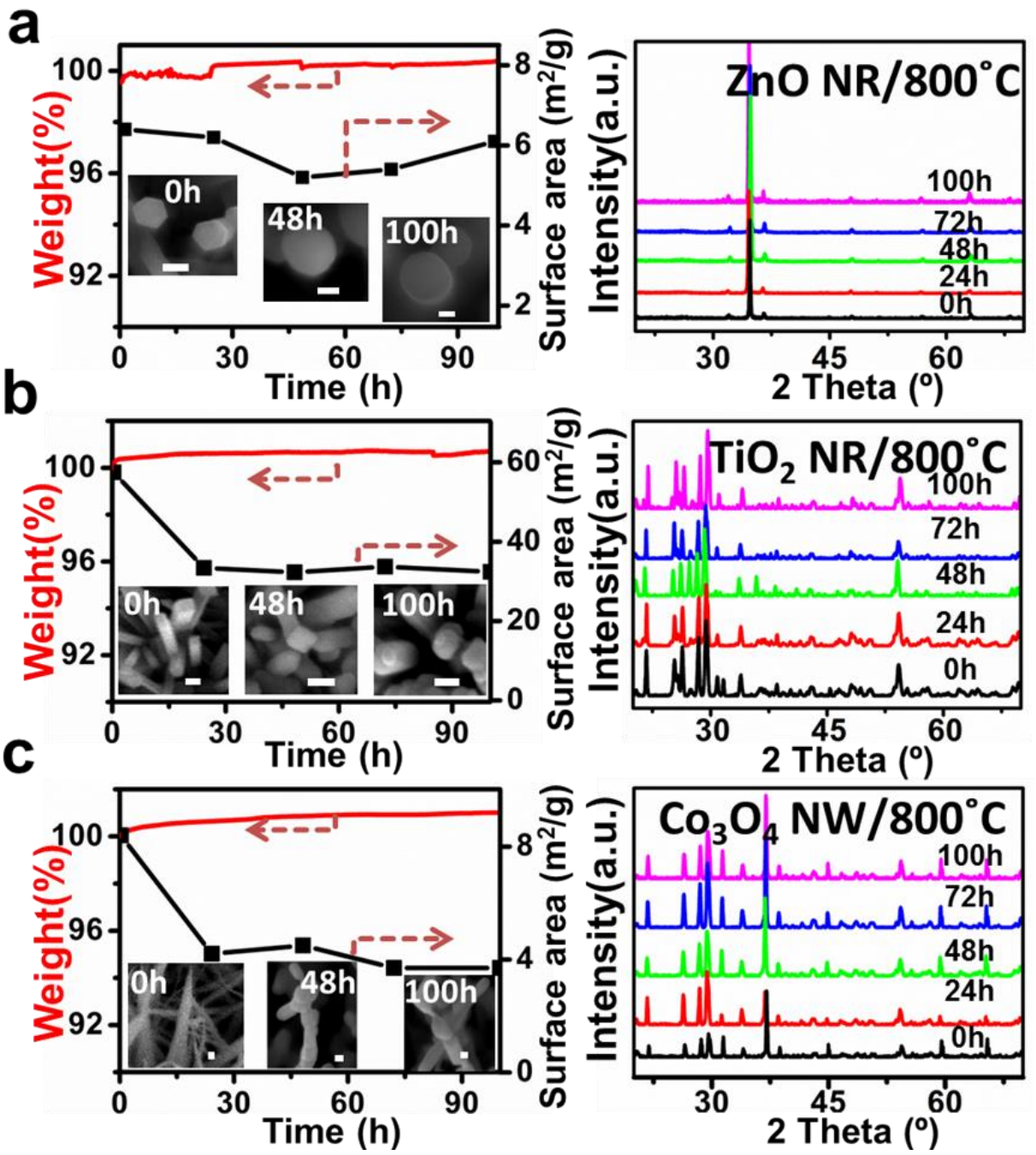

Figure 2.10. Morphology, weight loss and crystal structure characterization of typical monolithic nano-array catalysts during 100 hours' thermal annealing at 800 °C.

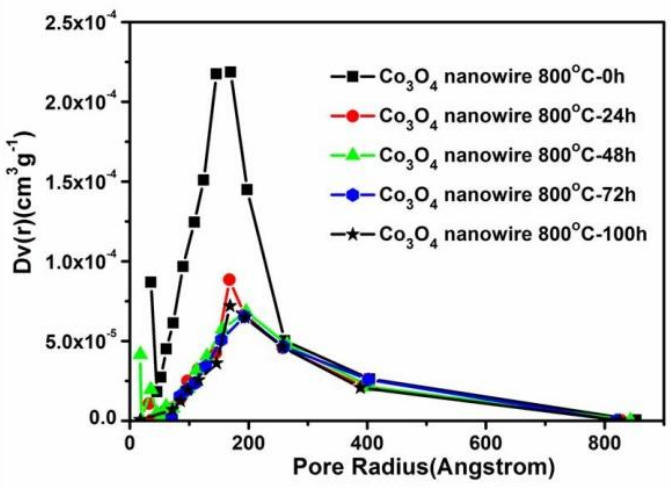

Figure 2.11. Pore size distribution of Co_3O_4 porous nanowires array on cordierite monolith after different annealing time at 800 ^oC.

Due to the polycrystalline nature and the templated synthetic strategy, the CeO_2 nanotubes array suffers from poor thermal stability. TGA-DSC spectra and the corresponding SEM images after thermal analysis experiments on the CeO_2 nanotube array based monolith sample are shown in Figure 2.12. After 1000 ^oC TGA test, the uniform layer of CeO_2 nanotube array cracked into isolated islands ~10 μm wide individually, which are composed of intact CeO_2 nanotube array. However, CeO_2 nanotube array morphology retained in large scale after 400 ^oC TGA test. With increasing TGA temperature to 500 ^oC, the nanotube array structure collapsed as a result of sintering effect, with some of them easily peeled off from the monolith substrate during the sample preparation. These results indicate that the template-induced CeO_2 nanotube array needs to work below 500 ^oC in order to maintain their robustness. Compared with the thermal analysis spectra of bare cordierite monolith in Figure 2.12d and metal oxide nano-array monolithic catalysts, the small peak on DSC curve around 100 ^oC was also observed in all those spectra, which suggest the peak around 100 ^oC originated from the monolith substrate with nothing to do with metal oxide nano-arrays.

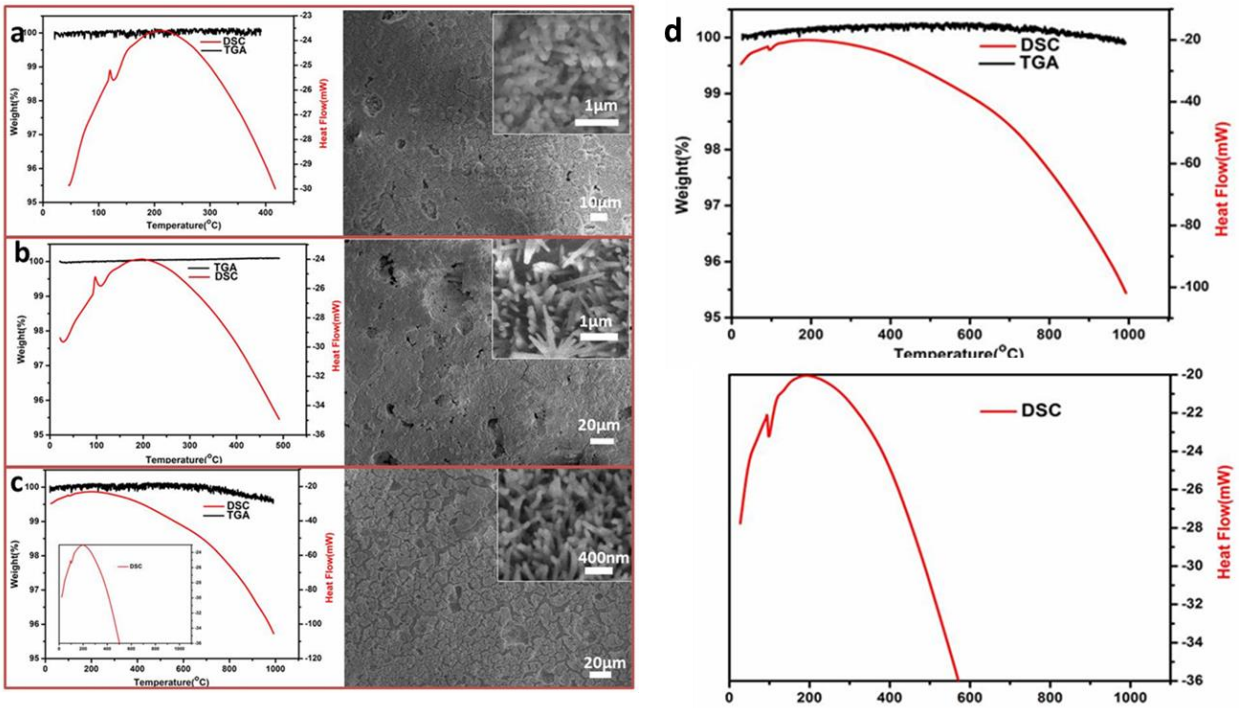

Figure 2.12. Thermal analyses (TGA/DSC) spectra and the corresponding SEM images after testing of CeO_2 nanotubes array: a) 400 ^oC b) 500 ^oC c) 1000 ^oC; d) thermal analyses (TGA and DSC) spectra of bare cordierite monolith substrate.

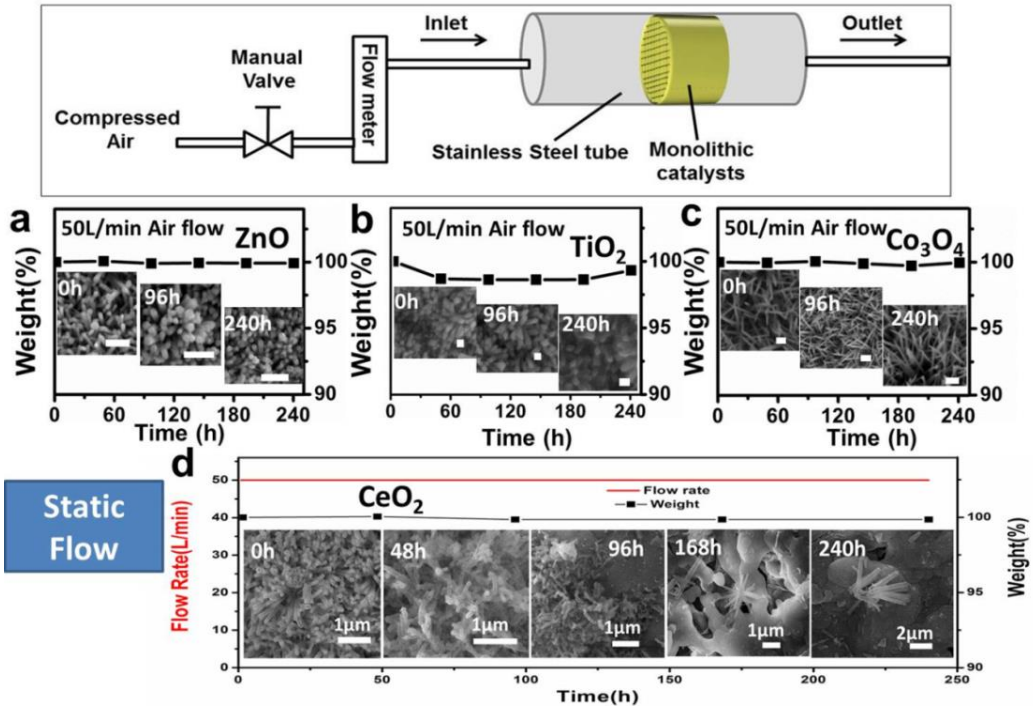

Figure 2.13. Experimental set-up for mechanical robustness study of monolithic nano-array catalysts. Time dependent morphology and weight loss at constant air flow of 50L/min: a) ZnO nanorod array; b) TiO_2 nanorod array; c) Co_3O_4 nanowire array; d) CeO_2 nanotube array.

The measured BET surface area of TiO_2 nanorod array monolith decreased by ~43%, from 57 m^2/g to 33 m^2/g after 24 hours' annealing at 800 °C. After that, surface area stayed constant throughout the remaining 76 hour isothermal process. Similar to TiO_2 nanorods, the surface area of Co_3O_4 nanowire array monolith decreased from 8 m^2/g to 4 m^2/g after 24 hours' annealing at 800 °C, and then remained stable for the next 76 hours. However, the surface area of ZnO nanorod array monolith remained constant without obvious decrease in the 100 hour annealing at 800 °C. The decrease in surface area for nano-array monolithic catalysts upon the high temperature annealing is due to the sintering induced densification followed by grain growth. However, compared with the significant surface area decrease in conventional powder-form catalysts (50% decrease in ZnO; >80% decrease in TiO_2 and Co_3O_4) under high temperature, ZnO, TiO_2 and Co_3O_4 nano-array monoliths demonstrated much higher thermal stability in both short-term and long-term scales (5%, 43%, and 56% surface area decrease for ZnO, TiO_2, and Co_3O_4, respectively). The well-separated but densely-packed nano-arrays effectively defined and utilized spaces between individual nanostructures with high surface area, therefore suppressing the sintering induced densification and grain growth.

In order to test the nano-array adhesion and structure stability, we applied high velocity air flow (static 50 L/min or pulsatile flow) on the nano-array monoliths for 10 days, and monitored the nano-array morphological variation and weight loss throughout. The results summarized in the Figure 2.13 suggested that ZnO, TiO_2, and Co_3O_4 nano-array monoliths exhibited excellent mechanical stability under static air for 10 days. From the inset SEM images, the nano-array

morphology retained with little change throughout. The weight losses of above three nano-array monolithic catalysts were less than 1% individually. For CeO_2 nanotube array, however, after flushing for 48 hours, serious structure damage was observed (Figure 2.13d), some of CeO_2 nanotubes were blown down by air flow and started to aggregate. Continuing flushing for another 48 hours, large area of bare substrate appears on the monolith substrate and nearly half of the CeO_2 nanotubes were blown away. And after flushing for 168 hours, it is difficult to find CeO_2 nanotube array on the cordierite channels and just a few nanotubes left on the monolith surface. The weak adhesion in CeO_2 nanotube arrays to the substrates is due to the template process involved in their growth. Both ZnO seed layer removal and non-uniform distribution of CeO_2 coating on ZnO nanorod array templates have played important roles in drastically reducing the adhesion upon removal of ZnO nanorod templates.

A pulsatile flow flushing set up was also introduced for testing the mechanical stability of the as-prepared nanostructure array monolith catalysts. During the test, air flow was switched between 0 and 60 L/min and controlled by a manual switch. 200 cycles were performed in each test. SEM was used to analyze the morphology change in a large scale after experiments. Shown in Figure 2.14, all the as-prepared nanostructure exhibit high stability and maintain the array structure and morphology after 200 cycles of high pulsatile air flow. On the other hand, directly grown single crystal TiO_2 and ZnO nano-array monolithic catalysts show great stability and vibration resistance to mechanical vibrations (>1 hour) introduced by Sonicator (42 KHz, 135 W) in both distilled water and ethanol. While Co_3O_4 porous nanowire and CeO_2 nanotube arrays show some damage due to the polycrystalline nature and non-uniformity of thickness throughout the length of individual nanowire or nanotube.

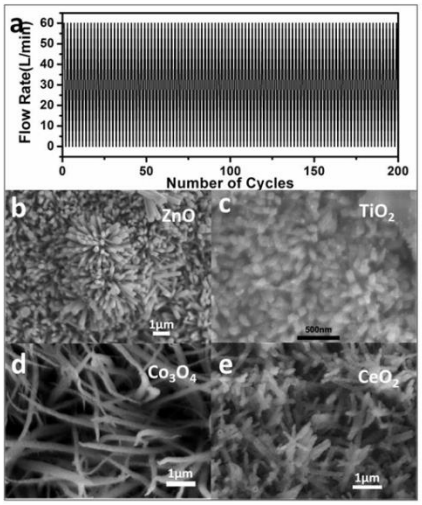

Figure 2.14. Pulsatile flow flushing and corresponding SEM images after testing: a) flow-rate VS circles; b) ZnO nanowires array; c) TiO_2 nanorods array after test; d) Co_3O_4 porous nanowire array after test; e) CeO_2 nanotubes array after test.

Temperature programmed H_2 reduction were carried out to evaluate the stability of metal oxide nanostructure array in reduction atmosphere. TiO_2 nanorods on cordierite monolith show high stability and inertness in H_2 atmosphere. There is no peak in the range of 20-750 ^oC and no structure change (Figure 2.15). ZnO nanorods on monolith substrate start to be reduced at 450 ^oC and get peak centered at 550 ^oC. The whole reduction window ranged from 450 ^oC to 650 ^oC. TPR spectra of Co_3O_4 porous nanowires array on cordierite monolith and SEM image after TPR are shown in Figures 2.15b and 2.15d, respectively. There is a very large H_2 consuming peak ranged from 250-550 ^oC and centered at 350 ^oC, which suggests that reduction reaction may happen. No obvious structure changes were observed on the nanowire array structure under SEM. However, the XRD after TPR shows a Co peak in the spectrum confirms that certain amount of Co_3O_4 were reduced into metal Co in the TPR process. CeO_2 nanotube array on monolith substrate were also tested. There is a wide H_2 consuming peak ranged from 300-650 ^oC and centered at 400 ^oC and 550 ^oC respectively. And no obvious structure changes were observed on

the nanotube array structure under SEM. After TPR-H_2 testing, there seems to be no ZnO left on the monolith substrate under SEM investigation. All ZnO nanorods are reduced in to Zn in TPR process and Zn evaporated with the carrier flow in the process. Therefore, ZnO nanorods array are stable in reduced atmosphere below 450 ^oC.

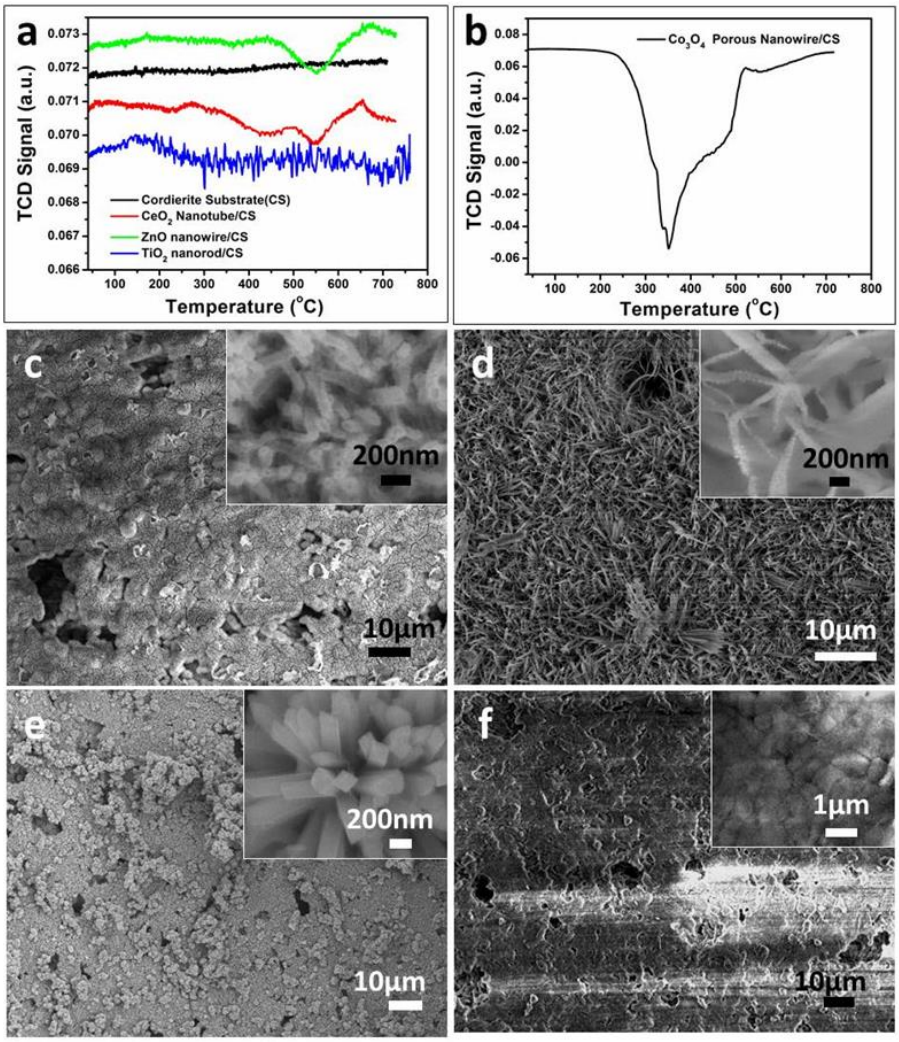

Figure 2.15. TPR-H_2 spectra and corresponding SEM images after testing: a) TPR-H_2 spectra of bare cordierite, CeO_2 nanotube on cordierite, ZnO nanowires on cordierite, TiO_2 nanorod on cordierite; b) TPR-H_2 spectra of Co_3O_4 porous nanowire on cordierite; c) CeO_2 nanotubes array after TPR test; d) Co_3O_4 porous nanowire array after test; e) TiO_2 nanorods array after TPR test; f) ZnO nanowires array after test.

2.3.5. Tunable catalytic activity by rational geometry control of nano-array catalyst

The clear purview of morphology and metal-metal oxide support interaction dependence of catalytic activity in nanostructured catalysts holds crucial importance in their rational design, synthesis, and application. To gain such understanding, however, is a non-trivial task. Here we use the nano-array monolithic catalysts as a model platform to practically investigate the catalytic activity dependence on the nanostructure size, shape (crystal facets), and metal-support interaction. Taking Pt/ZnO nano-array catalysts as an example, we investigated the Pt dispersion effect on ZnO nano-arrays with different aspect ratio (length/diameter), and also investigated the metal-metal oxide support interaction effect on CO oxidation over ZnO nano-arrays with different predominant crystal facets. As shown in Figure 2.16, nano-arrays of ZnO nanoplates with (0001) polar surface predominantly exposed and ZnO nanorods with different lengths (1 μm and 5.5 μm) are successfully fabricated with equal amount of 2 nm Pt nanoparticles loaded.

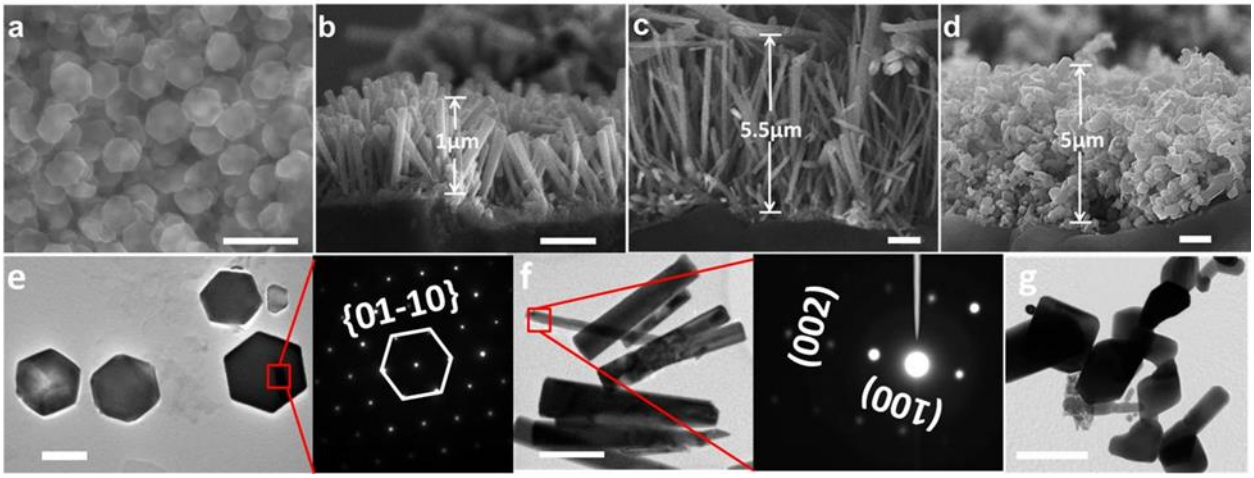

Figure 2.16. Electron microscopy characterization of ZnO nano-arrays with different shapes and sizes. SEM images of a) nanoplates; b) 1 μm nanowire; c) 5 μm nanowire; d) wash-coated ZnO powders. TEM images of e) ZnO nanoplate with electron diffraction pattern; f) ZnO nanowires with electron diffraction pattern; g) ZnO powders.

It is noticeable in Figure 2.17a that, with similar Pt loading, 5.5 μm ZnO nanowire array monolithic catalysts exhibited better CO oxidation catalytic activity than 1 μm ZnO nanorod array. The T_{10} temperature of 5.5 μm Pt/ZnO nanowire array decreased by ~10 °C (220 °C) compared to that of the 1 μm one. Similarly, the T_{50} and T_{100} temperatures of 5.5 μm Pt/ZnO nanowire array decreased significantly, ~30 °C lower than those of 1 μm one. The calculated catalytic activities (per gram of Pt) at 230 °C for the 5.5 μm and 1 μm Pt/ZnO nanowire arrays are 4.1 mmol and 1.1 mmol, respectively (Table 2.5). The CO conversion efficiency enhancement with increasing nanowire length may be due to a higher dispersion of Pt nanoparticles on longer ZnO nanowires, associated with their increased chance for strong ZnO-Pt interaction and active sites.

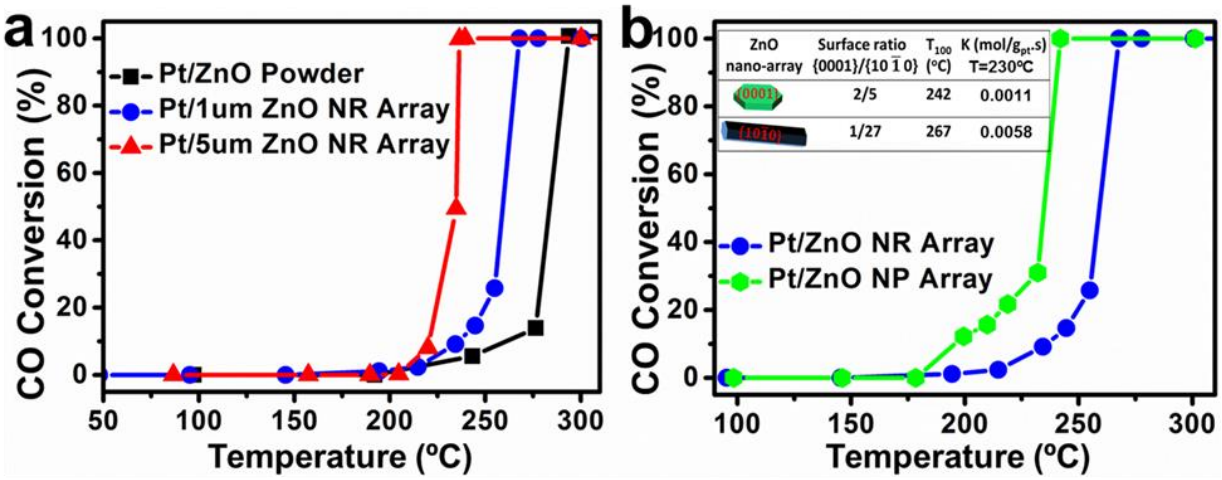

Figure 2.17. Catalytic CO oxidation performance of Pt loaded on ZnO nano-arrays with different lengths and shapes.

Catalyst	T_{10} (°C)	T_{50} (°C)	T_{100} (°C)	ICP loading (Pt/MO, mg/mg)	Pt loading Ratio (g/L)
1μm Pt/ZnO NR	230	260	267	0.034/2.284	0.49
5μm Pt/ZnO NR	220	234	236	0.035/5.13	0.51
Pt/ZnO NP	195	235	242	0.019/1.092	0.28

Table 2.5. Catalytic performance data of various ZnO nano-array (nanorod (NR) and nanoplate (NP)) monolithic catalysts

On the other hand, to investigate the shape dependence of catalytic behavior, ZnO nano-arrays made of nanorods and nanoplates with the same mass loading were uniformly grown on monolithic substrates. These catalysts have predominant {0001} or $\{01\bar{1}0\}$ crystal surfaces, and crystal surface area ratios. With the identical mass loading over ZnO nano-arrays, normalized amount, crystallinity and size of Pt nanoparticles, the Pt-ZnO interface effect on different ZnO crystal facets was successfully investigated over the CO oxidation behavior. The CO light-off curves in Figure 2.17b clearly suggest that, Pt/ZnO nanoplate array catalysts exhibited ~20 °C lower T_{100} (242 °C) than ZnO nanorod array catalysts. Given the identical experimental parameters control, the catalytic activity difference between the nanoplate and nanorod catalysts is due to the different crystal surface area ratio of {0001} to $\{10\bar{1}0\}$ (inset of Figure 2.17b), i.e., the different Pt-ZnO facets interaction effect. The interaction of Pt and Zn^{2+} could lead to localized electron transfer on Zn-terminated (0001) surface, resulting in lower CO desorption temperature may be responsible for the lower CO oxidation temperature in Pt/ZnO nanoplate than that of Pt/ZnO nanorod.

2.4. Conclusions

Several features and advantages of nano-array based monolithic catalyst over powder wash-coated monolithic catalyst are summarized as follows.

- Good uniformity and controlled nano-array thickness as well as free of binders
- High materials utilization efficiency with an order of magnitude reduction of catalyst usage (both oxide support and noble metals) without catalytic performance sacrificed
- Good thermal and mechanical stabilities, small surface area and weight loss during prolonged durations of high temperature aging and high velocity gas flux
- Well-defined catalyst structures with controlled geometry and orientation, providing a good platform to understand the exact structure-property relationship of monolithic catalyst
- Adjustable catalytic activity by manipulating nanostructure size and shape as well as controlled chemical composition.

Although the selected metal oxide nano-arrays demonstrated here still have a long way to go before it could be considered the best options as either supports or catalytically active materials for the low temperature catalytic oxidation, it is worth noticing that these selected metal oxide systems provide us with the model systems to better understand and design the new class of nano-array based structured catalysts with better performance and functions for various energy and environmental applications.

In summary, the metal oxide nano-array based monolithic catalysts represent a new and effective model platform for bridging catalytic nanomaterials science and engineering with the practical

industrial catalysis and enhancing the predictive catalysis science through the enabled exacting relations between tunable nanomaterials size, shape, structure, tailorable metal support interaction and multifunctional catalytic performances. It is worth pointing out that a wide spectrum of single-component or multicomponent nano-array building blocks can be integrated with various geometrical, chemical, structure and functional properties for the nano-array monolithic devices. Therefore, the 3D configurated nano-array based monoliths provide a general strategy for integration of different functional nanostructure arrays with commercially available monolithic substrates and may bring up a broad array of nanostructure based monolithic devices with ultra-efficient, robust and multifunctional performance for various catalytic energy, environmental and biotechnology applications.

2.5. Reference

[1] Stitt, E. H., *Chemical Engineering Journal*, **2002**, *90*, 47–60.

[2] Boger, T., Heibel, A. K., Sorensen, C. M., *Industrial and Engineering Chemistry Research*, **2004**, *43*, 4602–4611.

[3] Cybulski, A., Moulijin, J. A., *Structured Catalysts and Reactors*, Taylor Francis, **2006.**

[4] Li, X., Wen, Z., Ci, S., Chen, J., He, Z., *Nano Energy*, **2012**, *1*, 751–756.

[5] Poh, C. K., Lim, S. H., Tian, Z., Lai, L., Feng, Y. P., Shen, Z., Lin, J., *Nano Energy*, **2013**, *2*, 28–39.

[6] Tüysüz, H., Chan,C. K., *Nano Energy*, **2013**, *2*, 116–123.

[7] Ni, J., Chen, L., Lin, J., Kawi, S., *Nano Energy*, **2012**, *1*, 674–686.

[8] Pan, H., Zhang, Y. W., *Nano Energy*, **2012**, 1, 488–493.

[9] Ho, V. T., Nguyen, N. G., Pan, C. J., Cheng, J. H., Rick, J., Su, W. N., Lee, J. F., Sheu, H. S., Hwang, B. J., *Nano Energy*, **2012**, *1*, 687–695.

[10] Williams, J. L., *Catalysis Today*, **2001**, *69*, 3–9.

[11] Tomašić, V., Jović, F., *Applied Catalysis A:General*, **2006**, *311*, 112–121.

[12] Royer, S., Duprez, D., *ChemCatChem*, **2011**, *3*, 24–65.

[13] Lin, H. F., Valsaraj, K. T., *AIChE Journal*, **2006**, 52, 2271–2280.

[14] Xie, X., Li, Y., Liu, Z. Q., Haruta, M., Shen, W., *Nature*, **2009**, *458*, 746–749.

[15] Yang, H. G., Sun, C. H., Qiao, S. Z., Zou, J., Liu, G., Smith, S. C., Cheng, H. M., Lu, G. Q., *Nature*, **2008**, *453*, 638–641.

[16] Si, R., Flytzani-Stephanopoulos, M., *Angewandte Chemie International Edition*, **2008**, *47*, 2884–2887.

[17] Hughes, M. D., Xu, Y. J., Jenkins, P., McMorn, P., Landon, P., Enache, D. J., Carley, A. F., Attard, G. A., Hutchings, G. J., King, F., Stitt, E. H., Johnston, P., Griffin, K., Kiely, C. J., *Nature*, **2005**, *437*, 1132–1135.

[18] Ren, Z., Guo, Y., Wrobel, G., Knecht, D. A., Zhang, Z., Gao, H., Gao, P. X., *Journal of Materials Chemistry*, **2012**, *22*, 6862–6868.

[19] Qiao, B., Wang, A., Yang, X., Allard, L., Jiang, Z., Cui, Y., Liu, J., Li, J., Zhang, T., *Nature Chemistry*, **2011**, *3*, 634–641.

[20] Herzing, A. A., Kiely, C. J., Carley, A. F., Landon, P., Hutchings, G. J., *Science*, **2008**, *321*, 1331–1335.

[21] Guo, Y., Zhang, Z., Ren, Z., Gao, H., Gao, P. X., *Catalysis Today*, **2012**, *184*, 178–183.

[22] Li, S., Liu, G., Lian, H., Jia, M., Zhao, G., Jiang, D., Zhang, W., *Catalysis Communication*, **2008**, *9*, 1045.

[23] Zhou, H. P., Wu, H. S., Shen, J., Yin, A. X., Sun, L. D., Yan, C. H., *J. Am. Chem. Soc.* **2010**, *132*, 4998.

[24] Kim, C. H., Qi, G., Dahlberg, K., Li, W., *Science*, **2010**, *327*, 1624.

[25] Boger, T., Heibel, A. K., Sorensen, C. M., *Ind. Eng. Chem. Res.*, **2004**, *43*, 4602.

[26] Ji, Y., Easterling, V., Graham, U., Fisk, C., Crocker, M., Choi, J. S., *Appl. Catal. B*, **2011**, *103*, 413.

[27] Carlsson, P. A., Skoglundh, M., Thormählen, P., Andersson, B., *Top. Catal*., **2004**, 30-31, 375.

[28] Roberts, G. W., Chin, P., Sun, X., Spivey, J. J., *Appl. Catal. B*, **2003**, 46, 601.

[29] Ren, Z., Botu, V., Wang, S., Meng, Y., Song, W., Guo, Y., Ramprasad, R., Suib, S. L., Gao, P. X., *Angewandte Chemie International Edition*, **2014**, *53*, 7223.

[30] Ren, Z., Guo, Y., Gao, P. X., *Catalysis Today*, **2015**, *258*, 441.

[31] Guo, Y., Ren, Z., Xiao, W., Gao, P. X., *Catalysis by Materials with Well-Defined Structures*, edited by Zili Wu and Steven Overbury, Elsevier, **2015**.

[32] Wang, S., Ren, Z., Song, W., Guo, Y., Zhang, M., Suib, S. L., Gao, P. X., *Catalysis Today*, **2015**, *258*, 549.

[33] Ren, Z., Wu, Z., Song, W., Xiao, W., Guo, Y., Ding, J., Suib, S. L., Gao, P. X., *Appl. Catal. B*, **2016**, 180, 150.

[34] Guo, Y., Liu, G., Ren, Z., Piyadasa, A., Gao, P. X., *CrystEngComm*, **2013**, *15*, 8345.

[35] Ren, Z., Guo, Y., Liu, C., Gao, P. X., *Frontiers in Chemistry*, **2013**, *1*, 18.

[36] Wang, S., Ren, Z., Guo, Y., Gao, P. X., *The Lightest Metals: Science and Technology from Lithium to Calcium*, John Wiley, **2015**.

[37] Ren, Z., Guo, Y., Zhang, Z., Liu, C., Gao, P. X., *Journal of Materials Chemistry A*, **2013**, *1*, 9897.

[38] Xiao, W., Guo, Y., Ren, Z., Wrobel, G., Ren, Z. Y., Lu, T., Gao, P. X., *Crystal Growth & Design*, **2013**, 13, 3657.

[39] Gao, P. X., Shimpi, P., Gao, H., Liu, C., Guo, Y., Cai, W., Liao, K. T., Wrobel, G., Zhang, Z., Ren, Z., Lin, H. J., *International Journal of Molecular Science*, **2012**, *13*, 7393.

[40] Guo, Y., Zhang, Z., Ren, Z. Gao, P. X., *Catalysis Today*, **2012**, *184*, 178.

[41] Sonstrom, P. *Catal. Sci. Technol.*, **2011**, *1*, 830-838.

[42] Ferrizz, R. M., Stuecker, J. N., Cesarano, J., Miller, J. E. *Ind. Eng. Chem. Res.* **2005**, *44*, 302-308.

[43] Arnby, K., Assiks, J., Carlsson, P.-A., Palmqvist, A. & Skoglundh, M. *Journal of Catalysis*, **2005**, *233*, 176-185.

[44] Alexeev, O. S., Chin, S. Y., Engelhard, M. H., Ortiz-Soto, L. & Amiridis, M. D., *J. Phys. Chem. B* **109**, 23430-23443, (2005).

[45] Kim, K.-J., Seo, H.-S. & Ahn, H.-G. *Res. Chem. Intermed.* **2011**, *37*, 1165-1172.

[46] Li, S., Liu, G., Lian, H., Jia, M., Zhao, G., Jiang, D., Zhang, W., *Catalysis Communication*, **2008**, *9*, 1045.

[47] Zhou, H.-P. *J. Am. Chem. Soc.* **2010**, *132*, 4998-4999.

Chapter 3

Fabrication of monolithic Co_3O_4 nano-array catalyst for high performance nitric oxide (NO) oxidation

3.1. Introduction

The burning of fossil fuels has made air pollution and globe warming an inevitable environmental problem that imposes threats to both ecological and social systems and it is therefore critical to develop highly efficient catalysts to regulate the greenhouse gas emission[1-4]. Among all the pollutant gas, nitrogen oxide (NO_x) participates in ozone layer depletion and contributes to acid rains and smog. Considerable research interest has therefore been focused on reduction of nitrogen oxide emission mainly from automobiles and fossil fuel power plants. Popular techniques tackling the NO_x removal include selective catalytic reduction (SCR)[5-8] and NO_x storage and reduction (NSR)[9-12], both of which convert NO_x into nitrogen. The nitric oxide (NO) oxidation into nitric dioxide (NO_2) is the key to nitrogen oxide conversion in both situations, because NO_2 is much easier to be either reduced into nitrogen or absorbed by storage materials such as alkaline metal oxide.[9, 10] Particularly, the ability to efficiently catalyze nitric oxide (NO) oxidation into nitric dioxide (NO_2) is one of the major technological challenges in order to allow the reduction of NO_2 into nitrogen or absorption by storage materials such as alkaline metal oxide at temperature as low as 200-300 ^oC[13-15].

As a widely used device for industrial and automotive exhaust treatment, a monolithic catalyst is usually fabricated by wash-coating a layer of powder catalyst onto ceramic or metal honeycombs, which compose well-aligned channels for gas flow reactions. However, such traditional manufacturing process lacks effective control of catalysts' physical and chemical

structure, adhesion to the substrate and dispersion uniformity, all of which lead to relatively low materials utilization efficiency and compromised catalytic performance. In recent decades, the rapidly developing bottom-up paradigm for nanostructures assembly has been proved to enable rational integration of functional building blocks in a controlled manner[16] and has opened up a new avenue for designing devices in energy storage and conversion[17-19] as well as catalysis[20-23]. The characteristic high surface area and well exposed surface due to ordered arrangement of nanostructures will be able to allow efficient gas-solid interactions and thus effective contact with catalytically active sites[24].

In addition to the rationalized manufacturing, another hurdle that hinders the development of NO oxidation catalyst is that the platinum group metal (PGM) is usually involved and is often supported on a porous layer of high surface area. It is of high necessity to develop active, stable and non-precious catalyst for large scale substitution of the current PGM based materials to reduce the cost. As a relatively more cost-effective material compared with noble metals, cobalt based oxides have recently been reported to act as an active catalyst for various reactions including carbon monoxide oxidation[25-28], NO oxidation[29-31], methane combustion[32], ethanol steam-reforming[33, 34], oxygen evolution reaction[35, 36] and so on. When reduced to nanoscale dimension, cobalt based catalyst exhibits superior performance. Typically, Xie et.al reported the low temperature CO oxidation by using well-faceted Co_3O_4 nanorod[26]. Co_3O_4 nanocrystals supported on graphene were found to have high activity for oxygen reduction reaction[37].

Herein we have successfully incorporated the merits of hierarchical nanostructure to develop an ultraefficient catalytic honeycomb for NO oxidation without any usage of PGM. Co_3O_4 nanostructure arrays (nano-arrays)[20] were successfully grown on ceramic cordierite honeycombs by a facile hydrothermal process followed by calcination in air at 300 °C. Different

morphologies including close packed flower structures and ordered nanowire arrays were obtained by introducing different cobalt precursors. The evolution of flower structure was thoroughly studied and the growth mechanism was proposed. The as-prepared catalytic honeycombs exhibit high performance NO oxidation with NO conversion of about 80%, which is better than the Co_3O_4 nanopowders prepared from the same hydrothermal process. A series of stability tests demonstrate the catalytic honeycombs are capable of long term use with maintained efficiency in either cyclic or steady isothermal condition. The as-prepared catalytic honeycombs also show good adaptability under temperature fluctuations. Systematic investigation reveals the catalytic performance is determined by the quantity of Co^{3+} on the surface as well as the surface area tuned by different grain size and porosity of the Co_3O_4 nanowires.

3.2. Experimental Section

3.2.1. Materials Synthesis

Cobalt acetate tetrahydrate ($Co(C_2H_3O_2)_2 \bullet 4H_2O$), cobalt nitrate hexahydrate ($Co(NO_3)_2 \bullet 6H_2O$) and cobalt chloride hexahydrate ($CoCl_2 \bullet 6H_2O$) were used as cobalt precursors. To grow hierarchical Co_3O_4 nanowires arrays onto monolithic honeycombs, a piece of ceramic cordierite honeycomb was ultra-sonicated for 30 minutes in distilled water, acetone and ethanol in sequence to remove the residual contamination. The substrate was then suspended into 10 mL aqueous solution of cobalt precursors (0.5mol L^{-1}). The purple solution was magnetically stirred for 30 minutes before condensed urea solution was slowly added. Typical concentration of urea solution was 5-10 mol L^{-1}. The mixed solution was then transferred into water bath for hydrothermal synthesis with temperature of 90 °C and the reaction time was set to be 12 hours. After the container was cooled to room temperature, the substrate was withdrawn from the

solution and was carefully rinsed to remove the residual precipitate from the solution. The substrate was then transferred into box furnace and annealed at 300 °C for 4 hours. To prepare Co_3O_4 nanopowder based catalytic honeycombs, Co_3O_4 powders were first prepared by the same hydrothermal process with the same chemical precursors. After the 12 hours reaction, the powders at the bottom of the reaction container were collected and carefully rinsed by deionized water and ethanol. The powders were then dried overnight and annealed at 300 °C. The obtained Co_3O_4 nanopowders were then dispersed into a mixture of ethanol and distilled water under rigorous stirring and were deposited onto the cordierite honeycombs by wash-coating process. The loading amount of the nanopowders was controlled to be the same as the nanowires directly grown on the honeycombs.

3.2.2. Structure and Catalytic Characterization

The as-prepared Co_3O_4 nano-array catalyst was characterized by powder x-ray diffraction (XRD) using BRUKER AXS D5005 X-ray diffractometer (Cu Kα radiation, λ=1.540598 Å). The morphology and structure were characterized using a field emission scanning electron microscope (FE-SEM, JEOL 6335F) and a high resolution transmission electron microscope (HRTEM, JEOL JEM-2010, 200 kV). The TEM samples were prepared by scratching nanowires off the honeycombs and dispersing in ethanol, which was then dropped onto the carbon film coated copper grid. X-ray photoelectron spectroscopy (XPS) was performed with a Scanning Auger Multi Probe PHI Spectrometer (Model 25-120) equipped with Mg source operating at 250 W. The signal was filtered with a hemispherical analyzer (pass energy = 100 eV for survey spectra and 25 eV for fine spectra). The C(1s) photoelectron line at 284.6 eV was used as an internal standard for the correction of the charging effect in all samples. The BET surface area

and pore size distribution were characterized by gas sorption analyzers (NOVA 1000, Quantachrome Co. and Micromeritics ASAP 2020).

Catalytic performance was evaluated using a home-built bench reactor, with inlet attached with a multi-gas delivery system with mass flow control, and outlet connected to a Fourier transform infrared spectrometer (FTIR, Thermo-fisher Nicolet 6700). Three pieces of Co_3O_4 nano-array rooted cordierite honeycombs were aligned in series in a stainless steel tube for catalytic NO oxidation evaluation. Small amount of quartz wool were put at both ends of the honeycombs to keep the honeycombs' position fixed under fast gas flow. Each honeycomb substrate has six channels and is therefore 2mm×3mm in cross section and around 13mm in length. The loaded amount of Co_3O_4 nano-arrays was measured to be ~10 wt. % of the honeycomb. The gas flow rate was set to be 200mL per minute and the space velocity is therefore ~50,000/h. Before the catalytic test, the samples were treated in in pure nitrogen to get rid of residual air in the stainless steel tubes. The inlet gas consists of 500 ppm NO and 10% oxygen balanced by nitrogen. FTIR was used to quantify the gas concentration change. A series of FTIR spectra of NO with different concentrations (ranging from 10 ppm to 500 ppm) were collected for the calibration before the catalytic performance characterization. Based on the calibration, the quantitation method was built by Quantitative TQ Analyst, the quantification software associated with the Thermo-fisher Nicolet 6700 FTIR. Partial least squares (PLS) was utilized for the quantitation analysis. During calibration and catalytic reaction, each spectrum was collected after half an hour when the peaks' shape and intensity became stable without changes. This helps eliminate the contribution from intermediate products throughout the reaction.

3.3 Results and Discussions

3.3.1. Self-assembly and Structure Characterization

Scheme 3.1 illustrates the fabrication of such Co_3O_4 nano-arrays-based catalytic honeycomb. We chose cordierite honeycomb and stainless steel as the support and Co_3O_4 nano-arrays were directly assembled through a modified one-pot hydrothermal process followed by ambient thermal annealing. During the hydrothermal synthesis, the honeycombs were suspended in the uniform mixture solution of cobalt salt and urea. The cordierite honeycombs consist of half-inch long square channels (cross section 1mm×1mm for each individual channel). Specifically, 0.5 mol L^{-1} of cobalt nitrate ($Co(NO_3)_2•6H_2O$), cobalt acetate ($Co(CH_3COO)_2•4H_2O$) and cobalt chloride ($CoCl_2•6H_2O$) were prepared and rigorously stirred with suspending honeycomb for half an hour. The condense urea solution ($CO(NH_2)_2$, 10 mol L^{-1}) was slowly added dropwise at 50 °C. The as-prepared solution was then transferred to the water bath for hydrothermal synthesis at 90 °C. As can be seen from Figure 3.1a-c, uniform and densely packed nanowires have grown directly on the 3D ceramic cordierite honeycombs. Different cobalt precursors have led to different hierarchical architectures with various geometry and morphology. When acetate or nitrate was used as the cobalt source, the nano-arrays were formed by stacking and interconnection of flower-shaped structures. The typical length of each individual nanowire that composes the flowers was measured to be several micrometers (3-5 μm) and the diameter was about 50 nm. However, if we start with cobalt chloride, the building blocks for nano-arrays turn out to be leaf-like nanowires with sharp tips. The leaf-like nanowires have a larger diameter of about 100 nm. The cross section view of such nano-arrays in Figure 3.1b clearly reveals wires of ~ 10 um in lengths, longer than those prepared from either acetate or nitrate. Compared with Co_3O_4 nano-arrays evolved from acetate and nitrate, the nanowires produced from chloride are found to be loosely interconnected but are oriented in a much more ordered fashion. The X-ray

diffraction patterns in Figure 3.1f confirm all three types of nanowires array prepared from different cobalt precursors correspond to Co_3O_4. For convenience, Co_3O_4 nano-arrays obtained from acetate, nitrate and chloride are designated as CA, CN and CC respectively. A closer look at the growth process shows that the hydrothermal synthesis would give rise to complicated compounds, though after ambient annealing they all transform into cobalt oxide. Specifically, when nitrate and acetate were used as starting materials, X-ray diffraction in Figure 3.2 indicates cobalt hydroxide-carbonate was formed. Nevertheless cobalt chloride led to produce cobalt chloride-hydroxide-carbonate. The hydrothermal formation of these compounds is in good agreement with recent progress in Co_3O_4 synthesis[38,39]. The as-prepared Co_3O_4 nano-arrays template the morphology from these complex compounds evidenced by SEM images in Figure 3.2, which reveals that the thermal annealing contributes to the chemical transformation without structural damage.

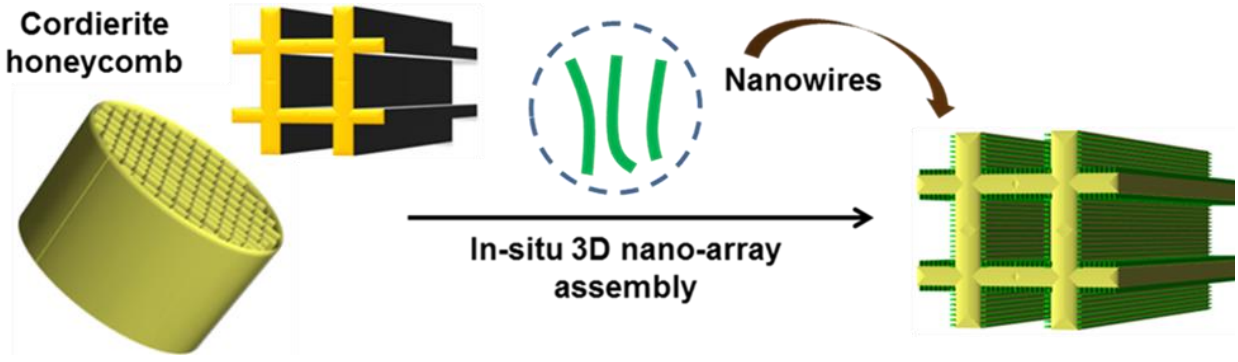

Scheme 3.1. Schematic illustration for procedures to develop catalytic honeycombs structured with hierarchical Co_3O_4 nano-arrays.

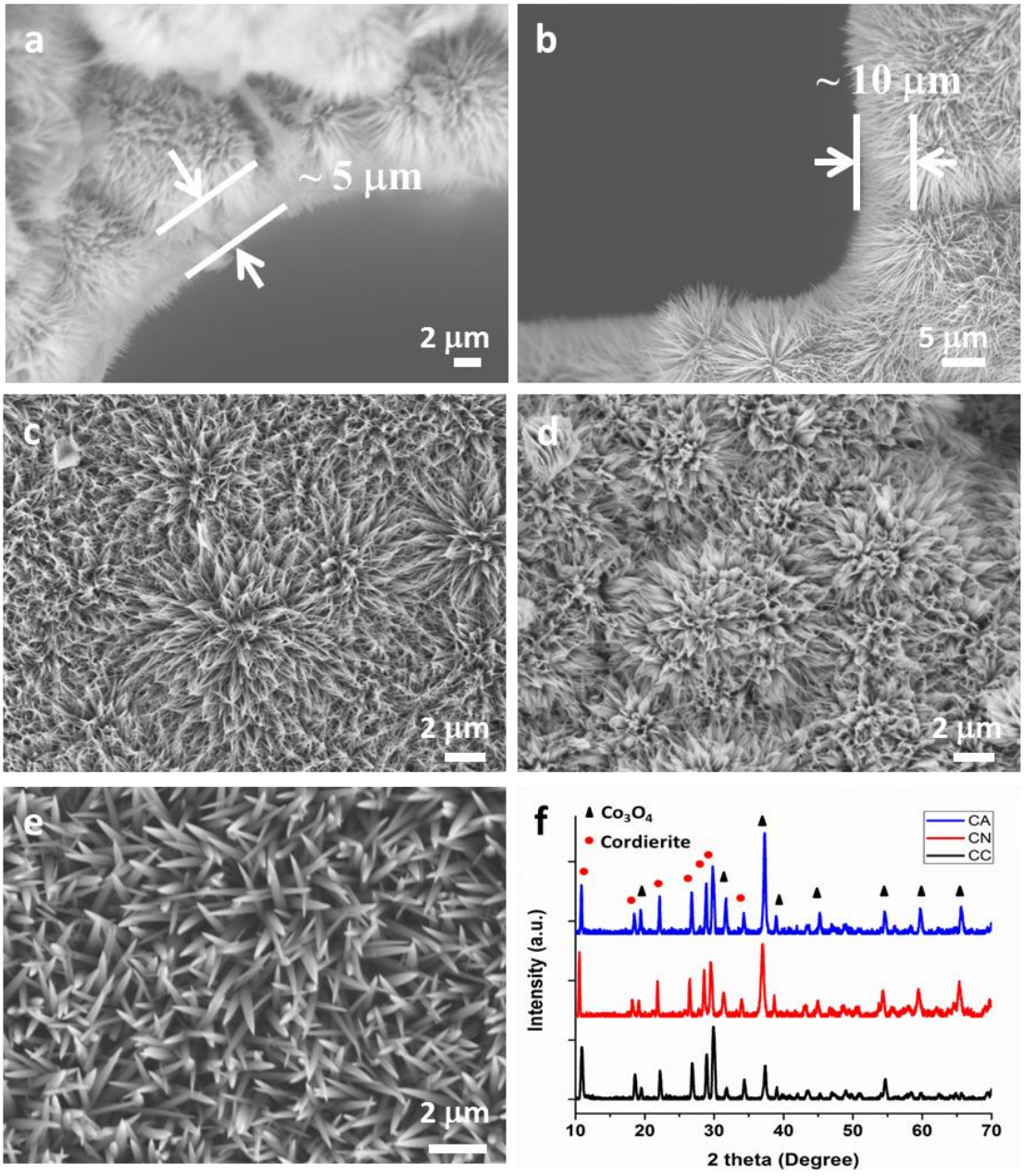

Figure 3.1. (a-b) SEM images of a close view at the corner from an individual channel of the catalytic honeycombs prepared by cobalt nitrate and cobalt chloride respectively; (c-e) Magnified SEM images of Co_3O_4 nano-arrays made from (c) cobalt nitrate, (d) cobalt acetate and (e) cobalt chloride. (f) X-ray diffraction patterns of Co_3O_4 nano-arrays on cordierite honeycomb substrate.

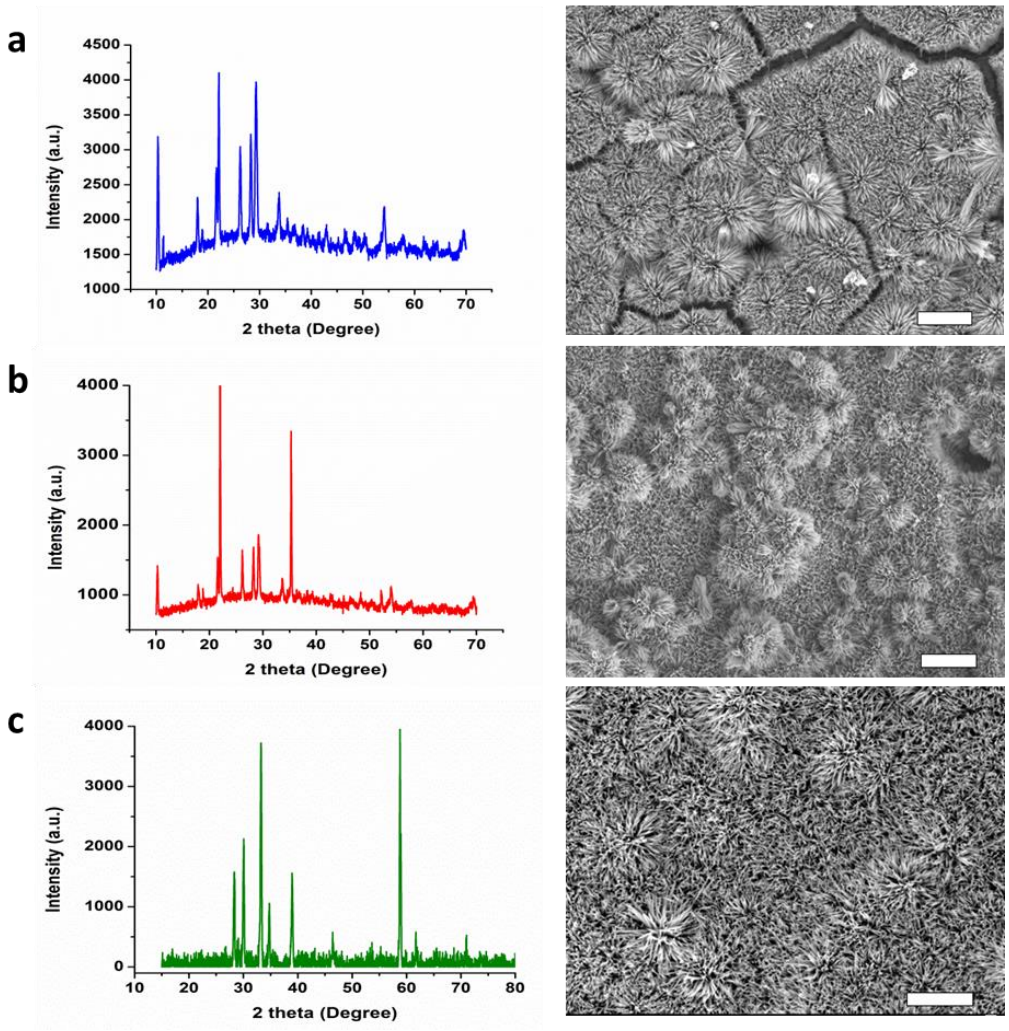

Figure 3.2. SEM images and corresponding XRD patterns of precursor nano-arrays synthesized from a) cobalt nitrate; b) cobalt acetate and c) cobalt chloride. Scale bars: 10 μm.

3.3.2. Growth Mechanism and Morphology Evolution

To guarantee the successful large scale preparation of these nano-arrays-based honeycombs, it is important to understand the structure and morphology evolution of these different Co_3O_4 nano-arrays prior to the catalytic performance characterization. When starting with chloride, only the density of Co_3O_4 nanowires increases with reaction time changing from 4 hours to 12 hours (Figure 3.3) and thus makes the nano-arrays more uniform. Therefore, it can be concluded that the nanowire morphology was determined at the very beginning of the synthesis and the

prolonged reaction time only leads to the nanowire growth. Despite the fact that both nitrate and acetate will lead to similar flower-shaped morphology, the pathways through which the flowers blossom differ. Figure 3.4 displays the morphology change of CN and CA at different reaction stages. When the reaction time was shortened to 4 hours, some aggregate of dumbbell structures were observed in the case of nitrate indicated by Figure 3.4a. Magnified images in Figure 3.4b show the dumbbells are self-assembled by twisted and bended nanowires. However, acetate produced porous aggregates mainly compose of platelets with reaction time of 4 hours. Most of such aggregates are spherical in shape. When the reaction time is prolonged to 8 hours, both precursors give rise to flower structures similar to the final products achieved at 12 hours (Figure 3.4c and 3.4e). This phenomenon implies that the platelets elongate with increased time and the porous aggregates therefore grow into urchins of stretching elongated platelets.

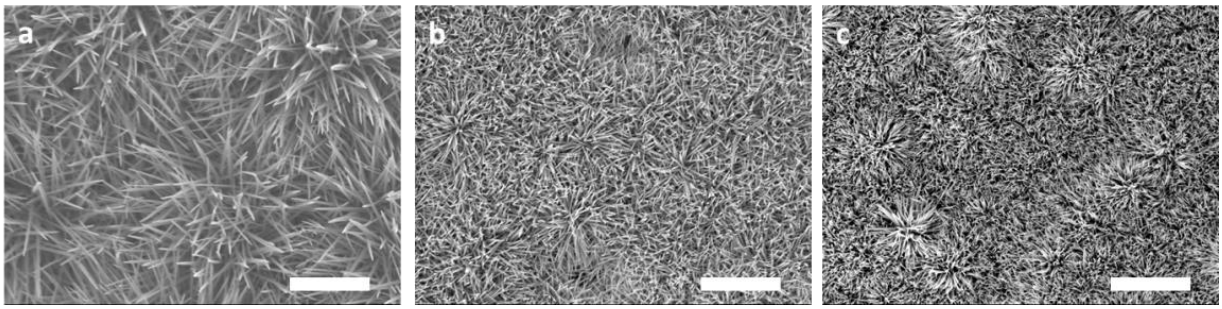

Figure 3.3. Morphology of Co_3O_4 nano-arrays prepared from cobalt chloride after a) 4 hours; b) 8 hours and c) 12 hours. Scale bars: 10 μm.

A growth mechanism illustrated in Figure 3.4g and 3.4h has thus been proposed based on the observation. When nitrate is used as precursor, the nano-arrays form through a "dumbbell aggregation" process. Specifically, pristine nanowires come into shape and self-assemble to produce dumbbell-shaped bundles. These bundles with different orientations then begin to intertwine as time increases and lead to densely grown nano-arrays. A different scenario takes

place if the reaction starts with acetate and the synthesis seems to proceed with an "elongation-splitting" process. First, platelets instead of nanowires appear and randomly get packed to form spherical aggregates. The platelets' aspect ratio increases owing to their elongation as reaction continues. As a result, preliminary flowers or urchins come into shape when the reaction lasts for 8 hours. It is noticed in magnified SEM image Figure 3.4f, however, that the flowers obtained from acetate are composed of nanowires not as narrow as those observed in the case of nitrate. Only when the reaction is further elongated to 12 hours will these nanowires get dense and thin. It is therefore plausible to conclude that the flower petals will finally split into several branches to blossom. Recently, the hierarchical flower architecture was reported to facilitate the electron transport in energy storage[40-42] and interfacial interaction in catalysis[22,43,44]. However, the formation of such dumbbell structure at the initial stage of Co_3O_4 nanowire array development has not been fully understood yet. Similar phenomenon was observed in the synthesis of other hierarchical nanostructures where crystal splitting induced by fast crystal growth is believed to be the driving force. [45-48]

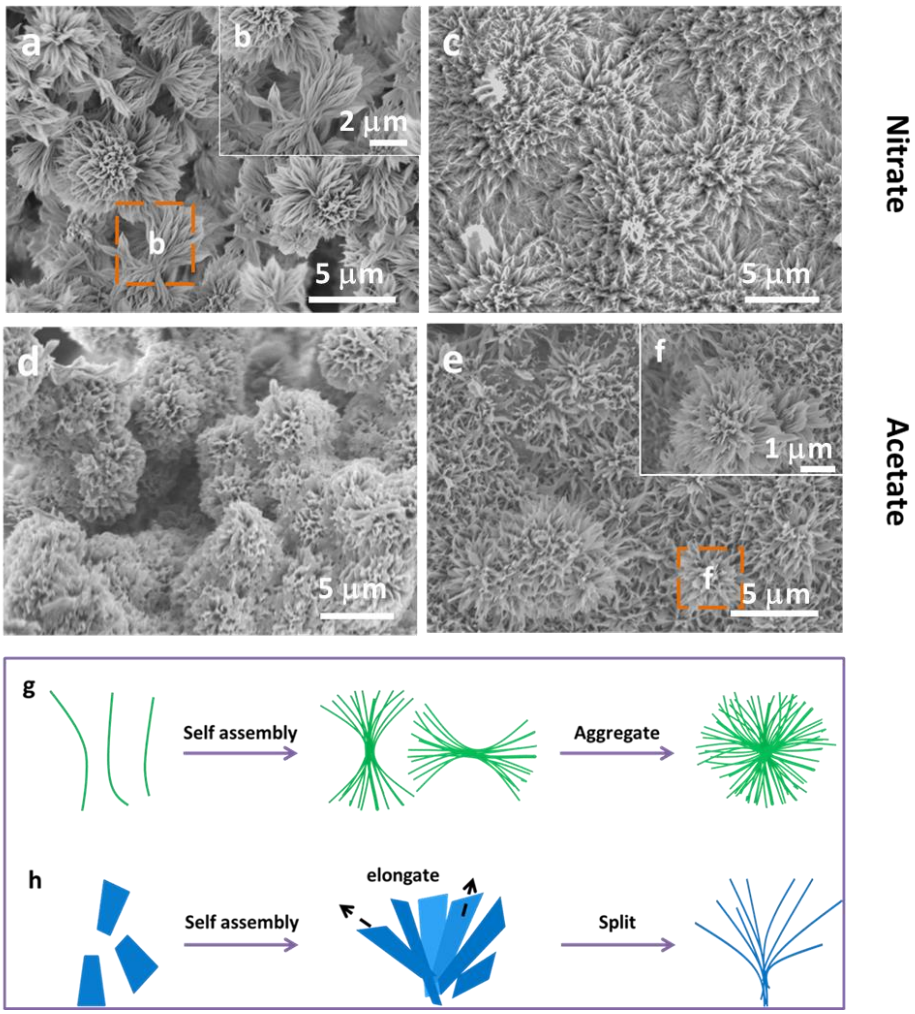

Figure 3.4. SEM images of product obtained from different precursors with different reaction time. (a), (b) 4 hours using cobalt nitrate; (c) 8 hours using cobalt nitrate; (d) 4 hours using cobalt acetate; (e), (f) 8 hours using cobalt acetate. Schematic illustrations of morphology evolution of Co_3O_4 nano-arrays using (g) cobalt nitrate; (h) cobalt acetate.

3.3.3. Catalytic NO Oxidation Performance

Three pieces of Co_3O_4 loaded cordierite honeycombs were aligned in series in a stainless steel tube for catalytic NO oxidation reaction characterizations. Each of the honeycombs has six channels and is therefore 2mm×3mm in cross section and 13mm in length. The amount of loaded Co_3O_4 nano-arrays, ~11 mg, was measured to be ~10 wt. % of the bare cordierite honeycomb substrate. The gas flow rate was set to be 200 mL per minute and the space velocity is therefore

calculated to be ~50,000 h^{-1}. The inlet gas consists of 500 ppm NO and 10% oxygen balanced by nitrogen. Fourier transform infrared spectroscopy (FTIR) was used to quantify the gas concentration change. For a typical catalytic activity test, the temperature was elevated from room temperature (usually ~25 °C) to as high as 400 °C and the NO conversion efficiency was recorded at each individual temperature by FT-IR spectra collection and quantification. Figure 3.5a shows the nano-arrays-based honeycombs have remarkable NO conversion performance. Both CA and CN reach the NO to NO_2 conversion as high as 80% at a relatively low temperature of 275 °C. CC reaches its maximum conversion, ~75% of NO into NO_2 at 325 °C. The NO conversion begins to drastically increase at 150 °C for CA and CN but at 200 °C for CC. The honeycombs constructed with Co_3O_4 nano-arrays demonstrated better catalytic performance compared with the Co_3O_4 nanopowders prepared from the same hydrothermal method. When cobalt acetate or cobalt nitrate was used as the precursor, the Co_3O_4 nanopowders achieved maximum NO conversion at 300 °C, which was 25 °C delayed compared with the nano-arrays counterparts. However, the Co_3O_4 nanopowder prepared from cobalt chloride reached the highest conversion of NO at the same temperature as the nano-arrays. Compared with CA and CN nano-arrays, the maximum NO conversion of CA and CN powders decreased from 80% to 65%. When cobalt chloride acted as the precursor, the maximum conversion decreased from 70% to 50%. The TEM images in Figure 3.6 reveal that the morphology of nanopowders prepared from cobalt nitrate is a mixture of nanoparticles and nanowires while nanoparticles dominate the geometry of the nanopowders synthesized from cobalt acetate and chloride. The BET surface area characterization in Figure 3.7 together with calculation in Table 1 and Table 2 displays that the nanowire arrays have a much larger surface area compared with that of nanopowders. The better catalytic performance of nanowire arrays may be ascribed to the facilitated diffusion and gas-

solid interaction enabled by the large surface area. More insights regarding the advantages of nanowires geometry over nanopowders will be investigated in the future.

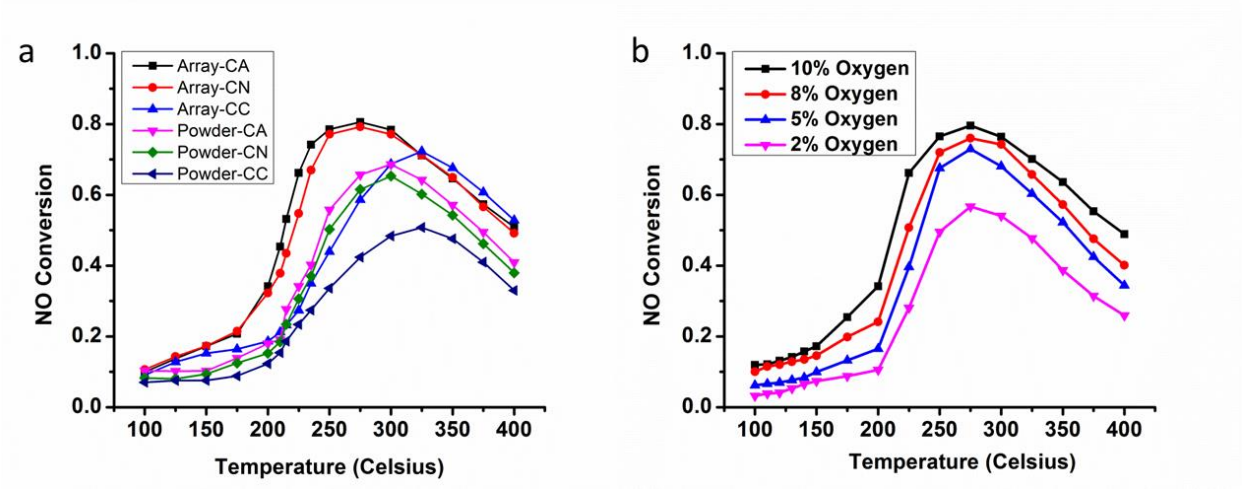

Figure 3.5. (a) NO oxidation performance of catalytic Co_3O_4 nano-arrays and powders prepared from different precursors; (b) Catalytic NO conversion performance by CA with varied oxygen concentration.

The detailed calculation of BET surface areas of nano-arrays without cordierite monolith is explained as follows. The BET surface area of blank honeycombs was measured to be 0.35 $m^2 g^{-1}$. We assume the measured BET surface area of honeycombs structured with nano-arrays is approximately the linear summation of contributions from blank honeycomb and the nano-arrays. The weight of nano-arrays constitutes ~10% of the total weight of honeycombs. Therefore, the BET surface area of nano-arrays S_A is calculated by

$$S_A = \frac{S(m_h + m_A) - S_h m_h}{m_A}$$

m_h: mass of the honeycomb; m_A: mass of the nano-arrays (weight difference of honeycomb substrate before and after nano-arrays growth); S_h: BET surface area of blank honeycomb; S: BET surface area of honeycomb structured with Co_3O_4 nano-arrays.

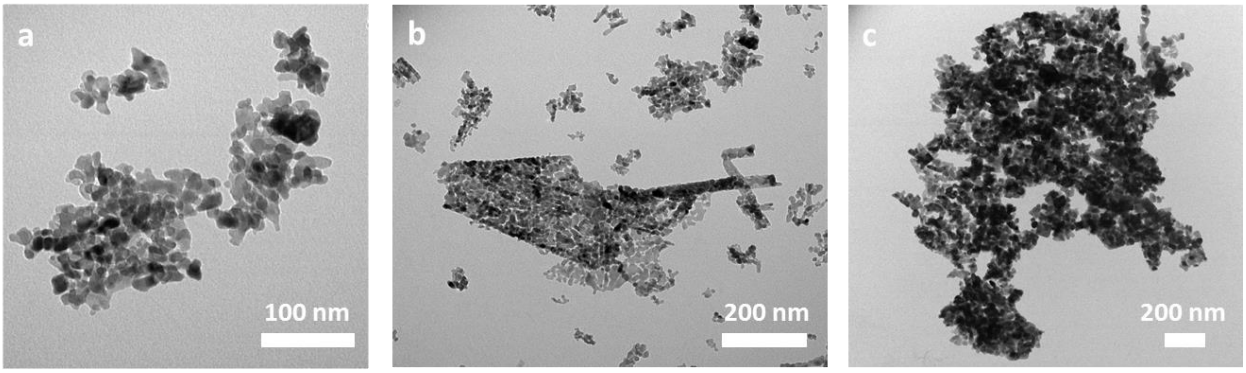

Figure 3.6. TEM characterization of Co_3O_4 nanopowders prepared from a) cobalt acetate; b) cobalt nitrate and c) cobalt chloride.

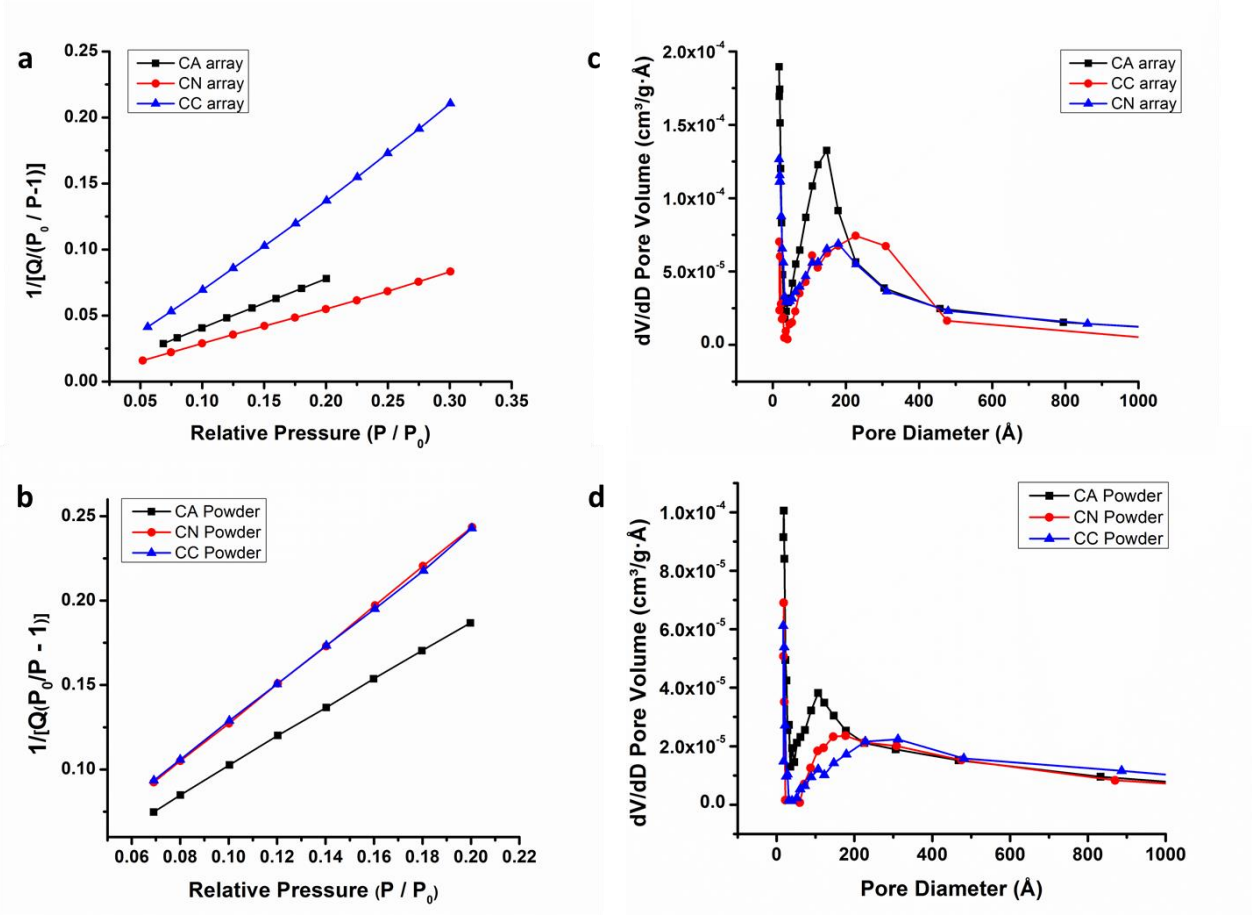

Figure 3.7. a-b) BET surface area measurement and c-d) pore size distribution characterization for different Co_3O_4 nano-arrays and nanopowders respectively. The pore size distribution plot is BJH adsorption dV/dD pore volume versus pore diameter with Harley Faas correction.

With honeycombs	Grain size (nm)	BET surface area (m^2/g)	Pore diameter(nm)
CA-300 C	20-30	12.5	15
CN-300 C	25-40	16.1	15
CC-300 C	60-80	8.4	25

Table 3.1. Surface area calculation of Co_3O_4 nanowire arrays.

With honeycombs	BET surface area (m^2/g)	Pore size (nm)
CA-powders	4.8	12
CN-powders	3.8	15-20
CC-powders	3.7	30

Table 3.2. BET surface area characterization and pore size distribution results for Co_3O_4 nanopowders prepared by the same hydrothermal process as nano-arrays synthesized from different cobalt precursors.

The nitric oxidation reaction is a reversible reaction and the NO_2 formation is believed to inhibit the NO conversion. However, in our catalytic test the inlet oxygen concentration (10%) is sufficiently high compared with NO (500 ppm) and it is therefore reasonable to consider the NO oxidation as irreversible. The reaction rate is thus only dependent on concentration of NO and O_2. By varying the partial pressure of both NO and O_2, the kinetic analysis shown in Figure 3.8 determines the reaction orders of NO and O_2 when each type of Co_3O_4 nanowire was used as catalyst. Table 3.3 provides calculation results on the apparent activation energy, pre-exponential factor and the turn-over frequency. The apparent activation energy and the pre-exponential factor were obtained by Arrhenius plot, where reaction constant k was calculated based on the measured reaction rates and reaction orders. The apparent activation energy and pre-exponential factor is obtained by the Arrhenius plot of lnk vs (-1/T). Reaction constant value k was calculated from reaction rate $r = kP_{NO}^{a}P_{O_2}^{b}$ where a and b are the reaction orders determined

from Figure 3.8. The turn-over frequency (TOF) is calculated by using Co^{3+} as the active sites. The population ratio of Co^{3+} and Co^{2+} is determined from deconvoluted XPS spectra in Figure 3.7. In CA and CN the Co^{3+} possesses 65% while in CC this proportion is 59%. Specifically,

$$TOF = \frac{Converted\ NO\ (mol \cdot s^{-1})}{Active\ sites\ number\ (mol)}$$

$$Converted\ NO\ (mol \cdot s^{-1}) = \frac{500\ ppm \times conversion\ (\%) \times flow\ rate\ (L \cdot s^{-1})}{22.4\ L/mol}$$

where flow rate=200 mL/min=1/300 (L/s). $Active\ sites\ number\ (mol) = 3 \times \frac{m_{Co_3O_4}}{M_{Co_3O_4}} \times \eta$

where $m_{Co_3O_4}$ stands for the mass of the grown Co_3O_4 nano-arrays on the honeycomb, $M_{Co_3O_4}$ represents the molecular weight of Co_3O_4 (240 g/mol) and η is the portion of Co^{3+}, which is determined by XPS analysis. Specifically, for CA and CN nano-arrays, $\eta = 65\%$ while for CC nano-array, $\eta = 59\%$.

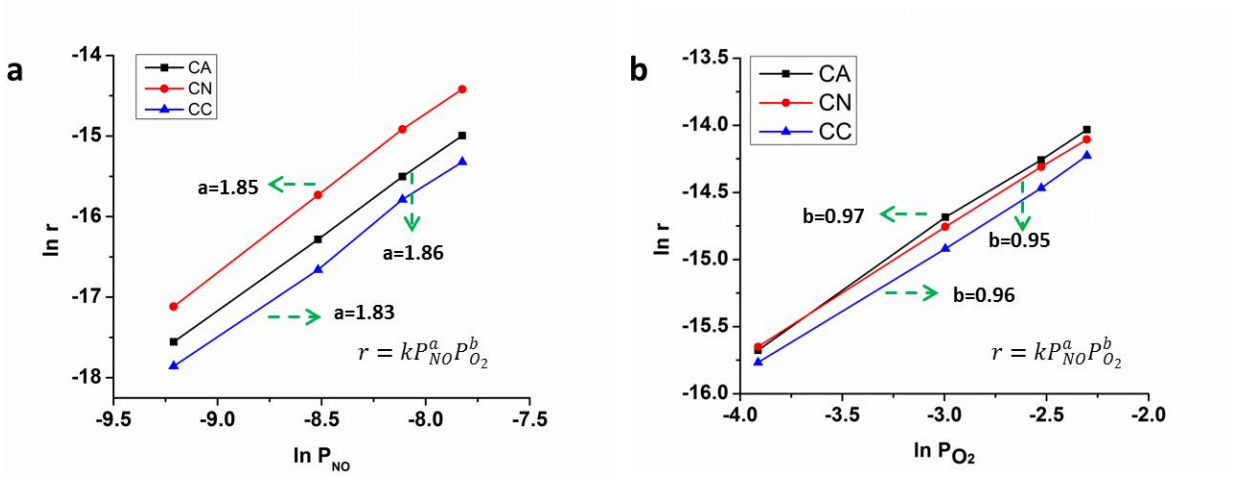

Figure 3.8. Reaction rates measured at 100 °C as a function of CO or O_2 concentration over different Co_3O_4 nanowire arrays. The concentration of CO was adjusted from 100 ppm to 400 ppm and the concentration of oxygen was tuned from 2% to 10%.

All three types of Co_3O_4 nanowire arrays have almost the same activation energy and therefore have the same active site. The pre-exponential factor k_0 which reflects the number of active sites were also calculated. The Co_3O_4 nano-arrays CA and CN prepared from cobalt acetate and cobalt nitrate respectively have larger k_0 compared with Co_3O_4 prepared from chloride. It can be concluded that more active sites are exposed in CA and CN which contributes to the fast take-off of the NO conversion curve. The turn-over frequency was thus calculated by using Co^{3+} as the active sites, the amount of which was determined by the XPS analysis. The active sites determination and XPS characterization will be discussed with more details later. Varied oxygen concentration has led to different NO conversion efficiency. As we can see from Figure 3.5b that by using Co_3O_4 nano-arrays catalytic honeycombs prepared from cobalt acetate, considerable NO conversion (~55%) still maintains when the oxygen concentration drops to 2%. Such Co_3O_4 nano-array catalysts, therefore, are reliable to work not just in lean condition (oxygen rich atmosphere), but also in the rich (fuel rich, dilute oxygen) atmosphere, which is very important for the clean combustion processes, such as the low temperature internal combustion engine applications.[13, 49, 50]

Table 3.3. Apparent activation energy, pre-exponential factor and turn-over frequency (TOF)

Temperature (°C)	Conversion	Rate (mol g^{-1} s^{-1})	TOF (s^{-1})
110	10%	6.54×10^{-7}	8.1×10^{-5}
120	12%	7.70×10^{-7}	9.5×10^{-5}
130	14.2%	9.11×10^{-7}	1.12×10^{-4}
140	16.3%	1.05×10^{-6}	1.29×10^{-4}
150	18.8%	1.21×10^{-6}	1.49×10^{-4}

Co_3O_4 prepared from cobalt acetate: Apparent activation energy $E_a = 20.6\ kJ/mol$; Pre-exponential factor $k_0 = 5433\ mol \cdot g^{-1} \cdot s^{-1}$

Temperature (°C)	Conversion	Rate (mol g^{-1} s^{-1})	TOF (s^{-1})
110	10.9%	7.16×10^{-7}	8.6×10^{-5}
120	12.9%	8.47×10^{-7}	1.02×10^{-4}
130	15.2%	9.98×10^{-7}	1.2×10^{-4}
140	17.3%	1.14×10^{-6}	1.37×10^{-4}
150	19.8%	1.30×10^{-6}	1.57×10^{-4}

Co_3O_4 prepared from cobalt nitrate: Apparent activation energy $E_a = 20.1\ kJ/mol$; Pre-exponential factor $k_0 = 5102\ mol \cdot g^{-1} \cdot s^{-1}$

Temperature (°C)	Conversion	Rate (mol g^{-1} s^{-1})	TOF (s^{-1})
110	9.80%	6.13×10^{-7}	8.56×10^{-5}
120	11.60%	7.25×10^{-7}	1.01×10^{-4}
130	13.60%	8.50×10^{-7}	1.18×10^{-4}
140	15.70%	9.82×10^{-7}	1.37×10^{-4}
150	17.80%	1.11×10^{-6}	1.55×10^{-4}

Co_3O_4 prepared from cobalt chloride: Apparent activation energy $E_a = 20.1\ kJ/mol$; Pre-exponential factor $k_0 = 3840\ mol \cdot g^{-1} \cdot s^{-1}$

3.3.4. Catalyst Stability Characterization

Another important aspect of a reliable catalyst is its long term stability in terms of catalytic performance. A series of stability characterizations have therefore been conducted. The as-prepared Co_3O_4 nano-arrays catalytic honeycombs all exhibit remarkable catalytic stability during cyclic NO oxidation test. Specifically, all three types of Co_3O_4 nano-arrays catalytic honeycombs went through 10 catalytic cycles with temperature ramping from 25 °C to 400 °C. As can be seen from Figure 3.9a through 3.9c, only minor degradation of catalytic activity took place between the first and the fifth cycle. Both CN and CA catalytic honeycombs maintain their maximum NO conversion of above 75% at 275 °C. At the same time, the highest NO conversion

occurring at 325 °C for CC catalytic honeycomb stayed above 60%. All three catalytic honeycombs experienced less than 5% degradation compared with the freshly-prepared honeycombs after 5 cycles. However, no further degradation was observed after another five cycles were added. Figure 3.9d tracks the mass change of catalytic honeycombs after each cycle and it is obvious that the weight of each Co_3O_4 nano-array catalyst stay constant, which indicates no catalyst loss throughout the test.

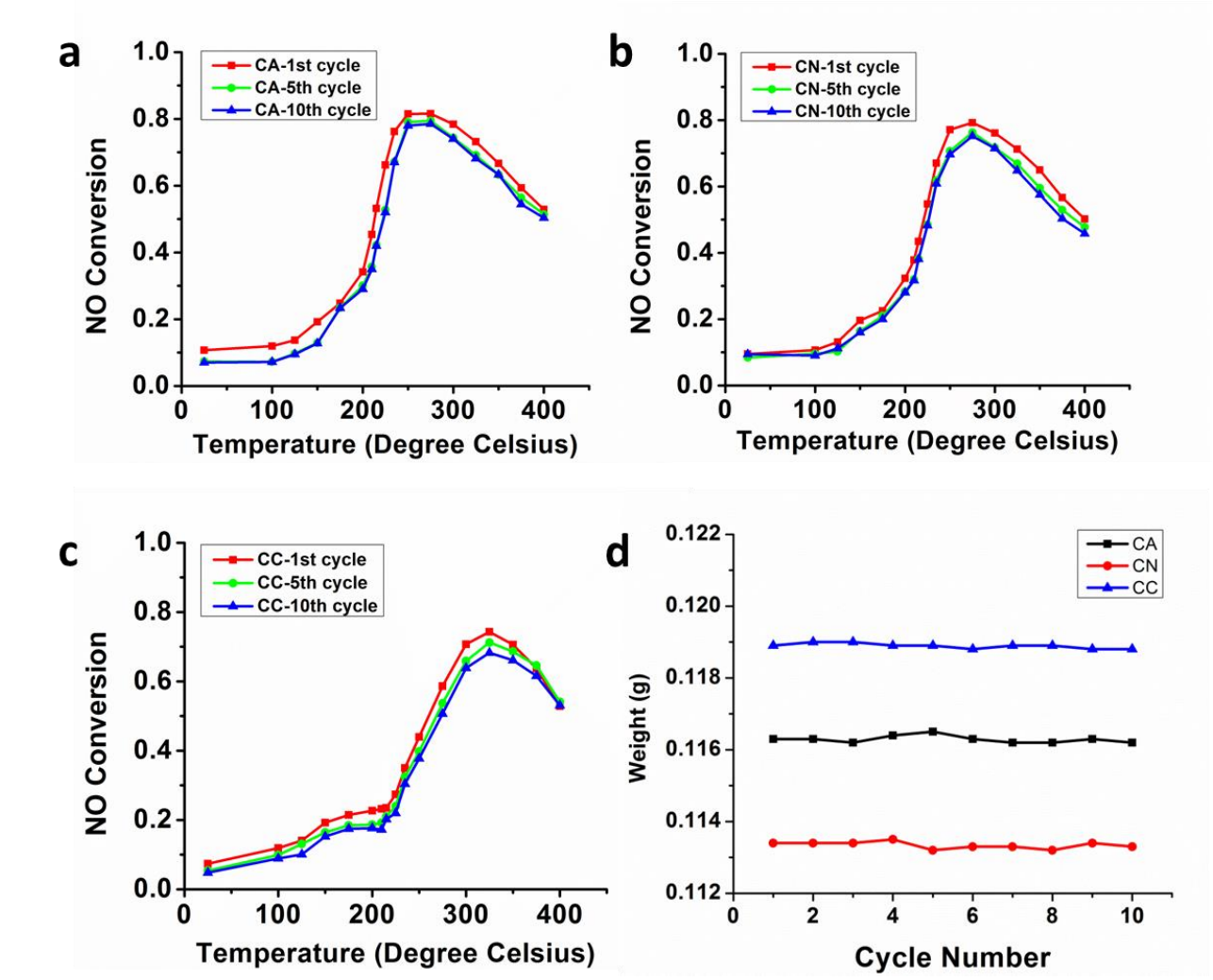

Figure 3.9. Cyclic catalytic NO oxidation performance by (a) CA; (b) CN and (c) CC. (d) Weight measurement of catalytic honeycombs during cyclic test.

There are always temperature fluctuations in practice. For example, the temperature of automobile exhaust varies with the working conditions of the engine. It is therefore critical to measure the adaptability of catalytic activity to the temperature fluctuation. In addition to the previous test of cyclic performance, which only involves the temperature ramping-up, catalytic performance with repeated heating and cooling was investigated.

Figure 3.10a illustrates the NO conversion curves with respect to cyclic temperature change from 150 °C to 400 °C. Using CA catalytic honeycomb as an example, the curves are not strictly symmetric with temperature change which indicates minor difference in NO conversion during heating and cooling. However, the temperature for the maximum NO conversion stayed the same during cooling process and no degradation of catalytic activity can be observed. Such catalytic stability under cyclic heating and cooling makes the Co_3O_4 nano-arrays catalytic honeycomb suitable for use under temperature fluctuation. Long term isothermal catalytic stability of these catalytic honeycombs was studied by monitoring the isothermal NO conversion change at the temperature where maximum conversion was achieved. The reaction was elongated to 20 hours with temperature fixed to 275 °C for CN and CA, and 325 °C for CC, respectively. The NO conversion efficiency was quantified every 2 hours using FT-IR. Figure 3.10b demonstrates stable NO conversion without any degradation during the 20 hours' test for all three honeycombs. CN and CA maintain maximum NO conversion of ~80% and CC's stayed above 75%. The weight change of catalyst was also monitored and no obvious weight loss was found. Electron microscopy was applied to examine the morphology and structure changes after all of the different stability characterizations. Figure 3.10c through 3.10e are the typical SEM images of the used Co_3O_4 nano-arrays. The used catalytic nano-arrays exhibit no morphology changes

with well-maintained structure and orientation so that there is no physical damage throughout the experiments.

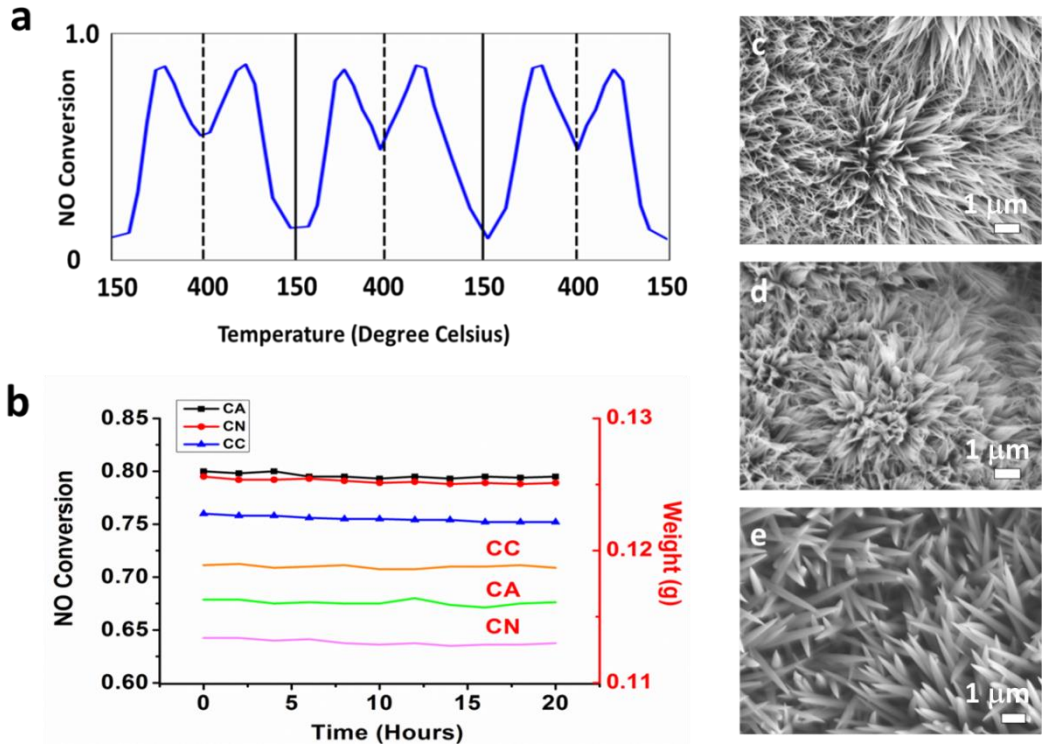

Figure 3.10. (a) Catalytic NO oxidation performance with repeated heating and cooling; (b) NO oxidation efficiency and weight measurement during long term steady investigation at 275 °C for CA and CN and 325 °C for CC; (c)-(e) SEM images for structure and morphology characterization of CN,CA and CC respectively after all stability tests.

3.3.5. Catalytic Performance Discussion

After the fabrication as well as the catalytic stability of nano-arrays was successfully studied and characterized, an intermediate problem that needs to be addressed is why different cobalt precursors lead to different NO conversion performance. X-ray Photoelectron Spectroscopy (XPS) was therefore used to investigate the surface chemistry of Co_3O_4 nano-arrays. Figure 3.11a demonstrates a set of Co 2p peaks located at ~780 eV and 795 eV corresponding to Co

$2p_{3/2}$ and Co $2p_{1/2}$ respectively. Each peak is the summation of signals from Co^{2+} and Co^{3+}. In Co_3O_4, Co^{2+} has higher binding energy than Co^{3+}.[51-53] From the deconvoluted spectra in Figure 3.11a, it is concluded that the peaks at 779 eV and 794 eV with a small satellite signal around 788 eV correspond to Co^{3+}. The peaks at 781 eV and 797 eV are characteristic of Co^{2+}.[54] Detailed calculation from the deconvoluted peaks reveals that the intensity ratio of Co^{3+} and Co^{2+} are different in Co_3O_4 nano-arrays from different precursors. The ratio of Co^{3+} / Co^{2+} on the surface of CA and CN is found to be 1.85 (Co^{3+}: 65%; Co^{2+}: 35%) while it is only 1.4 (Co^{3+}: 58%; Co^{2+}: 42%) in the case of CC. Since CA and CN exhibit similar NO conversion performance, which is better than CC, the Co^{3+} on the surface therefore acts as the active sites and its quantity determines the capability of catalytic NO conversion into NO_2. Further evidence was extracted from X-ray diffraction (XRD). Figure 3.11b displays the X-ray diffraction spectra of different Co_3O_4 nano-arrays supported by cordierite honeycombs. Both Co_3O_4 and cordierite honeycomb are detected with the denoted peaks in Figure 3.11b that are well indexed to Co_3O_4 (JCPDS No.090418) and ceramic cordierite (JCPDS No.120303). Co_3O_4 has a cubic spinel structure with Co^{3+} occupied in octahedral sites and Co^{2+} in tetrahedral sites. {220} planes mainly contain Co^{3+} ions while {111} planes only have Co^{2+}. The intensity of X-ray diffraction peaks reflects the relative amount of crystal planes. Table at the bottom panel of Figure 3.11 displays the relative intensity of each peak with respect to standard intensity from the JCPDS card. It reveals that anisotropic growth takes place and the {111} planes constitute the largest portion of all Co_3O_4 nano-arrays because (111) peak has the highest relative intensity. However, the relative intensity of {220} planes in CC is lower (~ 0.57) compared with those of CA (~ 0.73) and CN (~ 0.71). In this sense, Co_3O_4 nano-arrays prepared from cobalt chloride have less {220} planes involved in average, which gives rise to the lower portion of Co^{3+} as evidenced by

XPS spectrum. The qualitative XRD results further confirms that Co^{3+} ions act as active sites that is responsible for catalytic NO oxidation.

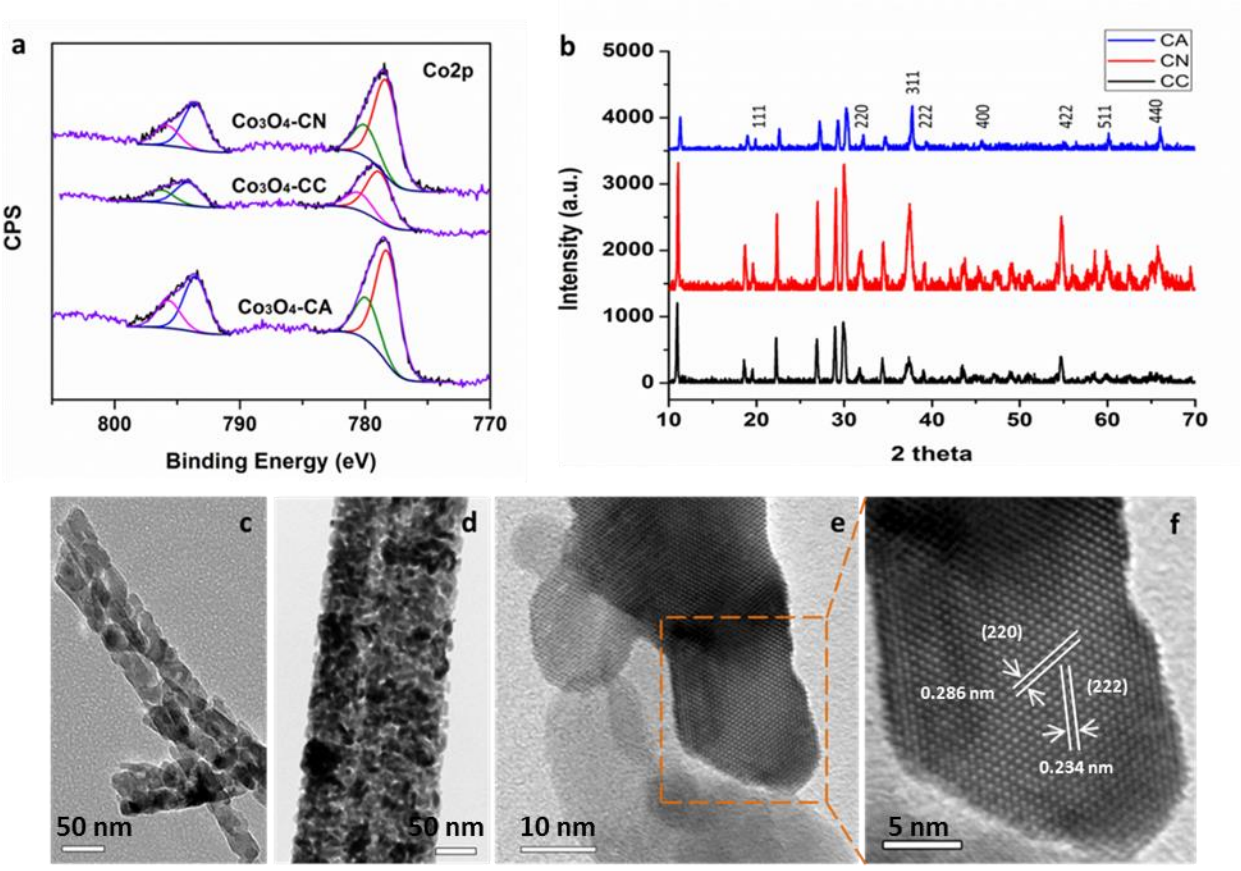

Diffraction Planes	{111}	{220}	{311}	{222}	{400}
SI	200	400	1000	120	250
RI-CA	1.01	0.73	0.5	0.83	0.72
RI-CN	0.98	0.71	0.65	1.5	0.73
RI-CC	1.1	0.57	0.32	1.67	0.4

Figure 3.11. (a) Deconvoluted X-ray photoelectron spectroscopy (XPS) spectra of Co 2p; (b) X-ray diffraction of catalytic honeycombs of different Co_3O_4 nano-arrays; TEM characterizations of (c) CN, (d) CC and (e) CA; f) HRTEM lattice imaging of CA. Table: standard intensity (**SI**) and relative intensity (**RI**) of primary crystal planes of Co_3O_4.

Transmission electron microscopy (TEM) images in Figure 3.11c through 3.11e confirm the porous structure of Co_3O_4 nanowires. The grain sizes for CA, CN and CC were measured to be 20-30 nm, 25-40 nm and 60-80 nm respectively by TEM observation in Figure 3.12-3.13, which are also confirmed by calculation from XRD spectrum using Scherrer equation. The Brunauer-Emmett-Teller (BET) surface area and pore size distribution analysis was therefore conducted to study the correlation between the porous structure and the catalytic NO conversion. The blank cordierite honeycomb has the BET surface area of $0.35 m^2 g^{-1}$. With subtracted contribution from the honeycomb support, the CN catalytic nano-arrays has the specific surface area of 158.1 $m^2 g^{-1}$, larger than those of CA (122.6 $m^2 g^{-1}$) and CC (81.1 $m^2 g^{-1}$). As concluded from Figure 3.5, CA and CN have a relatively faster light-off. It is therefore proved that the faster reaction rate originates from larger surface area originating from the reduced grain size in the porous structure. CA and CN have larger surface area and pore volume, which make CA and CN better catalytic honeycombs than CC in terms of faster reaction rate and thus relatively lower conversion temperature.

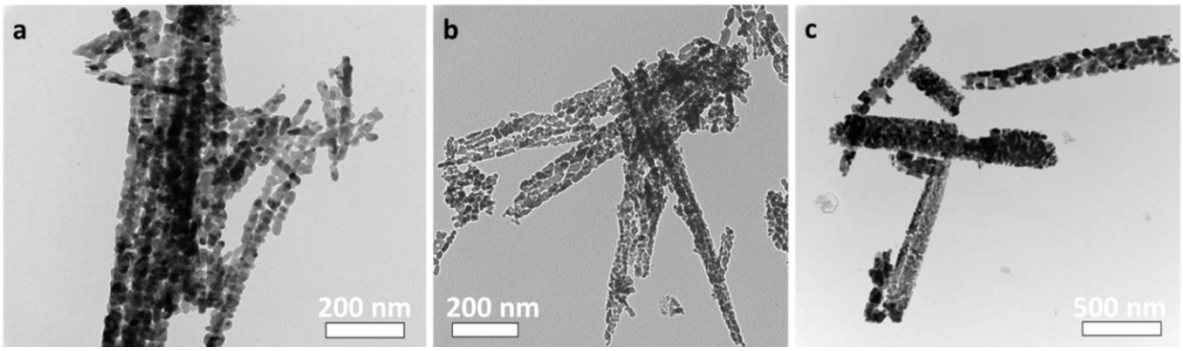

Figure 3.12. TEM characterization of Co_3O_4 nano-arrays prepared from a) cobalt nitrate; b) cobalt acetate and c) cobalt chloride.

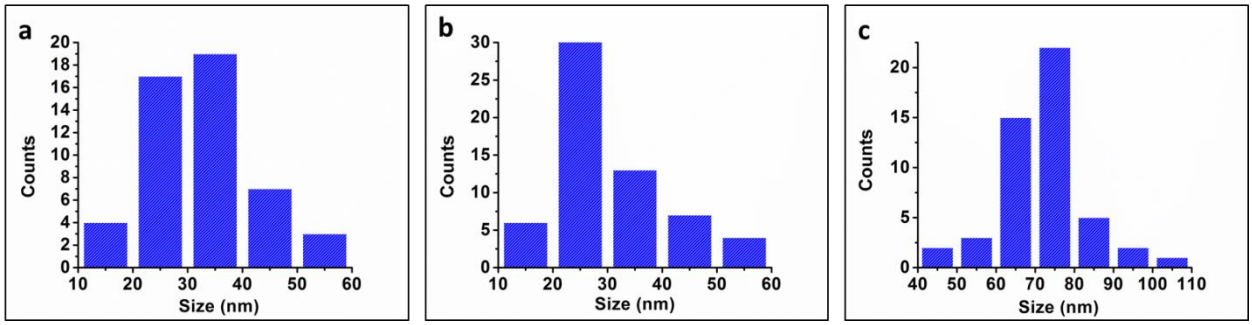

Figure 3.13. Statistical grain size distribution of Co_3O_4 prepared from different cobalt sources as observed in the TEM images in Figure S4. a) cobalt nitrate; b) cobalt acetate; c) cobalt chloride.

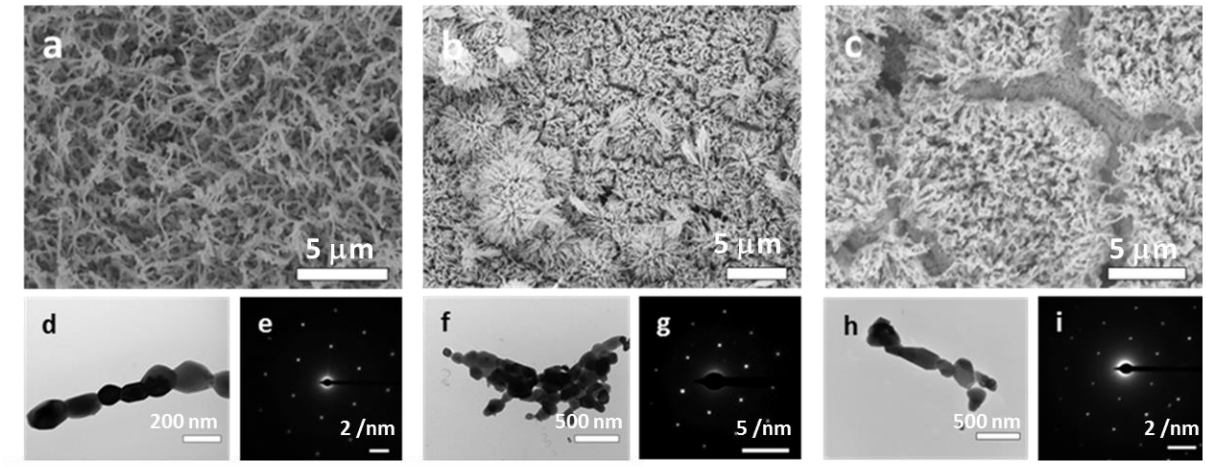

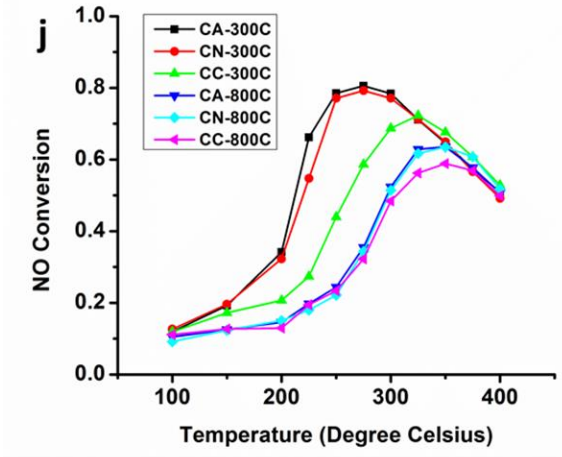

Co_3O_4 [a] nanoarray	Grain size (nm)	BET surface area (m^2 g^{-1})	T_M (Degree Celsius)
CA-300 C	20-30	122.6	275
CN-300 C	25-40	158.1	275
CC-300 C	60-80	81.1	325
CA-800 C	150-200	39.4	350
CN-800 C	150-200	38.7	350
CC-800 C	150-200	37.2	350

[a] Co_3O_4 prepared from acetate (CA), nitrate (CN) and chloride (CC).

Figure 3.14. SEM images of 800 °C annealed Co_3O_4 nano-arrays prepared from a) cobalt nitrate; b) cobalt acetate and c) cobalt chloride. TEM characterizations of 800 °C annealed Co_3O_4 nano-arrays prepared from d) cobalt nitrate; f) cobalt acetate and h)-cobalt chloride. e) g) i) are

selected area electron diffraction patterns respectively. Scale bars: a)-c) 5 □m; d) 200 nm; e) 2 nm^{-1}; f) 500 nm; g) 5 nm^{-1}); h) 500 nm; i) 2 nm^{-1}. j) Catalytic NO conversion of Co3O4 nano-arrays annealed at different temperatures.

Since the grain size of the porous structure leads to various surface areas and impacts the catalytic performance, further experiments were designed to tune the grain size and the porosity of different Co_3O_4 nano-arrays. Figure 3.14a-c display the SEM images of Co_3O_4 nano-arrays obtained by annealing at 800 °C for 4 hours. The flower shapes of CA retain while in CN and CC the nano-arrays collapse and the nanowires become kinked. As demonstrated in Figure 3.14a, the morphology of CN nano-arrays transform into networks of nanowires which are no longer porous. It is clearly seen in Figure 3.14c that the CC nano-arrays seem to crack into separate islands with voids in between. Each individual nanowire is no longer well shaped but bended. Further TEM characterization shows the nanowires are assembled by solid particles and these particles are not well oriented and thus not forming straight nanowires. Selected area electron diffraction (Figure 3.14e, 3.14g, 3.14i) reveals that these particles are single crystalline. Surprisingly, all three types of Co_3O_4 nanowires prepared from different cobalt precursors are found to be assembled by particles of the same size. The typical size of these irregular particles is about 150-200 nm, which is ascribed to the sintering effect that promotes small grains to merge and recrystallize into bigger particles.

BET surface area measurement concludes that high temperature annealing has successfully suppressed the surface area, evidenced by TEM characterization in Figure 3.14d through 3.14h, and changed the structure into nonporous. Specifically, the surface area decreased by 70% in CA and CN while 55% in CC. The grain sizes of all these three types of Co_3O_4 nano-arrays were determined to be 150-200 nm by TEM observation. As a result, the reduced surface area (~40 m^2

g^{-1}) and the increased grain size have deteriorated the catalytic NO oxidation efficiency. Figure 3.14j and Figure 3.15 illustrates the catalytic performance of NO oxidation using these 800 °C annealed nano-arrays. Surprisingly, all three types of Co_3O_4 nano-arrays achieve maximum NO conversion at the same temperature of 350 °C which is delayed compared with the previous freshly prepared Co_3O_4 nano-arrays annealed at 300 °C. The maximum NO conversion has decreased from 80% to 65% for CA and CN and from 75% to 60% for CC. With the summary in the table at the bottom right of Figure 3.14, the temperature (T_M) where maximum conversion occurs is thus influenced by the surface area tuned by different grain sizes. Without 800 °C annealing, the similar BET surface area and grain size make the previously prepared CA and CN achieve their maximum NO conversion at the same temperature. This temperature for CC, however, is delayed because CC has much larger grains but smaller surface area. The difference of maximum NO conversion efficiency may be ascribed to different amount of surface Co^{3+} as illustrated by previous XPS spectrum. The larger population of Co^{3+} would promote the catalytic activity and result in higher catalytic conversion at the same temperature. Therefore, the Co^{3+} population determines the maximum catalytic nitric oxide conversion that Co_3O_4 hierarchical nano-arrays can achieve and the surface area adjusted by thermal annealing contribute to the catalytic conversion temperature.

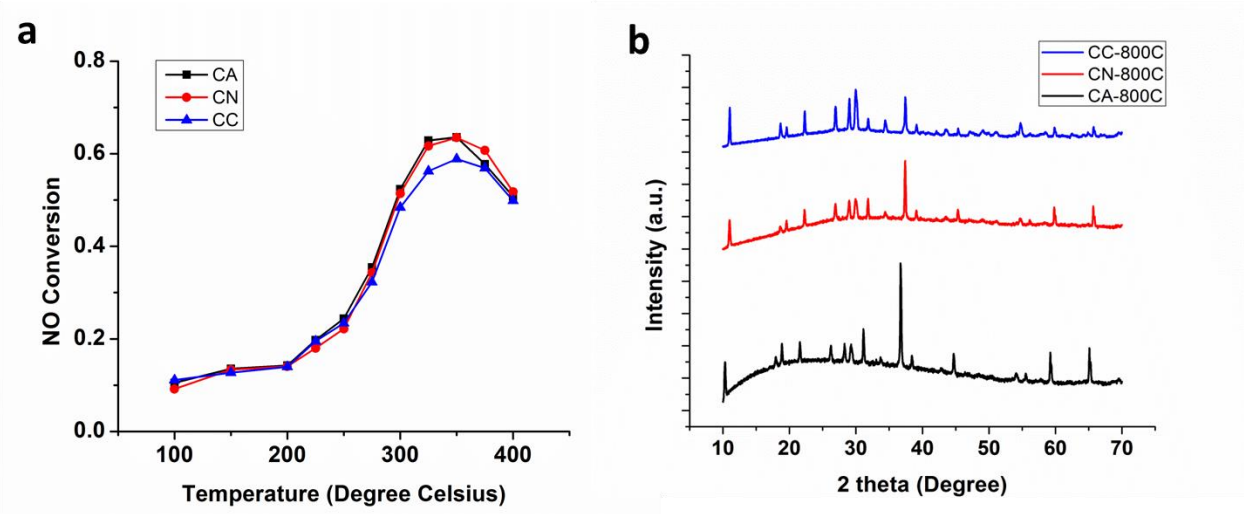

Figure 3.15. a) Catalytic NO oxidation performance of Co_3O_4 nano-arrays based catalytic honeycombs prepared by annealing at 800 °C. b) XRD spectra of 800 °C annealed Co_3O_4 nano-arrays honeycombs.

3.4. Conclusions

In summary, a new type of noble metal-free catalytic honeycomb has been successfully developed by rational assembly of hierarchical Co_3O_4 nano-arrays onto three dimensional ceramic and stainless steel substrates. Cobalt precursors were found to induce different assembly fashions for Co_3O_4 nano-arrays growth. Different Co_3O_4 growth mechanisms including "dumbbell aggregation" and "elongation-splitting" have been proposed. The as-prepared catalytic honeycombs exhibited high performance NO oxidation with NO conversion efficiency as high as 80%. Systematic tests and characterizations regarding different aspects of catalyst stability demonstrated that such nano-arrays based catalytic honeycombs were able to sustain their high NO conversion for either cyclic or long term steady isothermal operation. Meanwhile, the catalytic honeycombs showed great adaptability to temperature fluctuations with repeated heating and cooling. The difference in catalytic NO oxidation performance was studied by closely looking at the surface chemistry and microstructure. The NO conversion capability of

Co_3O_4 nano-arrays was determined by the amount of Co^{3+} on the surface, which acted as the active sites. The relative amount of Co^{3+} on catalyst surface was quantitatively determined by XPS and qualitatively analyzed by XRD. BET and TEM characterization revealed the temperature for maximum NO conversion was dependent on the surface area tuned by the grain size as well as the porous nature of nanowires. Increased surface area with the reduced grain size would help achieve the maximum NO conversion at a lower temperature. Thermal annealing at different temperatures was demonstrated to tune the porosity, grain size and thus surface area of Co_3O_4 nano-arrays. Regardless of the precursor difference, the 800 °C annealing produced nonporous Co_3O_4 nano-arrays with similar grain size and surface area and therefore catalytic honeycombs prepared from different cobalt precursors can be tuned to exhibit their maximum NO conversion at the same temperature.

3.5. Reference

[1] Arakawa, H., Aresta, M., Armor, J. N., Barteau, M. A., Beckman, E. J., Bell, A. T., Bercaw, J. E., Creutz, C., Dinjus, E., Dixon, D. A., Domen, K., DuBois, D. L., Eckert, J., Fujita, E., Gibson, D. H., Goddard, W. A., Goodman, D. W., Keller, J., Kubas, G. J., Kung, H. H., Lyons, J. E., Manzer, L. E., Marks, T. J., Morokuma, K., Nicholas, K. M., Periana, R., Que, L., Rostrup-Nielson, J., Sachtler, W. M. H., Schmidt, L. D., Sen, A., Somorjai, G. A., Stair, P. C., Stults, B. R. and Tumas, W., *Chemical Reviews*, 2001, **101**, 953-996.

[2] Granger, P., and Parvulescu, V., *Chemical Reviews*, 2011, **111**, 3155-3207.

[3] Fritz, A., Pitchon, V., *Applied Catalysis B: Environmental*, 1997, **13**, 1-25.

[4] Haga, F., Nakajima, T., Miya, H., Mishima, S., *Catalysis Letters*, 1997, **48**, 223-227.

[5] Amiridis, M. D., Zhang, T., Farrauto, R. J., *Applied Catalysis B: Environmental*, 1996, **10**, 203-227.

[6] Klingstedt, F., Arve, K., Eränen, K., Murzin, D. Y., *Accounts of Chemical Research*, 2006, **39**, 273-282.

[7] Mou, X., Zhang, B., Li, Y., Yao, L., Wei,X., Su, D. S., Shen, W., *Angewandte Chemie International Edition*, 2012, **51**, 2989-2993.

[8] Huang, Z., Gu, X., Wen, W., Hu, P., Makkee, M., Lin, H., Kapteijn, F., Tang, X., *Angewandte Chemie International Edition*, 2012, 52, 660-664.

[9] Fridell, E., Persson, H., Westerberg, B., Olsson, L., Skoglundh, M., *Catalysis Letters*, 2000, **66**, 71-74.

[10] Liu, G., Gao, P. X., *Catalysis Science & Technology*, 2011, **1**, 552-568.

[11] Sharma, M., Harold, M. P., Balakotaiah, V., *Industrial & Engineering Chemistry Research*, 2005, **44**, 6264-6277.

[12] Yu, J. J., Wang, X. P., Li, L.D., Hao, Z. P., Xu Z. P., Lu, G. Q., *Advanced Functional Materials*, 2007, **17**, 3598-3606.
[13] Wang, W., McCool, G., Kapur, N., Yuan, G., Shan, B., Nguyen, M., Graham, U. M., Davis, B. H., Jacobs, G., Cho, K. and Hao, X., *Science*, 2012, **337**, 832-835.
[14] Li, K., Tang, X., Yi, H., Ning, P., Kang, D., and Wang, C., *Chemical Engineering Journal*, 2012, **192**, 99-104.
[15] Park, E., Chin, S., Jeong, J., and Jurng, J., *Microporous and Mesoporous Materials*, 2012, **163**, 96-101.
[16] Gao, P.X., Shimpi, P., Gao, H., Liu, C., Guo, Y., Cai, W., Liao, K. T., Wrobel, G., Zhang, Z., Ren, Z., and Lin, H. J., *International Journal of Molecular Sciences*, 2012, **13**, 7393-7423.
[17] Jiang, J., Li, Y., Liu, J., Huang, X., Yuan, C., and Lou, X. W., *Advanced Materials*, 2012, **24**, 5166-5180.
[18] Wang, Z. L. and Song, J., *Science*, 2006, **312**, 242-246.
[19] Reddy, A., Gowda, S. R., Shaijumon, M. M., and Ajayan, P. M., *Advanced Materials*, 2012, **24**, 5045-5064.
[20] Guo, Y., Ren, Z., Xiao, W., Liu, C., Sharma, H., Gao, H., Mhadeshwar, A. and Gao, P. X., *Nano Energy*, 2013, **2**, 873-881.
[21] Sun, Q., Ren, Z., Wang, R., Wang, N., and Cao, X., *Journal of Materials Chemistry*, 2011, **21**, 1925-1930.
[22] Ren, Z., Guo,Y., Wrobel, G., Knecht, D.A., Zhang, Z., Gao, H. and Gao, P. X., *Journal of Materials Chemistry*, 2012, **22**, 6862-6868.
[23] Guo, Y., Zhang, Z., Ren, Z., Gao, H. and Gao, P. X., *Catalysis Today*, 2012, **184**, 178-183.
[24] Sun, J., Li, Y., Liu, X., Yang, Q., Liu, J., Sun, X., Evans, D. G. and Duan, X., *Chemical Communications*, 2012, **48**, 3379-3381.
[25] Thormählen, P., Skoglundh, M., Fridell, E. and Andersson, B., *Journal of Catalysis*, 1999, **188**, 300-310.
[26] Xie, X., Li, Y., Liu, Z., Haruta, M. and Shen, J., *Nature*, 2009, **458**, 746-749.
[27] Jansson, J., *Journal of Catalysis*, 2000, **194**, 55-60.
[28] Hu, L., Sun, K., Peng, Q., Xu, B., and Li, Y., *Nano Research*, 2010, **3**, 363-368.
[29] Xie, Y., Dong, F., Heinbuch, S., Rocca, J. J., and Bernstein, E. R., *Physical Chemistry Chemical Physics*, 2010, **12**, 947-959.
[30] Yung, M. M., Holmgreen, E. M., Ozkan, U., *Journal of Catalysis*, 2007, **247**, 356-367.
[31] Ayoub, M., Faisal Irfan, M., and Zuhairi Abdullah, A., *Environmental Progress & Sustainable Energy*, 2011, 31, 553-557.
[32] Hu, L., Peng, Q. and Li, Y., *Journal of the American Chemical Society*, 2008, **130**, 16136-16137.
[33] Llorca, J., Homs, N., Sales, J. and de la Piscina, P. R., *Journal of Catalysis*, 2002, **209**, 306-317.
[34] Batista, M. S., Santos, R. K., Assaf, E. M., Assaf, J. M. and Ticianelli, E. A., *J Power Sources*, 2004, **134**, 27-32.
[35] Jiao, F. and Frei, H., *Energy & Environmental Science*, 2010, **3**, 1018-1027.
[36] Surendranath, Y., Kanan, M. W. and Nocera, D. G., *Journal of the American Chemical Society*, 2010, **132**, 16501-16509.
[37] Liang, Y., Li, Y., Wang, H., Zhou, J., Wang, J., Regier, T., Dai, H., *Nat Mater*, 2011, **10**, 780-786.
[38] Xiong, S., Chen, J. S., Lou, X. W., and Zeng, H. C., *Advanced Functional Materials*, 2012, **22**, 861-871.
[39] Wang, B., Zhu, T., Wu, H. B., Xu, R., Chen, J. S., Lou, X. W., *Nanoscale*, 2012, **4**, 2145-2149.
[40] Yang, H., Wu, X. L., Cao, M. H. and Guo, Y. G., *The Journal of Physical Chemistry C*, 2009, **113**, 3345-3351.
[41] Xiao, Y., Liu, S., Li, F., Zhang, A., Zhao, J., Fang, S. and Jia, D., *Advanced Functional Materials*, 2012, **22**, 4051-4051.

[42] Xu, Y., Zheng, L., Wu, C., Qi, F., and Xie, Y., *Chemistry – A European Journal*, 2011, **17**, 384-391.
[43] Ding, Y., Wan, Y., Min, Y. L., Zhang, W. and Yu, S. H., *Inorganic Chemistry*, 2008, **47**, 7813-7823.
[44] Liu, L., Liu, H., Zhao, Y. P., Wang, Y., Duan, Y., Gao, G., Ge, M. and Chen, W. *Environmental Science & Technology*, 2008, **42**, 2342-2348.
[45] Tang, J. and Alivisatos, A., *Nano Letters*, 2006, **6**, 2701-2706.
[46] Deng, H., Liu, C., Yang, S., Xiao, S., Zhou, Z. K. and Wang, Q. Q., *Crystal Growth & Design*, 2008, **8**, 4432-4439.
[47] Cha, S. I., Kim, Y., Yun, M. J., Hwang, K. H., Seo, S. H., Shin, Y., Moon, J. H. and Lee, D. Y., *Nanoscale*, 2013, 5, 753-758.
[48] Wang, Q., Liu, B., Wang, X., Ran, S., Wang, L., Chen, D. and Shen, G., *Journal of Materials Chemistry*, 2012, **22**, 21647-21653.
[49] Farrauto, R. J., *Science*, 2012, **337**, 659-660.
[50] Koltsakis, G. C. and Stamatelos, A. M., *Progress in Energy and Combustion Science*, 1997, **23**, 1-39.
[51] Yung, M., Holmgreen, E. and Ozkan, U., *Catalysis Letters*, 2007, **118**, 180-186.
[52] Pietrogiacomi, D., Tuti, S., Campa, M.C. and Indovina, V., *Applied Catalysis B: Environmental*, 2000, **28**, 43-54.
[53] Epling, W.,Hoflund, G., Weaver, J., Tsubota, S. and Haruta, M., *The Journal of Physical Chemistry*, 1996, **100**, 9929-9934.
[54] Ding, Y., Zhu, L., Huang, A., Zhao, X., Zhang, X. and Tang, H., *Catalysis Science & Technology*, 2012, **2**, 1977-1984.

Chapter 4

Large-scale nano-array manufacturing and transition metals doping of Co_3O_4 nano-array for low temperature hydrocarbon and CO oxidation

4.1. Introduction

In the past few decades, three-dimensional (3D) array of nanostructured materials have been widely introduced to enable improved or unique performances in electronics[1,2], optical devices[3-5], lithium-ion batteries[6], solar cells[7], light-emitting diodes[8], microfluidics[9], biomedical devices[10], self-cleaning surface[11] and super adhesives[12]. However, to enhance and promote the widespread applications of nanostructure enabled functional devices, the easy integration of performance enhanced nanostructured materials with the practical 3D substrates commercially available represent one of the better strategies[13]. For example, cordierite monoliths, structured with hundreds of honeycomb channels, is widely known as an ideal 3D support for various energy and environmental catalysts and dominantly used in both stationary and automobile exhaust emission after-treatment devices[12]. Compared with pellet shape supports, monolithic substrate has much larger geometric surface area and thus significantly increases the surface area per unit volume of the catalyst system[14]. Meanwhile, straight channels of monoliths can function as a bundle of parallel, single-pass reactors and its highly open front area results both low pressure drops and fast catalytic processes with less catalysts deactivation tendency due to the easy pass-through of poisoning sources in the emission gas such as heavy hydrocarbons. Moreover, the low heat capacity of cordierite ceramics provides a good heat transfer, and hence catalysts inside the

channels are able to quickly reach the operation temperatures, maintain uniform temperatures and dissipate hot spots[15].

In our previous study, we have developed a general hydrothermal method to in-situ grow a wide range of metal oxide nanostructure arrays (nano-arrays) on 3D monolithic substrates to enable a new class of robust, tunable and highly efficient nano-array based structured catalysts[16]. However, uniform nano-arrays growth on 3D monolith in a large scale is still a challenge. Different from 2D planar substrates, the confined space within the monolith channels partially contributes to the uneven distribution and transport of precursor solution, hindering the uniform growth of nano-arrays along the channel surfaces during the low temperature hydrothermal synthesis. In addition, the much rough and porous substrate surfaces resulting from the normally extrusion manufacturing process also makes it difficult to achieve uniform and vertical distribution of nano-arrays throughout the entire substrate channels[17]. Therefore, the influence of various growth parameters on nano-arrays' uniformity on 3D monolith is still not clear. Specifically, for our Co_3O_4 Nano-array system, which was proved to be a promising low temperature oxidation catalyst with high performance catalytic CO/NO oxidation, we would like to further extend the hydrothermal synthesis to commercially large cordierite monoliths for preliminary engine test and potential practical application in catalysis industry. In this chapter, we will first use ZnO nano-array growth as an example to investigate the hydrothermal growth under external energy generated by mechanical agitation that facilitates the mass transfer. The large scale production of Co_3O_4 nano-array will then be discussed and the transition metal doping effects leading to tunable catalytic activity will be revealed for low temperature hydrocarbon/CO performance.

4.2. Mechanical agitation assisted hydrothermal growth-A case study of ZnO nano-array

By using well-designed mechanical agitation, we successfully achieved uniformly distributed ZnO nanorod (ZnO NR) arrays throughout the entire monolithic cordierite honeycomb by a hydrothermal process. Mechanical agitations such as ultrasonic vibration and magnetic stirring methods were found to be a key parameter for enhancing the nanostructure seeding and growth uniformity throughout the entire multi-channeled substrate during dip-coating and low temperature hydrothermal growth process. Computational fluid dynamics analysis suggests the control over mechanical agitation parameters such as stirring rate may help control the flow field, therefore the uniformity of precursor access for nanostructure growth throughout individual channel surfaces. A series of systematic experiments were designed and conducted to establish the relationship between various hydrothermal growth parameters and the morphology and uniformity of ZnO NR arrays. Finally, we provide a strategy to improve the orientation and order of ZnO NR arrays by introducing pre-growth process (base growth) in a high precursor concentration solution. The understanding demonstrated here could work as a general guidance to the manufacturing of advanced nanostructured materials based practical 3-D devices.

4.2.1. Experimental section

Chemicals. Zinc acetate dihydrate ($Zn(CH_3COO)_2 \cdot 2H_2O$, M.W.: 219.49) and zinc nitrate hexahydrate($Zn(NO_3)_2 \cdot 6H_2O$, M.W.:297.47) were purchased from Fisher Scientific. Hexamethylenetetramine (HMT, 99%) was bought from Acros Organics. All chemicals used for the synthesis of ZnO NR arrays in this work were used as received without further purification. The cordierite monolithic substrates were provided by Corning Inc. (Corning, NY). The cordierite monolith is of 1 mm×1 mm square channels and 100 μm in channel wall thickness, with a diameter in a range of one inch to a few inches.

Hydrothermal Synthesis. To achieve uniformly distributed ZnO NR arrays throughout the multi-channel cordierite monolith, we introduced two major steps in the nanostructure growth process: (1) substrate surface ZnO seeding, (2) hydrothermal ZnO nanostructure growth. In the first step, monolithic cordierite substrates of 1″ in diameter and 1 cm long (Figure 2a) was first rinsed by de-ionized water and ethanol in an ultrasonic bath, and then dipped in a 20 mM zinc acetate ethanol solution while sonicated for 1 minute. The monolithic cordierite was then taken out and baked on a hot plate at 150ºC for 5 minutes. The sonicated dip-coating process was repeated for 10 times to ensure enough seed nanoparticles stick onto the substrate channel surfaces. The dip-coated substrate was then annealed at 350ºC for 5 hours to enhance the ZnO seeds crystallinity and orientations along [002]. In the following hydrothermal process, equal mole (12.5mM, 25 mM or 50 mM) zinc nitrate and hexamethylenetetramine (HMT, 99%, ACROS) were dissolved in 200 mL de-ionized water as precursor. The pre-annealed dip-coated substrate was then grown in the as-prepared precursor at different temperatures (70ºC, 80ºC or 90ºC) for 6 hours. The as-grown ZnO NR arrays were rinsed in de-ionized water and cleaned in an ultrasonic ethanol bath for 10 minutes. Finally, the cordierite monolith sample with grown ZnO NR arrays was dried at 80ºC in air for further testing and characterization.

Characterization. The morphology and microstructure of synthesized ZnO NR arrays were examined by a field emission scanning electron microscope (FE-SEM, JEOL 6335E). A transmission electron microscope (TEM, JEOL JEM-2010F) was used to bright field imaging and the corresponding electron diffraction analysis of the grown ZnO NRs. The crystalline structure of a typical sample was analyzed by an x-ray diffractometer (XRD, BRUKER AXSD D5005) using a Cu Kα radiation wavelength of 1.5406 Å. FEI Strata 400S dual-beam Focused Ion Beam (FIB) equipped with EDAX Si(Li) EDS were used for the sample cutting and element

analysis. Weight measurements were conducted on a bench top balance from Denver instrument. Branson 5510 Sonicator (42 KHz, 135 W) was used for the ultrasound assisted seed layer coating. Fisher Scientific Isotemp hot plate with heating and stirring dual function was used for the hydrothermal growth. All measurements were performed at room temperature.

Computational Flow Analysis. In this study, Computational Fluid Dynamics (CFD) is employed to study the effect of mechanical agitation on the flow field and its implication on mass transport of precursors within the 3-D confined channels in the hydrothermal process. The flow analysis is performed using ANSYS Fluent, which is a commercial CFD solver suitable for a wide variety of compressible and incompressible flow problems [30]. The solution is modeled as a homogeneous, incompressible, Newtonian fluid with density $\rho = 998.2\ kg/m^3$ and dynamic viscosity $\mu = 1 \times 10^{-3}$ kg/m-s. Incompressible Navier–Stokes equations are used to describe momentum conservation using the finite-volume methods[18]. Large eddy simulation with dynamic Smagorinsky subgrid model is used to capture the unsteady phenomena. In the computation, the SIMPLE scheme is used for pressure–velocity coupling, the second-order bounded central differencing scheme is used to solve the momentum, and the second-order implicit scheme is used to advance the flow in time.

4.2.2. Results and Discussion

The overall schematic appearance of a typical monolithic substrate was shown in Figure 4.1a, while the inside cross-sectional view of each channel with uniform ZnO NR arrays was illustrated in Figure 4.1b. The ZnO nanorod array growth process was comprised of two stages, as seen in the growth process diagram (Figure 4.1c): (1) dip-coating of ZnO seed layer on the channel surfaces and (2) hydrothermal growth of ZnO NR arrays inside the channels. After dip-coating of seed layer, the average weight percentage of seed nanoparticles with respect to total

weight of the dipcoated substrate was determined to be ~1.6% (Figure 4.1d, purple) by directly weighing of more than 10 samples by a benchtop balance. After further hydrothermal growth, the average weight percentage of the synthesized ZnO NR arrays significantly increased to ~3.8% (Figure 4.1d, red), indicating the effective deposition and crystal growth. The formation kinetics of ZnO followed the below two-step reaction process, in which the weak base HMT decomposes and slowly release OH- to facilitate hydroxide precipitation and decomposition associated with the ZnO nanocrystal nucleation and growth[19]. **Step 1**: Thermal decomposition of HMT to formaldehyde and ammonia: $C_6H_{12}N_4 + 10H_2O \rightleftharpoons 6CH_2O + 4NH_4 + 4OH^-$; **Step 2**: Precipitation of Zn^{2+} ions: $Zn^{2+} + 2OH^- \rightleftharpoons ZnO + H_2O$ or $Zn^{2+} + 2OH^- \rightleftharpoons Zn(OH)_2 \rightleftharpoons ZnO + H_2O$.

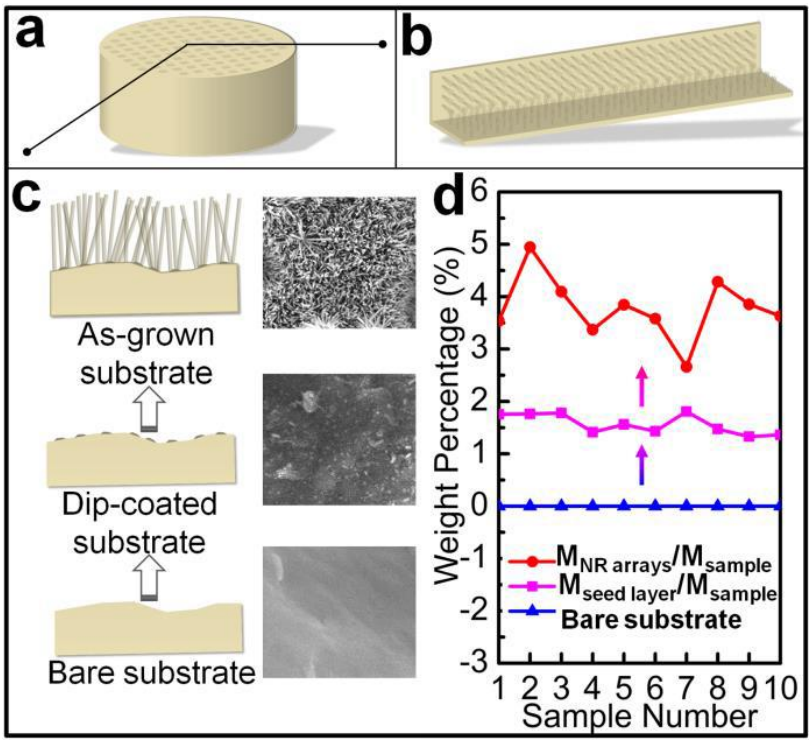

Figure 4.1. Schematic illustrations of a, monolithic cordierite substrate; and b, as-grown NR arrays inside each channel; c, Cross-sectional diagram of ZnO NR arrays growth process; d, The weight percentages of seed layer and as-grown ZnO NR arrays with respect to total mass of dip-coated and as-grown substrate, respectively.

The morphology and structure of as grown ZnO NR arrays based monolith substrate were firstly characterized by Scanning Electron Microscopy (SEM). Dense and uniform ZnO NR arrays grew throughout the multi-channel monolithic cordierite substrate (Figure 4.2a) (Figure 4.2b). A typical channel corner after nano-array growth was shown in Figure 4.2c, where a dense nano-array layer deposited uniformly throughout the channel surface. The inset EDX spectrum confirmed the ZnO content in the grown nanostructures. The zoom-in SEM image shown in Figure 4.2d directly proved the successful growth of ZnO nanorod arrays with good uniformity and ~100% surface coverage. The ZnO NR could even grow inside the substrate surface pores. The cross-sectional SEM image (Figure 4.2e) depicts the vertically oriented ZnO NRs with ~100nm in diameter and ~1.5 μm in length.

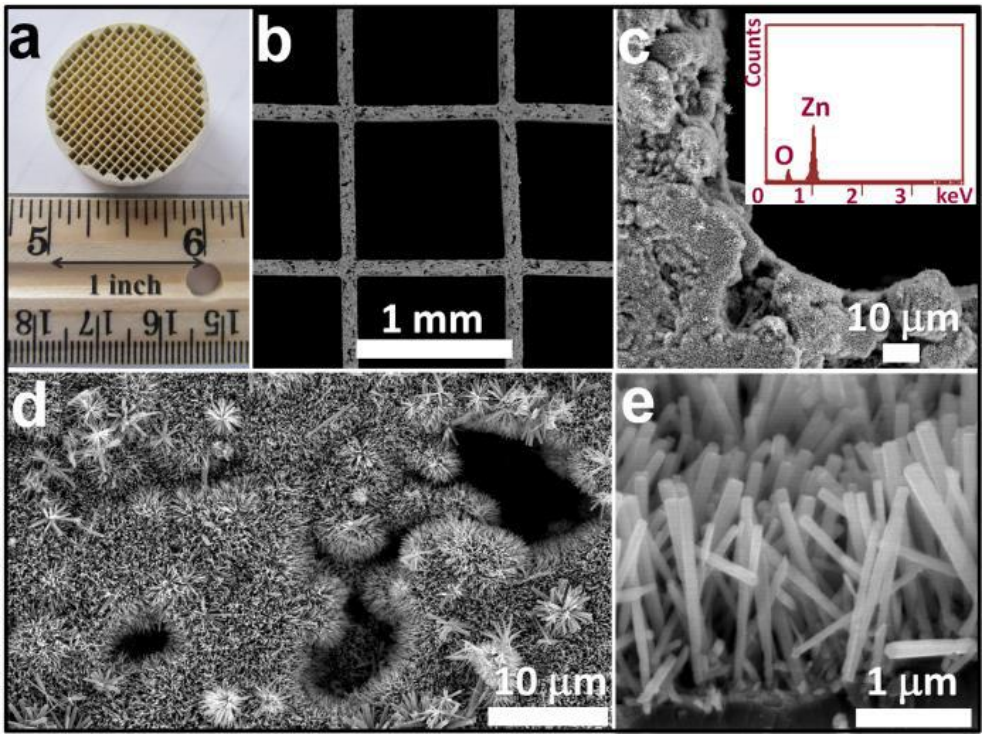

Figure 4.2. a) Typical photograph of ZnO nanorod arrays grown cordierite monolith (diameter: 1 inch, length: 1 cm, channel diameter: 1mm×1mm, channel wall thickness: 100 μm); b)-e) SEM

images of as-grown ZnO nanorod array on monolithic substrate at various magnifications in a cross-sectional view (b, c and e); and plan view (d). Inset in c: EDX spectrum of ZnO NR arrays.

To further unravel the nanorod array growth phenomenon inside the pores of cordierite monolith, a channel cross-sectional sample were prepared and imaged using an FEI Strata 400S DUALBEAM Focused Ion Beam (FIB) microscope. Shown in Figure 4.3a is the SEM secondary electron (SE) image of a slice of successfully cut substrate channel section grown with ZnO nanorod arrays. The zoom-in image in Figure 4.3b clearly displays a typical projection of the porous cordierite surface with pore size ~2μm in width and ~3 μm in depth. The corresponding TEM image from the FIB sample (Figure 4.3c) confirmed both the array structure of ZnO and the size of nanorod. Energy dispersive X-ray spectroscopy (EDX) equipped in FIB-SEM was used to explore the ZnO nanorod distribution in the porous cross section. From the EDX spectrum, peaks located in 0.5 KeV and 1.0 KeV are the O and Zn characteristic peaks, attribute to the as-grown ZnO nanorod arrays on monolith. While the peaks centered at 1.25eV, 1.5 eV and 1.8 eV are corresponding to the Mg, Al, Si energy peaks, which is the typical components of classical cordierite monolith substrate ($Mg_2Al_4Si_5O_{18}$). To get the clear view of ZnO distribution in the pores, we select Zn, Al and Pt as the characteristic elements to do the element mapping. As shown in Figure 4.3d, Al element (cyan) presented in a big portion of the scanned area and imaged the structure of cordierite substrate. Zn element (yellow) not only was detected between the pre-coated Pt layer (purple) and monolith substrate (cyan), but also fills up the pore in the form of nanorod array structure, consistent with the SEM observation in Figure 4.3b. Therefore ZnO nanorod array can not only grow on the channel surface, but also been grown into those surface pores in the cordierite monolith.

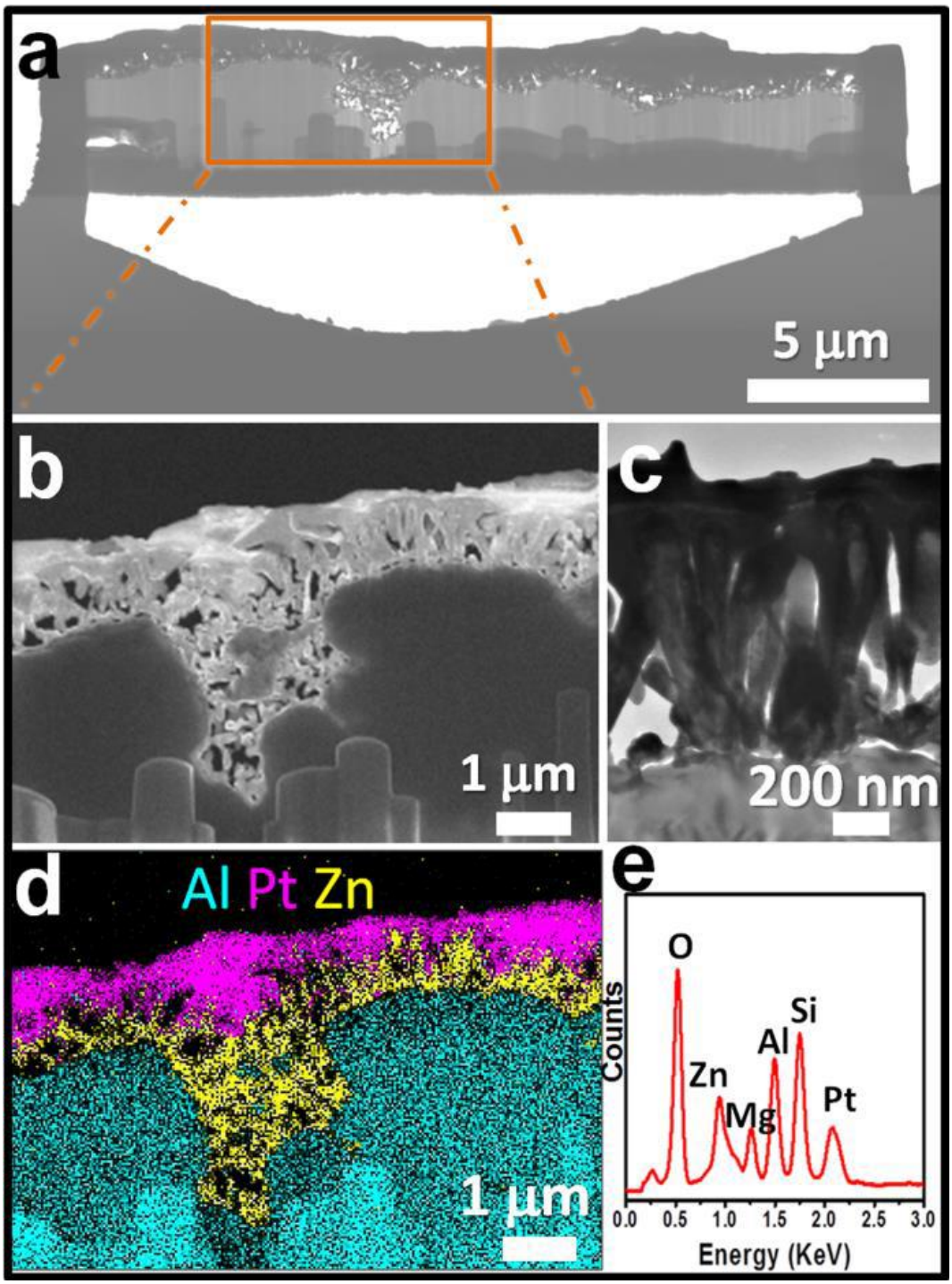

Figure 4.3. a) SEM image of an FIB-cut cross-section of cordierite substrate channel; b) and c) a zoom-in SEM and TEM images of selected areas of the FIB-cut cross section; d) and e) EDX mapping and collected spectrum corresponding to selected pinhole region in b).

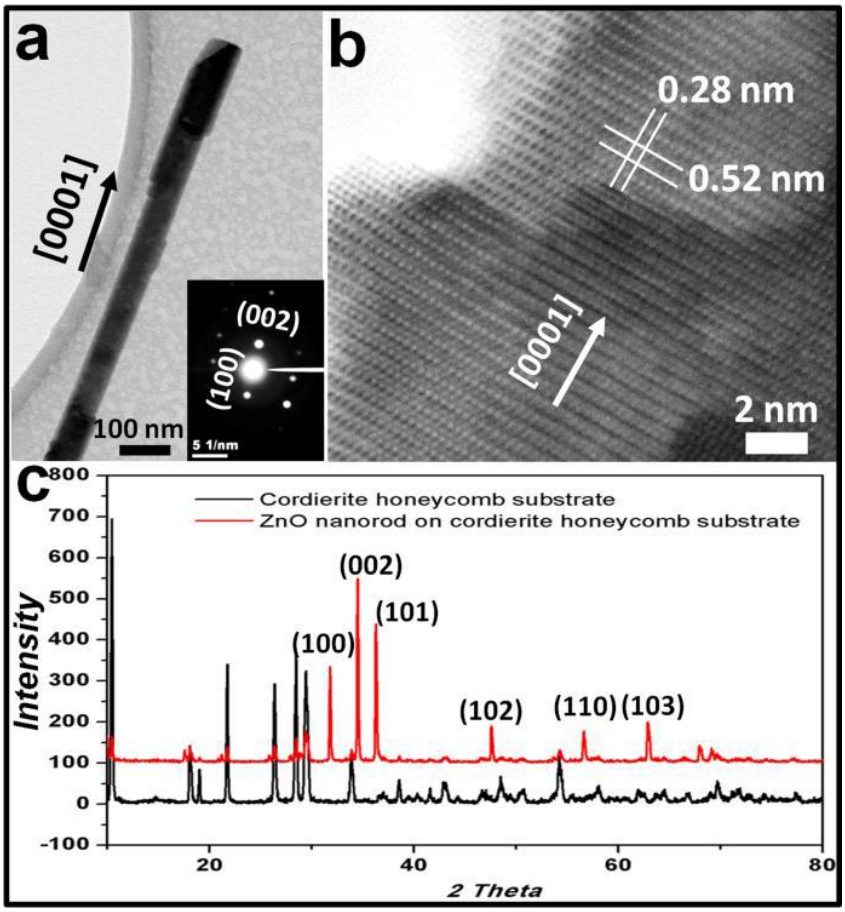

Figure 4.4. a) a TEM bright field image of typical ZnO nanorod and the corresponding selected area electron diffraction pattern in the inset; b) High resolution TEM image of selected area from single nanorod in a); c) XRD spectrum of an as-prepared samples.

Detailed morphology and structure of as-grown ZnO nanorod array were further investigated by TEM, High-Resolution TEM (HR-TEM) and X-ray Diffraction analysis. Shown in Figure 4.4a is a low magnification, bright-field TEM image of a ZnO nanorod collected from the nano-array monolith substrate. Selective area diffraction pattern (inset of Figure 4.4a) from the nanorod exhibits the typical diffraction pattern of hexagonal structure ZnO with growth direction along [0001]. The collected lattice image in Figure 4.4c shows the lattice spaces of 0.53nm and 0.28nm, corresponding to the inter-planar spacing of (0001) and (01-10) facets, respectively. This HRTEM results also confirm the ZnO nanorod growth direction along [0001] and the enclosing

surfaces by {1100} facets. The X-ray diffraction pattern of the after-growth substrate is shown in Figure 4.4c. Compared to values from Joint Committee on Powder Diffraction Standards (JCPDS) card for ZnO (JCPDS 036-1451), all peaks are well matched without impurity characteristic peaks detected, which further confirms that the uniform and pure ZnO nanorod arrays grown on monolith substrates.

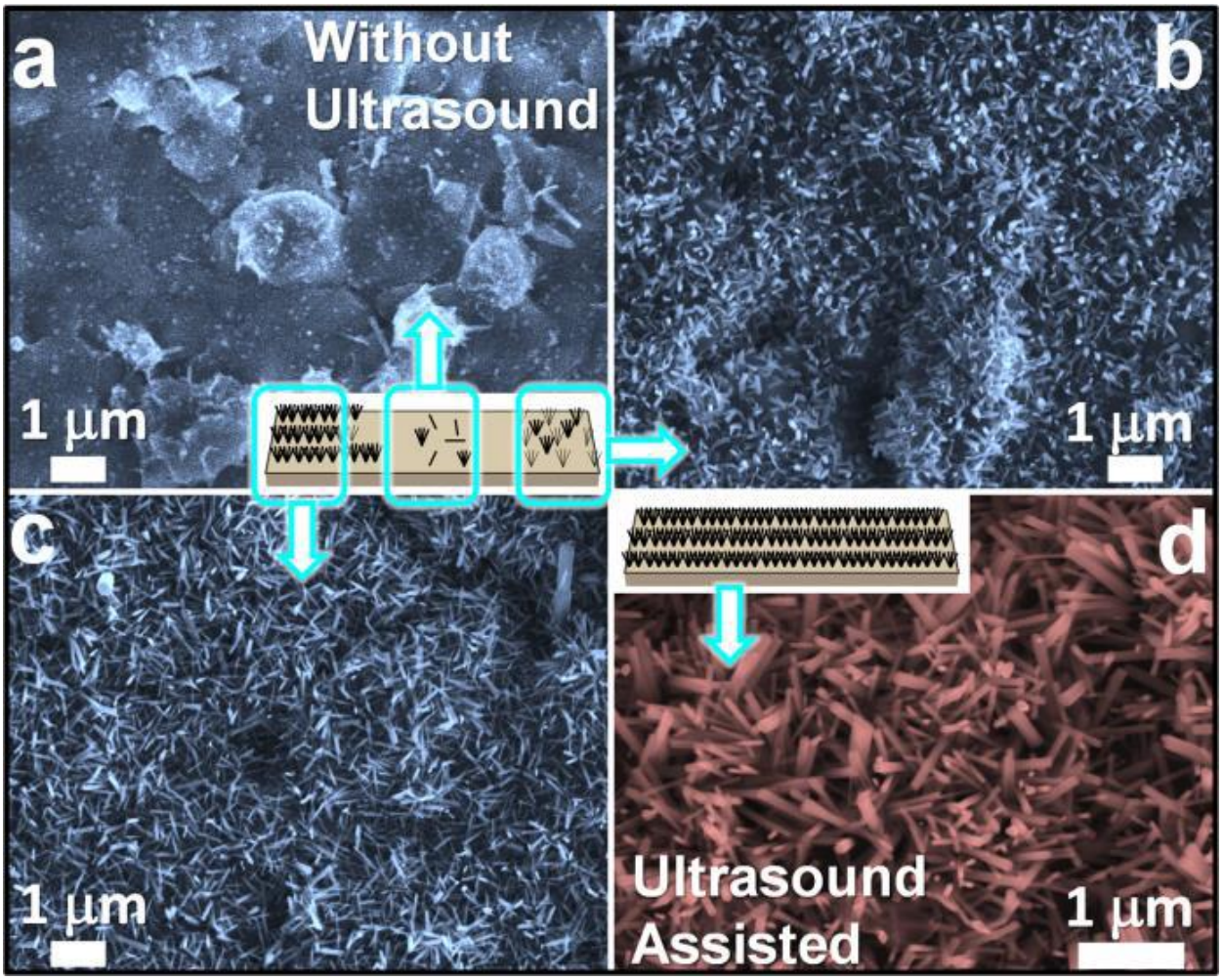

Figure 4.5. SEM images of synthesized ZnO NR arrays: a), b) and c) are different channel regions of an as-grown sample whose seed nanoparticles were dip-coated without ultrasonic vibration; d) ZnO NR arrays grown in the center channel surface region of an as-grown sample whose seed nanoparticles were dip-coated with ultrasonic vibration. Other growth parameters were kept constant.

Even through the growth of ZnO on planar substrate has been reported everywhere, to scale up of the uniform ZnO nanorod array on 3-D monolith with confined space multichannel is not an easy task. A two-step growth of ZnO nanostructure array on planar substrate was extensively reported[20, 21]. A layer of ZnO nano crystal with (002) oriented facet exposed play a critical role in the ZnO nanorod array growth. A batch of controlled experiments with and without (002) oriented ZnO seed layer suggested the necessity of a (002) oriented ZnO seed layer for growing vertically aligned nanorod arrays. However, to achieve uniform deposition of ZnO nanorod arrays throughout the 0.5 cm length cordierite substrate, the uniformity of seed layer across the channel length is proved to be important by comparing two different seeding processes, i.e., dip-coating with and without ultrasonic vibration. Without involving the ultrasonic vibration, ZnO NR arrays grown on dip-coated substrate showed poor uniformity throughout each channel, with relatively dense NR arrays presenting on the two ends (Figure 4.5b and 4.5c) but few and loose NR arrays in the center region (Figure 4.5a). In this case, the uneven distribution of ZnO seeds on the monolith channel led to the non-uniform distribution of ZnO nanorod arrays across the channel length. In this case, the diffusion limited uneven distribution of precursor concentration and air bubbles absorbed on the channel walls may contribute to the uneven distribution of ZnO seed layer. On the contrary, with ultrasonic vibration during the seed layer dip-coating process, dense ZnO NR arrays was obtained throughout the entire channel lengths on the seeded substrates, suggesting ultrasonic vibration during dip-coating an effective mean for improving uniformity of seed layers, and hence promoting uniform growth of NR arrays.

With the help of ultrasonic vibration during dip-coating, uniform NR arrays could be achieved on relatively short cordierite channel with length around 0.5 cm. As we further scale up the monolith substrate size, new problem emerges. For 1 cm cordierite channel, ZnO NR arrays were

dense on the channel end (Figure 4.6a) but loose in the center (Figure 4.6b), which may be attributed to inefficient reactants transport into center of each channel in the stagnant precursor condition based on the uniformly distributed seed layer on substrate, and hence few NR growth. To further understand the uniformity control over the nanostructure seeding and growth distribution in this hydrothermal process, we have conducted a simple computational fluid dynamics (CFD) study.

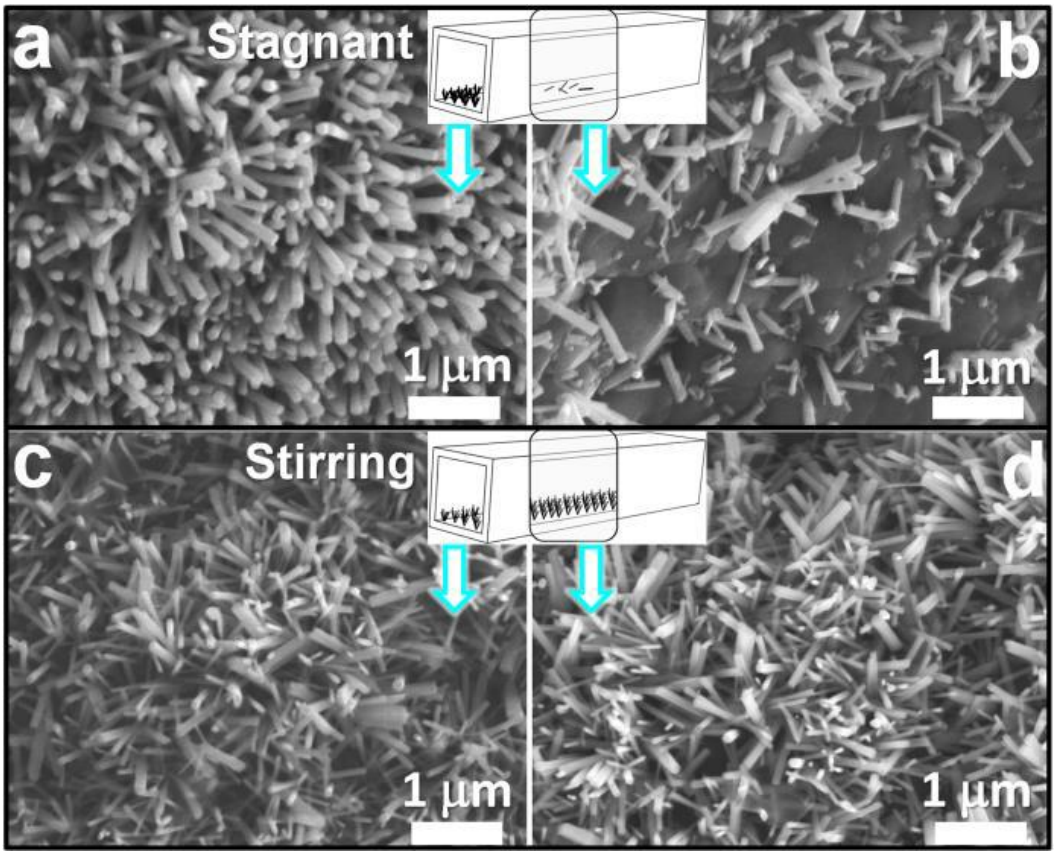

Figure 4.6. SEM images of ZnO NRs synthesized in stagnant (a and b) and stirring (c and d) solution conditions (a and c: edge area; b and d: center area). Other growth parameters were kept fixed.

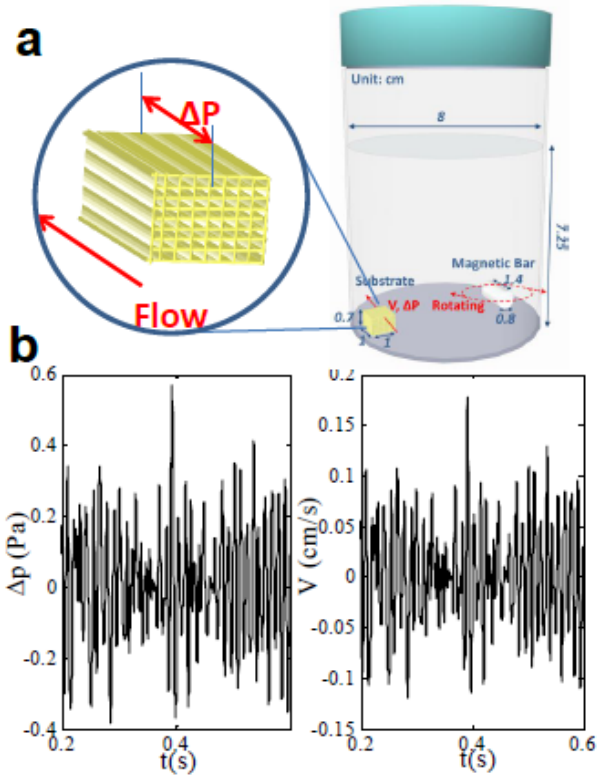

Figure 4.7: (a) Scheme of Hytrothermal process experimental setup and CFD computational model; (b) the pressure difference (Δ P) between the ends of the monolithic channel (1mmx1mmx10mm) and the resulting velocity in the channel from CFD modeling.

The computational model is shown in Fig. 4.7a. The cylindrical fluid volume in the reactor has a diameter of 8cm and a height of 7.25cm. The rectangular monolith substrate has a width of 1cm, a length of 1cm and a height of 0.7cm. The magnetic stirring bar is a regular octagonal prism with a span of the octagon 0.8cm and a height of 1.4cm and it rotates around the z-axis with a speed of 500 rpm. The monolith substrate and stirring bar lie on the bottom of the bottle with their centers being 6.6 cm apart. The computational model is gridded using a non-uniform tetrahedral mesh with a fine resolution near the surfaces of the monolith substrate and stirring bar. In total, the mesh contains approximately 2.5 million cells. A gird refinement study confirms that this mesh is sufficiently fine to resolve the flow feature induced by the magnetic stirring bar. In

the simulation, shear free boundary conditions are applied on the top surface of the fluid volume and non-slipping boundary conditions are applied on all the walls. Currently, the flow within the straight channels in the monolith substrate is not directly modeled. Instead, with the pressures at the front and end faces of monolith substrate are recorded during the simulation, the average velocities within the channels are inferred using the analytic flow solutions for laminar channel flow. The CFD results (Figure 4.7b) indicate that a small pressure drop between the ends of each channel can be generated by introducing a horizontally rotating stirring rod in the reactor. With the channels lying horizontally, this small oscillating pressure difference is capable of producing a convective flow that will flush the channel with fresh solutions in about every two minutes. The longer the channel is, the larger pressure drop is needed to flush the precursor solution through the channel and allow uniform nucleation and growth of nanorod arrays along the channel. Therefore by controlling the stirring speed and geometric locations, and allowing enough time for the transport of precursors to the surface of monolith substrates, the growth become uniform throughout the cordierite monolithic walls. Thus, we employed magnetic stirring during hydrothermal growth to promote reactants transport into channel center and achieve uniform NRs throughout long channel surface. As seen in Figure 4.6c and 4.6d, ZnO NR arrays grown in stirring precursor condition showed improved uniformity on long channel surface, owing to efficient and uniform reactants transport throughout the entire substrate. The experimental enhancement of nanostructure seeding and growth uniformity clearly validate this understanding and need for using mechanical agitation for enhancing the transport across the multiple channels within the cordierite monoliths, therefore the nucleation and growth uniformity of ZnO nanostructures in the sonication and stirring processes.

On the other hand, according to the simulation results reported in the literature and our experimental results, density and height of nano-arrays have been suggested to be important parameters for enabling highly efficient and active hierarchical nanocatalysts. However, the control of density or length of nanostructure array is not a trivial problem in a confined 3-D monolith channel. Reaction thermodynamics, kinetics, as well as microenvironment reactant diffusion[22] should be taken into consideration as an entity, which is also a fundamental scientific question for the other solution processing techniques besides hydrothermal processes.

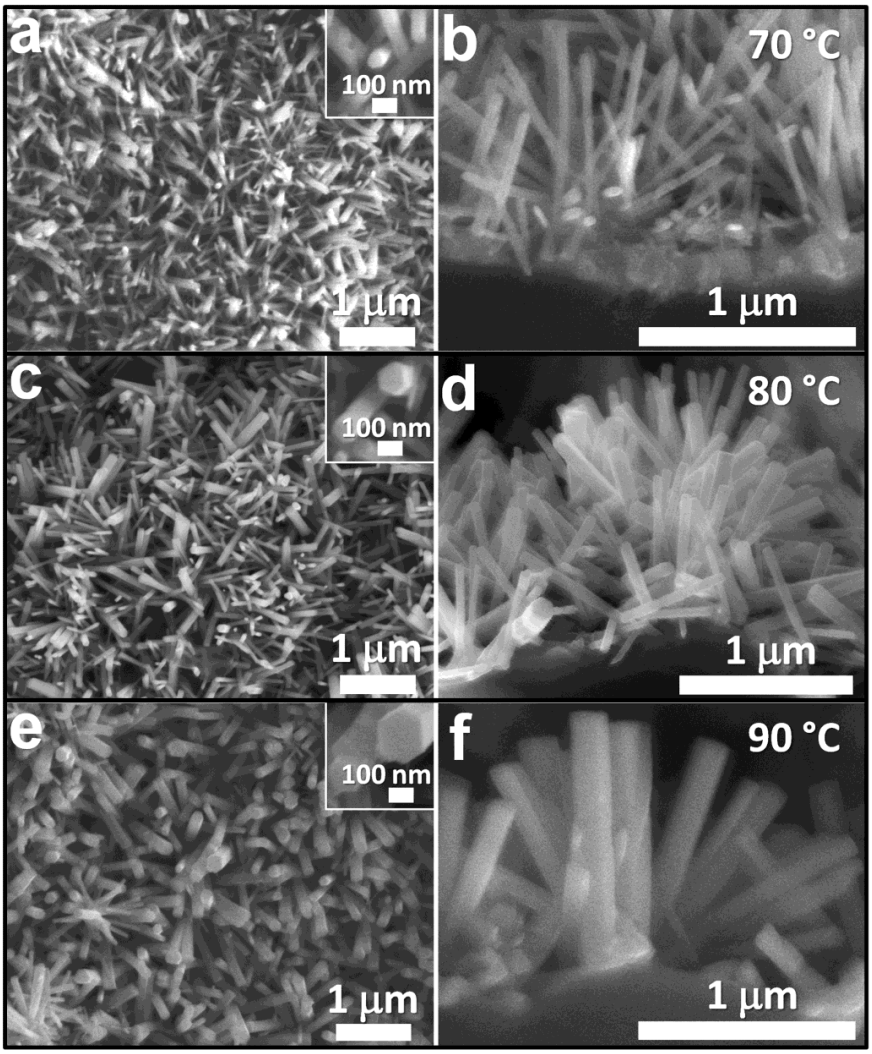

Figure 4.8. SEM images of ZnO NRs synthesized at different temperatures: 70°C (a and b), 80°C(c and d), and 90°C (e and f). Plan view: a), c) and f); Cross-sectional view: b), d) and f). Other growth parameters were kept fixed.

Meanwhile, the control over size and aspect ratio of ZnO NRs is also very important for allowing controlled growth and surface area of ZnO nano-arrays. Temperature has been investigated in hydrothermal synthesis, particularly on its influence to ZnO morphology and size. As observed from Figure 4.7, average length of NRs increased from 749 nm to 866 nm with increasing temperature from 70°C to 90°C. However, inconsistent trend was observed for average diameter, which was the smallest (84 nm) at 80°C and significantly larger (above ~120 nm) at either lower (70°C) or higher (90°C) temperature, as (002) face of ZnO crystal was more sensitive to temperature than other facets[23]. Detailed statistical results were shown in Table 1. As 80°C resulted in the smallest diameter and highest aspect ratio (10.2), 80°C was set to be the growth temperature for further study of precursor concentration effect.

Table 4.1. Statistical results of length and diameter at different temperatures and the corresponding aspect ratios.

Temperature (°C)	Length (nm)	Diameter (nm)	Aspect Ratio
70	749±28	153±6	4.9
80	858±33	84±3	10.2
90	866±39	121±5	7.1

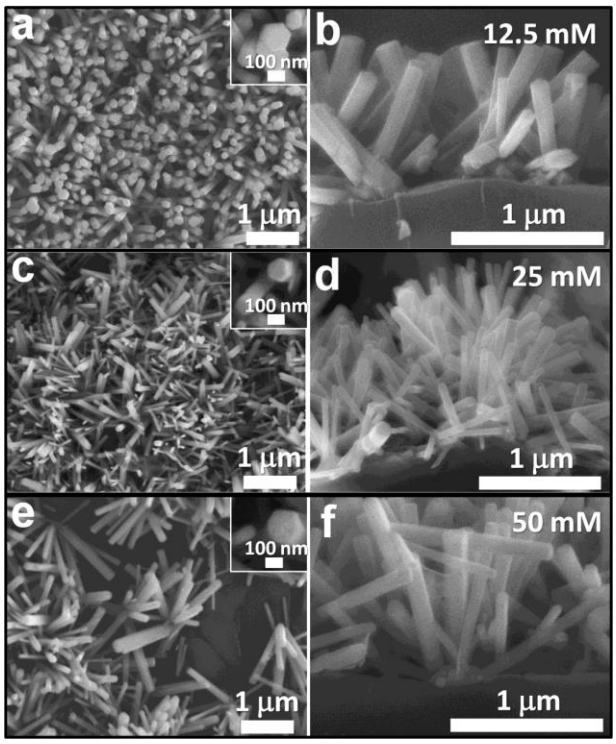

Figure 4.9. SEM images of ZnO NRs synthesized in different concentrations of equal molar Zn(NO3)2 and HMT solution: 12.5 mM (a and b), 25 mM (c and d), and 50 mM (e and f). Planar view: a), c) and e); Cross-section view: b), d) and f). Other growth parameters were kept fixed.

On the other hand, precursor concentration has been studied as another important parameter to control the nano-array size and morphology. With 80°C as the growth temperature, precursor concentration effect to the ZnO morphology and size was also carried out. Figure 4.9 demonstrated the effect of solvent concentration in precursor on the size of grown NRs. It was clear that both length and diameter of the as-grown ZnO NRs increased with increasing solvent concentration from 12.5 mM to 50 mM. Detailed statistical results were summarized in Table 4.2. The average length L (nm) and precursor concentration C (mM) was correlated by L = 2C + 798. Similarly, the relation between average diameter D (nm) and precursor concentration C (nm) was D = 2.1C+ 30.3. The increasing trend of length and diameter with concentration was attributed to

increasing super-saturation degree of precursor[24]. Thus adjusting concentration could be an effective way to control size and aspect ratio of ZnO NR arrays.

Table 4.2. Statistical results of length and diameter of NRs grown using different precursor concentrations and their corresponding aspect ratios.

Concentration (mM)	Length (nm)	Diameter (nm)	Aspect Ratio
12.5	818±31	54±2	15.1
25	858±33	84±3	10.2
50	897±41	132±6	6.8

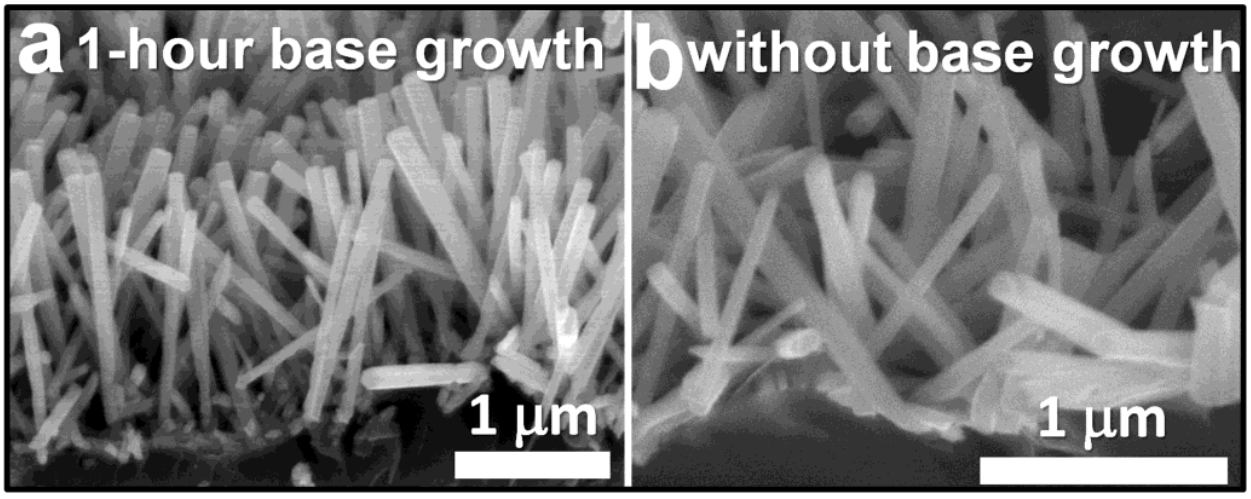

Figure 4.10. SEM images of ZnO NRs synthesized with (a) and without (b) pre-base growth in high concentration precursor. Other growth parameters were kept fixed.

Compared with the random nanostructure materials, vertical array structure with oriented direction and well-defined spacing could potentially enable better diffusion and exposure of active sites, which is beneficial to the catalytic process and filtration function. To further improve vertical alignment of ZnO NR arrays grown on a rough cordierite surface, 1-hour base growth in high concentration (50 mM) precursor was applied, which gave rise to a layer of ZnO crystal with (002) face vertically oriented. The pre-grown substrate was further grown in precursor with desired solvent concentration and temperature. The obtained ZnO NR arrays were

shown in Figure 4.10a, illustrating dense and vertical NR arrays with average length of ~1.5 μm. Comparing to average length without base grown (~0.86 μm), 76.8% enhancement of growth rate was achieved. Besides, the aspect ratio increased from 10.2 to 15.8 as well, indicating enhanced growth efficiency. A possible reason would be that high concentration base growth resulted in a better layer of (002) face oriented ZnO seeds, which further lower interface tension and energy for ZnO crystal nucleation and growth.

4.2.3. Conclusion

Uniform ZnO NRs arrays have been synthesized throughout monolith cordierite substrate by hydrothermal process in a large scale. Mechanical agitation such as ultrasonic vibration during dip-coating and magnetic stirring condition of the growth process plays a key role to improve mass transportation throughout 3-D spaced confined channel, as suggested in the computational flow analysis. The influence of hydrothermal growth parameter to nanorod array distribution, morphology and size were well designed and intensively investigated. We varied growth temperature and found that NRs grown at 80°C had a small diameter with the highest aspect ratio. Besides, we also demonstrated the linear relation between precursor concentration and NRs length or NRs diameter. Last but not the least, we introduced high concentration base growth to obtain vertically aligned ZnO NRs arrays on rough surface and the improvement strategy increased the growth rate of ZnO NRs by ~78%. The crystal growth understanding in 3D confined monolithic substrates achieved here could be extended to the nanocrystal growth and nanomanufacturing for the other types of 3-D devices.

4.3. Large scale manufacturing of transition metal doped Co_3O_4 nano-array catalyst

The increasingly stringent environmental regulations for CO, NO_x, HC and particulate matter (PM) emissions from mobile and stationary sources call for the development of new and highly efficient catalysts[25]. Meanwhile, clean and fuel efficient low temperature combustion (LTC) has held great promises in the pursuit of highly efficient engine, combustor, and turbine based energy devices, prompting the urgent need for low cost, efficient and robust catalytic emission control devices at low temperature. The state of the art Pt-group metal (PGM) based emission control catalysts rely on the significant usage of PGM (~1 wt.% loading) with a large amount of support washcoat such as mesoporous Al_2O_3 micro-particles on monolithic substrates, which generally account for ~20-200 μm thick coating on the monolith channel walls. The commercial catalytic after-treatment devices in automobiles (catalytic converters) integrate the bare monoliths with highly porous metal oxide support and catalysts with high surface area and activity[26]. The bare monoliths are constructed with parallel or honeycomb channels of ~1 millimeter in diameter. The metal oxide support or catalyst loading practically involves a less than ideal washcoating process due to the lack of effective control over the physical and chemical structure of the catalysts, substrate adherence, dispersion, and optimum materials utilization efficiency. Recently, we have successfully invented and demonstrated the integration of 3-D catalytic metal oxide nano-arrays onto channeled monolithic substrates. These monolithic nano-array catalysts were shown to reduce the catalyst usage by 10-40 times without sacrificing the catalytic performance. The nano-array architecture offers advantages of structural stability under high temperature or mechanical agitations, and high surface area to facilitate gas-solid interactions promoting catalytic activity[27, 28]. Despite the merits these nano-array catalysts could bring, the industrially relevant scale-up is required for bridging this nanotechnology with realistic industrial application. Herein, we report for the first time the scalable integration of nano-arrays onto large commercial monolithic

honeycombs (Figure 4.11), which can be directly used as structured oxidation catalysts. Through rational alloying with transition metals such as Ni and Zn, the cation populations and occupancies in spinel cobalt oxide, a high performance oxidation catalyst has been successfully created to tune the catalytic activity towards different oxidation reactions at low temperature[29].

4.3.1. Experimental section

Materials synthesis. The $M_xCo_{3-x}O_4$ (M=Co, Ni and Zn) nano-array catalysts were prepared by a hydrothermal synthesis followed by ambient annealing at 300°C. As illustrated in Figure 1b, 1/4 of the large commercial monolithic honeycomb was cut for the synthesis. The monolithic honeycomb substrate was first immersed in distilled water and acetone with ultrasonication for 30 minutes to remove residual contaminants inside the channels. Aqueous solution of cobalt nitrate hexahydrate ($Co(NO_3)_2•6H_2O$), nickel nitrate hexahydrate ($Ni(NO_3)_2•6H_2O$) as well as zinc nitrate hexahydrate ($Zn(NO_3)_2•6H_2O$) with concentration of 0.5 mol L^{-1} were prepared as the precursor for the reaction. For Co_3O_4 nano-array synthesis, the monolithic honeycomb was suspended in 300 mL $Co(NO_3)_2•6H_2O$ solution followed by the addition of 10 g urea under vigorous magnetic stirring until the solution becomes transparent. The mechanical agitation by magnetic stirring (~1200 rpm) was introduced during the hydrothermal synthesis to promote the mass transfer inside the 5cm long channels of the honeycomb. The reaction was maintained at 90°C for 12 hours. The honeycomb substrate was then rinsed by distilled water and dried at 80°C for 4 hours. As the final step, the ambient annealing at 300°C for 4 hours with the ramp rate of 20°C/min transforms the basic-carbonate nanowires into porous oxide. For the synthesis of $Ni_{0.5}Co_{2.5}O_4$ nano-arrays, 50 mL $Ni(NO_3)_2•6H_2O$ solution and 250 mL $Co(NO_3)_2•6H_2O$ were used. For the synthesis of $Zn_{0.5}Co_{2.5}O_4$ nano-arrays, 100 mL $Zn(NO_3)_2•6H_2O$ and 200 mL $Co(NO_3)_2•6H_2O$ were used as the precursor and 5 g of ammonia fluoride (NH_4F) was added to

prevent the phase segregation. It is worth noting that in the $Zn_{0.5}Co_{2.5}O_4$ nano-array synthesis, the Zn/Co ratio in the product (1:5), which is determined by EDS under TEM, is not the same as the ratio of the starting precursors (1:2). Compared with Ni, Zn is more difficult to be incorporated into the cubic spinel cobalt oxide lattice. By measuring the weight difference before and after the nano-array growth, the nano-arrays are found to constitute 10% to 14% by weight of the entire monolithic nano-array catalyst.

Catalyst characterization. The structural characterization of materials has been conducted by X-ray diffraction and electron microscopy in tandem with the energy dispersive X-ray spectroscopy. Specifically, The as-prepared nano-array catalysts were characterized by powder X-ray diffraction (XRD) using a BRUKER D2 X-ray diffractometer (Cu Ka radiation, $\lambda = 1.540598\ \dot{A}$). The morphology and structure were characterized using a field emission scanning electron microscope (FE-SEM, JEOL 6335F) and a high resolution transmission electron microscope (HRTEM, JEOL JEM-2010, 200 kV). The TEM samples were prepared by scratching nanowires off the honeycombs and dispersing in ethanol, which was then dropped onto the copper grid coated with carbon film. The BET surface area was characterized by Quantachrome NOVA 1000 Gas Sorption Analyzer and Micromeritics ASAP 2020 physisorption analyzer. The temperature-programmed desorption of O_2 (O_2-TPD) mass spectrometry analysis was conducted in a tube furnace equipped with a gas analyzer MKS coupled with a quadruple mass selective detector. The temperature was controlled by WATLOW F4 controller. 200 mg of catalyst was packed in a quartz tube reactor mounted within the tube furnace. The loaded sample was first purged under argon flow at 300 ºC for 1 h to clean the catalyst surface. After cooled down to room temperature, the sample was exposed to pure oxygen for 1.5 h. The catalyst was then purged with argon for 30 min to remove any surface physisorbed gases and residual feed

gas from the streams. After purging, the catalyst was heated under a flow of argon from room temperature to 800 ºC with a heating ramp of 10 ºC/min. The flow rate for all these steps was controlled to be 200 sccm.

Catalytic performance evaluation. A BenchCAT reactor (Altamira Instruments) was used for both methane combustion and CO oxidation test. Dycor Dymaxion mass spectrometer and Agilent MicroGC were equipped for the gas species analysis in the product stream. Catalytic methane combustion performance was carried out in a temperature range of 20–800°C using 5sccm of 10% CH_4/N_2, 10 sccm of pure O_2, and 35 sccm of argon (1% CH_4, 20% O_2, 9% N_2 and 70% Ar). Catalytic CO oxidation test was performed in a temperature range of 20-200° C using 5 sccm of 10% CO/N_2, 5 sccm of pure O_2 and 40 sccm of argon (1% CO, 10% O_2, 9% N_2 and 80% Ar).

Three pieces of monolithic nano-array honeycomb catalysts (2×3 channels in cross section and 1 cm long in channel length for each piece) were loaded into the quartz tube with inner diameter of ¼ inch (~0.64 cm). With the total flow rate of 50 sccm, the space velocity was controlled to be around 45,000/h. The total weight of the three pieces of the monolithic nano-array honeycomb was around 0.15g. Considering the 10% to 13% nano-array loading, the actual catalytic active materials was about 15 mg to 20 mg. specifically the nano-array loading was measured to be 16.6 mg for Co_3O_4, 17 mg for $Ni_{0.5}Co_{2.5}O_4$ and 16.2 mg for $Zn_{0.5}Co_{2.5}O_4$. The effect of this small difference in the materials usage will be eliminated by calculating the reaction rate normalized by catalyst weight.

4.3.2. Results and Discussion

We started with a urea hydrolysis process to first prepare basic carbonate nanowire arrays and the spinel cobaltite $M_xCo_{3-x}O_4$ nano-arrays (M=Co, Zn, Ni; x=0.5) were obtained after ambient

annealing at 300°C. To guarantee a uniform deposition of nanowire arrays inside the long channels, mechanical agitation by a rotating stirring bar was used to promote the mass transfer during the synthesis. Scanning electron microscope (SEM) images in Figure 4.12 show that the nanowire arrays are uniformly distributed inside the monolithic honeycomb channels. The nanowires are around 10 mm in length. X-ray diffraction (XRD) patterns in the Supporting Information, Figure 4.13 confirm the formation of spinel cobaltite without phase segregation. Using cordierite honeycomb substrate (JCPDS: 120303) as the reference, the diffraction peak shifts due to the introduction of Zn and Ni can be calculated, and the shift towards lower diffraction angle reveals an increase in the lattice parameter after partial replacement of Co atoms by Zn and Ni. Transmission electron microscopy (TEM) characterization in Figure 4.11c shows the nanowires are porous in nature. The measured interplanar spacing in Figure 4.11d corresponds to {111} planes of Co_3O_4 and the zone axis is determined to be $<1\bar{1}0>$ based on crystallographic relations. The grain exposes the {110} surfaces that are perpendicular to the $<1\bar{1}0>$ directions owing to the cubic structured cobaltites. Figure 1e and f show that in both Zn and Ni substituted cobalt oxides, the major exposed crystal facets are also {110}. EDS characterization of several nanowires under TEM (Supporting Information, (Figure 4.13c) confirms the ratio of both Zn/Co and Ni/Co to be 1:5. Ammonium fluoride (NH_4F) is required for the preparation of $Zn_{0.5}Co_{2.5}O_4$ nanowire arrays. Without the use of NH_4F, phase segregation happens as indicated Figure 4.14 leading to no controlled nanowire morphology.

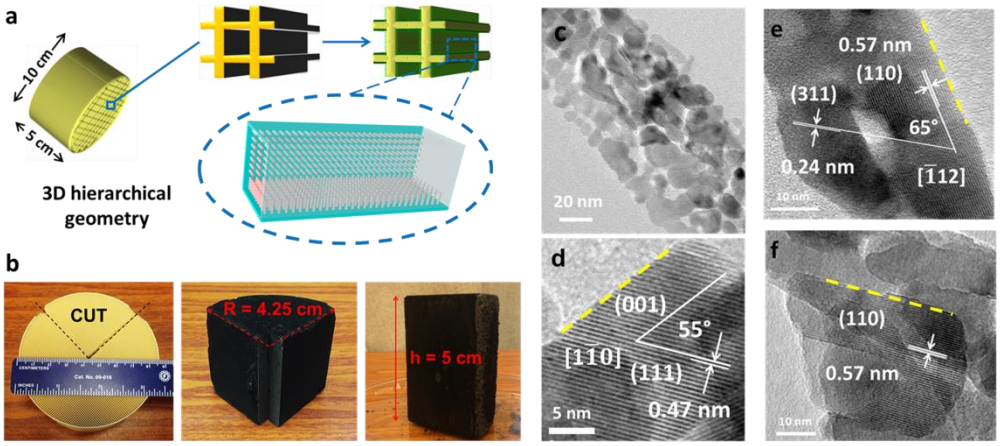

Figure 4.11. a) Monolithic integration of nano-arrays on commercialized honeycomb supports; b) Photographs of a piece of monolithic nano-array catalyst; c) TEM characterization of the Co_3O_4 nanorrays; HRTEM investigation of d) Co_3O_4, e) $Ni_{0.5}Co_{2.5}O_4$, and f) $Zn_{0.5}Co_{2.5}O_4$ nano-arrays.

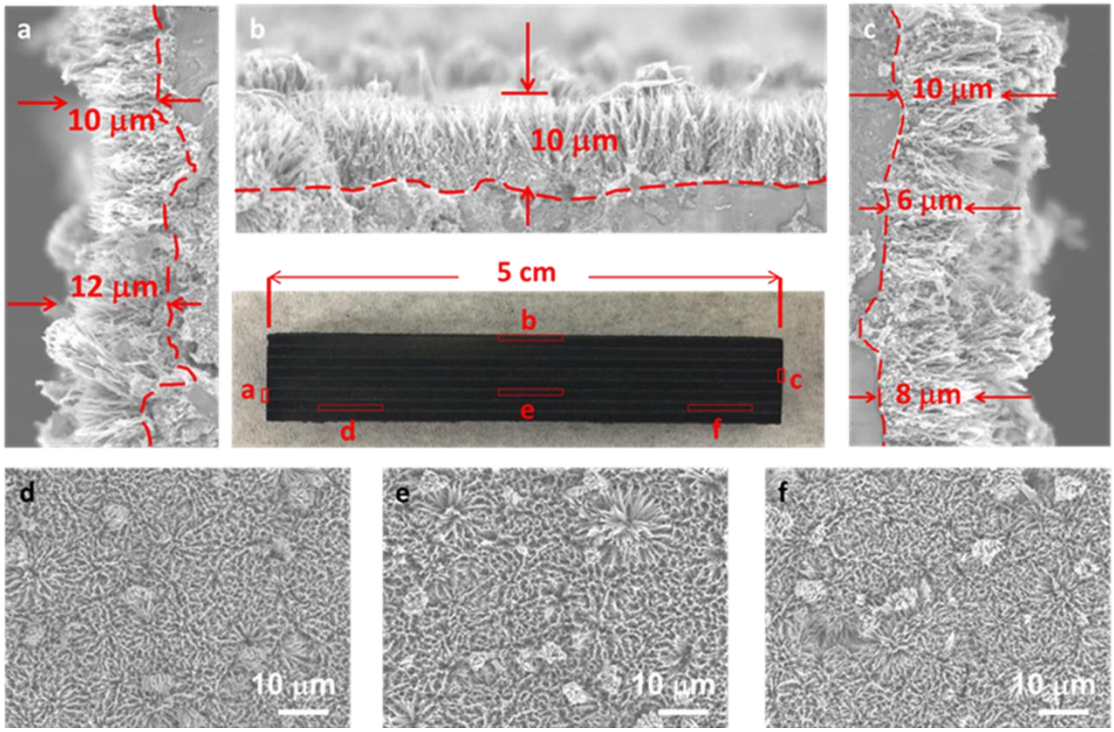

Figure 4.12. Large-area SEM investigation of the nano-arrays grown inside the monolithic honeycomb channels, revealing a uniform coverage of nanowires (circa 10 μm in length) was achieved throughout the 5 cm long honeycomb channels.

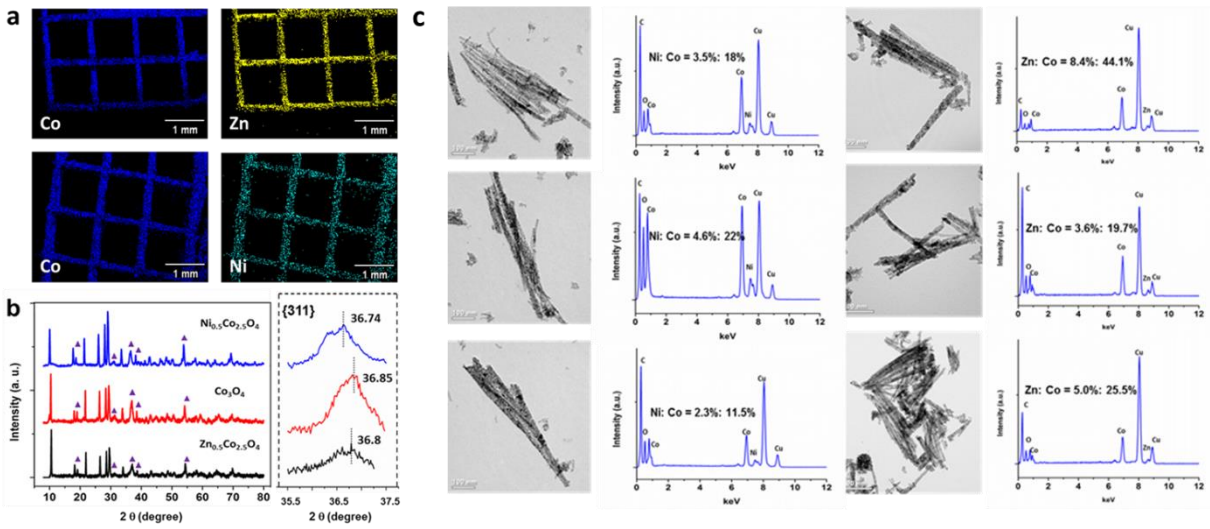

Figure 4.13. a) Large area elemental mapping of Co, Ni and Zn distribution on the monolithic honeycombs by EDS under SEM; b) XRD patterns of monolithically integrated $M_{0.5}Co_{2.5}O_4$ nano-arrays with the denoted peaks well corresponding to the spinel cobaltite. Using the rest peaks (JCPDS#120303) from cordierite honeycombs as the reference, the diffraction peak shift induced by Ni and Zn substitution was calculated. The incorporation of Ni and Zn leads to the crystal lattice expansion with diffraction peaks shifting to smaller angles based on Bragg's equation; c) Regular TEM imaging and EDS characterization of the as-prepared $Ni_{0.5}Co_{2.5}O_4$ and $Zn_{0.5}Co_{2.5}O_4$ nanowires.

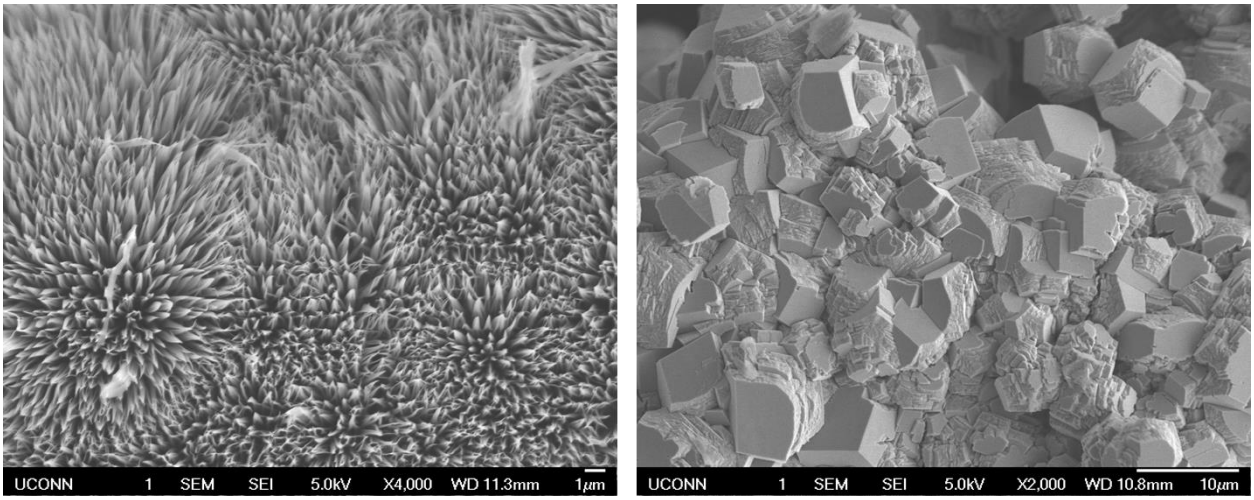

Figure 4.14. SEM characterization of $Zn_{0.5}Co_{2.5}O_4$ nano-arrays synthesized with and without adding NH_4F. The NH_4F was found to prevent the precipitation of large chunks, which was further confirmed to be $ZnCO_3$.

The effect of mechanical agitation upon mass transfer was investigated by SEM characterization of the center region in the 5 cm long monolithic honeycomb channels. Figure 4.15a and Figure 4.15b represent the typical observation of the nanowire growth in the center region without the introduction of mechanical agitation by rigorous magnetic stirring. Very few nanowire arrays come into shape and the coverage is not uniform. The magnified SEM image in Figure 4.15b reveals the dumbbell shaped assembly of the nanowires, which are believed to be the product at the early reaction stage according to our previous study. However, with the magnetic stirring maintained throughout the synthesis process, the center region starts to develop nano-array morphology. Figure 4.15c and Figure 4.15d depict the nano-arrays obtained in the center of an individual channel with the slow magnetic stirring (800 rpm) and fast stirring (1200 rpm) respectively. The stronger mechanical agitation by the increased stirring rate is found to promote the homogenous coverage of nanowires with better-defined array-like morphology.

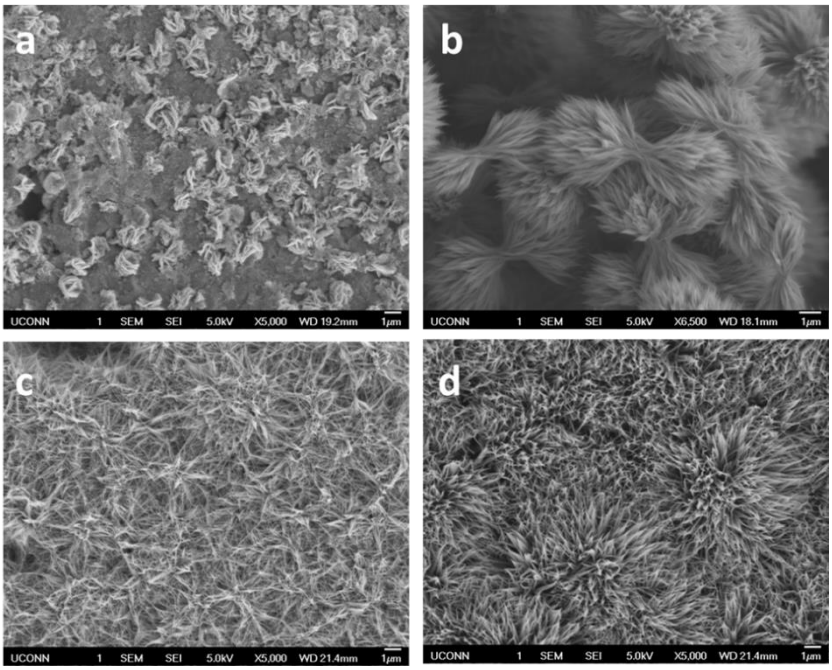

Figure 4.15. a-b) The typical observation of the nanowire growth in the center region without the introduction of mechanical agitation by rigorous magnetic stirring; c-d) the nano-arrays

obtained in the center of an individual channel with c) the slow magnetic stirring (800 rpm) and d) fast stirring (1200 rpm) respectively.

Figure 4.16 shows the $Ni_{0.5}Co_{2.5}O_4$ and Co_3O_4 nano-arrays exhibit the best methane combustion and CO oxidation performance, respectively. The Ni substitution leads to the total oxidation of methane at temperature lower than 600°C with only about 15 mg catalytic material usage. Neither Ni nor Zn substitution contribute to better CO oxidation activity. The incorporation of Ni, however, promotes CH_4 conversion.

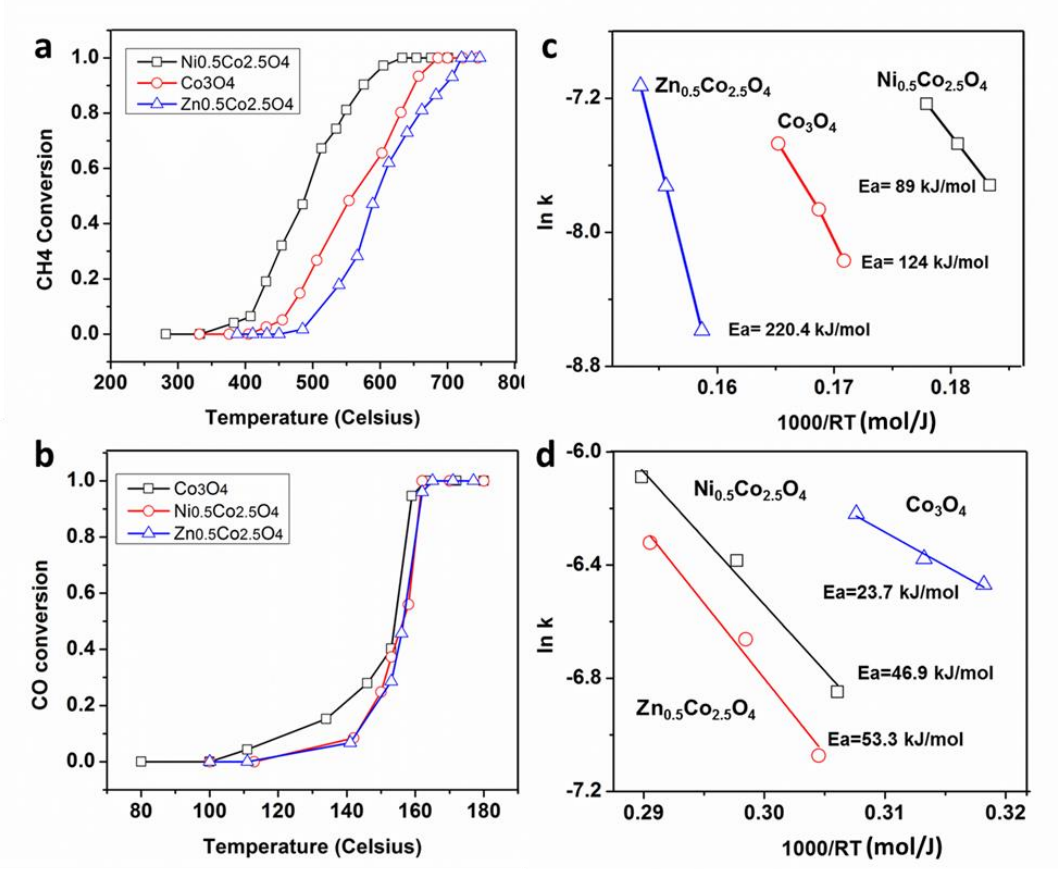

Figure 4.16. a) Catalytic methane combustion and b) CO oxidation performance of $M_{0.5}Co_{2.5}O_4$ (M=Co, Ni and Zn) nano-array catalyst and c-d) the corresponding Arrhenius plots for the reaction kinetics.

In order to perform the reaction kinetics analysis, the BET surface area of blank honeycombs

was measured to be 0.35 $m^2 g^{-1}$. We assume the measured BET surface area of honeycombs structured with nano-arrays is approximately the linear summation of contributions from blank honeycomb and the nano-arrays. Therefore, the BET surface area of nano-array S_A is calculated by

$$S_A = \frac{S(m_h + m_A) - S_h m_h}{m_A}$$

m_h: mass of the honeycomb;

m_A: mass of the nano-arrays (weight difference of honeycomb substrate before and after nano-array growth);

S_h: BET surface area of blank honeycomb;

S: BET surface area of honeycomb structured with $M_{0.5}Co_{2.5}O_4$ nano-arrays.

Table 4.3. The BET surface area calculation results.

	Bare substrate + Nanoarrays (g)	Nanoarrays loading (wt%)	S (m^2/g)	S_A (m^2/g)
Co_3O_4	0.2	11.1	17.5	155.6
$Ni_{0.5}Co_{2.5}O_4$	0.2	11.4	17	146.2
$Zn_{0.5}Co_{2.5}O_4$	0.2	10.8	15.4	141

Normalizing the reaction rate by surface area, the calculated activation energy values for methane oxidation are listed in Figure 4.16. The introduction of Ni into the Co_3O_4 lattice leads to a smaller activation energy (Ea=89kJ/mol) which shows the enhanced reaction kinetics. However, Zn incorporation does not contribute to better catalytic activity with the activation energy of 220.4 kJ/mol. For CO oxidation, the doping of both Ni and Zn leads to deteriorated activity with larger activation energy.

Since the introduction of foreign atoms contributes to enhanced catalytic performance towards methane combustion, we will therefore focus on methane combustion as the probe reaction to characterize the effect of foreign atoms towards the catalyst stability. The stability of catalytic

activity was characterized by maintaining the reaction temperatures at which 10% and 90% conversion of methane were achieved according to the light-off curve in Figure 4.16. In addition, isothermal stability test was performed at the reaction temperature of 600°C. At the temperature of low conversion (10%), the $Ni_{0.5}Co_{2.5}O_4$ nano-arrays demonstrate better stability than Co_3O_4 nano-arrays during the consecutive 72 hours reaction monitored by MicroGC. However, at the temperature of high conversion (90%), both nano-arrays exhibit similar stability. Reaction kinetics usually dominates at the low conversion and it is thus reasonable to conclude the Ni substitution enhance the both activity and stability of the catalyst towards methane combustion. As shown in the Figure 4.17, isothermal stability test performed at the temperature of 600°C shows the methane conversion decays faster in the case of $Ni_{0.5}Co_{2.5}O_4$ nano-arrays compared with that of Co_3O_4 nano-arrays, which indicates Co_3O_4 nano-arrays may have better thermal stability.

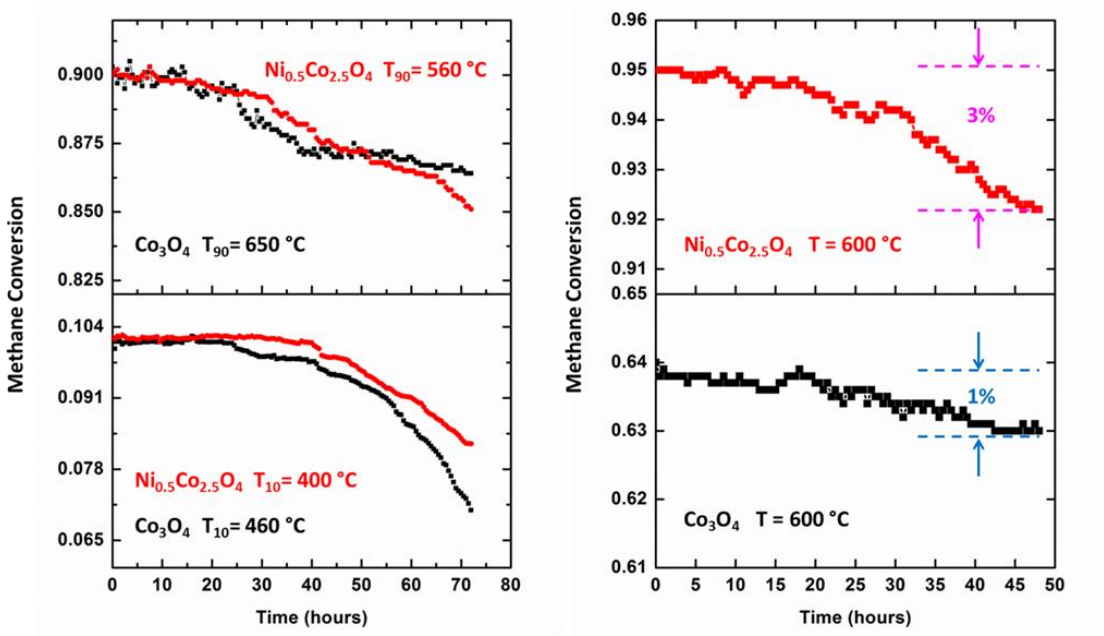

Figure 4.17. Catalytic stability test of $Ni_{0.5}Co_{2.5}O_4$ and Co_3O_4 nano-arrays for methane combustion.

To understand why different dopants lead to different reaction activity, we would like to first know the occupation of dopant atoms in the lattice. The calculations were performed with density functional theory (DFT) as implemented the VASP code. The semi-local (PBE) exchange-correlation approximation with a cutoff energy of 520 eV captured the valence O 2s, 2p and Co 3d, 4s states. Electron-core interactions were treated by projector-augmented (PAW) potentials, and all calculations were spin polarized. Co_3O_4 exist in a spinel structure, with two Co coordinated atoms. Co^{2+} at the tetrahedral site whereas Co^{3+} at the octahedral site. The experimental and computed lattice constants of the Co_3O_4 are 8.07 Å and 8.09 Å, and in good agreement with each other. Using the optimized lattice structure a 56 atom bulk model was constructed, and the foreign atoms (M = Ni and Zn) were introduced into the lattice at the two sites to replace the original Co atoms. Experimental evidence indicates that $Zn_xCo_{3-}xO_4$ and $Ni_xCo_{3-}xO_4$ increases the lattice parameter (x=0.5), a similar result was observed in our models with a lattice parameter of 8.13 Å and 8.11 Å respectively. The stability of the substitution was measured by the formation energy:

$$\mathbf{E_{Sub}} = \frac{\mathbf{E_{bulk}^{M_xCo_{3-x}O_4}} - \mathbf{E_{bulk}^{Co3O4}} - \mathbf{n_M(\mu_M - \mu_{Co})}}{\mathbf{n_M}}$$

$$\mathbf{\mu_i} = \mathbf{E_{bulk}^{MxOy}} - \frac{\mathbf{y}}{\mathbf{x}}\mathbf{E_{O2}}$$

where $E_{bulk}^{M_xCo_{3-x}O_4}$ and E_{bulk}^{Co3O4} are the total energy of substituted and clean Co_3O_4, respectively. μ_i (i = Co, Ni and Zn) are the elemental chemical potentials taken with respect to their corresponding oxides. n_M is the total number of substituent atoms in the model.

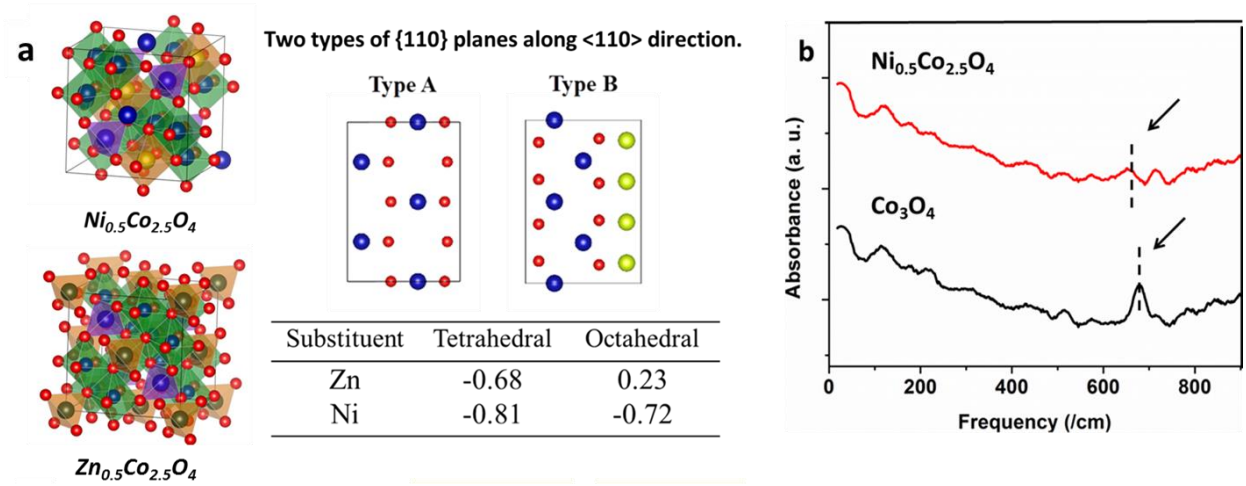

Figure 4.18. a) Crystal structure determination of $Ni_{0.5}Co_{2.5}O_4$ and $Zn_{0.5}Co_{2.5}O_4$ by DFT calculation of substitution energy (eV) of Ni and Zn; b) Raman spectra of Co_3O_4 and $Ni_{0.5}Co_{2.5}O_4$.

Co_3O_4 exists in a spinel structure with Co^{2+} at the tetrahedral sites, whereas Co^{3+} occupies the octahedral sites coordinating with O atoms. Figure 4.18a shows that the substitution by Zn is only favored in the tetrahedral sites, as the substitution energy is positive in the octahedral sites. However, the preference of Ni occupying the tetrahedral (-0.81 eV) over the octahedral sites (-0.72 eV) is marginal based on thermodynamic considerations. Raman spectra of $Ni_{0.5}Co_{2.5}O_4$ and Co_3O_4 are shown in Figure 4.18b. The high frequency mode located within 650–700 cm^{-1} corresponds to the vibrational modes of octahedral Co^{3+} while the mode at about 200 and 400 cm^{-1} is characteristic of tetrahedral Co^{2+}.[30] With decreased population of this high-frequency band and retained intensity of tetrahedral Co^{2+} in Figure 4.18b, Ni substitutes for Co in the octahedral sites.

From previous TEM characterization, the spinel cobaltite nanowires mainly expose {110} planes, which were reported to be the active planes for catalytic oxidation reactions[31]. The {110} planes were thus selected for further surface reaction investigations. From the bulk structures, the active

(110) surface terminations of Co_3O_4 with foreign atoms were created to model the effect of substitute atoms on gas - surface interactions. Two different surface terminations; i) type A containing only octahedral Co^{3+} atoms, and ii) type B containing both tetrahedral Co^{2+} and octahedral Co^{3+} atoms were modeled. The binding of the key adsorbates; CH_3*, O*, H* and CO* were explored, with their stability investigated by the binding energy.

$$\mathbf{E_{Bind}} = \frac{\mathbf{E_{surface}^{adsorbate}} - \mathbf{E_{surface}^{clean}} - \mathbf{n_{ads}E_{adsorbate}}}{\mathbf{n_{ads}}}$$

where $E_{surface}^{adsorbate}$ and $E_{surface}^{clean}$ are the total energies of a surface with and without an adsorbate. $E_{adsorbate}$ is the gas phase energy of an adsorbate while, n_{ads} is the total number of adsorbate molecules on the surface.

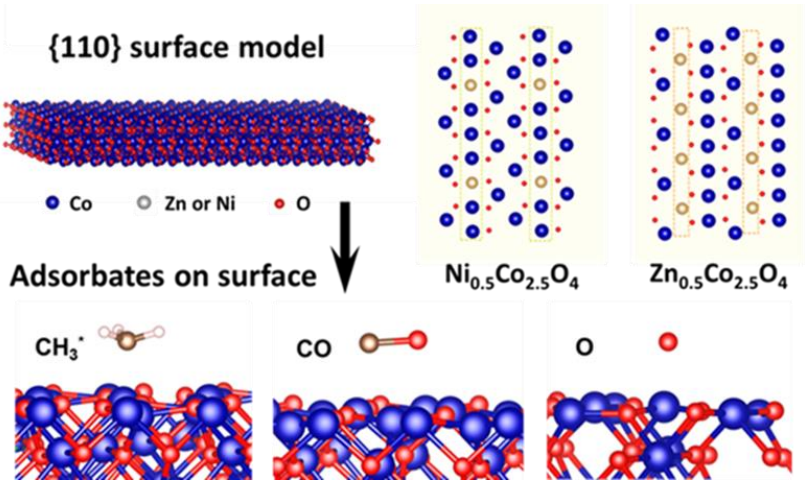

Figure 4.19. The surface construction and adsorption energy computation by density functional theory (DFT).

Adsorbate	Site	$Zn_{0.5}Co_{2.5}O_4$	$Ni_{0.5}Co_{2.5}O_4$	
		Type B	Type A	Type B
O	Co	-1.85	0.11	-0.96
O	Zn	0.48	- -	- -
O	Ni	- -	0.47	-0.23
CO	Co	-2.53	-1.69	-2.5
CO	Zn	-1.18	- -	- -
CO	Ni	- -	-1.28	-2.59
CH_3	Co	-2.03	-1.66	-1.66
CH_3	Zn	-2.29	- -	- -
CH_3	Ni	- -	-1.01	-1.56
CH_3	O	-1.62	-2.3	-1.31
H	O	-3.04	-3.18	-2.77
H	Co	-2.79	-1.91	-1.01
H	Zn	-2.42	- -	- -
H	Ni	- -	-1.65	-0.78

Table 4.4. DFT calculations of binding energies (eV) for adsorbates on different sites of {110} surfaces.

There are two types of {110} surfaces as depicted in Figure 4.19. The type A surfaces only consist of octahedral sites while the type B surfaces have both octahedral and tetrahedral sites. As Zn is only likely to replace tetrahedral Co atoms, only type B sites were simulated for $Zn_{0.5}Co_{2.5}O_4$, and both types of surfaces were considered for $Ni_{0.5}Co_{2.5}O_4$. For catalytic hydrocarbon combustion, early studies suggest that dissociative adsorbed oxygen determines the low-temperature activity (Eley–Rideal mechanism)[32], while some recent reports propose lattice oxygen is involved[33]. To clarify which mechanism dominates, we first calculate the oxygen adsorption energy on the {110} surface of cobaltite. As summarized in Table 4.4, the O adsorption energy on tetrahedral Zn is positive (0.48 eV), indicating that Zn substitution suppresses oxygen adsorption compared to oxygen adsorption at a Co (-0.96 eV) site. Ni (-0.23

eV) is also not as favorable. This result corresponds quite well to the temperature-programmed oxygen desorption (O_2-TPD) spectrum in Figure 4.19 with no desorption shoulder observed for

$Zn_{0.5}Co_{2.5}O_4$ at temperatures below 300°C, where most molecular and dissociatively adsorbed oxygen desorb. The peaks located at around 400°C represent the surface lattice oxygen desorption. The surface lattice oxygen of $Ni_{0.5}Co_{2.5}O_4$ is found to be the most active while that of Co_3O_4 is slightly more active than $Zn_{0.5}Co_{2.5}O_4$. The surface lattice oxygen activity from O_2-TPD has the same tendency with the catalytic methane combustion activity. Moreover, as shown in Figure 4.16, the catalytic methane conversion starts at temperatures higher than 350 °C where dissociative oxygen is less likely to adsorb, surface lattice oxygen dominates in the catalytic methane combustion.

Catalytic CH_4 combustion usually begins with C-H bond activation where the activated H is attacked by oxygen on the catalyst surface[34]. Furthermore, DFT results shown in Table 4.4 suggest that H has a much a stronger affinity towards surface oxygen than CH_3, and CH_3 has more negative adsorption energy on metal sites than on surface oxygen sites. Therefore when H is adsorbed on surface oxygen, the CH_3 radicals prefer to sit on metal active sites (Co, Ni, and Zn). The calculated binding energy reveals CH_3 is most stable on Zn and least stable on Ni. For total oxidation of methane, however, the desorption and further oxidation of CH_3 by either lattice or atmospheric oxygen are keys to the reaction rate. In this regard, Ni can facilitate CH_3 desorption and this also explains why $Ni_{0.5}Co_{2.5}O_4$ exhibits better activity.

For catalytic CO oxidation on Co_3O_4, however, the reaction mechanism has been well-studied. Based on the Mars Van Krevelen mechanism, the CO molecules first adsorb to metal active sites extracting adjacent lattice oxygen to form CO_2 and desorb leaving oxygen vacancies. The lattice

oxygen is further regenerated by atmospheric O2. The DFT calculations show both Zn and Ni are not favorable for CO adsorption on type A {110} surfaces. For type B {110} surfaces in $Ni_{0.5}Co_{2.5}O_4$, however, the CO adsorption energy is similar for Ni and Co. A detailed study on Ni substitution is thus necessary to interpret the CO adsorption and to elucidate why the Ni incorporation leads to active surface lattice oxygen favorable for catalytic CH_4 combustion.

A series of Ni-substituted cobalt oxide ($Ni_xCo_{3-x}O_4$, $0.27<x<1.5$) nano-arrays were prepared by the same hydrothermal processing. Figure 4.20 illustrates the X-ray photoelectron spectroscopy (XPS) results of O1s signals for $Ni_xCo_{3-x}O_4$. The broad peaks can be deconvoluted into four major components (lattice oxygen, surface OH group, defective oxygen, and adsorbed moisture). Quantitative analysis (Table 4.5) reveals the surface defective oxygen population increases from 14% to 22% as more Ni is incorporated. Meanwhile the surface lattice oxygen population decreases from 49% to 38%. , the Ni^{3+} composition starts to increase as more Ni is incorporated into the lattice. This is because the Ni^{2+} occupies the octahedral Co site where Co^{3+} is originally located. The incorporation of Ni thus creates deficiency of positive charges. In order to maintain the charge neutrality, part of Ni^{2+} needs to transform into higher valence state (Ni^{3+}) or oxygen vacancies appear to compensate the positive charge loss. From the quantitative analysis of deconvoluted O 1s signal in Figure 4.20, defective oxygen concentration on the surface starts to increase. Such a sequence of defective oxygen to lattice oxygen ratio corresponds perfectly with the activity of methane combustion shown in Figure 4.20b–d. With high defective oxygen to lattice oxygen ratio on the surface, the mobility of surface lattice oxygen can be greatly improved. As an oxide catalyst for hydrocarbon combustion, the higher lattice oxygen mobility usually leads to higher catalytic activity. A similar behavior has been reported in other oxides and perovskites for hydrocarbon combustion[35]. For catalytic CO oxidation, however, the deficiency

in surface lattice oxygen leads to the slower CO_2 formation and desorption, which lowers the catalytic activity.

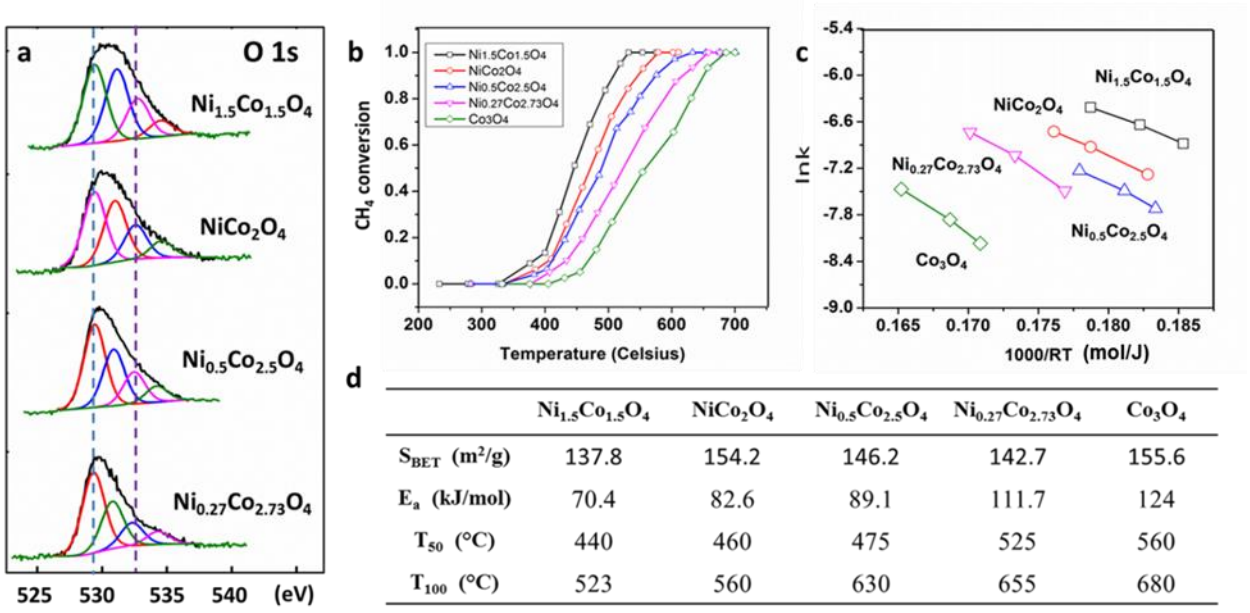

d

	$Ni_{1.5}Co_{1.5}O_4$	$NiCo_2O_4$	$Ni_{0.5}Co_{2.5}O_4$	$Ni_{0.27}Co_{2.73}O_4$	Co_3O_4
S_{BET} (m^2/g)	137.8	154.2	146.2	142.7	155.6
E_a (kJ/mol)	70.4	82.6	89.1	111.7	124
T_{50} (°C)	440	460	475	525	560
T_{100} (°C)	523	560	630	655	680

Figure 4.20. a) XPS spectra of $Ni_xCo_{3-x}O_4$ with different Ni/Co ratios; b) enhanced methane combustion with higher Ni concentration; c) Arrhenius plots of $Ni_xCo_{3-x}O_4$ for methane combustion; d) Summary of surface area, apparent activation energy and characteristic reaction temperatures of $Ni_xCo_{3-x}O_4$.

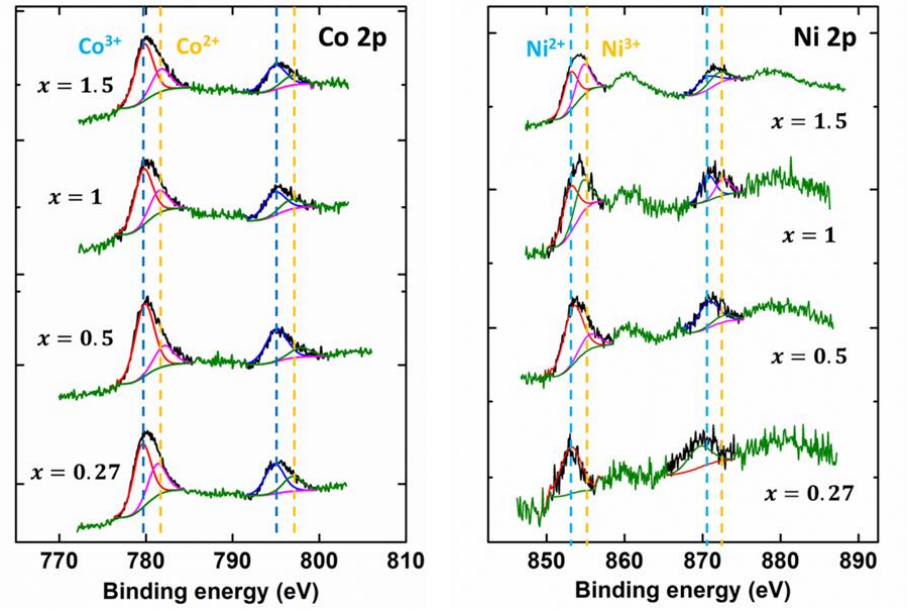

Figure 4.21. Fine XPS spectra of Co 2p and Ni 2p for a series of $Ni_xCo_{3-x}O_4$ with different Ni/Co ratios. The Co 2p and Ni 2p signal can be deconvoluted into Co^{2+} and Co^{3+}, and Ni^{2+} and Ni^{3+} respectively. The Co^{2+} binding energy is larger than that of Co^{3+} and the Ni^{3+} binding energy is larger than that of Ni^{2+} as illustrated by the dash lines in the spectra.

	O 1s			
	lattice	-OH	defect	H_2O
$Ni_{0.27}Co_{2.73}O_4$	49.20 ± 1.73%	28.82 ± 2.01 %	14.11 ± 1.43%	7.87 ± 1.62 %
$Ni_{0.5}Co_{2.5}O_4$	46.28 ± 1.56%	30.00 ± 1.74%	16.09 ± 1.32%	7.63 ± 1.57%
$NiCo_2O_4$	42.02 ± 1.81%	31.39 ± 1.48%	18.51 ± 1.71%	8.08 ± 1.66%
$Ni_{1.5}Co_{1.5}O_4$	38.08 ± 1.60%	32.68 ± 1.88%	21.47 ± 1.59%	7.77 ± 1.88%

	Co 2p		Ni 2p	
	Co^{2+}	Co^{3+}	Ni^{2+}	Ni^{3+}
$Ni_{0.27}Co_{2.73}O_4$	29.22 ± 2.34%	70.78 ± 2.12%	100%	- -
$Ni_{0.5}Co_{2.5}O_4$	18.49 ± 1.79%	81.51 ± 1.87%	79.58 ± 1.45%	20.42 ± 1.82%
$NiCo_2O_4$	13.00 ± 1.43%	87.00 ± 1.67%	59.13 ± 1.53%	40.87 ± 1.76%
$Ni_{1.5}Co_{1.5}O_4$	30.12 ± 1.54%	69.88 ± 1.73%	55.24 ± 1.81%	44.76 ± 1.93%

Table 4.5. Summary of the determination and quantitative analysis for surface O, Co and Ni.

As shown in O_2-TPD, the bulk lattice oxygen desorbs at a lower temperature (ca. 750 °C) after Ni and Zn are introduced to the spinel lattice. The desorption peak indicates $Ni_{0.5}Co_{2.5}O_4$ is less stable than $Zn_{0.5}Co_{2.5}O_4$. Further investigation by XRD reveals $Ni_xCo_{3-x}O_4$ annealed at 400 °C, 500 °C and 600 °C are stable without thermal decomposition when $x<0.5$ (Figure 4.22) which thus makes $Ni_xCo_{3-x}O_4$ nano-arrays ($x<0.5$) suitable for low temperature catalytic methane combustion. Although the catalytic activity can be enhanced by Ni alloying, the increased Ni concentration ($x>0.5$) deteriorates the thermal stability of $Ni_xCo_{3-x}O_4$ with NiO precipitation[36]. It is thus of necessity to balance the increased catalytic conversion efficiency and the possible

operation temperature induced thermal decomposition when $Ni_xCo_{3-x}O_4$ is used for catalytic hydrocarbon combustion.

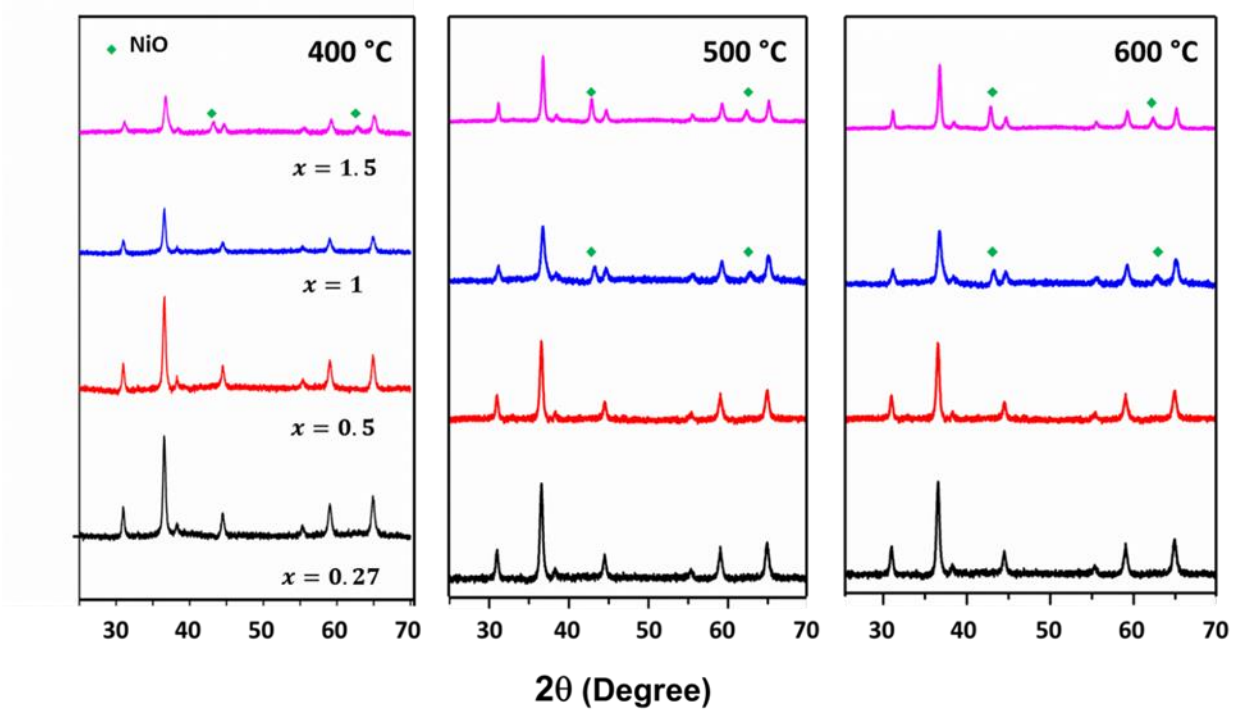

Figure 4.22. XRD characterization of the as-prepared $Ni_xCo_{3-x}O_4$ annealed at 400°C, 500°C and 600°C respectively.

In summary, a series of large-scale Co_3O_4-based nano-array catalysts have been cost-effectively integrated onto large commercial cordierite monolithic substrates with controlled substitution alloying of various cations such as Zn and Ni. The monolithically integrated spinel nano-arrays exhibit tunable catalytic performance toward low temperature CO and CH_4 oxidation by selective cations occupancy and concentration, which lead to adjusted adsorption-desorption behavior and surface defect population. This may provide a feasible approach of scalable fabrication and rational manipulation of nano-arrays for various catalytic oxidation reactions towards lower temperature.

4.4. Conclusion

In this chapter we start with the case study of ZnO nanowires growth on the three dimensional monolithic cordierite honeycomb substrates of confined channels. The mechanical agitation produced by the rotating magnetic bars placed in the reactors for the hydrothermal synthesis has been proved to promote the mass transfer of the precursor solutions throughout the channels during the synthesis and give rise to a uniform coverage of ZnO nanowires all over the monolithic cordierite honeycombs. This provides us with a feasible strategy to achieve uniform deposition of well-aligned nanostructures onto large monoliths which is critical for scalable manufacturing of monolithic nano-array catalysts. In the later context, we further successfully demonstrated the fabrication of Co_3O_4 nano-array catalyst at the industry relevant scales and produced a prototype product which can be potentially equipped on board for the automotive emission test. We successfully introduced the transition metal dopants to the spinel Co_3O_4 lattice to adjust the catalytic performance toward hydrocarbon and carbon monoxide oxidation. Different transition metals (Ni and Zn) have been introduced to the lattice replacing Co in the different positions (Zn takes tetrahedral sites and Ni takes octahedral sites) as evidenced by both density functional theory calculation and Raman spectroscopy. The dopants have been discovered to result in different catalytic activities from different reactions. For example, Ni has been demonstrated to promote the CH_4 oxidation due to the enhanced lattice oxygen by Ni incorporation while both Ni and Zn do not contribute to better CO oxidation activity because the CO adsorption on the doped surface has been hindered from the density functional theory calculation. The adjusted catalytic activity achieved by rational transition metal doping is believed to provide a feasible strategy for high performance catalyst design by rational materials selection and processing. The demonstrated success of scalable manufacturing of monolithic

nano-array catalysts has opened up new opportunities for catalysis industry to develop high performance yet low cost and energy saving catalyst for a variety of applications such as automotive emission controls and petrochemical industry.

4.5. Reference

[1] Tian, B.; Cohen-Karni, T.; Qing, Q.; Duan, X.; Xie, P.; Lieber, C. M. *Science* , **2010**, 329, 830-834.

[2] Cui, S.; Li, Y.; Guo, Y.; Liu, H.; Song, Y.; Xu, J.; Lv, J.; Zhu, M.; Zhu, D. *Adv. Mater.*, **2008**, 20, 309-313.

[3] Liang, D.; Huo, Y.; Kang, Y.; Wang, K. X.; Gu, A.; Tan, M.; Yu, Z.; Li, S.; Jia, J.; Bao, X.; Wang, S.; Yao, Y.; Wong, H. S. P.; Fan, S.; Cui, Y.; Harris, J. S. *Adv. Energy Mater.*, **2012**, 2, 1150-1150.

[4] Zhang, Y.; Grady, N. K.; Ayala-Orozco, C.; Halas, N. J. *Nano Lett.*, **2011**, 11, 5519-5523.

[5] Guo, Y.; Tang, Q.; Liu, H.; Zhang, Y.; Li, Y.; Hu, W.; Wang, S.; Zhu, D. *J. Am. Chem. Soc.*, **2008**, 130, 9198-9199.

[6] Liu, B.; Zhang, J.; Wang, X.; Chen, G.; Chen, D.; Zhou, C.; Shen, G. *Nano Lett.*, **2012**, 12, 3005-3011.

[7] Jeong, S.; Garnett, E. C.; Wang, S.; Yu, Z.; Fan, S.; Brongersma, M. L.; McGehee, M. D.; Cui, Y. *Nano Lett*., **2012**, 12, 2971-2976.

[8] Lee, J. M.; Choung, J. W.; Yi, J.; Lee, D. H.; Samal, M.; Yi, D. K.; Lee, C.-H.; Yi, G.-C.; Paik, U.; Rogers, J. A.; Park, W. I. *Nano Lett*., **2010**, 10, 2783-2788.

[9] Chen, G.; McCandless, G. T.; McCarley, R. L.; Soper, S. A. *Lab Chip*, **2007**, 7, 1424-1427.

[10] Shalek, A. K.; Robinson, J. T.; Karp, E. S.; Lee, J. S.; Ahn, D.-R.; Yoon, M.-H.; Sutton, A.; Jorgolli, M.; Gertner, R. S.; Gujral, T. S.; MacBeath, G.; Yang, E. G.; Park, H. *Proc. Natl. Acad. Sci. U.S.A.*, **2010**, 107, 1870-1875.

[11] Yao, X.; Song, Y.; Jiang, L. *Adv. Mater.*, **2011**, 23, 719-734.

[12] Qu, L.; Dai, L.; Stone, M.; Xia, Z.; Wang, Z. L. *Science*, **2008**, 322, 238-242.

[13] Shi, J.; Hara, Y.; Sun, C.; Anderson, M. A.; Wang, X. *Nano Lett.*, 2011, 11, 3413-3419.

[14] Korotkikh, O.; Farrauto, R. *Catal. Today*, **2000**, 62, 249-254.

[15] Roberts, G. W.; Chin, P.; Sun, X.; Spivey, J. J. *Appl. Catal., B*, **2003**, 46, 601-611.

[16] Guo, Y.; Ren, Z.; Xiao, W.; Liu, C.; Sharma, H.; Gao, H.; Mhadeshwar, A.; Gao, P.-X. *Nano Energy*, **2013**, 2, 873-881.

[17] Lee, Y.-J.; Sounart, T. L.; Scrymgeour, D. A.; Voigt, J. A.; Hsu, J. W. P. *J. Cryst. Growth*, **2007**, 304, 80-85.

[18] ANSYS Fluent. http://www.ansys.com/

[19] Ashfold, M. N. R.; Doherty, R. P.; Ndifor-Angwafor, N. G.; Riley, D. J.; Sun, Y. *Thin Solid Films*, **2007**, 515, 8679-8683.

[20] Qian, X.; Liu, H.; Guo, Y.; Song, Y.; Li, Y. *Nanoscale Res. Lett.*, **2008**, 3, 303 - 307.

[21] Gao, H.; Staruch, M.; Jain, M.; Gao, P.-X.; Shimpi, P.; Guo, Y.; Cai, W.; Lin, H.-j. *Appl. Phys. Lett.*, **2011**, 98, 123105.

[22] Shimpi, P.; Gao, P.-X., Goberman, D. G.; Ding, Y. *Nanotechnology*, **2009**, 20,125608.

[23] Guo, M.; Diao, P.; Wang, X.; Cai, S. *J. Solid State Chem.*, **2005**, 178, 3210-3215.

[24] Zhao, J.; Jin, Z.-G.; Liu, X.-X.; Liu, Z.-F. *J. Eur. Ceram. Soc.*, **2006**, 26, 3745-3752.

[25] Lin, J., Qiao, B., Liu, J., Huang, Y., Wang, A., Li, L., Zhang, W., Allard, L. F., Wang, X., Zhang, T., *Angew. Chem. Int. Ed.*, **2012**, 51, 2920-2924.

[26] Williams, J. L., *Catal. Today*, **2001**, 69, 3-9.

[27] Xiao, W., Guo, Y., Ren, Z., Wrobel, G., Ren, Z. Y., Lu, T., Gao, P. X., *Cryst. Growth Des.*, **2013**, 13, 3657-3664.

[28] Sun, J., Li, Y., Liu, X., Yang, Q., Liu, J., Sun, X., Evans, D. G., Duan, X., *Chem. Commun*., **2012**, 48, 3379-3381.

[29] Hu, L., Sun, K., Peng, Q., Xu, B., Y. Li, *Nano Res.*, **2010**, 3, 363-368.

[30] Windisch, C. F., Exarhos, G. J., Owings, R. R., *J. Appl. Phys.*, **2004**, 95, 5435-5442.

[31] Xie, Y., Dong, F., Heinbuch, S., Rocca, J. J., Bernstein, E. R., *Phys. Chem. Chem. Phys.*, **2010**, 12, 947-959.

[32] Sokolovskii, V. D., *Catal. Rev.*, **1990**, 32, 1-49.

[33] Bahlawane, N., *Appl. Catal. B*, **2006**, 67, 168-176.

[34] Burch, R., Crittle, D. J., Hayes, M. J., *Catal. Today*, **1999**, 47, 229-234.

[35] Li, J., Fu, H., Fu, L., Hao, J., *Environ. Sci. Technol*., **2006**, 40, 6455-6459.

[36] Cabo, M., Pellicer, E., Rossinyol, E., Castell, O., SuriÇach, S., Bar, M. D., *Cryst. Growth Des*., **2009**, 9, 4814-4821.

Chapter 5

In-situ spectroscopy investigation upon transition metal doping effects, reaction mechanism and thermal stability of monolithic Co_3O_4 nano-array based catalyst

5.1. Introduction

Hydrocarbons emission generated from mobile and stationary combustion sources, such as automobiles, petrochemical and power generation plants, represent a major group of pollutants to the environment[1-3]. With increasingly stringent regulation imposed upon the emission control, highly efficient catalysts is greatly demanded in order to efficiently remove hydrocarbons and other pollutants such as CO, NO_x and particulate matters. Although Pt group metals (PGM) is still dominant in catalysts for automotive emission control[4-7], considerable attention has been paid for the search of cost-effective and highly efficient new catalysts for catalytic oxidation at low temperature[8-11]. Typical examples include transition metal oxides[12-15] and complex oxides such as perovskites[16-21]. As a typical transition metal oxide, Co_3O_4 nanostructure has been widely studied as a promising candidate for low temperature catalytic oxidation. For example, mesoporous Co_3O_4 has been reported to achieve complete CO oxidation at -60 °C[22]. Co_3O_4 nanorods enclosed with {110} planes can fully convert CO to CO_2 at -77 °C[23].

Recently, we have successfully invented and demonstrated a new catalyst configuration, i.e., the nanostructure-array (nano-array) based monolithic catalysts, where hierarchical nanostructures such as nanowire arrays are integrated onto commercial cordierite honeycombs[24-26]. Such monolithic nano-array geometry and spatial arrangement is shown to help reduce the catalyst usage by 10–40 times with good catalytic oxidation performance and thermal/mechanical

robustness. Furthermore, the porous Co_3O_4 nano-array based monolithic catalysts have demonstrated a remarkable 80% NO to NO_2 conversion at temperatures lower than 300 °C, displaying a much better catalytic oxidation performance than wash-coated Pt monolithic catalysts, i.e., with higher efficiency, lower reaction temperature and cost[27]. We have further demonstrated the scalability of transition metal doped Co_3O_4 nano-array catalyst with complete methane oxidation capability at temperatures below 600 °C with the catalyst usage lower than 20 mg[28]. Specifically, Ni doping was found to enhance the catalytic activity for the catalyst performance towards lower temperature. By first-principle calculation we discovered the incorporation of Ni into the spinel Co_3O_4 lattice facilitated the interaction between hydrocarbon and lattice oxygen[28]. However, more experimental evidence through detailed investigation upon the reaction mechanism is still required to better interpret the Ni doping effect for rational catalyst design towards low temperature hydrocarbon oxidation.

In this chapter we demonstrated the similar effect of Ni doping that led to enhanced reaction kinetics for low temperature propane oxidation by promoting the lattice oxygen activity. In situ DRIFTS in tandem with oxygen isotope exchange was employed to reveal the Mars-van Krevelen reaction mechanism where surface lattice oxygen acted as the active sites. The Ni doping effects upon structure stability studied by Raman scattering, XPS and XRD indicates a balance between promoted catalytic activity and decreased thermal stability for Ni doped Co_3O_4 nano-arrays is needed for practical application.

5.2. Experimental section

5.2.1. Synthesis of Ni-doped Co_3O_4 and pristine Co_3O_4 nanowire arrays

Hierarchical nickel cobaltite nanowire array catalysts were prepared via a facile solution chemistry strategy as we previously reported[27, 28]. Briefly, the monolithic honeycomb substrate was first immersed in distilled water and acetone and sonicated for 30 minutes to remove residual contaminants inside the channels. For synthesis of $Ni_xCo_{3-x}O_4$ nanowires, Aqueous solution of cobalt nitrate hexahydrate ($Co(NO_3)_2•6H_2O$) and nickel nitrate hexahydrate ($Ni(NO_3)_2•6H_2O$) with adjusted concentration ratio were prepared as the precursor for the reaction. The monolithic honeycomb was then suspended in 100 mL of the as-prepared precursor solution followed by the addition of 3 g urea under vigorous magnetic stirring until the solution becomes transparent. The reaction was maintained at 90°C for 12 hours. The honeycomb substrate was then rinsed by distilled water and dried at 80°C for 4 hours. Ambient annealing at 300°C for 4 hours with a ramp rate of 20°C/min transforms the basic-carbonate nanowires into porous oxide. For synthesis of Co_3O_4 nanowires, two types of cobalt precursors, cobalt nitrate and cobalt chloride, were used with all the other reaction conditions unchanged and the as-prepared nanowires were denoted as Co_3O_4 and Co_3O_4-Cl respectively.

5.2.2. Catalyst characterization

The structure characterization of nanowires has been performed by electron microscopy. Specifically, the morphology and structure were characterized using a field emission scanning electron microscope (FE-SEM, JEOL 6335F) and a high resolution transmission electron microscope (HRTEM, JEOL JEM-2010, 200 kV). The TEM samples were prepared by scratching nanowires off the honeycombs and dispersing in ethanol, which was then dropped onto the copper grid coated with carbon film. The element distribution was investigated by scanning transmission electron microscopy (STEM) based on the energy dispersive X-ray spectrometry (EDS).

The BET surface area was characterized by Quantachrome NOVA 1000 Gas Sorption Analyzer and Micromeritics ASAP 2020 physisorption analyzer. The temperature-programmed desorption of O_2 (O_2-TPD) as well as the temperature-programmed reduction by H_2 (H_2-TPR) was conducted in a tube furnace equipped with a gas analyzer MKS coupled with a quadruple mass selective detector. The temperature was controlled by WATLOW F4 controller. 200 mg of catalyst was packed in a quartz tube reactor mounted within the tube furnace. The loaded sample was first purged under 10% O_2 flow at 300 ºC for 1 h and then cooled down to room temperature. For O_2-TPD, the sample was exposed to pure oxygen for 1.5 h at room temperature. The catalyst was then purged with argon for 30 min to remove any surface physisorbed gases and residual feed gas from the streams. After purging, the catalyst was heated under a flow of argon from room temperature to 800 ºC with a heating ramp of 10 ºC/min. For H_2-TPR, the sample was exposed to 1% H_2 balanced by argon. With the temperature ramping from room temperature to 800 °C with rate of 10 ºC/min, the H_2 consumption was simultaneously monitored by mass spectrometry. The flow rate for all these steps was controlled to be 200 sccm.

5.2.3. Catalytic performance test

A BenchCAT reactor (Altamira Instruments) was used for propane oxidation test. Mass spectrometer and Agilent Micro-GC were equipped for the gas species analysis in the product stream. Catalytic performance test was carried out in a temperature range of 20–800°C using 15 sccm of 10% C_3H_8/N_2, 15 sccm of pure O_2, and 120 sccm of argon (1% C_3H_8, 10% O_2, 9% N_2 and 80% Ar) with a total flow rate of 150 sccm. Three pieces of monolithic nano-array honeycomb catalysts (2×3 channels in cross section and 1 cm long in channel length for each piece) were loaded into the quartz tube with inner diameter of ¼ inch (~0.64 cm). The space velocity was thus calculated to be ~50,000/h. The total weight of the three pieces of the

monolithic nano-array honeycomb was around 0.15g. Considering the 10% to 13% nano-array loading, the actual catalytic active materials were about 15 mg to 20 mg.

5.2.4. in-situ DRIFTS study of catalyst

To reveal the reaction mechanism during the catalytic reaction, DRIFTS was employed to characterize the chemical species on the catalyst surface. 3 mg catalyst was first mixed with 30 mg CaF_2 by grinding to render fine powders for IR characterization. IR spectra were collected using a Thermo Nicolet Nexus 670 spectrometer in diffuse reflectance mode (DRIFT) while the outlet stream was analyzed by quadrupole mass spectrometer (QMS) (OmniStar GSD-301 O2, Pfeiffer Vacuum). A pike Technologies HC-900 DRIFTS cell with volume of 6 mL was used as the in situ reaction chamber where powder catalyst was placed.

In C_3H_8 oxidation experiments, 30 mg fine powders (cobaltite nanowires mixed with CaF_2) were loaded into the DRIFT cell and were pretreated in 10% O_2 at 300 °C for 1 hour and the temperature was then slowly reduced to room temperature in the same atmosphere. Before the powders were exposed to the reaction gas mixture, they were first purged by helium to remove any adsorbed residuals on the catalyst surface. The reaction gas mixture consists of 1% C_3H_8, 10% O_2 balanced by helium with the total flow rate controlled to be 30 sccm so that the space velocity was kept same as that in the catalytic performance test. The reaction gas and helium were alternatively switched on to characterize the chemical species on the catalyst surface. Specifically, a series of IR spectra as well as QMS profiles were continuously collected in the reaction gas mixture as reaction proceeded at each temperature. After about 8 minutes' exposure to the reaction gases, the catalyst was purged by helium for the next 7 minutes during which IR spectra were also collected to reveal the surface chemical species. All the reported IR spectra are

difference spectra referenced to background spectra collected at each temperature after the pretreatment but prior to C_3H_8 oxidation reaction or C_3H_8-TPR.

In C_3H_8-TPR experiment, similar protocol was adopted. 30 mg fine powders (cobaltite nanowires mixed with CaF_2) were pretreated in 10% O_2 at 300 °C for 1 hour and the temperature was then slowly reduced to room temperature in the same atmosphere. Before the powders were exposed to 1% C_3H_8 (total flow rate: 30 sccm), they were purged by helium to remove any adsorbed residuals on the catalyst surface. A series of IR spectra and QMS profiles were collected when the 1% C_3H_8 was introduced. At each temperature, the propane gas was switched off after 3 minutes and the catalyst was purged by helium with IR spectra and QMS profiles recorded.

5.2.5. Surface oxygen replacement by isotopic $^{18}O_2$

The catalyst was first purged by 10% O_2 at 300 °C for 1 hour which was the pretreatment condition before the catalytic performance test. Helium was then introduced and the temperature was increased from 300 °C to 450 °C. The catalyst was kept in helium atmosphere at 450 °C for 15 minutes before 2% $^{18}O_2$ (ISOTEC, Sigma-Aldrich) was introduced (flow rate 30 sccm, balanced by helium) to initiate the surface lattice oxygen exchange. After another 15 minutes, the temperature was reduced to room temperature in the same atmosphere (2% $^{18}O_2$) and the catalyst was again purged by helium before the IR spectra for the propane oxidation in $^{16}O_2$ were collected.

5.2.6. Raman spectroscopy and X-ray photoelectron spectroscopy

Raman scattering spectra were recorded by a triple Raman spectrometer (Princeton Instrument Acton Trivista 555) equipped with a customized ellipsoidal mirror and a fiber optics bundle. Edge filters were used in front of the fiber optics bundle to block the laser irradiation ($\lambda_{ex.}$ = 532

nm) and a UV-enhanced liquid nitrogen cooled CCD detector was responsible for the signal detection and monitoring. Cyclohexane was employed as a standard for all the Raman shifts calibration. X-ray photoelectron spectroscopy (XPS) was performed with Kratos Analytical (Axis Ultra DLD) equipped with monochromatic Al Ka source operating at 1486.7eV. The signal was filtered with a hemispherical analyzer (pass energy 160eV for survey spectra and 20eV for narrow high resolution scan). The C 1s photoelectron line at 284.6eV was used as an internal standard for the correction of the charging effect in all samples.

5.3. Results

5.3.1. Structure characterization of nano-array catalysts by electron microscopy

The SEM images in Figure 5.1a through Figure 5.1c display the morphology and orientation of hierarchical Ni doped and pristine Co_3O_4 nanowires on the monolithic cordierite honeycombs. The morphology characteristics are consistent with our previous reports[24,27,28]. Briefly, nanowires have smaller diameter when nitrate is used as the precursor in the synthesis. As illustrated in Figure 5.1c, cobalt chloride leads to nanowires with sharp tips and the nanowires are arranged into arrays more orderly while cobalt nitrate gives rise to compact alignment of hierarchical nanoflowers. Meanwhile, no phase segregation is observed when Ni is added as dopant and the hierarchical nano-arrays retain their morphology. The corresponding HRTEM images in Figure 1d through Figure 5.1f reveal the crystalline nature of all the nanowires. The nanowires are discovered to be porous by regular TEM imaging. Figure 5.2a shows each individual nanowire is composed of multiple interconnected crystallites and voids can be easily seen within nanowires. Elemental mapping under STEM mode clearly reveals the homogeneous distribution of Ni in the nanowires which further confirms the successful doping of Ni in the Co_3O_4 lattice. It is worth noticing considerable amount of Cl has been detected by EDS in Co_3O_4-Cl nanowires. The

existence of surface Cl can be ascribed to the formation of different precursors from the urea hydrolysis in the synthesis. Previous study shows the preparation of Co_3O_4 nanowires involve several chemical reactions[29-31].

$$CO(NH_2)_2 + H_2O \rightarrow 2NH_3 \uparrow + CO_2 \uparrow$$

$$NH_3 \uparrow + H_2O \rightleftharpoons NH_4^+ + OH^-$$

$$CO_2 + H_2O \rightleftharpoons 2H^+ + CO_3^{2-}$$

$$Co^{2+} + xOH^- + yCO_3^{2-} + zH_2O \longrightarrow Co(OH)_x(CO_3)_y \bullet zH_2O$$

$$Co(OH)_x(CO_3)_y \bullet zH_2O + O_2 \longrightarrow Co_3O_4 + H_2O + CO_2 \uparrow$$

However, when chloride is used as precursor the chlorine ion participates in the reaction which results in the formation of $Co(OH)_x(CO_3)_yCl_k \bullet zH_2O$ that further decomposes into Co_3O_4 with Cl on the surface. The effect of chlorine upon the catalyst performance will be discussed later.

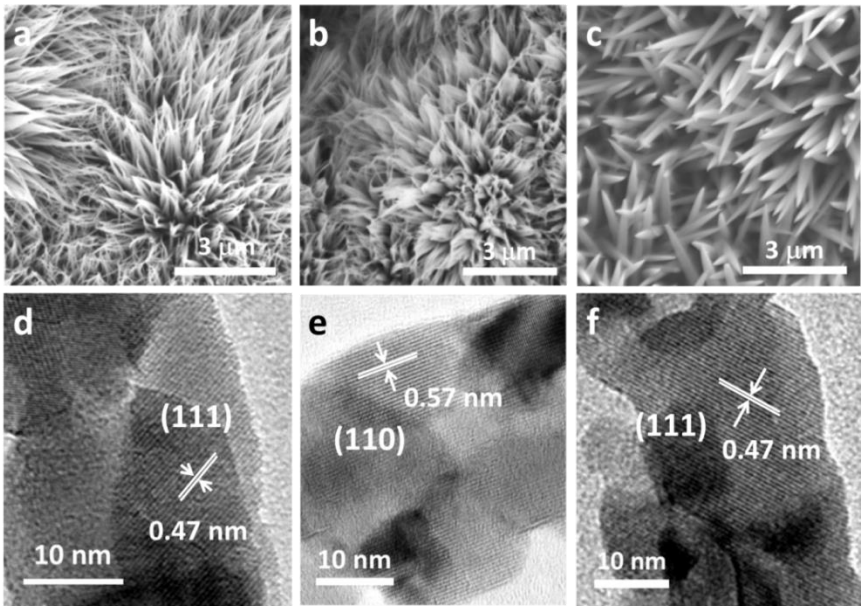

Figure 5.1. SEM images of the as-prepared nanowire array catalysts: a) Co_3O_4 nano-arrays; b) Ni doped Co_3O_4 nano-arrays ($Ni_{0.27}Co_{2.73}O_4$); c) Co_3O_4 nano-arrays prepared by chloride. High resolution TEM characterization of d) Co_3O_4 nanowires; e) $Ni_{0.27}Co_{2.73}O_4$ nanowires and f) Co_3O_4 nanowires (Co_3O_4-Cl) prepared by chloride.

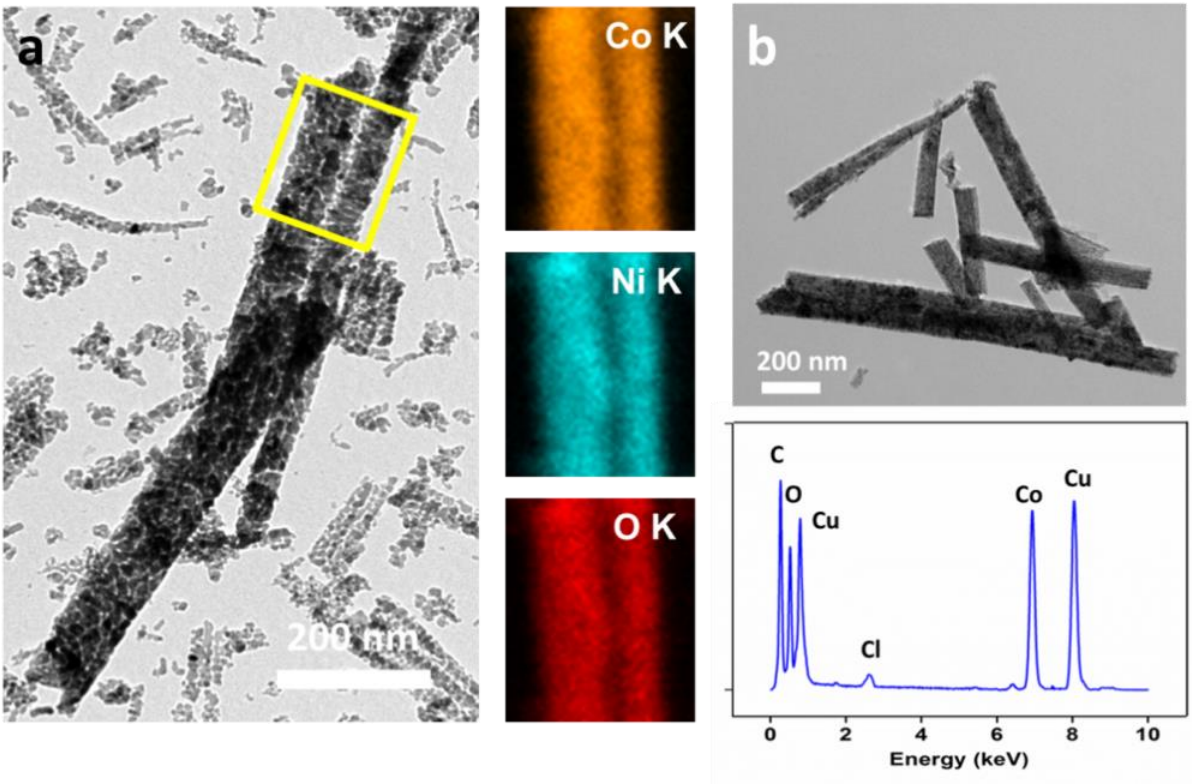

Figure 5.2. a) TEM image of $Ni_{0.27}Co_{2.73}O_4$ nanowires and the associated STEM mapping of the selected region showing the uniform distribution of Ni, Co and O within the nanowires; b) TEM characterization of Co_3O_4-Cl nanowires and the EDS spectrum.

5.3.2. Propane oxidation performance and reaction kinetics

Figure 5.3a exhibits the light-off curves of catalytic propane oxidation by three different nano-arrays. The Ni doped Co_3O_4 nano-arrays ($Ni_{0.27}Co_{2.73}O_4$) demonstrate the best performance catalyzing the propane oxidation at the lowest temperature (full conversion of C_3H_8 into CO_2 at 425 °C) while Co_3O_4-Cl achieves 100% conversion at 500 °C. Compared with pristine Co_3O_4 nano-arrays, the Ni doping is observed to enhance the catalytic activity. For example, the

temperatures for 20% and 50% conversion of C_3H_8 into CO_2 are 270 °C and 320 °C for $Ni_{0.27}Co_{2.73}O_4$ but are 295 °C and 350 °C for Co_3O_4 respectively. BET surface area analysis were performed by using 0.15 g monolithic nano-array catalysts (nanowires plus honeycomb) where the mass of nanowires were measured by the weight difference before and after the synthesis. The BET surface area of bare cordierite honeycomb was measured to be $0.35 m^2/g$. We assume the measured BET surface area of honeycombs structured with nano-arrays from Figure 5.3b is approximately the linear summation of contributions from bare cordierite and the grown nano-arrays. The BET surface area of nano-array A_{nw} is thus calculated by

$$A_{nw} = \frac{A(m_{sub} + m_{nw}) - A_{sub}m_{sub}}{m_{nw}}$$

m_{sub}: the mass of cordierite substrate;

m_{nw}: the mass of the nanowire arrays (weight difference of honeycomb substrate before and after nanowires growth);

A_{sub}: the measured BET surface area of bare cordierite substrate;

A: the measured BET surface area of cordierite structured with nano-arrays.

With the different mass loadings and the calculated BET surface areas of nano-arrays summarized in Table 5.1, the reaction rate for $C_3H_8 + 5O_2 \longrightarrow 3CO_2 + 4H_2O$ at certain temperature can be calculated by

$$r = \frac{1\% \times conversion\ [\%] \times flow\ rate\ [L/s]}{22.4\ L/mol \times m_{nw}[g] \times A_{nw}[m^2/g]}\ \ [mol/(m^2 s)]$$

where A_{nw} is the BET surface area of nanowires. As shown in Figure 5.3c, Ni doped Co_3O_4 nano-array exhibits higher reaction rate than both Co_3O_4 and Co_3O_4-Cl nano-arrays which confirms the enhanced reaction kinetics and activity by Ni doping. The rate difference between Co_3O_4 and Co_3O_4-Cl nano-arrays is not as obvious as those displayed in Figure 5.3a. The rate of Co_3O_4 nano-arrays converting C_3H_8 to CO_2 is only slightly higher than that of Co_3O_4-Cl nano-arrays at low temperature region (<300 °C) while at high temperature the rates are almost identical. It can thus be inferred that the inferior reaction activity of Co_3O_4-Cl nano-array revealed by conversion light-off in Figure 5.3a may result from its smaller surface area. To better reveal the reaction kinetics the apparent activation energies are calculated when C_3H_8 conversion is lower than 10%. For propane oxidation, the reaction rate can be expressed as $r = k[C_3H_8]^a[O_2]^b$ because the reaction is irreversible in the O_2 rich atmosphere (C_3H_8/O_2=1/10). Using Arrhenius equation, $r = Aexp(-\frac{E_a}{RT})[C_3H_8]^a[O_2]^b$ where E_a represents the apparent activation energy. When the propane conversion is very low (< 10%), the concentrations of both C_3H_8 and O_2 are approximately constant and the correlation between ln r and 1/RT is thus close to linear.

$$\ln r = -\frac{E_a}{RT} + lnA + aln[C_3H_8] + bln[O_2]$$

Ni doped Co_3O_4 nano-array exhibits much enhanced reaction kinetics with lowest apparent activation energy (E_a=32.5 kJ/mol) and Co_3O_4-Cl nano-array is kinetically sluggish (E_a=83.8 kJ/mol). The reaction kinetics study confirms the Ni doping is able to promote catalyst activity and the surface chlorine hinders the catalytic conversion at low temperature.

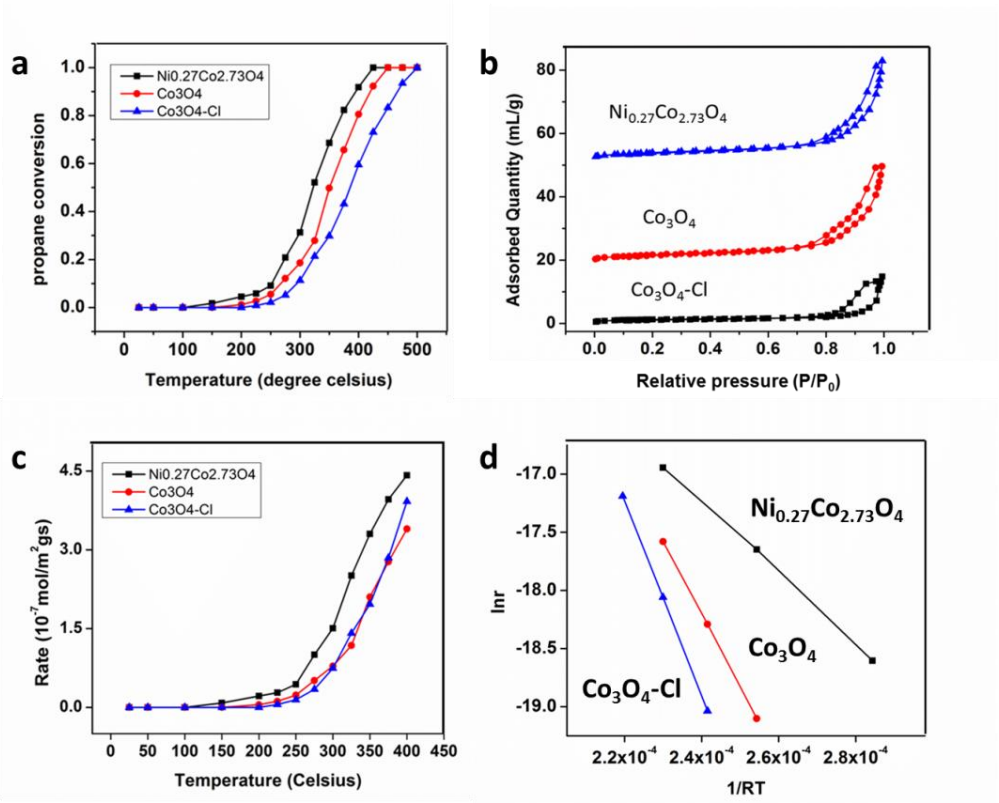

Figure 5.3. a) Light-off curves for catalytic propane oxidation by nano-array catalysts; b) BET surface area characterization of nano-array catalysts; c) Comparison of reaction rates of different nano-arrays; d) Arrhenius plots and apparent activation energy calculations for different nano-arrays.

sample	mass loading (mg)	surface area (m^2/g)	T_{50} (°C)	T_{100} (°C)	Ea (kJ/mol)
$Ni_{0.27}Co_{2.73}O_4$	13	148.3	320	425	32.5
Co_3O_4	13.6	151.1	350	450	62.5
Co_3O_4-Cl	16.7	81.1	385	500	83.8

T_{50}: the temperature at which 50% conversion of C_3H_8 is achieved; T_{100}: the temperature at which 100% conversion of C_3H_8 is achieved; Ea: the calculated apparent activation energy (when conversion < 10%).

Table 5.1. Summary of structure and reaction characteristics for nano-array catalysts.

5.3.3. Redox property and lattice oxygen activity

Redox property of nano-array catalysts have been investigated by H_2-TPR with H_2 consumption monitored by online QMS. Two reduction peaks were observed in Co_3O_4 based nano-arrays where the one located in the low temperature region around 300 °C corresponds to Co^{3+} reduction to Co^{2+} and the other at 400 °C represents Co^{2+} conversion to metallic Co[22,32]. It is clearly seen the incorporation of Ni into spinel Co_3O_4 lattice leads to better redox property since the temperatures for both Co^{3+} reduction to Co^{2+} and Co^{2+} to Co^0 are shifted towards lower temperature. Similar tendency has been observed in C_3H_8-TPR experiment for $Ni_{0.27}Co_{2.73}O_4$ and Co_3O_4 (Figure 5.4). The Co_3O_4-Cl nano-array, however, demonstrates much smaller reduction peaks compared with the other two samples. The smaller reduction peaks suggest the surface chlorine may deactivate Co-O bonds suppressing the lattice oxygen interaction with H_2 or C_3H_8. In Figure 5.5b, both $Ni_{0.27}Co_{2.73}O_4$ and Co_3O_4 exhibit O_2 desorption at temperature 400-450 °C corresponding to the surface lattice oxygen desorption. The desorption temperature for $Ni_{0.27}Co_{2.73}O_4$ nano-array is 40 °C lower than that of Co_3O_4 indicating the surface lattice oxygen is more active. However, almost no desorption has been observed at the same temperature region for Co_3O_4-Cl which further implies the Co-O bonding could be passivated by surface chlorine.

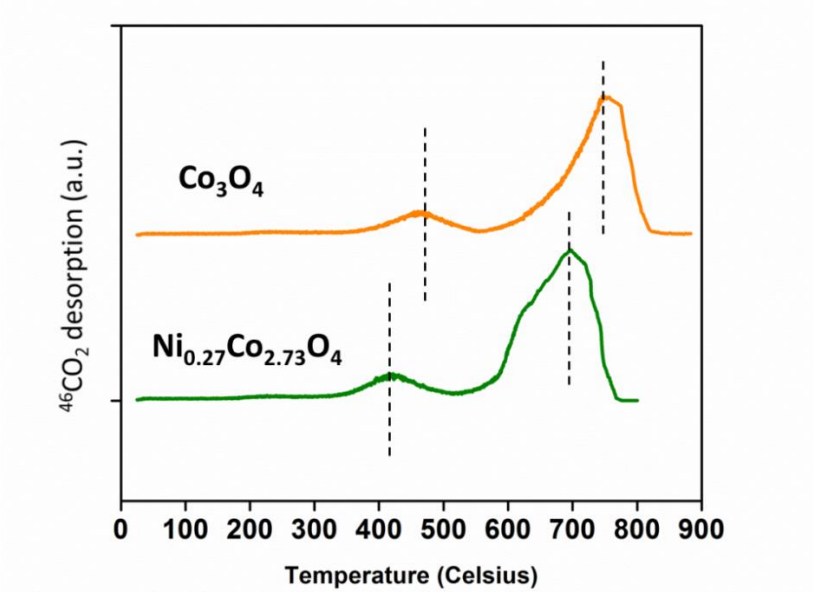

Figure 5.4. Temperature programmed $^{46}CO_2$ desorption during C_3H_8-TPR of $Ni_{0.27}Co_{2.73}O_4$ and Co_3O_4 nano-arrays. $^{46}CO_2$ signal was used for the redox property characterization since C_3H_8 and CO_2 have the same molecular weight.

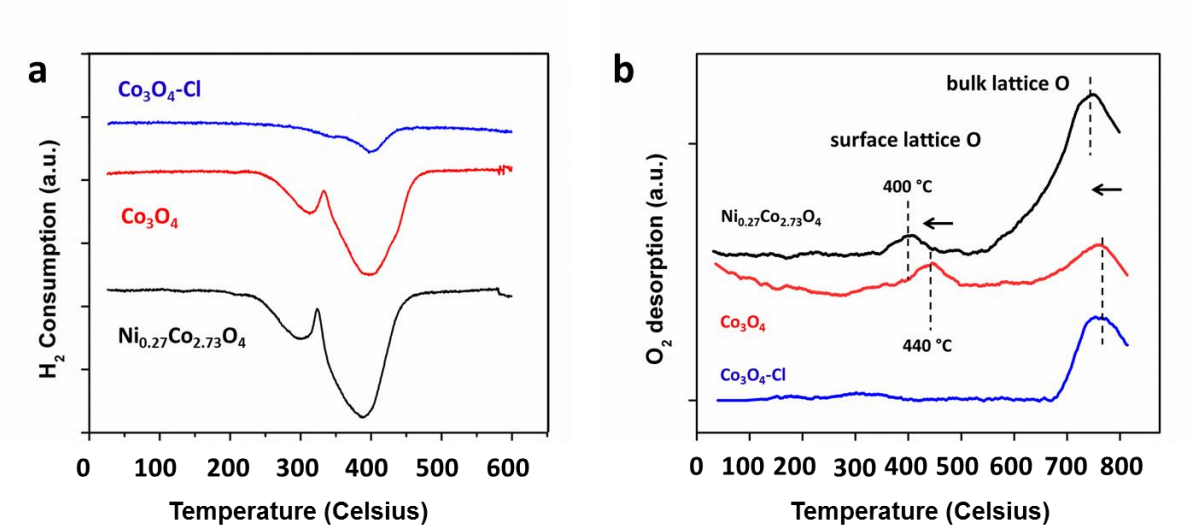

Figure 5.5. a) Redox property investigation upon nano-arrays by H_2-TPR; b) lattice oxygen activity study by O_2-TPD.

5.3.4. in situ DRIFTS study for propane oxidation

In situ DRIFTS was employed during propane oxidation to reveal more details of the reactions on catalyst surface and identify the surface chemical species evolution. In Figure 5.6, each

spectrum was collected after 8 minutes reaction at the specified temperature. The bands within wavenumber from 1000 to 1600 cm^{-1} are assigned to various carbonate species. Hydrocarbon and gaseous CO_2 peaks are located around 3000 cm^{-1} and 2350 cm^{-1} respectively. From DRIFTS spectra it is obvious to notice massive gaseous CO_2 production starting at 250 °C for Co_3O_4 and 200 °C for $Ni_{0.27}Co_{2.73}O_4$. It corresponds very well with the light-off curves in Figure 5.3. At temperatures higher than 400 °C, negligible amount of C_3H_8 can be detected indicating full conversion of C_3H_8 to CO_2. At each temperature the gas stream was switched to helium after 8 minutes reaction and a series of DRIFT spectra were collected to analyze the carbonate species. The right column of Figure 5.6 shows the DRIFT spectra after 7 minutes purging by helium which removes the gaseous species of hydrocarbon(~3000 cm^{-1}) and CO_2 (2350 cm^{-1}) on the surface. Bicarbonate (1400 cm^{-1}, 1220 cm^{-1}), bidentate carbonate (1595 cm^{-1}, 1044 cm^{-1}) and some uncoordinated CO_3^{2-} (1420 cm^{-1}) are identified at reaction temperatures below 100 °C for both nano-arrays[33,34]. As the reaction temperature increases above 150 °C, unidentate (1540 cm^{-1}, 1044 cm^{-1}) and polydentate carbonates (1432 cm^{-1}, 1346 cm^{-1}) become the major surface species[34-36]. It seems the Ni doping does not affect the nature of surface carbonate species. The assignment of IR bands to carbonate species is summarized in Table 5.2. For Co_3O_4-Cl the collected in situ DRIFT spectra is shown in Figure 5.7. Compared with Co_3O_4 nano-array, very small amount of carbonates have been produced on the Co_3O_4-Cl surface. This indicates the surface chlorine may either blocks the active sites or passivates the lattice oxygen which leads to the sluggish reaction kinetics of Co_3O_4-Cl nano-array towards propane oxidation at low temperature.

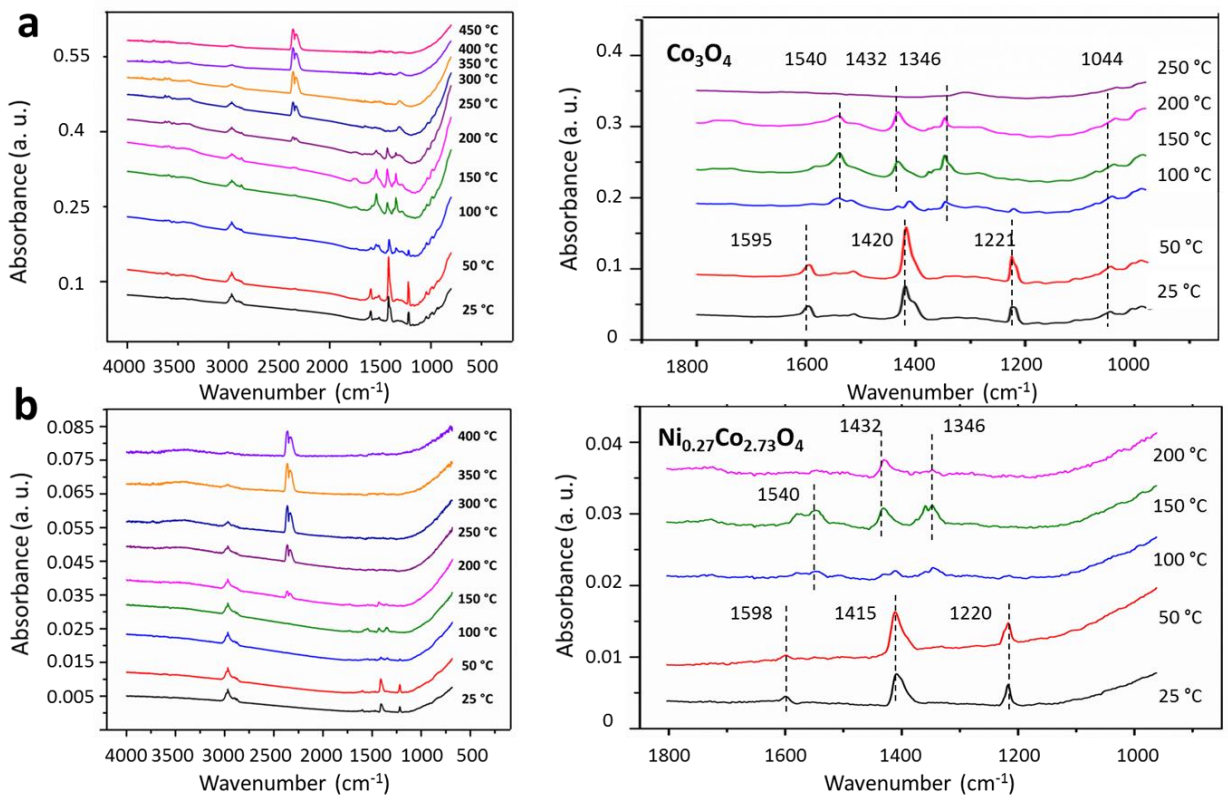

Figure 5.6. In situ DRIFT spectra for catalytic propane oxidation reactions by a) Co_3O_4 and b) $Ni_{0.27}Co_{2.73}O_4$ nano-arrays and the associated DRIFT spectra for surface carbonates identification.

Species	IR bands(cm^{-1})
bicarbonate	1400, 1220
bidentate carbonate	1595, 1044
unidentate carbonate	1540, 1044
polydentate carbonate	1432, 1346
uncoordinated CO_3^{2-}	1420

Table 5.2. Assignments of IR bands to related carbonates species on catalyst surface.

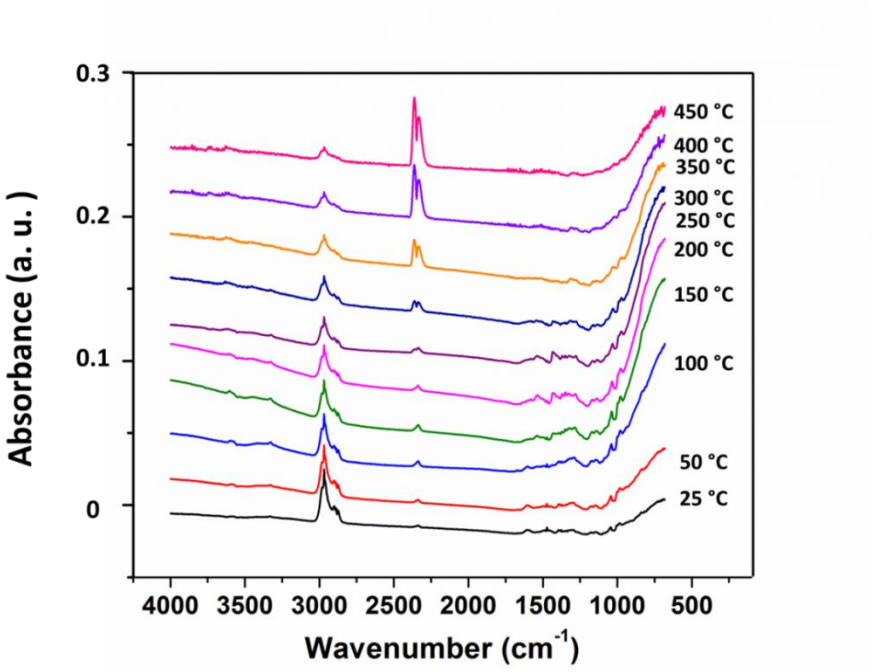

Figure 5.7. *In situ* DRIFT spectra collected at Co_3O_4-Cl nano-arrays surface during propane oxidation at difference temperatures.

Two important features are worth noticing in Figure 5.6. (1) 100 °C is a critical temperature at which the carbonate species start to transform from bicarbonate and bidentate carbonate to unidentate and polydentate carbonates; (2) At 250 °C the formed carbonates seem thermally unstable since the IR spectrum collected after helium purging differs from the one collected after 8 minutes reaction. It is thus necessary to study the dynamic evolution of carbonate species at different temperatures.

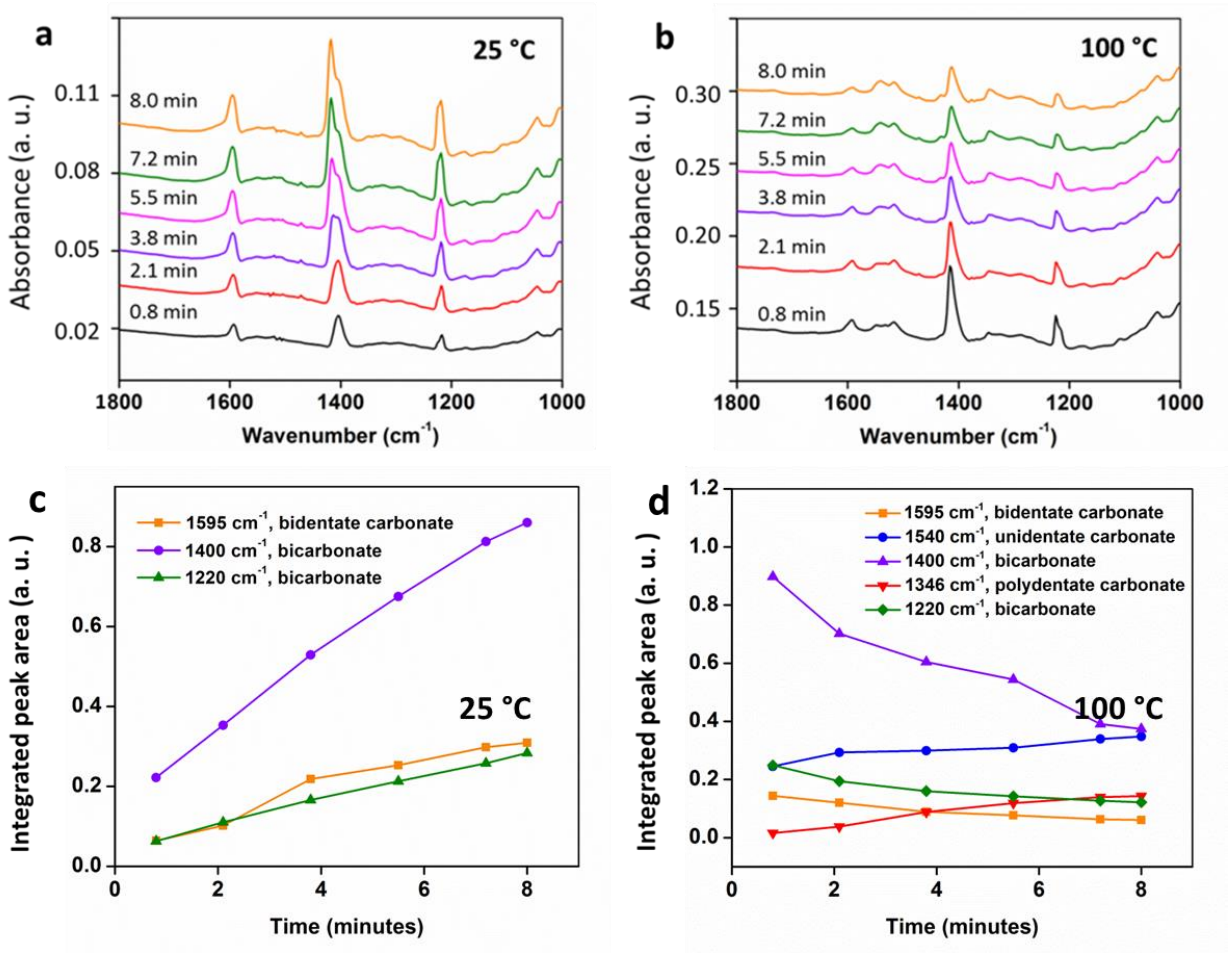

Figure 5.8. a-b) Time dependent in situ DRIFT spectra for propane oxidation at 25 °C and 100 °C revealing the dynamic evolution of surface carbonates on Co_3O_4 nano-arrays; c-d) Calculated peak areas indicating the dynamic quantity change of typical carbonates.

Figure 5.8 shows the in situ DRIFT spectra collected during propane oxidation at 25 °C and 100 °C with the dynamic carbonate quantity change revealed by integrating the corresponding peak areas. It is clearly observed carbonates rapidly appear on the catalyst surface even when the reaction time is less than 1 minute. At 25 °C the bicarbonate and bidentate carbonate concentration will not be saturated even until reaction lasts for more than 8 minutes. However, the intensity of bicarbonate and bidentate carbonate peaks gradually declines at 100 °C while the peaks of unidentate (1540 cm^{-1}) and polydentate carbonates (1346 cm^{-1}) starts to get obvious.

This coincides with Figure 5.6 that a mixture of different carbonates exists at 100 °C and with temperature further increased to 150 °C bicarbonate and bidentate carbonate will disappear. However, both unidentate and polydentate carbonates are not stable above 200 °C. Figure 5.9 depicts the evolution of carbonates formed during propane oxidation at 250 °C after helium is purged. The intensity of peaks at 1432 cm^{-1} and 1346 cm^{-1} (polydentate carbonate) as well as 1540 cm^{-1} (unidentate) drastically decays after one minute. The decomposition temperature of unidentate and polydentate carbonates should be above 250 °C. Meanwhile, bicarbonate and bidentate carbonate are only stable below 150 °C as confirmed by both temperature dependent DRIFT in Figure 5.6 and time dependent DRIFT spectra in Figure 5.8.

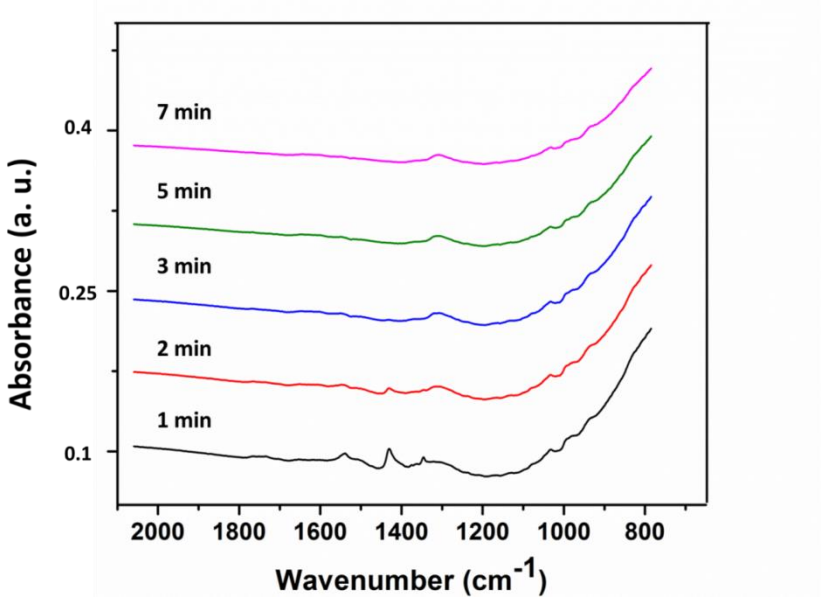

Figure 5.9. Dynamic carbonate evolution on Co_3O_4 nano-arrays surface during helium purging at 250 °C after catalytic propane oxidation at 250 °C for 8 minutes.

5.3.5. In situ DRIFTS study for C_3H_8-TPR

In addition to in situ DRIFTS study of propane oxidation, a series of DRIFT spectra were also recorded for the C_3H_8-TPR process. Figure 5.10 displays the DRIFT spectra collected at the Co_3O_4 and $Ni_{0.27}Co_{2.73}O_4$ catalysts surface after introducing 1% C_3H_8 for 3 minutes followed by

the helium purging. Similar carbonates are produced at temperatures lower than 200° C in the absence and presence of gaseous O_2. Bicarbonate, bidentate carbonate and some uncoordinated CO_3^{2-} still appear at low temperature (< 100 °C) while unidentate and polydentate carbonate are formed above 150 °C. Compared with the DRIFT spectra of propane oxidation in Figure 5.6, the IR band intensities are weak in the TPR process because of the shorter exposure to propane (3 minutes). Since the surface carbonate formation is independent on the O_2 in the reaction feed, carbonates are speculated to be produced from propane interaction with surface lattice oxygen and the propane oxidation follows the Mars-van Krevelen mechanism where surface lattice oxygen acts as the reaction active sites[23,37-39]. This proposed reaction mechanism will be further verified later by isotope experiment.

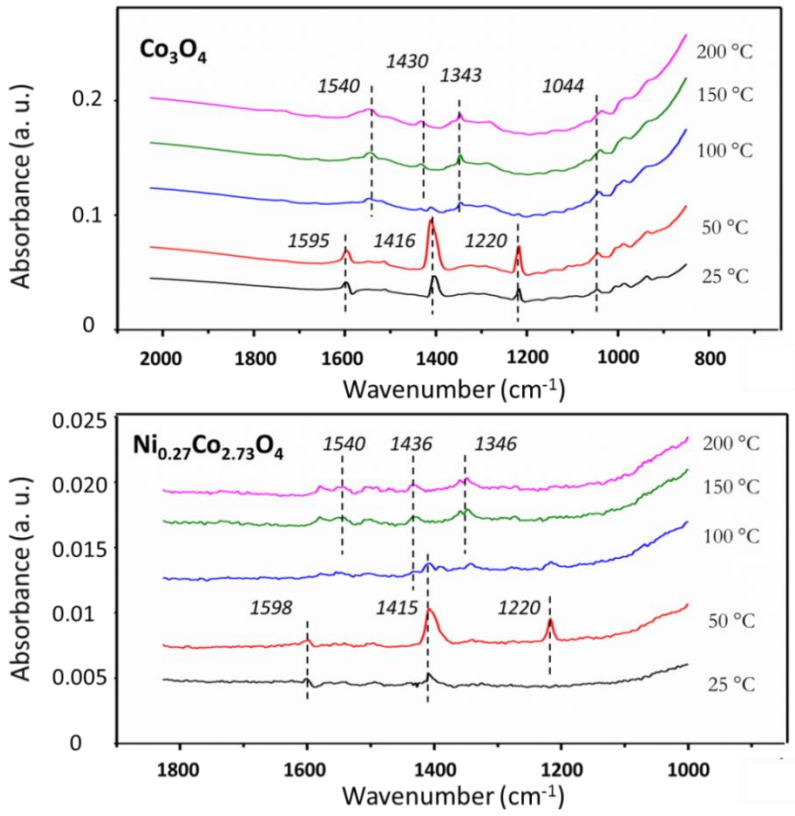

Figure 5.10. In situ DRIFT spectra recorded for surface carbonates identification during C_3H_8-TPR upon Co_3O_4 and Ni-doped Co_3O_4 nano-arrays.

5.4. Discussion

5.4.1. Enhanced reaction kinetics by Ni doping

As illustrated in Figure 5.3 the Ni doping of Co_3O_4 leads to enhanced catalytic propane oxidation performance. The temperature programmed H_2 and C_3H_8 reduction both reveals the better redox property of $Ni_{0.27}Co_{2.73}O_4$ nano-arrays by enabling reaction with H_2 and C_3H_8 at lower temperature. Temperature programmed O_2 desorption analysis confirms the surface lattice oxygen can be activated by the introduced Ni in the spinel lattice. The enhanced lattice oxygen activity results from the enriched surface oxygen defects in Ni-doped Co_3O_4 as verified in our previous study[28]. When Ni is incorporated to the Co_3O_4 lattice, it replaces Co atoms in the octahedral site where Co has six coordination O atoms. The octahedral Co exhibits valence state Co^{3+} while the substitute Ni has valence state of Ni^{2+}. Such loss of positive charges is compensated by creating oxygen vacancies to retain the charge neutrality. The existing oxygen defects result in unsaturated surface lattice oxygen which is more active. Since the in situ propane oxidation and propane-TPR investigation by DRIFTS show the catalytic propane oxidation proceeds via Mars-van Krevelen mechanism, the surface lattice oxygen activity is responsible for the reaction kinetics at low temperature. The Ni doping enhances the surface lattice oxygen activity by creating rich oxygen defects on the catalyst surface and therefore promotes the reaction kinetics.

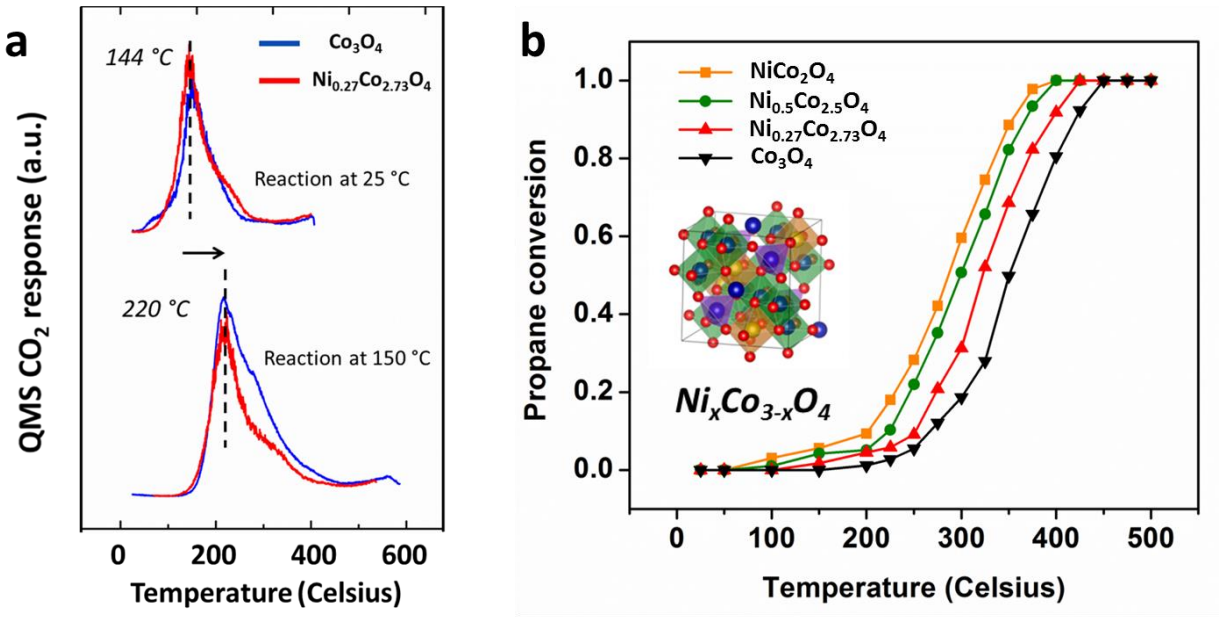

Figure 5.11. a) The measured quantity of surface carbonates generated at low and high reaction temperatures on Ni-doped Co_3O_4 and Co_3O_4 nano-arrays by temperature-programmed CO_2 desorption (CO_2-TPD); b) Catalytic propane oxidation performance of $Ni_xCo_{3-x}O_4$ nano-arrays with controlled Ni concentrations.

In addition the DRIFTS study has shown the formation of carbonates is an important step for the catalytic propane oxidation at low temperature. However, the different reaction kinetics should not result from different surface reactions because both Ni doped Co_3O_4 and pristine Co_3O_4 nano-arrays produce the same types of carbonate species. The temperature programmed CO_2 desorption was employed to study the quantity of carbonates produced on catalyst surface at different temperatures. Reaction feed (1% C_3H_8, 10% O_2 balanced by helium, flow rate 30 sccm) was introduced to the catalyst surface (30 mg catalyst powder) and the reaction was sustained for 15 minutes at 25 °C and 150 °C respectively. Helium was then switched on for purging and the temperature was slowly reduced to 25 °C. CO_2 desorption was monitored by QMS when temperature ramped from 25 °C to 600 °C. In Figure 5.11a, the carbonates formed by reaction at 25 °C have a desorption peak at 144 °C and those formed at reaction temperature of 150 °C

desorb at 220 °C. This observation is consistent with some features revealed by the DRIFT spectra in Figure 5.6. At 25 °C, bicarbonate and bidentate carbonate are the major surface carbonate species which begin to disappear when the temperature is elevated to 150 °C. It indicates both bicarbonate and bidentate carbonate are not stable above 150 °C. Therefore 144 °C seems to be the critical temperature of decomposition. Moreover, this also verifies the coexistence of bicarbonate, bidentate, unidentate and polydentate carbonate at 100 °C while only unidentate and polydentate are detected at 150 °C. From CO_2-TPD, unidentate and polydentate carbonate decompose at 220 °C which coincides with the fact that no carbonate can be detected in DRIFTS during reaction at temperature above 250 °C.

It is worth noting that more carbonates are formed on the surface of $Ni_{0.27}Co_{2.73}O_4$ nano-array at reaction temperature of 25 °C (integrated QMS peak area: $Ni_{0.27}Co_{2.73}O_4$ 2.21×10^{-8} > Co_3O_4 1.94×10^{-8}) while at 150 °C there is larger quantity of carbonates on Co_3O_4 surface (integrated QMS peak area: $Ni_{0.27}Co_{2.73}O_4$ 2.63×10^{-8} < Co_3O_4 3.59×10^{-8}). This may suggest Ni doping favors the formation of bicarbonate and bidentate carbonate. As more carbonate was generated within the same reaction time, the interaction between propane and lattice oxygen was promoted on Ni doped Co_3O_4 surface. However, the CO_2 formation rate is not only dependent on how fast propane interacts with lattice oxygen to form carbonate but also is dependent on how easily the carbonates will decompose. Given bicarbonate and bidentate carbonate are less thermally stable than unidentate and polydentate carbonate[40], the Ni doping is able to facilitate CO_2 formation from carbonate decomposition which leads to enhanced reaction kinetics at low temperature (< 150° C). The larger quantity of carbonates produced on Co_3O_4 surface at higher temperature may be ascribed to the larger surface lattice oxygen concentration of Co_3O_4 as revealed by XPS. Since these carbonates are more stable and are thus more difficult to desorb, they might hinder the

further interaction between propane and surface oxygen. The effect of Ni doping upon the catalytic performance has been further demonstrated in Figure 8b where the light-off curves for $Ni_xCo_{3-x}O_4$ nano-arrays are exhibited. The increased Ni concentration has led to propane conversion at lower temperature.

5.4.2. Reaction mechanism verification

To further validate the previously proposed Mars-van Krevelen reaction mechanism, in situ DRIFTS study has been employed during the propane oxidation on the isotopic $^{18}O_2$ treated catalyst surface (Figure 5.12) where surface lattice oxygen ^{16}O has been replaced by ^{18}O at 450 °C. Figure 5.13 shows the comparison of the DRIFT spectra collected at the different catalyst surfaces (pretreated with $^{16}O_2$ and $^{18}O_2$) during propane oxidation ($^{16}O_2$ in reaction feed) from 25 °C to 200 °C. As can be seen in Figure 9a, bicarbonate and bidentate carbonate still appear at low temperature on the $^{18}O_2$ treated surface. However, the bands shift to lower wavenumbers because of isotopic ^{18}O in the carbonate. For example, the bicarbonate peak shifts from original 1222 cm^{-1} to 1215 cm^{-1} and bidentate carbonate shifts from 1595 cm^{-1} to 1586 cm^{-1}. It implies that propane still interacts with surface oxygen (^{18}O) even in the presence of $^{16}O_2$ in the reaction feed. As reaction temperature is increased to 100 °C, unidentate and polydentate carbonates start to form with the bands shifted to lower wavenumbers, e.g. 1540 cm^{-1} shifts to 1530 cm^{-1}. However, as reaction proceeds no such shift can be observed at higher temperature (150 °C and 200 °C) and the previously shifted band goes back to its original wavenumber (1530 cm^{-1} back to 1540 cm^{-1}) making the DRIFT spectra identical to those pretreated with $^{16}O_2$. It indicates the surface ^{18}O has been gradually consumed and the surface lattice oxygen has been replenished by the gas phase $^{16}O_2$. Therefore the carbonates formed at extended reaction period and at higher temperature do not contain ^{18}O and the band shift will no longer be observed.

Based on this DRIFTS observation together with the previous results, it is clear the catalytic propane oxidation on Co_3O_4-based nano-arrays proceeds via the Mars-van Krevelen mechanism where propane interacts with surface lattice oxygen and the surface with oxygen vacancies created by CO_2 desorption are replenished by the gaseous O_2. The O_2 in the reaction feed does not directly contribute to CO_2 formation.

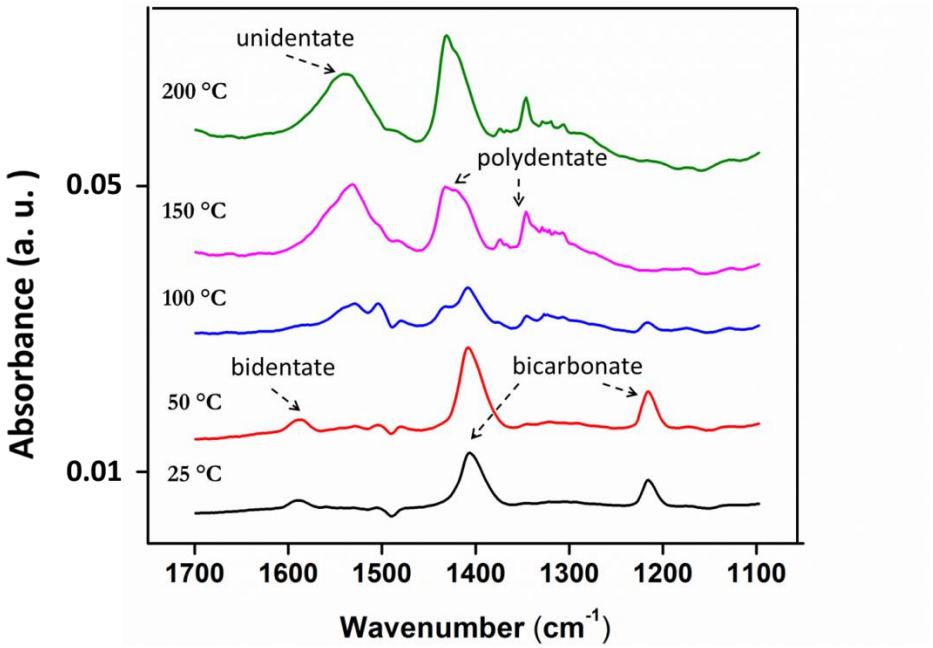

Figure 5.12. *In situ* DRIFT spectra recorded during catalytic propane oxidation on $Ni_{0.27}Co_{2.73}O_4$ nano-array surface after ^{18}O isotopic exchange treatment at 450 °C.

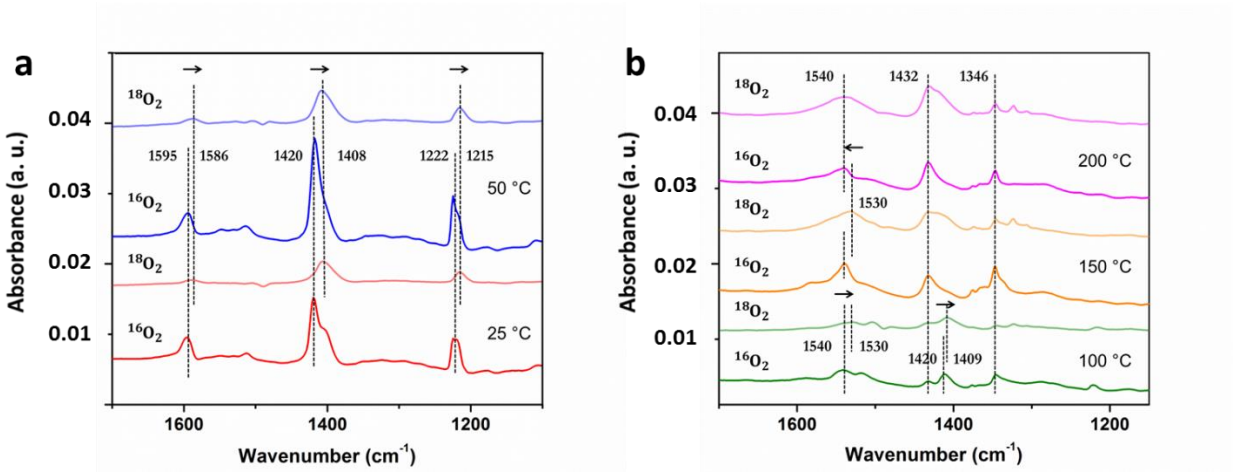

Figure 5.13. In situ DRIFT spectra recorded for comparison of surface carbonates formed during propane oxidation (in $^{16}O_2$ atmosphere) on $^{16}O_2$ and $^{18}O_2$ treated $Ni_{0.27}Co_{2.73}O_4$ nanowire surfaces.

5.4.3. Ni doping effect on catalyst stability

Both this study and our previous results have demonstrated the Ni doping enhances reaction kinetics and promotes hydrocarbon oxidation at low temperature[28]. However, $Ni_xCo_{3-x}O_4$ has been reported to be not stable under high temperature especially when the Ni concentration is high[41, 42]. Raman scattering was applied to study the structure change of Ni doped Co_3O_4 at different temperatures.

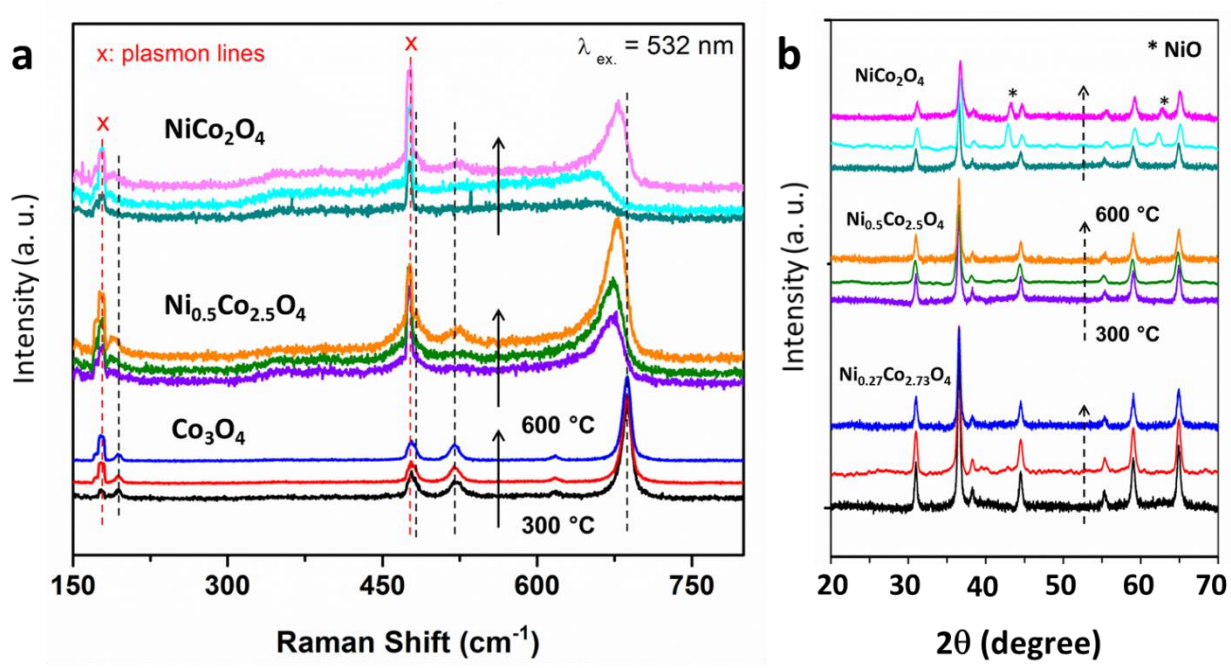

Figure 5.14. a) Raman scattering spectra for $Ni_xCo_{3-x}O_4$ nano-arrays of adjusted Ni concentrations that are annealed at different temperatures (300 °C, 450 °C and 600 °C); b) XRD spectra for Ni doped Co_3O_4 nano-arrays at different temperatures.

As shown in Figure 5.14a, the black dash lines mark the characteristic peaks of Co_3O_4[43]. When the temperature changes from 300 °C to 600 °C, no structure change is observed in Co_3O_4 and thus Co_3O_4 is stable under 600 °C. The incorporation of Ni leads to the shift of characteristic

peaks towards lower wavenumbers with suppressed intensity. When the Ni concentration is relatively low ($Ni_{0.5}Co_{2.5}O_4$), the Raman spectra at 300 °C and 450 °C are identical. However, with temperature elevated to 600 °C, the intensity of Co_3O_4 characteristic peaks starts to increase a little bit indicating the precipitation of Ni out of the spinel lattice. In the case of $NiCo_2O_4$, the increased Ni concentration further deteriorates the structure stability at high temperature. Ni starts to be removed from the lattice at 450 °C corresponding very well with the previous report that the decomposition of $NiCo_2O_4$ takes place above 400 °C. Figure 5.14b displays the XRD spectra of Ni doped Co_3O_4 annealed at different temperatures. In the case of $NiCo_2O_4$, NiO precipitates out of the lattice at 450 °C and 600 °C which is consistent with the Raman spectra. $Ni_{0.27}Co_{2.73}O_4$ seems stable below 600 °C with no phase segregation observed in XRD spectra. For $Ni_{0.5}Co_{2.5}O_4$, however, NiO has not been detected by XRD at 600 °C while Raman scattering shows possible phase transition. Given the small intensity change in Raman spectra, phase segregation may still exist with only small amount of NiO segregation.

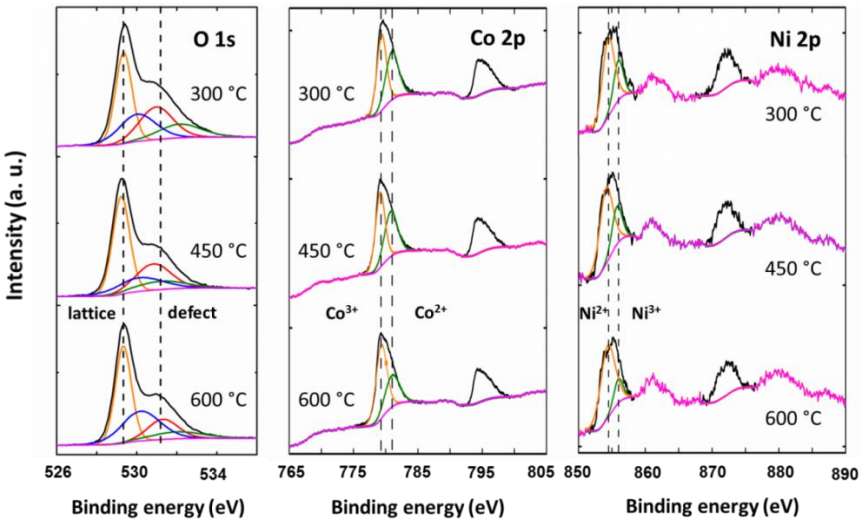

Figure 5.15. X-ray photoelectron spectra of $Ni_xCo_{3-x}O_4$ (x=0.5) nano-arrays after ambient annealing at different temperatures, revealing the tunable oxygen defect population and surface chemical valence states.

To better understand the effect of thermal annealing upon $Ni_{0.5}Co_{2.5}O_4$, XPS was utilized to characterize the valence states change and surface defects. Figure 5.15 shows the deconvoluted XPS spectra for O, Co and Ni in $Ni_{0.5}Co_{2.5}O_4$ after annealing at different temperatures. The broad O 1s peaks can be deconvoluted into four major components (lattice oxygen, surface OH group, oxygen defects, and adsorbed moisture)[28, 44]. The quantitative results in Table 5.3 reveal high temperature annealing mitigates the oxygen defects (vacancies) on surface. While only small difference on the ratios of lattice O/defective O, Co^{3+}/Co^{2+} and Ni^{2+}/Ni^{3+} is discovered at 300 °C and 450 °C, annealing at 600 °C results in a drastic population increase of Ni^{2+} and lattice oxygen. The increase of Co^{3+} concentration may be ascribed to the NiO precipitation so Ni atoms no longer occupy octahedral sites where Co^{3+} are originally located. It might also be due to the ambient annealing during which the catalyst surface is oxidized by the atmospheric O_2. Figure S5 displays the light-off curves of propane oxidation for $NiCo_2O_4$ nano-arrays annealed at different temperatures. It is clearly observed high temperature annealing (450 °C and 600 °C) results in worse catalytic activity due to the decreased catalyst structural stability. It is worth noting, however, in our study 100% propane oxidation can be achieved at temperature lower than 400 °C where all the Ni doped Co_3O_4 nano-array catalyst are thermally stable. Nevertheless, for other hydrocarbon combustion where higher temperature is required (e. g. methane combustion) a balance between enhanced activity and decreased structural stability of the Ni doped Co_3O_4 nano-array catalysts needs to be considered.

Annealing temperatures	O 1s	Co 2p	Ni 2p
	O_{latt}/O_{def}	Co^{3+}/Co^{2+}	Ni^{2+}/Ni^{3+}
300 °C	1.39	1.17	2.52
450 °C	1.8	1.22	2.66
600 °C	2.56	1.76	4.77

Table 5.3. Quantitative results of deconvoluted XPS spectra of O 1s, Co 2p and Ni 2p on the surface population ratios of lattice and defective oxygen, Co^{2+} and Co^{3+}, Ni^{2+} and Ni^{3+}. $2p_{3/2}$ signals were used for the quantitation of Co and Ni valence states.

5.5. Conclusion

In summary, Co_3O_4 based nano-array catalysts have been successfully fabricated and exhibit high activity towards propane oxidation at low temperature. Ni doping was discovered to enhance the reaction kinetics and promote the catalytic activity. In situ DRIFTS investigation helps reveal the catalytic reaction mechanism with further confirmation by oxygen isotope experiment. The thermal stability of Ni doped Co_3O_4 nano-array has been studied by Raman scattering coupled with XPS characterization. The major findings from this study can be summarized as follows.

1) The doping of Ni into the spinel Co_3O_4 lattice enhances the reaction kinetics and allows low temperature oxidation by promoting the activity of lattice oxygen and creating oxygen defects on the catalyst surface.

2) The Ni doping is discovered to favor the formation of thermally less stable carbonates (bidentate and bicarbonate species) on catalyst surface and thus facilitates the CO_2 desorption at lower temperature.

3) Surface chlorine on Co_3O_4 nano-arrays has been found detrimental to propane oxidation, due to either blocking of the active sites or passivating of the Co-O bonds on catalyst surface by Cl.

4) In situ DRIFTS in addition with oxygen isotope experiment reveals the catalytic propane oxidation proceeds via the Mars-van Krevelen mechanism where surface lattice oxygen functions as active sites for oxidizing propane.

5) Raman scattering, XRD and XPS analysis confirm the segregation of NiO from the $Ni_xCo_{3-x}O_4$ lattice at high temperature resulting in decrease of both thermal stability and catalytic activity.

5.6. Reference

[1] Caplain, I.; Cazier, F.; Nouali, H.; Mercier, A.; Déchaux, J.-C.; Nollet, V.; Joumard, R.; André, J.-M.; Vidon, R. *Atmospheric Environment* , **2006**, *40*, 5954.

[2] Gordon, R. J.; Mayrsohn, H.; Ingels, R. M. *Environmental Science & Technology,* **1968**, *2*, 1117.

[3] Schauer, J. J.; Kleeman, M. J.; Cass, G. R.; Simoneit, B. R. T. *Environmental Science & Technology,* **2002**, *36*, 1169.

[4] Shelef, M.; Graham, G. W. *Catalysis Reviews,* **1994**, *36*, 433.

[5] Kočí, P.; Kubíček, M.; Marek, M. *Industrial & Engineering Chemistry Research,* **2004**, *43*, 4503.

[6] Koltsakis, G. C.; Stamatelos, A. M. *Progress in Energy and Combustion Science,* **1997**, *23*, 1.

[7] Collins, N.; Twigg, M. *Topics in Catalysis,* **2007**, *42-43*, 323.

[8] Tikhomirov, K.; Kröcher, O.; Elsener, M.; Wokaun, A. *Applied Catalysis B: Environmental,* **2006**, *64*, 72.

[9] Liu, W.; Flytzanistephanopoulos, M. *Journal of Catalysis,* **1995**, *153*, 304.

[10] Grillo, F.; Natile, M. M.; Glisenti, A. *Applied Catalysis B: Environmental,* **2004**, *48*, 267.

[11] Wu, Z.; Li, M.; Overbury, S. H. *Journal of Catalysis,* **2012**, *285*, 61.

[12] Tian, Z.-R.; Tong, W.; Wang, J.-Y.; Duan, N.-G.; Krishnan, V. V.; Suib, S. L. *Science,* **1997**, *276*, 926.

[13] Fu, Q.; Yang, F.; Bao, X. *Accounts of Chemical Research,* **2013**, *46*, 1692.

[14] Zhu, Z.; Lu, G.; Zhang, Z.; Guo, Y.; Guo, Y.; Wang, Y. *ACS Catalysis*, **2013**, *3*, 1154.

[15] Baldi, M.; Escribano, V. S.; Amores, J. M. G.; Milella, F.; Busca, G. *Applied Catalysis B: Environmental*, **1998**, *17*, L175.

[16] Seiyama, T. *Catalysis Reviews*, **1992**, *34*, 281.

[17] Arai, H.; Yamada, T.; Eguchi, K.; Seiyama, T. *Applied Catalysis*, **1986**, *26*, 265.

[18] Kim, C. H.; Qi, G.; Dahlberg, K.; Li, W. *Science*, **2010**, *327*, 1624.

[19] Saracco, G.; Geobaldo, F.; Baldi, G. *Applied Catalysis B: Environmental*, **1999**, *20*, 277.

[20] McCarty, J. G.; Wise, H. *Catalysis Today*, **1990**, *8*, 231.

[21] Zhu, J.; Li, H.; Zhong, L.; Xiao, P.; Xu, X.; Yang, X.; Zhao, Z.; Li, J. *ACS Catalysis*, **2014**, *4*, 2917.

[22] Song, W.; Poyraz, A. S.; Meng, Y.; Ren, Z.; Chen, S.-Y.; Suib, S. L. *Chemistry of Materials*, **2014**, *26*, 4629.

[23] Xie, X. W.; Li, Y.; Liu, Z. Q.; Haruta, M.; Shen, W. J. *Nature*, **2009**, *458*, 746.

[24] Guo, Y.; Ren, Z.; Xiao, W.; Liu, C.; Sharma, H.; Gao, H.; Mhadeshwar, A.; Gao, P.-X. *Nano Energy*, **2013**, *2*, 873.

[25] Xiao, W.; Guo, Y.; Ren, Z.; Wrobel, G.; Ren, Z.; Lu, T.; Gao, P.-X. *Crystal Growth & Design*, **2013**, *13*, 3657.

[26] Guo, Y.; Liu, G.; Ren, Z.; Piyadasa, A.; Gao, P.-X. *CrystEngComm*, 2013, *15*, 8345.

[27] Ren, Z.; Guo, Y.; Zhang, Z.; Liu, C.; Gao, P.-X. *Journal of Materials Chemistry A*, **2013**, *1*, 9897.

[28] Ren, Z.; Botu, V.; Wang, S.; Meng, Y.; Song, W.; Guo, Y.; Ramprasad, R.; Suib, S. L.; Gao, P.-X. *Angewandte Chemie International Edition* , **2014**, *53*, 7223.

[29] Xiong, S.; Chen, J. S.; Lou, X. W.; Zeng, H. C. *Advanced Functional Materials*, **2012**, *22*, 861.

[30] Wang, B.; Zhu, T.; Wu, H. B.; Xu, R.; Chen, J. S.; Lou, X. W. *Nanoscale* , **2012**, *4*, 2145.

[31] Xiao, Y.; Liu, S.; Li, F.; Zhang, A.; Zhao, J.; Fang, S.; Jia, D. *Advanced Functional Materials*, **2012**, *22*, 4051.

[32] Fei, Z.; He, S.; Li, L.; Ji, W.; Au, C.-T. *Chemical Communications*, **2012**, *48*, 853.

[33] Tang, C.-W.; Hsu, L.-C.; Yu, S.-W.; Wang, C.-B.; Chien, S.-H. *Vibrational Spectroscopy*, **2013**, *65*, 110.

[34] Luo, J.-Y.; Meng, M.; Zha, Y.-Q.; Guo, L.-H. *The Journal of Physical Chemistry C*, **2008**, *112*, 8694.

[35] Binet, C.; Daturi, M.; Lavalley, J.-C. *Catalysis Today*, **1999**, *50*, 207.

[36] Pozdnyakova, O.; Teschner, D.; Wootsch, A.; Kröhnert, J.; Steinhauer, B.; Sauer, H.; Toth, L.; Jentoft, F. C.; Knop-Gericke, A.; Paál, Z.; Schlögl, R. *Journal of Catalysis*, **2006**, *237*, 17.

[37] Doornkamp, C.; Ponec, V. *Journal of Molecular Catalysis A: Chemical*, **2000**, *162*, 19.

[38] Pang, X.-Y.; Liu, C.; Li, D.-C.; Lv, C.-Q.; Wang , G.-C. *ChemPhysChem.*, **2013**, *14*, 204.

[39] Grasselli, R. *Topics in Catalysis*, **2002**, *21*, 79.

[40] Li, C.; Sakata, Y.; Arai, T.; Domen, K.; Maruya, K.; Onishi, T. *Journal of the Chemical Society, Chemical Communications*, **1991**, 410.

[41] Cabo, M.; Pellicer, E.; Rossinyol, E.; Castell, O.; Suriñach, S.; Baró, M. D. *Crystal Growth & Design*, **2009**, *9*, 4814.

[42] Iliev, M. N.; Silwal, P.; Loukya, B.; Datta, R.; Kim, D. H.; Todorov, N. D.; Pachauri, N.; Gupta, A. *Journal of Applied Physics*, **2013**, *114*.

[43] Hadjiev, V. G.; Iliev, M. N.; Vergilov, I. V. *Journal of Physics C: Solid State Physics*, **1988**, *21*, L199.

[44] Liu, Z.-Q.; Xu, Q.-Z.; Wang, J.-Y.; Li, N.; Guo, S.-H.; Su, Y.-Z.; Wang, H.-J.; Zhang, J.-H.; Chen, S. *International Journal of Hydrogen Energy*, **2013**, *38*, 6657.

Chapter 6

Other applications of nano-array integrated functional catalysts – photocatalytic water treatment

6.1. Introduction

Photocatalytic degradation of toxic organic compounds represents a promising technology for waste water disposal,[1–3] for which semiconductor nanoparticles are a viable class of candidates due to ease of preparation and flexible utilization under both artificial illumination and sunlight.[4–6] However, the homogeneous suspension of photocatalytic nanoparticles imposes great difficulty upon recovery and collection. In the past decade, the loading of photocatalytic nanoparticles onto inert substrates as well as the incorporation of magnetic nanoparticles are found to facilitate the separation.[7–9] However, the light harvest efficiency could be suppressed by the existent inactive substrate, the recombination at the magnetic core–semiconductor shell interface may lead to deterioration of photocatalytic performance.[10] The design of a robust and recoverable photocatalyst has remained a big challenge.

Meanwhile, much effort has been devoted to promote photocatalyst efficiency based on the structure–property relationship. As an example, one-dimensional (1D) nanowires have exhibited unique physical, chemical and biological properties compared with nanoparticles and hold great potential to enhance the comprised nanodevices' performance.[11–14] Recently, the assembly of sophisticated hierarchical nanoarchitectures is believed to be able to help extend the functionality of low dimensional nanostructures to 3D space in a controlled manner.[15–18] Koosh ball structured nanomaterials with high surface area represent a typical example of such architectures[19–23] and have already found preliminary applications in lithium ion batteries,[24] water treatment[25] and solar

cells.[26] It is worth noting that the ZnO nanowire assembled hierarchical koosh ball architecture enables elongated light path[26] and great performance towards photocatalytic degradation.[27]

In this work, we successfully demonstrate the facile synthesis of a unique koosh ball structure with a conformal ZnO nanowire array grown on the surface of various magnetic core–shell particles ($Fe_xO_y@SiO_2$). The incorporation of a silica layer in between not only stabilizes the magnetic core from dissolution but also alleviates the electron–hole recombination at the interface,[28,29] thus promoting the photocatalytic performance. In addition to the enabled rational integration and effective utilization of desired functionality from different constituents, another feature of our koosh ball architecture lies in the conformal nanowires grown on the three-dimensional microscale substrate for the first time. The introduced simple hydrogen annealing not only simultaneously tunes the phase transition of the magnetic core and the fluorescence of the nanowire shell, but also helps clarify the correlation between nanowire surface defects and photocatalytic property.

6.2. Experimental section

6.2.1. Synthesis of magnetite (Fe_3O_4) nanoparticles

The magnetite nanoparticles 600 nm in diameter were synthesized by a facile hydrothermal process. In a typical experiment, 1 g of ferric chloride hexahydrate ($FeCl_3•6H_2O$, 97%, Alfa Aesar) and 3.6 g of polyvinylpyrrolidone (PVP, average Mw 58 000, K29-32, Acros) were dissolved in 35 mL of ethylene glycol (EG, Fisher Scientific) to form a clear solution. 3 g of sodium acetate (NaAc, Sigma-Aldrich) was added subsequently and the solution was then sonicated for 15 minutes. The precursor was transferred to a Teflon-lined autoclave and was heated for 10 hours at 200 °C.

6.2.2. Synthesis of the $Fe_3O_4@SiO_2$ core–shell structure

A modified Stober process was used to produce a uniform coating of SiO_2 onto Fe_3O_4. Briefly, 0.1 g of the as-prepared Fe_3O_4 nanoparticles was dispersed to form ferrofluid, and 20 mL of the ferrofluid was then added into ethanol and was sonicated for 30 minutes. 1.5 mL of ammonium hydroxide ($NH_3•H_2O$, Acros) was then added dropwise. 3 mL of tetraethyl orthosilicate (TEOS, 98%, Acros) was added by syringe and the reaction incubated for 8 hours while stirring.

6.2.3. Development of γ-$Fe_2O_3@SiO_2$–ZnO koosh ball nanoarchitectures

In order to synthesize γ-$Fe_2O_3@SiO_2$–ZnO koosh ball structures, the as-prepared $Fe_3O_4@SiO_2$ core–shell particles were immersed into dilute zinc acetate ($ZnAc_2$, Fisher Scientific) solution with magnetic stirring for 30 minutes. The solution was slowly evaporated at 80 °C and the remainder was annealed in the open air at 350 °C for 5 hours. The color of the sample changed from black to red brown. The powder was then dispersed into distilled water where zinc acetate ($ZnAc_2$) and hexamethylenetetramine (HMT, 99%, Acros) were added in equal concentrations (1 mM). After being sonicated for 15 minutes, the solution was heated to 80 °C and maintained at this temperature for 8 hours. The product was obtained by centrifugation and rinsed several times with distilled water and ethanol.

6.2.4. Koosh ball STEM sample preparation by focused ion beam microscope

The Strata 400 STEM DualBeam system, a field emission scanning electron microscope (FE-SEM) equipped with focused ion beam (FIB) and Flipstage/STEM assembly, was used for in situ STEM sample preparation and analysis. About 5 mm thick platinum was deposited on feature particles to help protect them from ion beam damage. Using 30 kV gallium ions at 9.3 nA, a 20 mm×10 mm×5 mm deep trench was milled on both sides of the features to make the cross-

sectional sample. The cross-section was sequentially thinned to about 1 mm with reduced current. Then the sample was attached to an Omni-probe manipulator so it could be mounted on the TEM grid. Lower FIB beam current was used to further thin the sample to a thickness of about 500 nm for EDX mapping and about 20 nm thick for STEM imaging.

6.2.5. Structure and morphology characterization

The morphology of the as-prepared products was characterized by a field emission scanning electron microscope (FESEM, JEOL 6335F, 10 kV) with an energy dispersive X-ray spectrometer (EDX). Transmission electron microscopy (TEM) and high-resolution TEM (HRTEM) imaging were performed by a JEOL JEM-2010F microscope. The as-prepared sample was dispersed in ethanol and then dropped onto a carbon film supported on a copper grid. The structure and composition of the products were studied with a Bruker AXS D5005 X-ray diffractometer (XRD, Cu Ka radiation, λ=1.540598 A). The XRD specimens were prepared by dropping particle suspensions onto the glass slides and evaporating several times to form a thick layer. Photoluminescence analysis was performed using a spectrofluorometer. A Nikon A1R spectral confocal microscope was utilized to detect the fluorescence under excitation.

6.2.6. Photocatalytic degradation of Rhodamine B (RhB)

The photodegradation of Rhodamine B (Sigma) was conducted using a Luzchem ring illuminator equipped with UVA light (356 nm, 220 W). Different samples including γ-Fe_2O_3 koosh ball, bcc-Fe koosh ball and commercialized ZnO nanopowder (~25 nm, Fisher Scientific) were dispersed in RhB solution (2.5×10^{-6} M). Before the measurement, the solution was kept in the dark for 20 minutes to achieve adsorption and desorption equilibrium. The concentration change of RhB was

recorded by UV-vis-NIR absorption spectroscopy (PerkinElmer) to investigate the efficiency of photodegradation.

6.3. Results and Discussion

6.3.1. Synthesis and characterization of γ-Fe_2O_3@SiO_2–ZnO koosh ball

To fabricate the γ-Fe_2O_3@SiO_2–ZnO koosh ball, a typical four step synthetic procedure was developed as illustrated in Fig. 6.1. First, magnetite (Fe_3O_4) nanoparticles were prepared by hydrothermal synthesis (Fig. 6.2) and a layer of silica was uniformly deposited by a modified Stober process.[30] The surface of these as-prepared core–shell structured particles was dip-coated with a zinc acetate solution. The particles were then annealed under ambient conditions at 350 °C to form a layer of ZnO nanoparticles with the core magnetite (Fe_3O_4) transformed to maghemite (γ-Fe_2O_3). The phase transformation of iron oxide was confirmed by X-ray diffraction (Fig. 6.2). The ZnO nanowire array was finally grown by a hydrothermal method onto the core–shell particles, forming the three-layer koosh ball architectures. The TEM images (Figure 6.3a–c) display the morphological evolution of the particles at each stage of synthesis. The core–shell structure of the Fe_3O_4@SiO_2 particle is confirmed in Figure 6.3a with a diameter of ~700 nm and a SiO_2 shell of ~50 nm thickness. A slice of the particle was obtained by focused ion beam (FIB) milling (Figure 6.3d) for high resolution TEM characterization. The lattice image of the Fe_3O_4@SiO_2 core–shell interface shown in Figure 6.3e reveals the polycrystalline Fe_3O_4 core and amorphous SiO_2 shell. The measured interplanar d-spacing of 0.25 nm in the nano-grains to the right of Fig. 3e matches the (311) atomic planes of Fe_3O_4. However, it is noteworthy that the FIB milled sample contains some embedded Pt nanoparticles in both the magnetite core and silica shell (arrowheads in Figure 6.3e and 6.4), as confirmed by the HRTEM lattice imaging (Figure 6.3), which are introduced from the deposited Pt protection layer before the FIB milling.

Fig. 3b indicates the successful ZnO nanoparticles loading after surface treatment. Furthermore, the HRTEM image in Figure 6.3f reveals the (0002) atomic planes of hexagonal wurtzite zinc oxide with an inter-planar d-spacing of 0.26 nm. The ZnO nanowires grown on the γ-Fe_2O_3@SiO_2 particles are measured in Figure 6.3c to be ~200 nm long. Detailed structure analysis on koosh ball nanoarchitectures has been performed. Fig. 5a displays a typical scanning electron microscopy (SEM) image of γ-Fe_2O_3@SiO_2–ZnO koosh balls ~1 μm wide. The ZnO nanowire array uniformly distributes around the spherical surface as shown by the magnified SEM image in Fig. 5b. Both bright-field and dark-field transmission electron microscopy (TEM) images in Fig. 5c and d, respectively, reveal the three-layered koosh ball architecture with a core–shell particle uniformly decorated by nanowires on the surface. The X-ray diffraction spectrum (Fig. 6) clearly identifies the existence of polycrystalline maghemite (JCPDS No.25-1402) and hexagonal wurtzite zinc oxide (JCPDS No. 36-1451). No peak in Figure 6 is observed for silica, which is confirmed to be amorphous by HRTEM analysis (Fig. 3 and 4). The energy dispersive X-ray spectroscopy (EDX) in Fig. 5d further confirms the existence of iron(Fe), silicon(Si), zinc(Zn) and oxygen(O) in the three-layer koosh ball architectures.

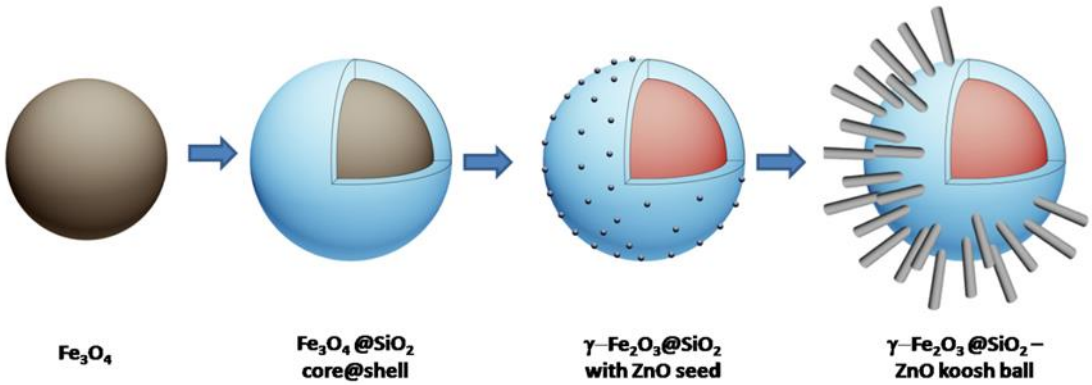

Figure 6.1.The schematic illustration of the growth process of a γ–Fe_2O_3@SiO_2-ZnO three-layered koosh ball nanoarchitectures.

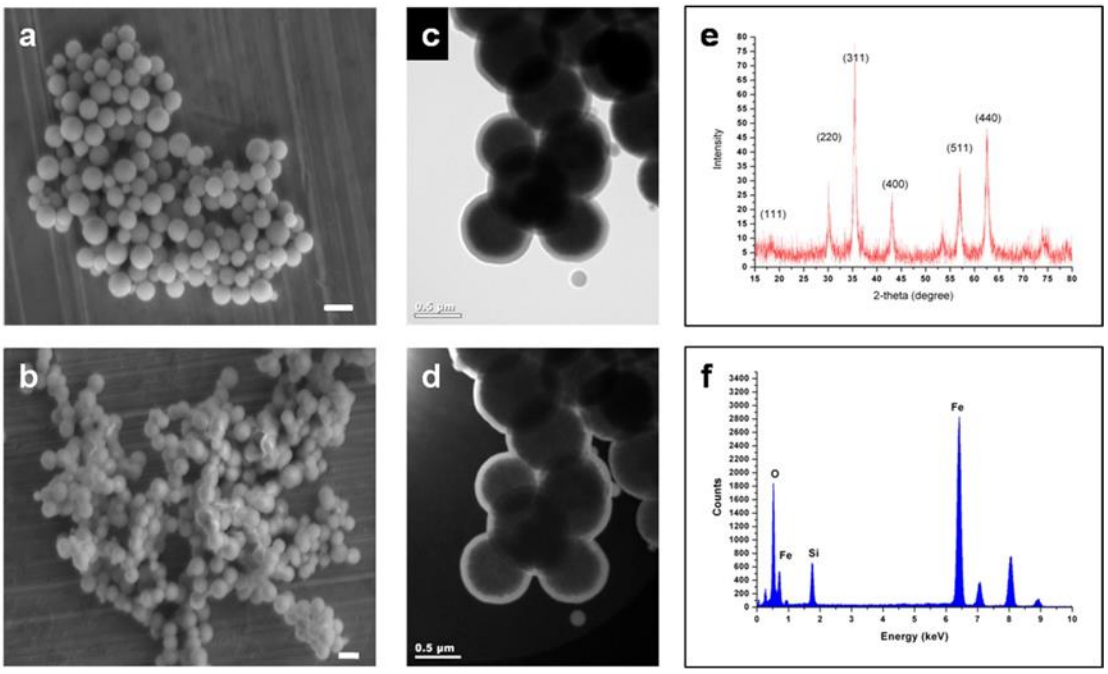

Figure 6.2. (a)A typical SEM image of Fe_3O_4 particles; (b) An SEM image of Fe_3O_4@SiO_2 core-shell structure; (c) Bright field TEM image of Fe_3O_4@SiO_2 core-shell structure; (d) Dark field TEM image of Fe_3O_4@SiO_2 core-shell structure; (e) XRD pattern of Fe_3O_4@SiO_2; (f) An EDX spectrum of Fe_3O_4@SiO_2. Scale bars in (a) and (b): 1μm.

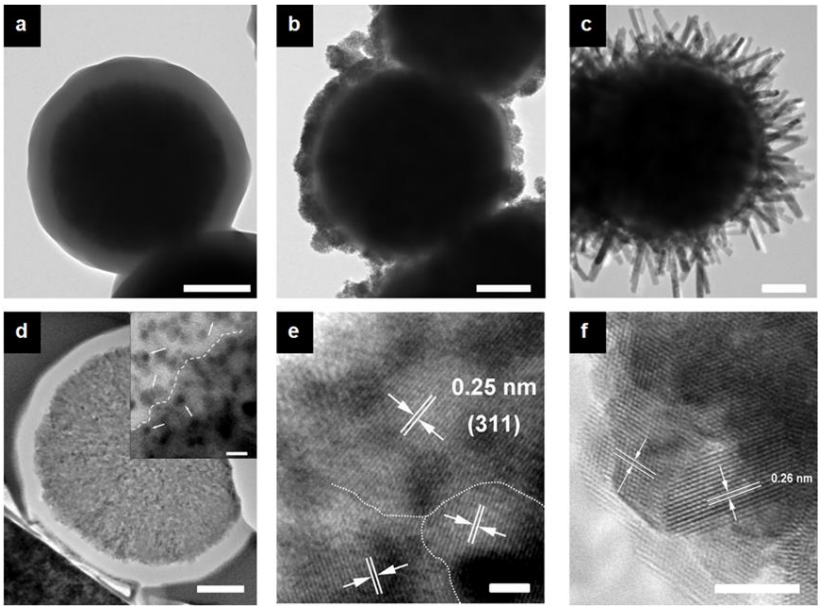

Figure 6.3. (a) A typical TEM image of core-shell Fe_3O_4@SiO_2 particles. (b) A typical TEM image of ZnO seeded core-shell Fe_3O_4@SiO_2 particles. (c) A typical TEM image of a koosh ball nanoarchitectures after ZnO nanowire growth. (d) An STEM image of a FIB milled HRTEM Fe_3O_4@SiO_2 particle sample. Inset: the magnified image of core-shell interface with

interface(dashed line) and arrowheads indicating embedded artifacts. (e) A HRTEM image at the Fe_3O_4-SiO_2 interface region with grain boundary (dot line). (f) A HRTEM image of ZnO seed particles. Scale bars in (a)-(d): 200 nm; (e): 2 nm; (f): 5 nm.

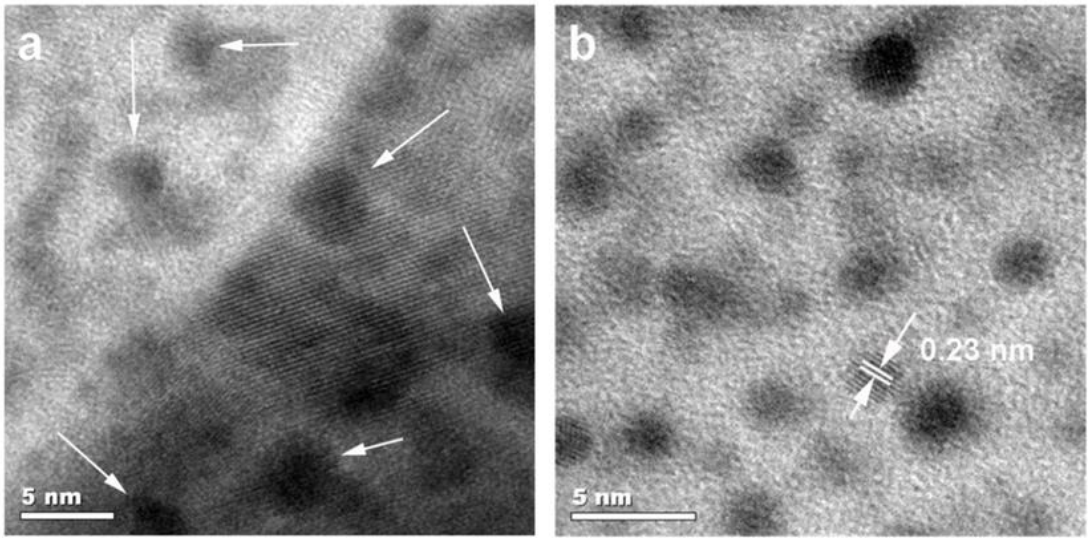

Figure 6.4. An HRTEM image of a) the interface between polycrystalline Fe_3O_4 core and amorphous SiO_2 shell (arrows indicates the Pt impurity); b) embedded Pt within SiO_2 shell. The lattice spacing 0.23nm corresponds to the separation Pt (111) atomic planes.

To gain more insight into the as-prepared koosh ball structure, a FIB microscope has been utilized to prepare the scanning transmission electron microscopy (STEM) samples. The STEM image in Fig. 5e shows the FIB milled cross-section of two closely packed koosh balls. The EDX mapping in tandem with the STEM imaging in Fig. 5c and 5d verifies the unique three layered architecture. The distribution map of elements Fe, Si, Zn and O is displayed in Figs. 5g–j, respectively. It is apparent that Fe exists in the core while Si distributes in a ring-like region of the inner part, confirming the core–shell structure. The Zn distribution exhibits a flower-like shape with a blank interior, indicating the successful ZnO nanowire decoration onto the core–shell spherical surface. The oxygen exists everywhere with its distribution corresponding to the koosh ball morphology.

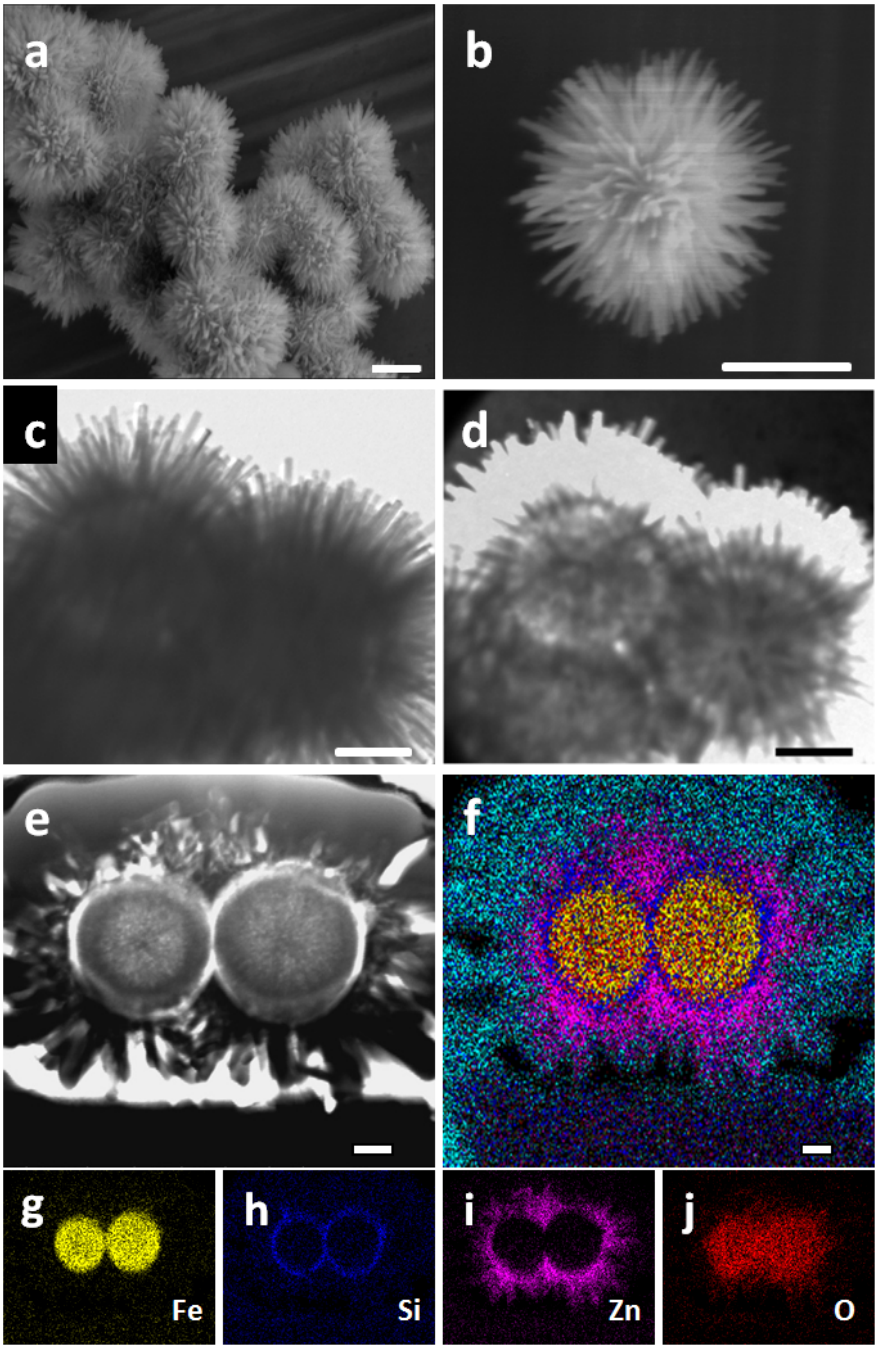

Figure 6.5. (a) A low magnification SEM image of typical koosh ball architectures. (b) A high magnification SEM image of a typical koosh ball. (c) A bright-field TEM image of koosh ball architectures. (d) A dark-field TEM image of the koosh balls in c). (e) An STEM image of FIB milled koosh ball nanoarchitectures. (f) An overall cross-sectional EDX elemental map of koosh ball nanoarchitectures. (g)-(j) Elemental distribution maps of individual elemental constituent (Fe, Si, Zn, O). Scale bars in a): 1 μm; b)-d): 500 nm; e)-f): 200 nm.

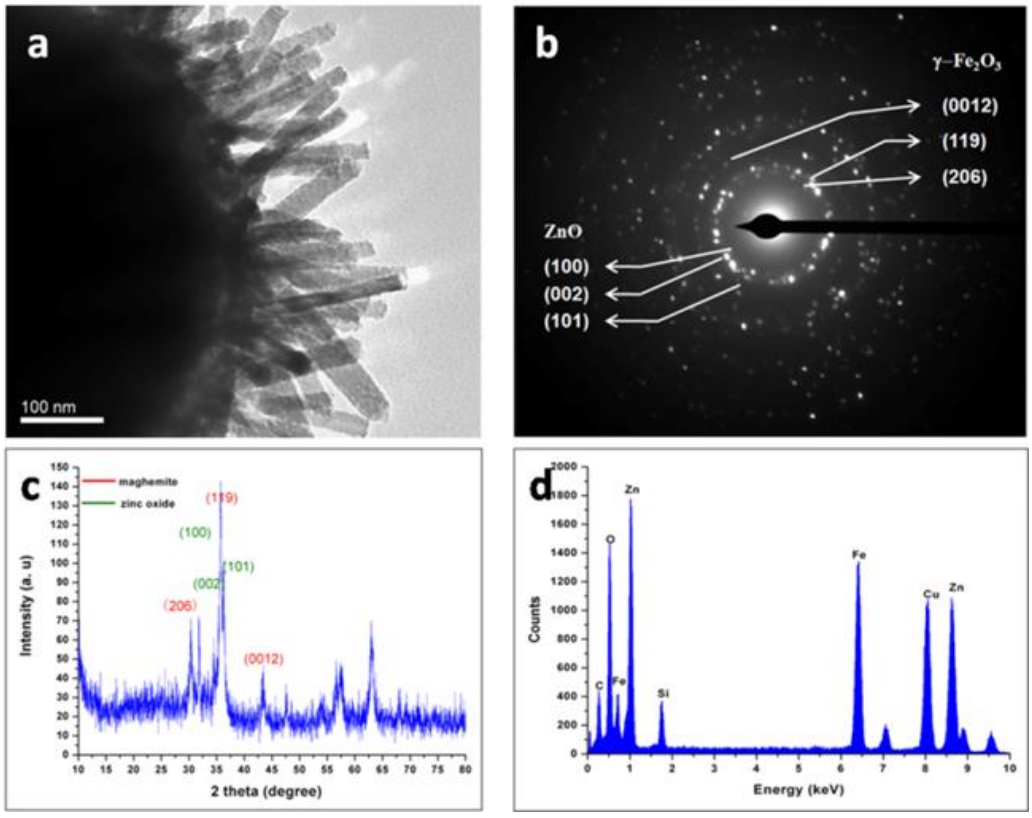

Figure 6.6. a) A TEM image of a γ–Fe_2O_3@SiO_2-ZnO koosh ball; b) Electron diffraction pattern corresponding to the γ–Fe_2O_3@SiO_2-ZnO koosh ball in a); c) A typical X-Ray diffraction pattern for γ–Fe_2O_3@SiO_2-ZnO koosh balls; d) An energy dispersive X-ray spectrum of γ–Fe_2O_3@SiO_2-ZnO koosh balls.

6.3.2. Structure tuning of koosh ball nanoarchitecture through H_2 post-annealing

Inspired by the success in Fe_3O_4-to-γ-Fe_2O_3 conversion during ZnO seed layer formation, we explored and developed the tunability of koosh ball architecture with different magnetic cores through different hydrogen post-annealings. To maintain the koosh ball morphology, temperature programmed reduction (TPR) has been utilized to help design the annealing process. In Figure 6.7, the reductive temperatures for Fe_2O_3 and ZnO nanowires were found to be 400 °C and 550 °C, respectively. Therefore, a facile strategy was developed to tune the phase transformation of iron oxide by hydrogen post-annealing at 400 °C with different concentrations. Figure 7d displays a series of magnetic koosh balls with retained morphology. Typically, γ-Fe_2O_3 koosh

balls annealed in forming gas (5% H_2, 95% N_2) will turn to bcc-Fe koosh balls while α-Fe_2O_3 koosh balls annealed with lower hydrogen concentration (1% H_2, 99% N_2) will transform to Fe_3O_4 koosh ball nanoarchitectures. The X-ray diffraction analysis identifies koosh balls with different iron oxide cores (Figure 8). The tunable phase transformation, which leads to iron oxides of different magnetic properties, may provide tunable magnetic cores for practical application.

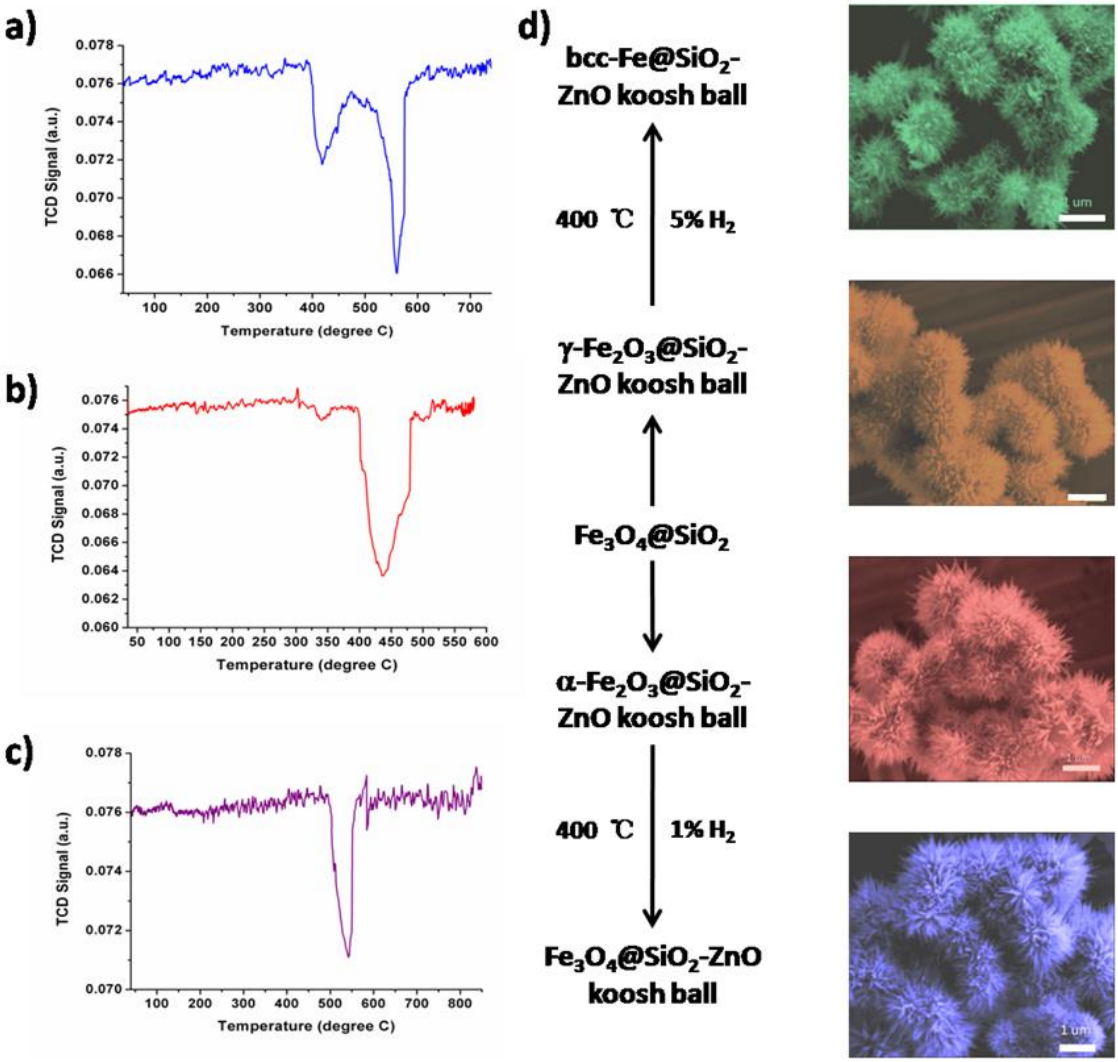

Figure 6.7. Temperature programmed reduction of (a) γ-Fe_2O_3@SiO_2-ZnO koosh ball nanoarchitectures; (b) γ-Fe_2O_3@SiO_2 core-shell nanoparticles; (c) hydrothermally grown ZnO

nanowires. (d) Controlled phase transition process to achieve various koosh ball nanoarchitectures with tunable magnetic cores. Scale bars: 1 μm.

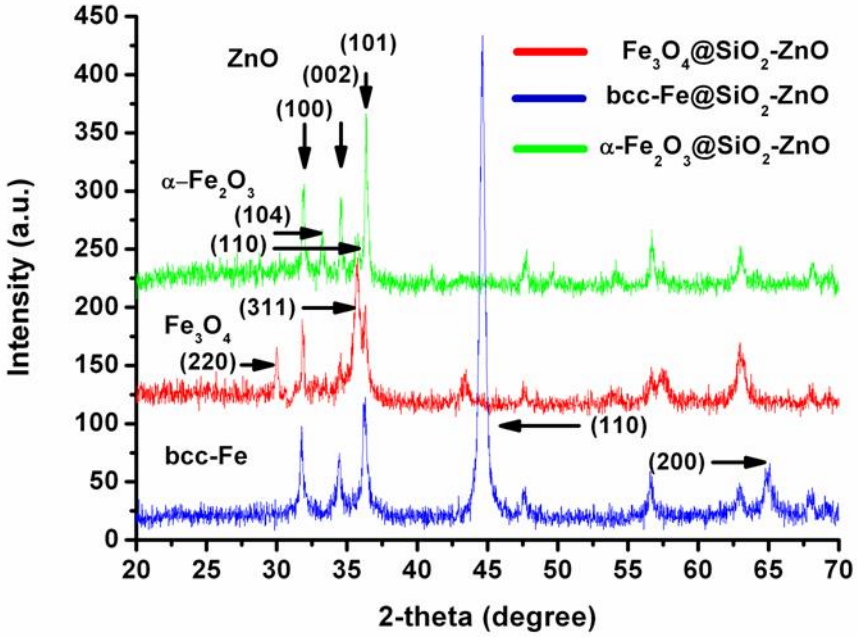

Figure 6.8. X-ray diffraction patterns of magnetic koosh ball nanoarchitectures derived from γ-Fe_2O_3 koosh ball.

6.3.3. Fluorescence and photocatalytic property of koosh ball nanoarchitectures

With the retained koosh ball morphology, the introduction of the H2 post-annealing has also modified the native surface defect states in ZnO nanowires. Photoluminescence (PL) spectra of different koosh ball nanoarchitectures were recorded under a 320 nm ultra-violet (UV) light excitation as displayed in Figure 6.11 and 6.13. The UV emission peak located at 380 nm is attributed to the near band edge emission of ZnO while the broad visible green emission peak (500–600 nm) is determined by surface oxygen defects.[31–33] In Figure 6.13, the as-prepared g-Fe_2O_3 and α-Fe_2O_3 koosh balls after hydrothermal growth exhibit the UV (380 nm), blue (430 nm) and relatively strong green emission (500–600 nm).

Confocal microscopy operated under violet excitation (405 nm) clearly confirms a blue emission within a wavelength range of 447±30 nm and a strong green emission within 525±22.5 nm (Figure 6.11). However, the koosh balls obtained after hydrogen annealing (bcc-Fe and Fe_3O_4 koosh balls) have their green emission quenched, which indicates the possible passivation of oxygen defects by hydrogen.[34,35] The increased surface area by 3D ZnO nanowire wrapping as well as the magnetic separability and tunability makes the unique koosh ball architecture a promising candidate for photocatalysis application. To clarify the photocatalytic effects from each component of the koosh ball, we have first investigated the RhB degradation by different SiO_2 coated core–shell magnetic particles.

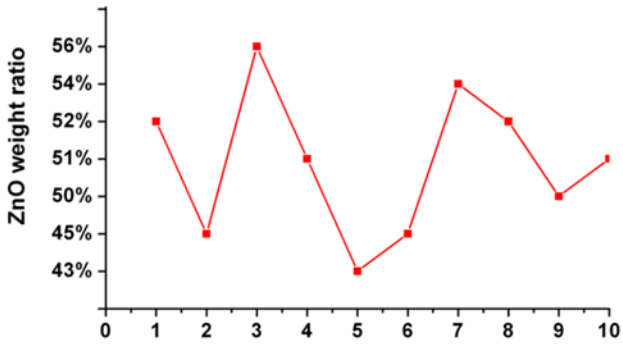

Before ZnO Growth	After ZnO Growth	ZnO Weight Ratio
2 mg	4.16 mg	52%
2 mg	3.63 mg	45%
2 mg	4.54 mg	56%
2 mg	4.08 mg	51%
2 mg	3.51 mg	43%
2 mg	3.64 mg	45%
2 mg	4.35 mg	54%
2 mg	4.26 mg	52%
2 mg	4.02 mg	49%
2 mg	4.09 mg	51%

Figure 6.9. The ZnO weight ratios within koosh balls measured by repeated experiments.

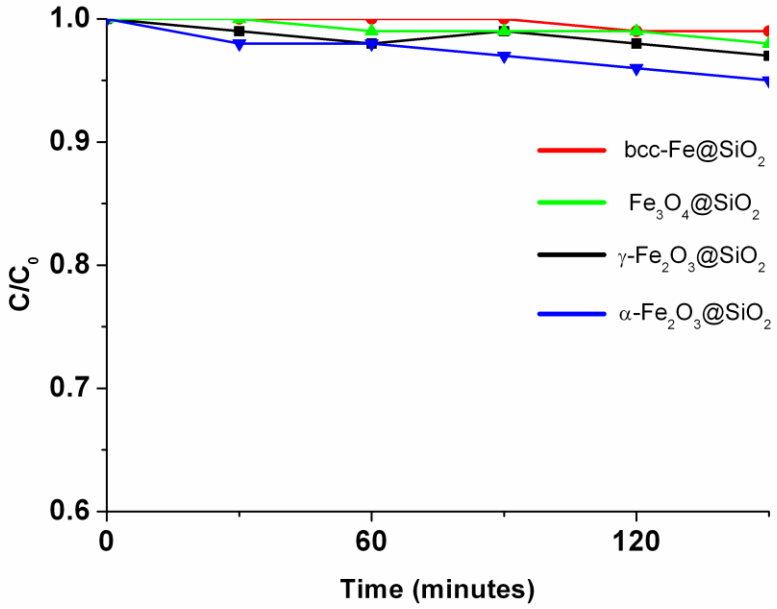

Figure 6.10. Photodegradation of RhB using various magnetic core-shell particles under UV irradiation.

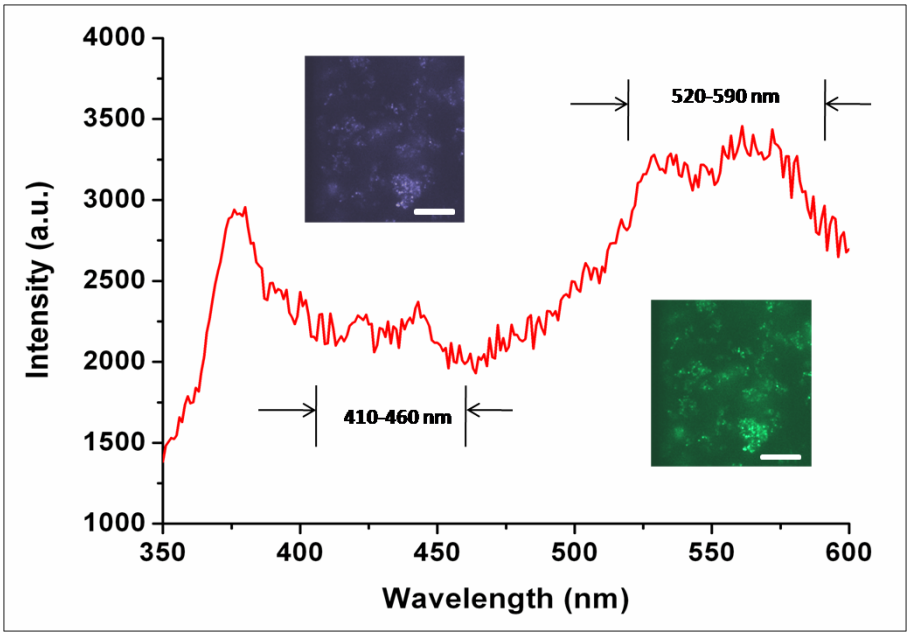

Figure 6.11. Photoluminescence spectrum of the as-prepared γ-Fe_2O_3@SiO_2-ZnO koosh ball nanoarchitectures. Inset: confocal microscopy imaging of visible blue and green emission. Scale bar: 10 μm.

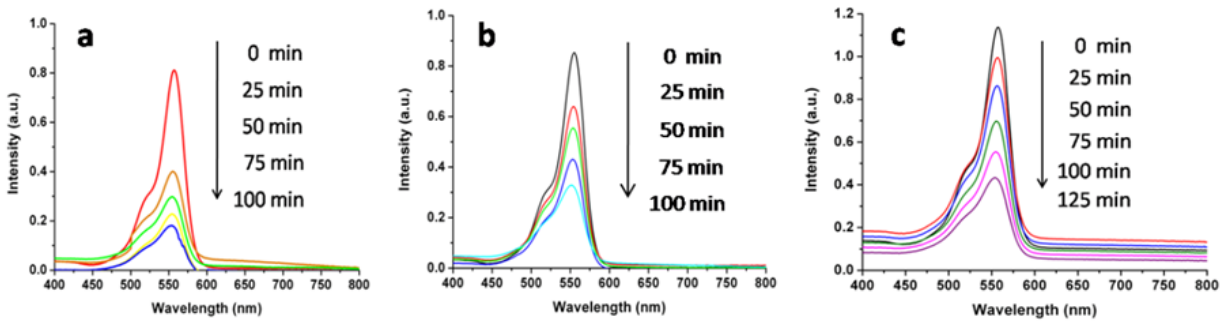

Figure 6.12. UV-vis-NIR absorption spectra of Rhodamine B solution after different duration of UV irradiation: a) 5 mg γ-Fe_2O_3 koosh balls; b) 5 mg bcc-Fe koosh balls; c) 2.5 mg ZnO nanopowder.

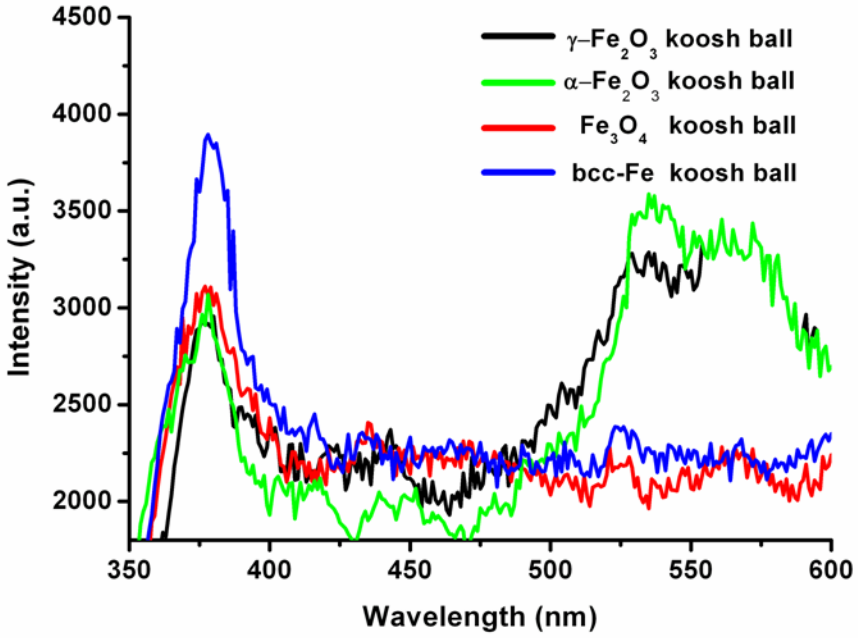

Figure 6.13. Photoluminescence spectra of koosh ball nanoarchitectures of different magnetic cores.

As can be seen from Figure 6.10, none of these core–shell particles exhibits considerable efficiency towards photodegradation of RhB and thus the 3D branched ZnO nanowires should be

the key constituent that contributes to the degradation. However, it is worth noting that the scientific understanding behind the photocatalytic efficiency of ZnO nanowires has remained controversial, especially in the organic dye molecule photodegradation. Different mechanisms related to defect chemistry have been proposed in previous research to interpret photocatalytic degradation of dye molecules.[36–39] For instance, the photocatalytic degradation of Rhodamine B (RhB) using ZnO has been attributed to a high concentration of surface and lattice oxygen defects,[40–42] which serve as active sites for photogenerated electron and hole trapping.[43,44] However, the surface defects such as hydroxyl impurity and dangling ligand may also serve as recombination sites that hinder the electron–hole pair separation.[45] It is noteworthy from the PL spectra that the hydrogen post-annealing promotes the UV emission indicating the improved electron–hole pair separation efficiency, which may enhance koosh balls' photocatalytic performance as well. To clarify which mechanism, whether the removal of ligand impurity or oxygen defects, predominantly contributes to photocatalytic degradation of RhB by the koosh ball nanoarchitecture, γ-Fe_2O_3 koosh balls with abundant oxygen defects and bcc-Fe koosh balls with improved UV emission were used for RhB degradation under UV irradiation. Comparing the UV adsorption spectra of RhB in Figure 6.10a and 6.10b, it is evident that the RhB degradation by the γ-Fe2O3 koosh ball is faster than the bcc-Fe koosh ball and the abundant oxygen defects seem to help accelerate the photodegradation. On the basis of this observation, we validate a mechanism for the koosh ball photocatalytic process that the oxygen defects on the nanowire surface act as trapping sites for photogenerated electrons and holes. These trapped electrons and holes give rise to an intermediate surface state, which is favorable for interaction with RhB molecules adsorbed on the nanowire defective surface. The carrier trapping not only enables separation of the photogenerated electron–hole pair but also triggers efficient charge

transport facilitating the degradation of adsorbed dye molecules on the surface. With decreased surface oxygen defects by hydrogen annealing, the electron transport at the nanowire–dye molecule interface may not be effective thus reducing photocatalytic performance.

Sample	E(X)	E(Y)	$E(X^2)$	$E(Y^2)$	E(XY)	LCC	K (min^{-1})
5 mgγ-Fe2O3 koosh ball	50	0.923827	3750	1.169082	65.72227	0.98329	0.0196
5 mg bcc-Fe koosh ball	50	0.472064	3750	0.330202	35.13595	0.995546	0.00913
2.5 mg ZnO	50	0.32378	3750	0.170626	25.18275	0.99174	0.00651

Figure 6.14. Computations of linear correlation coefficients and rate constants for different samples, which demonstrates a good linearity between reaction time and the natural logarithm of relative concentration C_0/C. (E: Expectation; statistical average. X: reaction time. Y: $\ln(C_0/C)$. LCC: Linear Correlation Coefficient. K: rate constant)

$$\mathrm{LCC} = \frac{\mathrm{E(XY)} - \mathrm{E(X)E(Y)}}{\sqrt{\mathrm{E(X^2)} - \mathrm{E^2(X)}}\sqrt{\mathrm{E(Y^2)} - \mathrm{E^2(Y)}}}$$

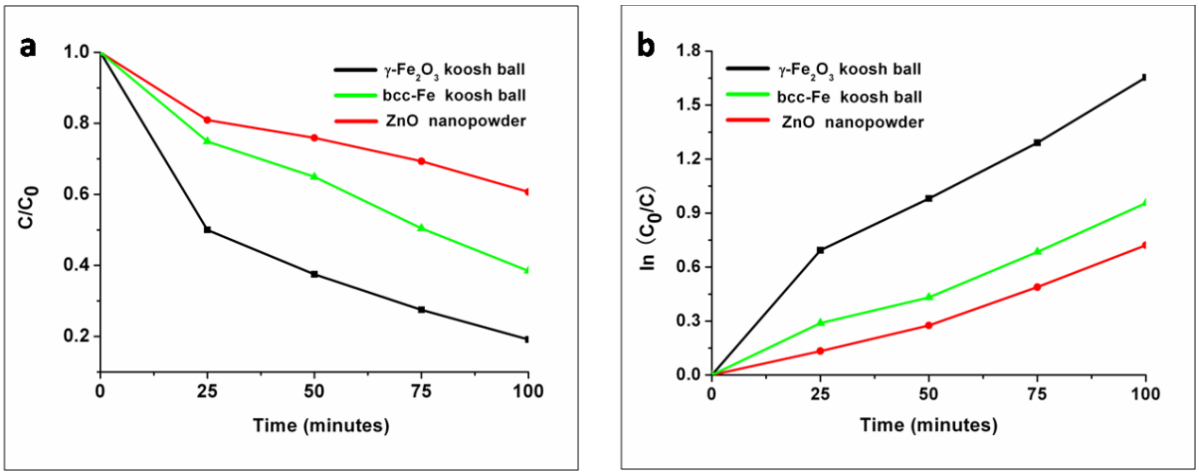

Figure 6.15. (a) Photodegradation of Rhodamine B by 2.5 mg commercial ZnO nanopowders; bcc-Fe@SiO_2-ZnO koosh balls and γ–Fe_2O_3@SiO_2-ZnO koosh balls. (b) Kinetic analysis for photocatalytic reactions.

Figure 6.15a further compares the photocatalytic performance between koosh ball nanoarchitecture and commercial ZnO nanopowder (25 nm in diameter). The weight ratio of ZnO constituent within koosh balls is calculated to be about 50% by repeated experiments (Figure 6.12). The same amount of ZnO involved in the koosh ball nanoarchitecture was found to give enhanced photodegradation efficiency. Kinetic analysis in Figure 6.15b reveals a linear relation between ln(C_0/C) and reaction time, with a linear correlation coefficient close to 1, which well corresponds to the quasi-first order reaction nature of RhB photodegradation (Figure 6.12). Quantitative results of reaction rate constant are obtained in Figure 6.12 by the calculated slopes of the linearly fitting curves. It is worth pointing out that the enhanced photocatalytic property towards degradation of dye molecules can be attributed to advantages from three-dimensional integration and rational combination of diverse functions from three constituents. First, the 3D extended ZnO nanowire branches promote the adsorption of organic dye molecules on the surface so that the degradation rate is enhanced. Secondly, the abundance of surface oxygen defects facilitates the charge transport towards the dye molecule, which largely accelerates the reaction. Third, the magnetic core will enable easy recovery of koosh balls and the controlled magnetic phase transition, which leads to γ-Fe_2O_3 and α-Fe2O3, may provide a co-catalyst towards photodegradation of other contaminant molecules. Lastly, the incorporation of insulating silica layer may prohibit the electron–hole recombination at the magnetic core and ZnO interface.

6.4. Conclusions

In summary, we have successfully developed a mild, wet chemical strategy to prepare multilayered koosh ball nanoarchitectures which enables uniform ZnO nanowire array growth on the 3D microscale spherical substrate. This unique architecture constitutes a tunable magnetic core and a fluorescent nanowire shell with enhanced photocatalytic performance towards dye degradation due to abundant surface oxygen defects. The koosh ball architecture will provide a unique structure design to achieve rational integration of multiple desired functionalities from dissimilar components and give improved nanomaterials performance. We believe the synthetic strategy and the nanoarchitectures demonstrated here could open up a new avenue for designing and fabricating complex 3D nanoarchitectures and their utilization in energy, environmental and biomedical applications, such as tunable and recyclable photocatalysis, magnetically directed drug targeting and delivery.

6.5. Reference

[1] L. Rizzo, S. Meric, M. Guida, D. Kassinos, V. Belgiorno, *Water Research*, **2009**, *43*, 4070.

[2] K. Tanaka, K. Padermpole, T. Hisanaga, *Water Research*, **2000**, *34*, 327.

[3] D. S. Bhatkhande, V. G. Pangarkar, A. A. C. M. Beenackers, *Journal of Chemical Technology & Biotechnology*, **2002**, *77*, 102.

[4] H. Tong, S. Ouyang, Y. Bi, N. Umezawa, M. Oshikiri, J. Ye, *Advanced Materials*, **2011**, DOI: 10.1002/adma.201102752.

[5] J. P. Wilcoxon, B. L. Abrams, in *Nanotechnology*, Wiley-VCH Verlag GmbH & Co. KGaA, **2010**, 51–124.

[6] D. Astruc, F. Lu, J. R. Aranzaes, *Angewandte Chemie International Edition*, **2005**, *44*, 7852.

[7] R. L. Pozzo, M. A. Baltanás, A. E. Cassano, *Catalysis Today*, **1997**, *39*, 219.

[8] S. Xuan, W. Jiang, X. Gong, Y. Hu, Z. Chen, *The Journal of Physical Chemistry C*,**2008**, *113*, 553.

[9] M. Ye, Q. Zhang, Y. Hu, J. Ge, Z. Lu, L. He, Z. Chen, Y. Yin, *Chemistry – A European Journal*, **2010**, *16*, 6243.

[10] D. Beydoun, R. Amal, G. K. C. Low, S. McEvoy, *The Journal of Physical Chemistry B*, **2000**, *104*, 4387.

[11] Y. Xia, P. Yang, Y. Sun, Y. Wu, B. Mayers, B. Gates, Y. Yin, F. Kim, H. Yan, *Advanced Materials*, **2003**, *15*, 353.

[12] Y. Cui, C. M. Lieber, *Science*, **2001**, *291*, 851.

[13] Z. L. Wang, J. Song, *Science*, **2006**, *312*, 242.

[14] G. R. Patzke, F. Krumeich, R. Nesper, *Angewandte Chemie International Edition*, **2002**, *41*, 2446.

[15] L.-Q. Mai, F. Yang, Y.-L. Zhao, X. Xu, L. Xu, Y.-Z. Luo, *Nat Commun.*, **2011**, *2*, 381.

[16] M. Rauber, I. Alber, S. Müller, R. Neumann, O. Picht, C. Roth, A. Schökel, M. E. Toimil-Molares, W. Ensinger, *Nano Letters*, **2011**, *11*, 2304.

[17] J. Shi, C. Sun, M. B. Starr, X. Wang, *Nano Letters*, **2011**, *11*, 624.

[18] K. Sun, Y. Jing, N. Park, C. Li, Y. Bando, D. Wang, *Journal of the American Chemical Society*, **2010**, *132*, 15465.

[19] D. Barreca, D. Bekermann, E. Comini, A. Devi, R. A. Fischer, A. Gasparotto, C. Maccato, C. Sada, G. Sberveglieri, E. Tondello, *CrystEngComm*, **2010**, *12*, 3419.

[20] F. Shao, J. Sun, L. Gao, S. Yang, J. Luo, *ACS Applied Materials & Interfaces*, **2011**, *3*, 2148.

[21] Z. Gu, M. P. Paranthaman, J. Xu, Z. W. Pan, *ACS Nano*, **2009**, *3*, 273.

[22] Y. Sun, J. Hu, N. Wang, R. Zou, J. Wu, Y. Song, H. Chen, H. Chen, Z. Chen, *New Journal of Chemistry*, **2010**, *34*, 732.

[23] T. Kim, E.-J. Cho, Y. Chae, M. Kim, A. Oh, J. Jin, E.-S. Lee, H. Baik, S. Haam, J.-S. Suh, Y.-M. Huh, K. Lee, *Angewandte Chemie International Edition*, **2011**, *50*, 10589.

[24] H. Zhou, S. Xiong, L. Wei, B. Xi, Y. Zhu, Y. Qian, *Crystal Growth & Design*, **2009**, *9*, 3862.

[25] H. Li, W. Li, Y. Zhang, T. Wang, B. Wang, W. Xu, L. Jiang, W. Song, C. Shu, C. Wang, *Journal of Materials Chemistry*, **2011**, *21*, 7878.

[26] J. Elias, C. Lévy-Clément, M. Bechelany, J. Michler, G.-Y. Wang, Z. Wang, L. Philippe, *Advanced Materials*, **2010**, *22*, 1607.

[27] Y. Lai, M. Meng, Y. Yu, X. Wang, T. Ding, *Applied Catalysis B: Environmental*, **2011**, *105*, 335.

[28] X. Yu, S. Liu, J. Yu, *Applied Catalysis B: Environmental*, **2011**, *104*, 12.

[29] D. Beydoun, R. Amal, G. Low, S. McEvoy, *Journal of Molecular Catalysis A: Chemical*, **2002**, *180*, 193.

[30] Y. Deng, D. Qi, C. Deng, X. Zhang, D. Zhao, *Journal of the American Chemical Society*, **2007**, *130*, 28.

[31] P. Shimpi, Y. Ding, E. Suarez, J. Ayers, P.-X. Gao, *Applied Physics Letters*, **2010**, *97*, 103104.

[32] Y. Gong, T. Andelman, G. F. Neumark, S. O'Brien, I. L. Kuskovsky, *Nanoscale Research Letters*, **2007**, *2*, 297.

[33] Y. Y. Tay, T. T. Tan, F. Boey, M. H. Liang, J. Ye, Y. Zhao, T. Norby, S. Li, *Physical Chemistry Chemical Physics*, **2010**, *12*, 2373.

[34] Y. H. Leung, A. B. Djurišić, Z. T. Liu, D. Li, M. H. Xie, W. K. Chan, *Journal of Physics and Chemistry of Solids*, **2008**, *69*, 353.

[35] Y. Tak, D. Park, K. Yong, "Characterization of ZnO nanorod arrays fabricated on Si wafers using a low-temperature synthesis method", **2006**, 24, 2047.

[36] G. Colón, M. C. Hidalgo, J. A. Navío, E. Pulido Melián, O. González Díaz, J. M. Doña Rodríguez, *Applied Catalysis B: Environmental*, **2008**, *83*, 30.

[37] F. Xu, Y. Shen, L. Sun, H. Zeng, Y. Lu, *Nanoscale*, **2011**, 3, 5020.

[38] J. Gupta, K. C. Barick, D. Bahadur, *Journal of Alloys and Compounds*, **2011**, *509*, 6725.

[39] Q. Wan, *Appl. Phys. Lett.*, **2005**, *87*, 083105.

[40] J. Liqiang, Q. Yichun, W. Baiqi, L. Shudan, J. Baojiang, Y. Libin, F. Wei, F. Honggang, S. Jiazhong, *Solar Energy Materials and Solar Cells*, **2006**, *90*, 1773.

[41] S. S. Warule, N. S. Chaudhari, B. B. Kale, M. A. More, *CrystEngComm*, **2009**, *11*, 2776.

[42] S. Baruah, *J. Appl. Phys.*, **2009**, *105*, 074308.

[43] J. Wang, P. Liu, X. Fu, Z. Li, W. Han, X. Wang, *Langmuir*, **2008**, *25*, 1218.

[44] Y. Zheng, C. Chen, Y. Zhan, X. Lin, Q. Zheng, K. Wei, J. Zhu, Y. Zhu, *Inorganic Chemistry*, **2007**, *46*, 6675.

[45] G. Xiong, U. Pal, J. G. Serrano, K. B. Ucer, R. T. Williams, *physica status solidi (c)*, **2006**, *3*, 3577.

Chapter 7

Other applications of nano-array integrated functional catalysts –water purification

7.1. Introduction

Ceramic monoliths, as one of the most popular 3D support substrate, are installed in almost every vehicle and power plant as support substrates in stationary and automobile catalytic exhaust emission control devices as a result of their high inertness to undesired reactions, low pressure drop, and enhanced mechanical and thermal stability.[1] However, usually the relatively low-surface-area monoliths will need a high surface area porous alumina particulate wash coat to help increase their surface area before or while loading the catalytically active materials such as noble metal nanoparticles. The intrinsically non-adherent particle-based wash coat may be easily subjected to high velocity flow erosion. The *in situ* grown nanostructured catalysts could enable enhanced thermal and mechanical robustness as well as improved catalytic efficiency.[2]

As an important catalyst support, titania (TiO_2) has been extensively studied. V_2O_5/TiO_2 has been suggested as one of the better catalysts for NO reduction under NH_3 for industrial power plants.[1,2] Latest research results demonstrate that the addition of TiO_2 to the conventional alumina wash coat support increases the NO_x absorber catalysts' sulfur tolerance, which is very important to enhance the catalysts' performance and lifetime.[3,4] TiO_2 has three polymorphs of different symmetries, including anatase, rutile and brookite, all of which can be described in terms of distorted TiO_6 octahedra with different symmetries or arrangements.[5,6] Anatase and rutile structures have been extensively studied, while the brookite structure is much less studied due to its lack in natural TiO_2 phases. Anatase TiO_2nanoparticles could be achieved with 200–

300 $m^2 g^{-1}$ high surface area by hydrolysis of an organic titanium compound such as tetraisopropyl titanate in aqueous solution.[1] Brookite or rutile structured TiO_2 is normally believed to have low surface area compared to anatase TiO_2 despite the higher thermal stability due to the difficulty for their fine structure synthesis.

In addition to the nanoparticles form, TiO_2 in the forms of nanorods, nanowires, and nanotubes have attracted extensive attention in the past two decades as a result of their unique shape-dependent electronic and optical properties[7–9] as well as their widespread applications in batteries,[10] solar cells,[11] sensors[12] and catalysis.[13] However, the crystal structure and symmetry of TiO_2 make the growth of oriented anisotropic single-crystalline TiO_2 films or nanorod arrays very difficult.[14] To date, there are only a few reports that describe heterogeneous growth of oriented single-crystalline TiO_2 nanorods or nanowires, but most growths are restricted to fluorine-doped tin oxide (FTO) substrates.[14,15] The growth process and mechanism of well-defined brookite TiO_2 nanorod arrays on 3D monoliths with confined space are not well understood. In addition, most heterogeneous growths rely on vapor phase techniques utilizing heterogeneous nucleation at very high growth temperatures.[16,17] Compared to the vapor deposition technique, solution-based methods are more suitable for low-cost commercial scale-up production.

In this work, we report a simple hydrothermal synthesis procedure which allows the one-step, large scale anisotropic growth of aligned, crystalline brookite TiO_2 nanorod arrays on the channel walls of 3D honeycomb monoliths. With the increase of hydrothermal treatment time, the brookite nanostructure morphology was identified to evolve from dispersive dandelion TiO_2 nanorod clusters to vertically aligned nanorod arrays fully covered on the monolith substrate. Based on the observation of the growth process, a possible heterogeneous nucleation–

dissolution–crystallization growth mechanism was proposed. The scale-up synthesis of TiO_2 nanorod arrays inside the 3D honeycomb monoliths enables a new type of 3D hybrid nanostructured catalyst support, which shows a great potential as a continuous flow fixed-bed absorbent for waste water treatment. The new type of as-prepared monolithic device also holds the potential for applications in various areas including catalyst supports, particulate matter filters, and environmental remediation and separation devices.

7.2. Experimental section

7.2.1. Chemicals

The dilute solution of $TiCl_3$ (0.15 M) was supplied by Spectrum Chemical MFG. Corp. Sodium chloride (NaCl) was purchased from Fisher Scientific. All chemicals are used directly after purchase without further purification. Cordierite monolith substrates were supplied by Honda Research Institute (Columbus, OH).

7.2.2. Preparation of TiO_2 nanorod arrays on ceramic monoliths

Nanostructured brookite TiO_2 was synthesized by hydrothermal treatment of aqueous titanium trichloride ($TiCl_3$) solutions with saturated sodium chloride (NaCl) (concentration around 5 M). Typically, 20 ml of the precursor solution, including 2 ml of $TiCl_3$ solution and 18 ml of deionized (DI) water saturated with NaCl, was placed in a Teflon-lined autoclave. Honeycomb cordierite monoliths were used as substrates and were put in the solutions. The solutions were then heated at 180 °C for 1–24 h. Then, the autoclave was cooled to room temperature. The honeycomb monoliths were taken out, rinsed thoroughly with deionized water and allowed to dry on a hot plate at 80 °C.

7.2.3. Organic dye contaminant removal from water

Adsorption tests were carried out using Rhodamine B (RhB) as the contaminant and TiO_2 nanorod-array coated monolith in a fixed absorbent bed in a continuous flow system. In the experiments, 1 mg RhB was dissolved in 250 ml de-ionized (DI) water to make an organic dye contaminated water (8.4×10^{-6} M). 10 ml RhB/water was used for the demonstration experiment. A syringe pump was used to control the flow rate at 1 ml min^{-1}. The absorbent bed contains 9 pieces of TiO_2 nanorod array coated monoliths with a total length of 9 cm. The total space velocity is ~167 h^{-1}. The concentration change of RhB solution after different numbers of treatment cycles was recorded by a UV-vis-NIR absorption spectrometer (PerkinElmer) to investigate the efficiency of the RhB removal process. All tests were carried out at room temperature, ~25 °C.

7.2.4. Characterization

The morphologies of the synthesized TiO_2 nanostructures were characterized by field-emission scanning electron microscopy (FESEM; JEOL 6335F Field Emission SEM) equipped with a Thermo Noran EDS detector, and by high-resolution transmission electron microscopy (HRTEM; JEOL 2010 FasTEM). The crystal structures were examined by X-ray diffraction (XRD) analysis with a Rigaku Mini Flex II Desktop X-ray Diffractometer. The BET surface area was characterized using a Quanta chrome Corporation NoVA 1000 Gas Sorption Analyzer and Micromeritics ASAP 2020 physisorption analyzer. The thermal stability of samples was investigated using a TA instruments SDT Q600.

7.3. Results and Discussion

Figure 7.1 shows a set of optical and scanning electron microscopy (SEM) images of 3D cordierite monolith and the TiO_2 nanorod arrays synthesized inside the monolith channels by

hydrothermal treatment of aqueous titanium trichloride ($TiCl_3$) solutions with saturated sodium chloride (NaCl) at 180 °C for 4 h. Figures 7.1a and 7.1b display the top view cross section of the monolith. The monolith has a cell density of 400 cells per square inch with a wall thickness of ~0.1 mm. Figure 7.1c shows the side view SEM images of the monolith. It can be clearly seen that the wall surface of the monolith is not a flat surface, but with certain porosity. The EDS analysis reveals the monolith to be of Si, Mg, Al, and Nb. The grown TiO_2 nanorods are highly aligned and densely packed on the monolith substrate with a diameter of ~50 nm and a length of ~250 nm (Figure 7.1c and 7.1d).

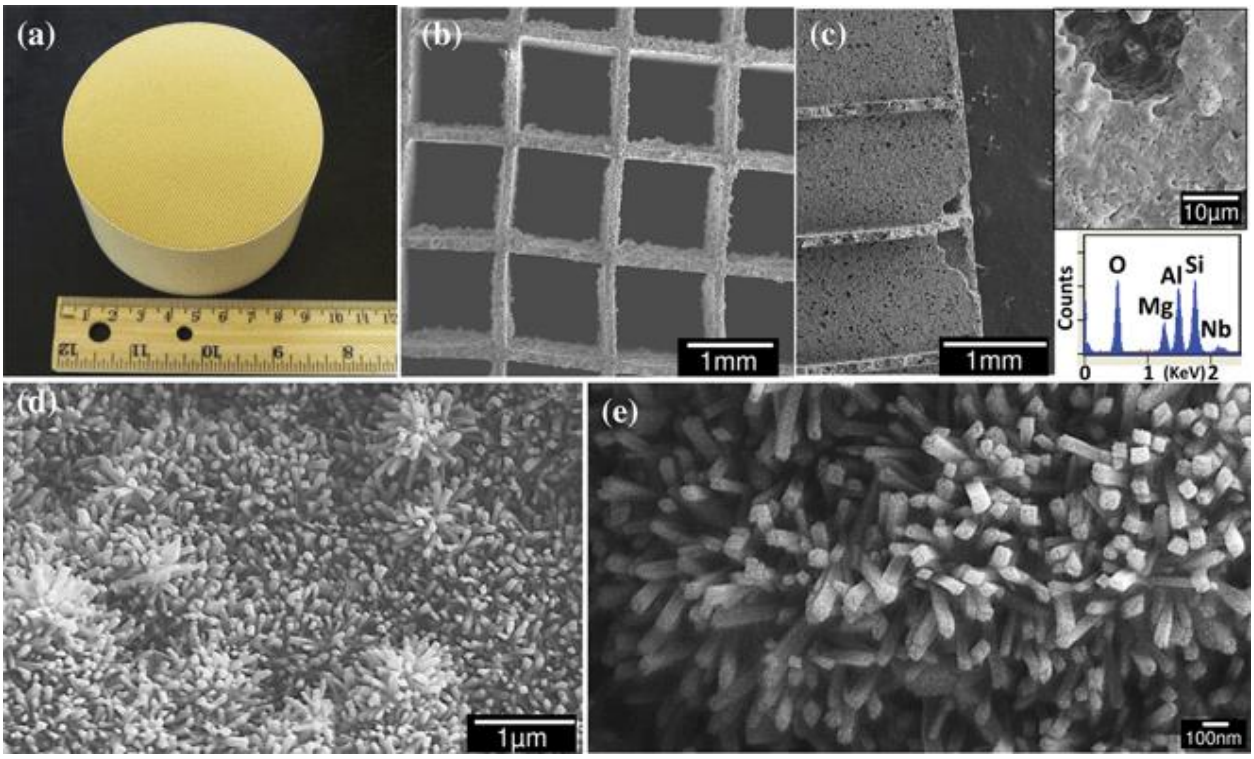

Figure 7.1 Top view optical (a) and SEM (b) images of the honeycomb monolith. (c) Side view SEM images of the honeycomb monolith and the corresponding EDX spectrum. (d and e) SEM images of TiO_2 nanorod arrays grown using 2 ml of $TiCl_3$, and 18 ml of NaCl-saturated DI water at 180 °C for 4 h on the 3D honeycomb monolith.

To investigate the growth behavior of TiO_2 nanorods inside the 3D cordierite monolith, hydrothermal treatment times of 1, 1.5, 2, 4 and 24 h were applied and the evolution of TiO_2 nanostructures was examined by SEM imaging analysis (Figure 7.2). With 1 h growth time, no obvious TiO_2 nanostructures grew on the wall surface of the monolith, as indicated in the SEM image in Figure 7.2a. Prolonging the reaction time to 1.5 h, the TiO_2 nanorod clusters were grown on the wall surface with a dandelion-like morphology with diameters in the range of 250–350 nm (Figure 7.2b). The TiO_2 nanorod clusters consisted of many close-packed TiO_2 nanorods grown in a radial outwards direction.

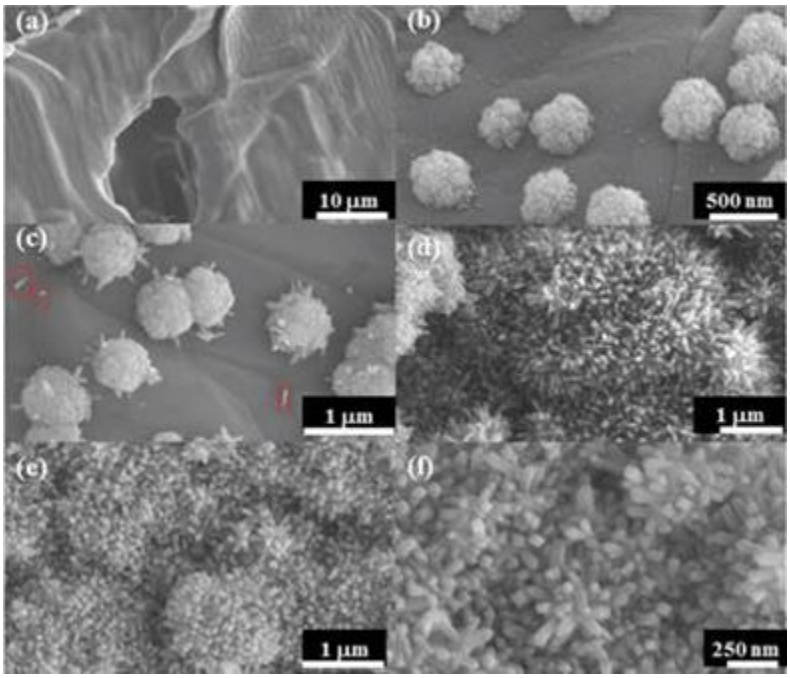

Figure 7.2. SEM images of TiO_2 nanostructures grown on 3D honeycomb monolith using 2 ml of $TiCl_3$, and 18 ml of NaCl-saturated DI water at 180 °C for different times. (a) 1, (b) 1.5, (c) 2, (d) 4, and (e, f) 24 h. Single TiO_2 nanorods were also found on the substrate surface when the hydrothermal treatment time is 2 h, as indicated by the boxes in (c).

Further prolonging the reaction time to 2 h, the TiO_2 nanorod clusters grew even bigger with diameters in the range of 400–500 nm (Figure 7.2c). At high magnification (Figure 7.2c), some

nanorods in the TiO_2 nanorod clusters grew longer than the others and clearly out of the dandelion-like sphere surface. More interestingly, some individual TiO_2 nanorods directly grew out of the substrate surface as indicated by the boxes in Figure 7.2c. When the reaction time increased to 4 h, highly aligned TiO_2 nanorod arrays grew on the cordierite substrate surface. Figure 7.2d shows the SEM image taken on an extremely rough surface of the substrate. It certainly confirmed the TiO_2 nanorods grew everywhere on the monolith surface, even on the porous surface in the substrate. When further increasing the reaction time to 24 h, no obvious morphology change was observed on the TiO_2 nanorod arrays.

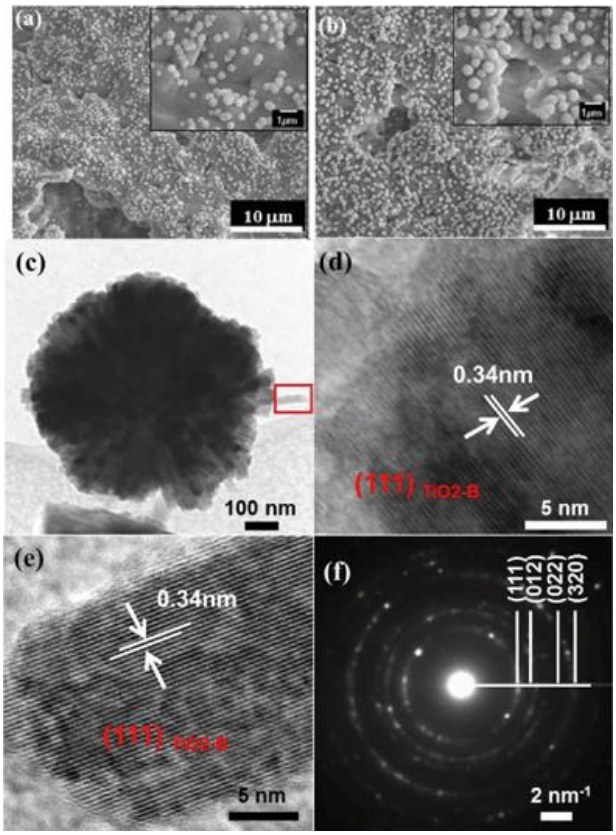

Figure 7.3. SEM images of the dandelion-like TiO_2 nanorod clusters inside the 3D honeycomb monolith grown at 180 °C for 1.5 h (a) and 2 h (b). (c) Low magnification and (d, e) high magnification (d: body part; e: tip part) TEM images of a dandelion-like TiO_2 nanorod cluster grown inside the 3D honeycomb monolith at 180 °C for 2 h. (f) ED pattern of the TiO_2 nanorod

cluster. The distance between the lattice fringes in (d–e) is 0.34 nm, which can be assigned to brookite (111).

As shown by the low magnification SEM images in Figure 7.3a and 7.3b, the TiO_2 nanostructures dispersively grew on the monolith after hydrothermal treatment for 1.5 and 2 h (Figure 7.3a and 7.3b), which confirms that the dandelion TiO_2 nanorod clusters grow all over the substrate with a very uniform distribution. The TiO_2 nanorods assembly and morphology were further characterized by transmission electron microscopy (TEM). Figure 7.3c shows the low-resolution TEM image of a typical TiO_2 nanorod cluster grown for 2 h. The dandelion-like sphere morphology and an out-grown TiO_2 nanorod (indicated in the box) were clearly identified. The diameter of the single TiO_2 nanorod is about 8–10 nm. The high-resolution TEM images in Figure 7.3d and 7.3e revealed the body and top portions of the TiO_2 nanorods, respectively. A clear set of lattice fringes was revealed with 0.34 nm spacing, suggesting the single crystalline nature of the grown TiO_2 nanorods. The electron diffraction (ED) pattern (Figure 7.3f) in a distinct ring form confirms the brookite structure of grown TiO_2 nanorods after 2 h hydrothermal treatment. The lattice fringes spacing of 0.34 nm can be assigned to the interplanar distance of single crystalline brookite TiO_2 (111).

Figure 7.4a shows the low-resolution TEM image of TiO_2 nanorods grown inside the 3D honeycomb monolith for 4 h. Compared with the TEM image of Figure 7.3c, no TiO_2 nanorod clusters were found when the hydrothermal treatment time was 4 h, indicating the conversion of dandelion-like TiO_2 nanorod clusters into aligned TiO_2 nanorod arrays. Figure 7.4b and 7.4c show the high-resolution TEM images of the body and top portions of a typical TiO_2 nanorod. The atomic planes corresponding to (111) are clearly visible with the same

interplanar distance of 0.34 nm, suggesting the single crystalline nature of the brookite TiO_2 nanorods grown after hydrothermal treatment for 4 h.

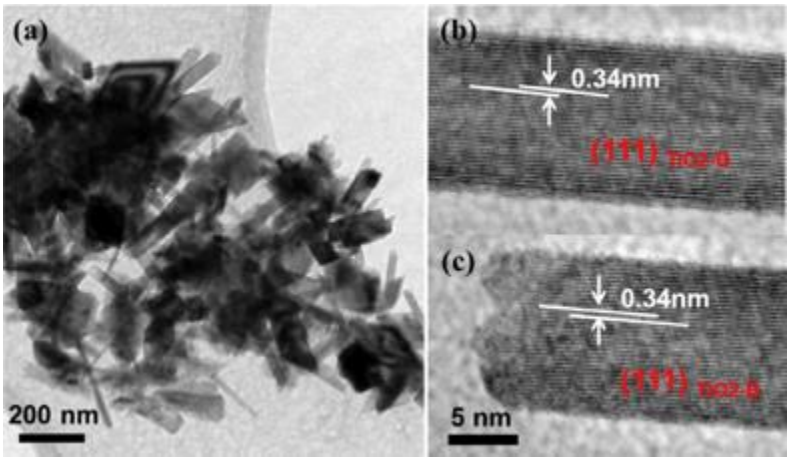

Figure 7.4. (a) Low-resolution TEM image of the TiO_2 nanorods grown inside the 3D honeycomb monolith at 180 °C for 4 h. (b, c) High-resolution TEM image of the body portion and top portion of one grown TiO_2 nanorod, respectively.

The brookite crystal structure of the grown TiO_2 nanorods at different hydrothermal treatment times was further confirmed by X-ray diffraction (XRD) analysis. Figure 7.5 shows the XRD patterns of the bare honeycomb monolith and the synthesized TiO_2 nanostructures inside the honeycomb monolith. Since the honeycomb monolith is a mixed oxide cordierite of SiO_2, MgO, Al_2O_3 and Nb_2O_5, some characteristic peaks of the honeycomb monolith overlap with the diffraction peaks of brookite TiO_2. As shown in Figure 7.5, when the hydrothermal time is less than 4 h, no obvious TiO_2 diffraction peaks appeared in the corresponding XRD pattern, although the TiO_2 nanorod clusters were obtained on the substrate surface according to the SEM imaging (Figure 7.3a and 7.3b). This might be due to their dispersive distribution (Figure 7.2b and 7.2c), and the extremely strong intensity from the exposed monolith substrate.

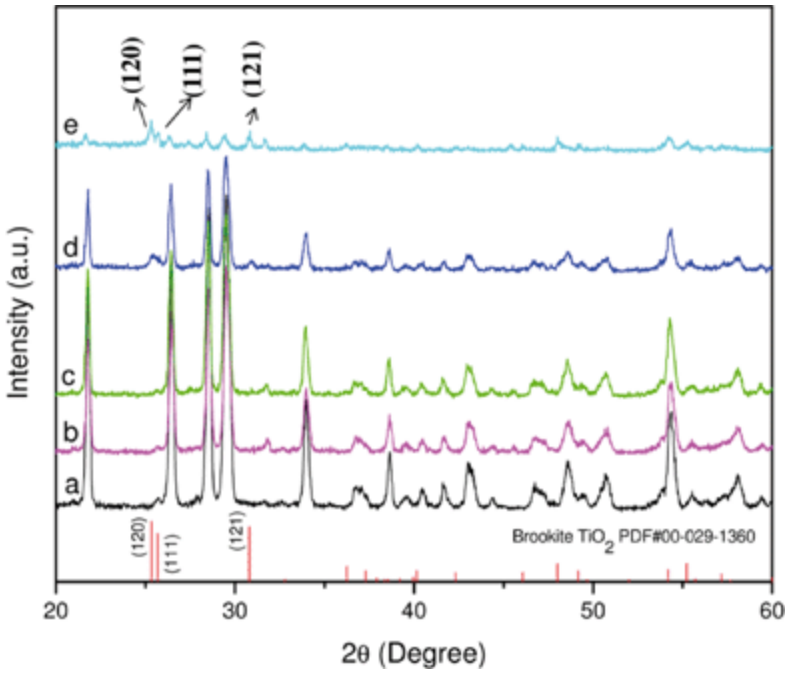

Fig. 7.5. XRD patterns of (a) the honeycomb monolith, and the samples of TiO_2 nanorods grown inside the 3D honeycomb monolith prepared at 180 °C for (b) 1.5, (c) 2, (d) 4, and (e) 24 h.

However, with increasing hydrothermal time, the weakening intensities from the substrate is accompanied by the enhanced intensities from the brookite TiO_2. As the hydrothermal treatment time increased to 4 h, two weak peaks appeared at about 25.4° and 25.7° corresponding to brookite (120) and (111), respectively (JCPDS No. 00-029-1360), which do not overlap with any diffraction peaks of the substrate. As the hydrothermal treatment time further increased to 24 h, the peaks in brookite (120) and (111) became more significant with higher intensities than those of substrate, suggesting a complete coverage of TiO_2 nanorod arrays on monolith as well as the further improved crystallinity.

Brookite TiO_2 with different morphologies has been reported in the literature. For example, Cozzoli *et al.* synthesized anisotropically shaped brookite TiO_2 nanocrystals using a surfactant-assisted nonaqueous strategy.[18] A self-regulated phase-switching seed-catalyzed mechanism was proposed to explain the heterogeneous nucleation of brookite TiO_2 on the initially generated *c*-

axis-elongated anatase TiO_2, and the anatase-to-brookite conversion. Sun *et al.* prepared high-quality brookite TiO_2 flowers in the presence of NaOH by a solution chemistry technique.[19] They proposed three steps for the synthesis of flower-like brookite TiO_2: (1) the transformation of layer structured titanate into brookite nanoparticles, (2) the evolution of brookite particles to the spindle-like shape, and (3) the assembly of these spindle-like particles into flower-like TiO_2. Obviously, the formation of the aligned TiO_2 nanorod arrays on the 3D honeycomb monolith could be different from these mechanisms. According to our time-dependent morphology evolution evidence (Figure 7.2–7.4), we could hypothesize that the formation of multi-nanostructures and morphology evolution from dandelion TiO_2 nanorod clusters to aligned nanorod arrays can be rationally expressed as a heterogeneous nucleation–dissolution–crystallization mechanism (Scheme 7.1). Generally, titanium tetrachloride ($TiCl_4$) or titanium alkoxides ($Ti(OR)_4$) are used as a titanium source to synthesize TiO_2. However, the reaction rate of Ti(IV) in forming TiO_2 is too fast. A high degree of supersaturation is obtained due to the production of many nuclei in the solution, which accelerates the homogeneous nucleation to produce TiO_2 nanoparticles. In our study, a low degree of supersaturation was achieved by using $TiCl_3$ as the titanium precursor due to the slow oxidation of Ti(III) by dissolved oxygen.

The low degree of supersaturation promotes the heterogeneous nucleation of TiO_2 on the wall surface of the honeycomb monolith.[20,21] Furthermore, a high concentration of chlorine ions in the solution helps the formation of brookite TiO_2, and also avoids the conversion of brookite into rutile after prolonging the hydrothermal treatment time.[22] The brookite structure was obtained at the very beginning of the reaction (Figure 7.3) and prolonging the reaction time from 4 h to 24 h does not change the brookite structure but improves its crystallinity (Figure 7.5). With the increase in hydrothermal time, the hydrothermal conditions changed into more acidic, which

might make the not well-crystallized TiO_2 nanorods dissolve and the dissolved TiO_2 in the solution might nucleate onto the existing nanorods, which is confirmed by the change of TiO_2 morphology from closely packed nanorod clusters to sparsely aligned arrays.

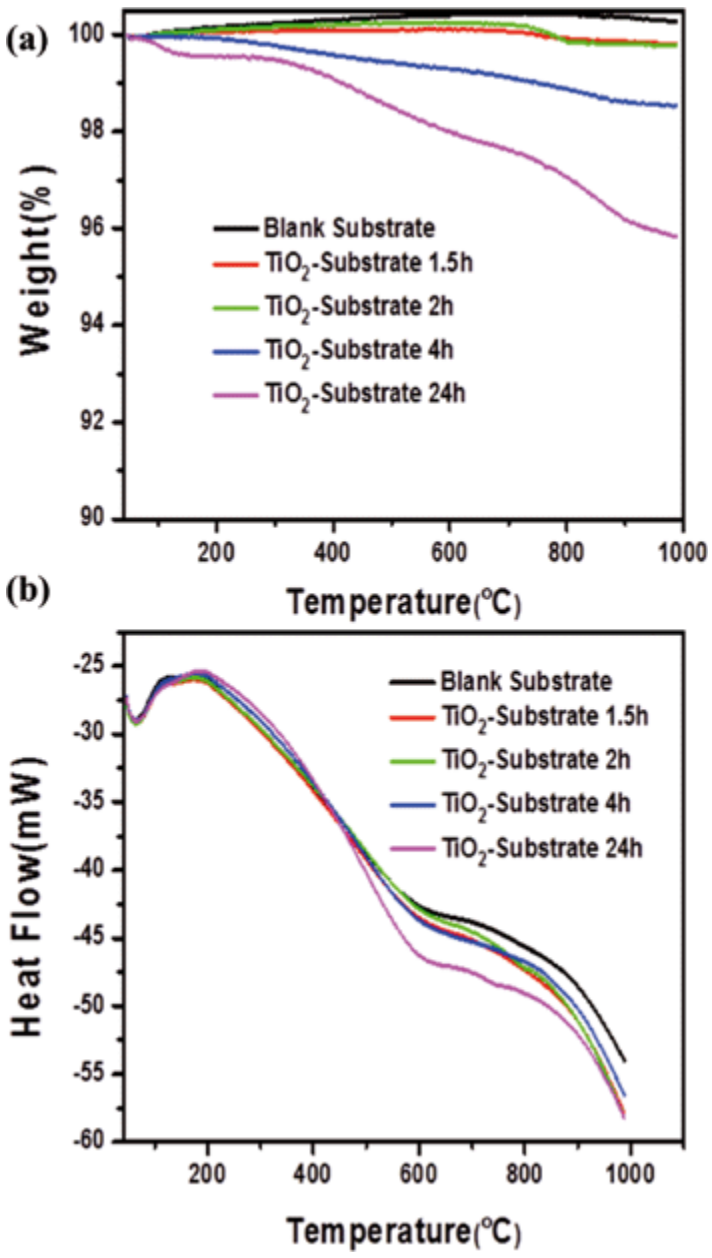

Figure 7.6. TGA (a) and DSC (b) spectra of TiO_2 nanorods grown inside the 3D honeycomb monolith prepared at 180 °C for 1.5 h, 2 h, 4 h, and 24 h.

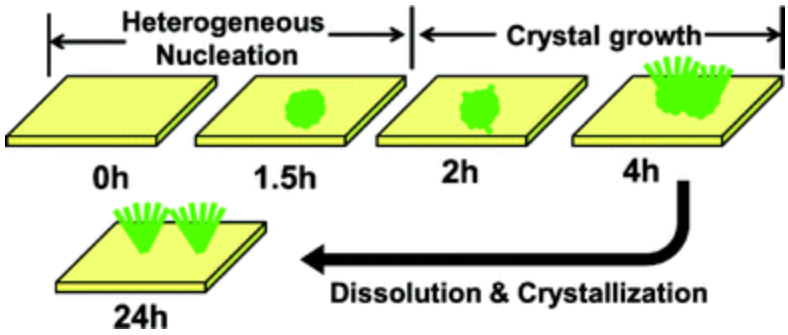

Scheme 7.1. The as-proposed TiO_2 heterogeneous nucleation–dissolution–crystallization growth mechanism.

To investigate the thermal stability of TiO_2 nanorod arrays coated hybrid monolith substrates, thermogravimetric analysis (TGA) and differential scanning calorimetry (DSC) were carried out in ambient conditions. The TGA and DSC curves are plotted in Figure 7.6. Blank honeycomb monolith substrate is very stable over the whole investigated temperature range. During the thermal analysis, different samples exhibit different degrees of weight loss. TiO_2 samples grown for 1.5 and 2 h show a similar weight loss with less than 1% in total. That is possibly due to their similar cluster morphology and relatively low density distribution. TiO_2 nanorod arrays grown for 4 h have less than 2% weight loss, while the TiO_2 nanorod arrays grown for 24 h have the highest weight loss of 3.5%. However, the highest weight loss is just about 3%, which suggests that TiO_2 nanorods arrays on the honeycomb monolith substrates are very stable in the temperature range of 20–800 °C.

The weight loss in the temperature range of 40–250 °C, about 2% for the sample grown for 24 h, is attributed to the evaporation of H_2O absorbed in the TiO_2 nanorods arrays. The peak at 700–800 °C might be contributed by the phase transition of TiO_2 nanorods from brookite structure to rutile structure. Clearly, the main weight loss is contributed by the loss of H_2O absorbed on TiO_2.

All DSC data exhibit almost the same plot, further proving that the main mass loss is caused by loss of H_2O.

To further investigate the thermal stability of TiO_2 nanorod arrays coated hybrid monolith substrates, isothermal annealing was conducted on as-prepared samples at 800 °C for 24 h. Mass loss *vs.*time spectra shown in Figure 7.7a depicts the *in situ* weight change in the isothermal process. After less than 2% weight loss, which has been proved by TGA–DSC tests to be the evaporation of absorbed H_2O on hybrid monolith substrate, there is almost no weight loss during the 800 °C isothermal annealing in air. Morphology after the high temperature aging was also investigated by SEM. As shown in Figure 7.7b, the nanorod array structure was retained very well with no observable morphology change for the individual nanorods. Moreover, there is also no obvious crack on the coated TiO_2 nanorod array in the large area under lower magnification. All the isothermal aging test results confirmed that the as-prepared TiO_2 nanorod arrays coated hybrid monolith substrates have very high thermal stability in air.

In the real world application, surface coating layers are inevitably exposed to humidity in the environment, contacting with either liquid water or steam. The hydrothermal stability of TiO_2 nanorod arrays coated hybrid monolith substrates at extreme conditions will be very helpful to evaluate the steam-related stability. In our experiments, we put TiO_2 nanorod arrays coated hybrid monolith substrates directly into a sealed autoclave filled with half volume of DI water. Then, we put the autoclave into an oven and sustained the temperature at 120 °C for 24 h after reaching 120 °C at a ramp rate of 1 °C per minute. The morphology of TiO_2 nanorod arrays after hydrothermal aging are displayed in Figure 7.7c and Figure 7.7d, which clearly show the densely packed and uniform nanorod array. It proved that the TiO_2 nanorod arrays coated hybrid

monolith substrates are quite stable at extreme hydrothermal conditions and show great promise for steam-related applications.

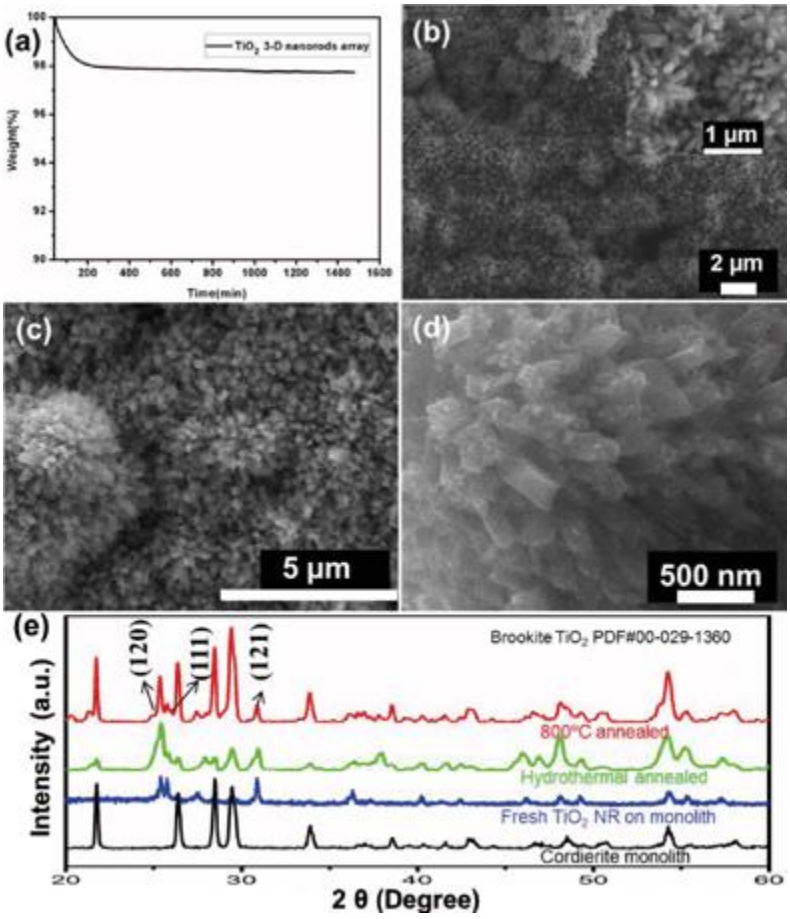

Figure 7.7. (a) Mass loss *vs.* time spectra of TiO_2 nanorods array during 800 °C 24 h annealing; (b) SEM image after 800 °C 24 h annealing; inset is the high magnification image; TiO_2 nanorods array after aging in boiling DI water at 120 °C for 24 h: SEM images of low magnification (c) and high magnification image (d); (e) XRD spectra of cordierite monolith, fresh TiO_2 nanorod arrays on monolith, hydrothermally aged TiO_2 nanorod arrays on monolith, and 800 °C annealed TiO_2nanorod arrays on monolith.

To further investigate the structural stability of TiO_2 nanorod arrays during the harsh thermal and hydrothermal treatments, the XRD spectra were compared for the fresh sample, 800 °C isothermal aging sample and 120 °C hydrothermal aging sample. Figure 7.7e revealed the

characteristic peaks at 25.4°, 25.7° and 30.8°, matching to brookite TiO_2 (120), (111) and (121) respectively (JCPDS No. 00-029-1360), which were retained very well after the 24 h high temperature thermal and hydrothermal aging. The XRD spectra directly proved the good thermal and hydrothermal stability of the as-prepared single crystal brookite TiO_2 nanorod array on cordierite monolith.

Table 7.1 Multi-point nitrogen adsorption BET specific surface area of TiO_2 nanorods grown honeycomb monolith substrate

	blank	TiO_2 substrate (1.5 h)	TiO_2 substrate (2 h)	TiO_2 substrate (4 h)	TiO_2 substrate (24 h)	HCl control sample
Surface area(m^2/g, with substrate)	0.3	0.5	8.6	44.1	58.8	0.2
Surface area(m^2/g, without substrate)	0	0	34.9	184.2	245.6	0

Surface area (with substrate) is experimental data collected by using a Micromeritics ASAP 2000, while BET surface area (without substrate) is estimated data which was calculated from the surface area (with substrate) by subtracting the contribution of monolith substrate. The calculation was performed according to the following rule:
a) Assuming $TiCl_3$ was completely converted into TiO_2 grown on the substrate;
b) For growth time shorter than 4 h, the TiO_2 nanorods array did not completely cover the substrate from SEM, $S = (S_{TiO2\ substrate} \times m_{TiO2\ substrate} - S_{Blank\ substrate} \times m_{TiO2\ substrate})/m_{TiO2}$;
c) For growth time longer than 4 h, TiO_2 nanorods array completely covered the substrate from SEM, $S = S_{TiO2\ substrate} \times m_{TiO2\ substrate}/m_{TiO2}$.

In the meantime, we investigated the specific BET surface area of TiO_2 nanorod arrays on honeycomb monolith grown for different times (Table 7.1). In our experiment, TiO_2 nanostructures grown for 1.5 h have the lowest BET surface area. That may be caused by the lowest coverage of TiO_2 nanorod clusters on the monolith substrate. BET surface area of TiO_2 nanostructures grown for 2 h is a little bit larger than that of the sample synthesized for 1.5 h. This could be attributed by the higher aspect ratio of single nanorod grown out of the

nanoclusters and higher TiO_2 coverage on the monolith. Though having similar nanorod array structure, the BET surface area of the TiO_2 nanostructure grown for 24 h is bigger than the sample grown for 4 h, which is because of the larger aspect ratio of TiO_2nanorods with increasing growth time. As shown in Table 7.1, the specific surface area of honeycomb monolith substrate increases after the deposition of TiO_2 nanorods. With the increasing growth time, the surface area increases drastically. It is worth noting that the grown TiO_2 nanorod arrays has a specific surface area as high as ~240 $m^2 g^{-1}$, ~3 times higher than the normal hydrolysis-derived anatase TiO_2 nanoparticles.[23–25]

As it is demonstrated, during the TiO_2 growth process, the precursor solution is very acidic with the pH value of ~1. It is reasonable to infer that after *in situ* growing the TiO_2 nanorod array, the increment of surface area may arise from two factors: 1) the surface area of coated TiO_2 nanorod array; 2) the net surface area increase of monolith substrate due to the acidic environment in TiO_2nanorod array growth. To shed light on the origin of the high surface area, control experiments were conducted by using HCl, NaCl and water as precursors. In the control experiments, the pH value was controlled as the theoretical value of $TiCl_3$ totally decomposed in the TiO_2 nanorod array growth process by adding HCl drop by drop. BET surface area was tested after complete drying of controlled samples overnight on an 80 °C hotplate. The BET surface area falls into the range below 1 $m^2 g^{-1}$ and is around 0.2 $m^2 g^{-1}$. It suggests that the surface area change induced by the acid etching during TiO_2 nanorod array growth is negligible. We can conclude that the main contributor of the high surface area monolithic device is the high surface area TiO_2 nanorod array grown on it.

With the characteristic of ultra-high surface area, the as-prepared catalytically active TiO_2 nanorod arrays on monolith might serve as an efficient absorbent in environmental remediation applications.[13] Furthermore, the merit of low pressure drop for monolithic devices enables its usage in a continuous flow system, which is more applicable in realistic large scale water treatment processes due to its low operating cost and good adaptability to versatile processes such as waste pipelines of industrial plants.[26] To confirm this potential, a proof-of-concept demonstration was carried out for the TiO_2 nanorod array coated monolith to be used as an absorbent device for water treatment using Rhodamine B (RhB) as the organic dye contaminant in water. Figure 7.8a illustrates the experimental setup for monolith-based fixed bed absorbents in a continuous flow treatment system. Specifically, in the lab scale demonstration, 10 ml RhB solution (8.4×10^{-6} M) flowed through the TiO_2 nanorod array coated monolithic absorbent bed with the flow rate of 1 ml min^{-1}, as controlled by a syringe pump (Figure 7.8b). The monolithic absorbent bed is composed of 9 pieces of vertically aligned monoliths with a length of 9 cm and cross-sectional area of 0.04 cm^2, and the space velocity is around 167 h^{-1} during the test. The UV-vis absorption peak intensity of RhB solution decreases with the increasing number of treatment cycles, with 45% of the original intensity after 12 cycles (Figure 7.8d). As a control sample, the bare monolithic substrate was also tested under the same experimental conditions. No concentration change (Figure 7.8e) was detected throughout the 12-cycle absorption treatment on the bare cordierite monolith sample. This suggests no absorption of RhB on bare monolith. However, a significant absorption was observed on the TiO_2 nanorod array coated monolith sample. The concentration of RhB solution drops quickly at the first 5 cycles, while the absorption after 5 cycles is slower than the first 5 cycles but the saturation is

not reached even after 12 cycle treatments, proving its potential as a highly efficient absorbent for industrial waste after treatment including, but not limited to, water treatment.

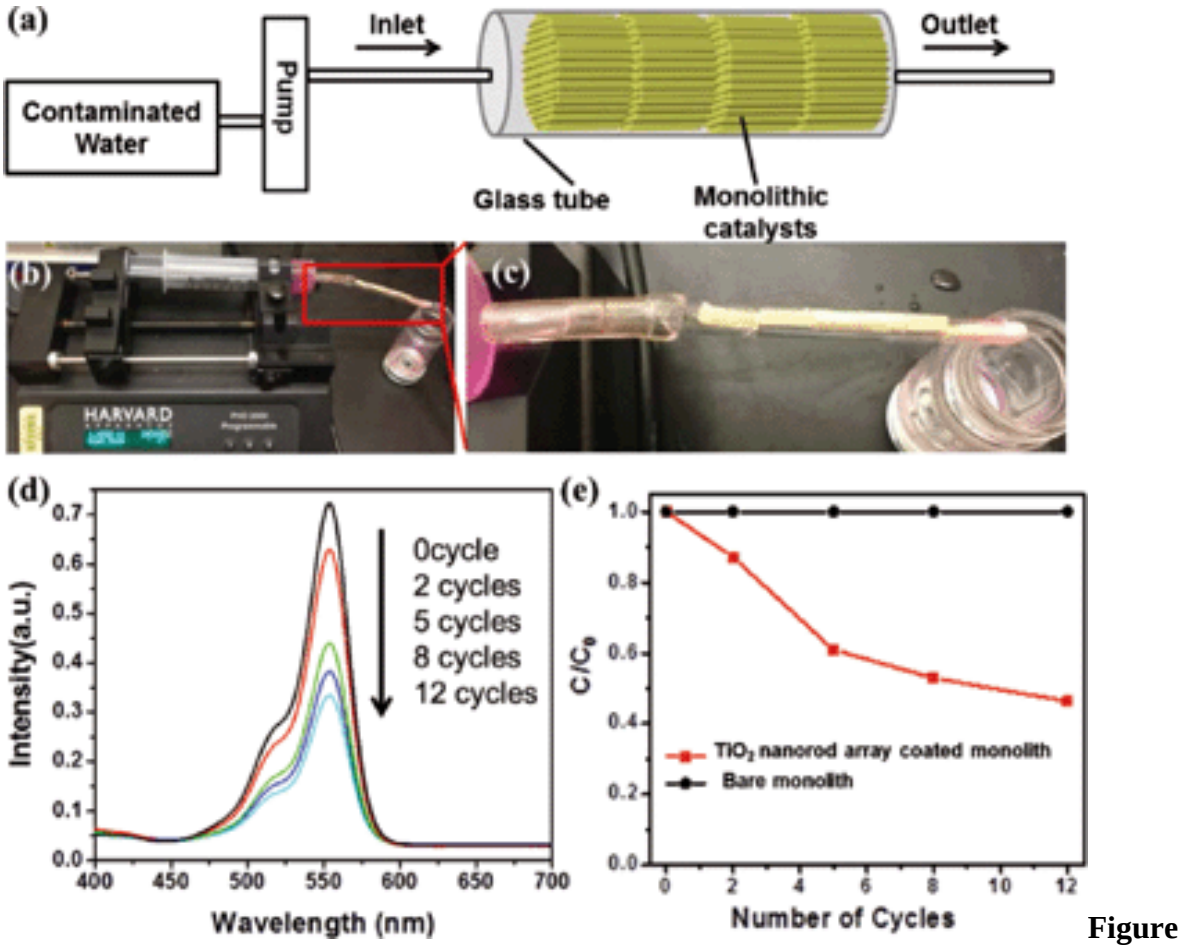

Figure 7.8. Proof-of-concept demonstration of the 3D TiO_2 nanorod arrays coated monolith as an adsorbent in an environmental application for the remediation of a dye pollutant in water: (a) schematic illustration of a continuous flow testing system; (b) photograph of the testing setup used for the demonstration experiment; (c) photograph of TiO_2 nanorod array coated monolith absorbent bed; (d) UV-vis absorption spectra of the RhB solutions after different number of fixed-bed flow adsorption cycles; (e) normalized concentration as a function of the number of flow adsorption cycles for a fresh TiO_2 nanorod array coated monolith absorbent and bare monolith control sample.

7.4. Conclusions

In summary, single crystalline brookite TiO_2 nanorod arrays were grown uniformly on the inner walls of a 3D honeycomb monolith by a hydrothermal approach. The evolution of TiO_2 nanorod clusters to TiO_2 nanorod arrays were observed while changing the hydrothermal treatment time. Slow oxidation of Ti(III) to Ti(IV) results in the maintenance of a low degree of supersaturation, which promotes the heterogeneous nucleation of brookite TiO_2 on the wall surface of the honeycomb monolith. In addition, the presence of excess Cl^- helps the formation of brookite TiO_2 and maintains the brookite crystal structure. The synthesized TiO_2 nanorods-based hybrid monolithic devices have high surface area and good thermal and hydrothermal stability. A proof-of-concept TiO_2 nanorod-array coated monolithic device was demonstrated with a promising performance as a continuous flow fixed-bed absorbent in water treatment. The ultra-high surface area and excellent stability make the as-prepared TiO_2 nanorod array monolithic devices promising for use in various energy and environmental applications such as emission control, industrial filtering, purification, and separation.

7.5. Reference

[1] C. W. Satterfield, *Heterogeneous Catalysis in Industrial Practice*, 2nd Edition, McGraw-Hill, Inc., New York, 1991.

[2] Y. Guo, Z. Ren, W. Xiao, C. Liu, H. Sharma, H. Gao, A. Mhadeshwar and P.-X. Gao, *Nano Energy*, 2013, **2**, 873-881

[3] J. Despres, M. Koebel, O. Kröcher, M. Elsener and A. Wokaun, *Appl. Catal., B*, 2003, **43**, 389–395

[4] S. M. Andonova, G. S. Sentürk and E. Ozensoy, *J. Phys. Chem. C*, 2010, **114**, 17003–17016

[5] M. R. Hoffmann, S. T. Martin, W. Choi and D. W. Bahnemann, *Chem. Rev.*, 1995, **95**, 69–96

[6] M. Gateshki, S. Yin, Y. Ren and V. Petkov, *Chem. Mater.*, 2007, **19**, 2512–2518

[7] A. P. Alivisatos, *Science*, 1996, **271**, 933–937

[8] Z. W. Pan, Z. R. Dai and Z. L. Wang, *Science*, 2001, **291**, 1947–1949

[9] P. D. Yang, H. Q. Yan, S. Mao, R. Russo, J. Johnson, R. Saykally, N. Morris, J. Pham, R. R. He and H. J. Cho, *Adv. Funct. Mater.*, 2002, **12**, 323–331

[10] L. Kavan, M. Grätzel, S. E. Gilbert, C. Klemenz and H. J. Scheel, *J. Am. Chem. Soc.*, 1996, **118**, 6716–6723

[11] B. Oregan and M. Grätzel, *Nature*, 1991, **353**, 737–740

[12] N. Wu, S. Wang and I. A. Rusakova, *Science*, 1999, **285**, 1375–1377

[13] Y. Guo, Z. Zhang, H. Gao, Z. Ren and P.-X. Gao, *Catal. Today*, 2012, **184**, 178–183

[14] B. Liu and E. S. Aydil, *J. Am. Chem. Soc.*, 2009, **131**, 3985–3990

[15] X. Feng, K. Shankar, O. K. Varghese, M. Paulose, T. J. Latempa and C. A. Grimes, *Nano Lett.*, 2008, **8**, 3781–3786

[16] C. C. Weng, K. F. Hsu and K. H. Wei, *Chem. Mater.*, 2004, **16**, 4080–4086

[17] C. A. Chen, Y. M. Chen, A. Korotcov, Y. S. Huang, D. S. Tsai and K. K. Tiong, *Nanotechnology*, 2008, **19**, 075611

[18] R. Buonsanti, V. Grillo, E. Carlino, C. Giannini, T. Kipp, R. Cingolani and P. D. Cozzoli, *J. Am. Chem. Soc.*, 2008, **130**, 11223–11233

[19] W. Hu, L. Li, G. Li, C. Tang and L. Sun, *Cryst. Growth Des.*, 2009, **9**, 3676–3682

[20] E. Hosono, S. Fujihara, K. Kakiuchi and H. Imai, *J. Am. Chem. Soc.*, 2004, **126**, 7790–7791

[21] E. Hosono, S. Fujihara, K. Kakiuchi, H. Imai, I. Honma and H. Zhou, *ACS Nano*, 2007, **1**, 273–278

[22] A. Pottier, C. Chanéac, E. Tronc, L. Mazeroles and J. Jolivet, *J. Mater. Chem.*, 2001, **11**, 1116–1121

[23] G. Colón, M. C. Hidalgo and J. A. Navío, *Catal. Today*, 2002, **76**, 91–101

[24] Y. Tang, P. Wee, Y. Lai, X. Wang, D. Gong, P. D. Kanhere, T.-T. Lim, Z. Dong and Z. Chen, *J. Phys. Chem. C*, 2012, **116**, 2772–2780

[25] S. K. Choi, S. Kim, S. K. Lim and H. Park, *J. Phys. Chem. C*, 2010, **114**, 16475–16480

[26] M. T. Uddin, M. Rukanuzzaman, M. M. R. Khan and M. A. Islam, *J. Environ. Manage.*, 2009, **90**, 3443–3450

Chapter 8

Summary and Outlook

In this dissertation we successfully brought a new type of structured catalyst, “monolithic nano-array catalysts”, to the playground of environmental catalysis for automotive emission control and water treatment. We first start with the introduction and discussion of the existing challenges associated with the catalyst preparation and the difficulty of relating industrial catalyst structure to its catalytic property to illustrate why developing catalyst featuring both high performance and new configuration is critical to mitigate the energy and environmental crisis. The advantages of monolithic nano-arrays have been successfully demonstrated by comparing their materials utilization, high performance and easily adjusted catalytic activity to those of conventional monolithic powder catalyst. The conventional thick wash-coated catalyst layers have been replaced with much thinner but ordered nano-arrays via a facile hydrothermal synthesis strategy which results in the spontaneous assembly and uniform deposition of nano-arrays all over the monolithic substrates. Several features and advantages of nano-array based monolithic catalyst over powder wash-coated monolithic catalyst are summarized as follows.

- Good uniformity and controlled nano-array thickness as well as free of binders
- High materials utilization efficiency with an order of magnitude reduction of catalyst usage (both oxide support and noble metals) without catalytic performance sacrificed
- Good thermal and mechanical stabilities, small surface area and weight loss during prolonged durations of high temperature ageing and high velocity gas flux

- Well-defined catalyst structures with controlled geometry and orientation, providing a good platform to understand the exact structure-property relationship of monolithic catalyst

- Adjustable high performance catalytic activity by manipulating nanostructure size and shape as well as controlled chemical composition.

In the later context, we demonstrate the 3D integration of nano-arrays and further introduce the scalable fabrication of nano-array based monolithic catalyst to the industry-relevant scale by addressing the mass transfer issue via the introduced mechanical agitation. This represents a big leap toward the real-world application at the large scale. The successfully achieved mass production of these monolithic nano-array catalysts enables the on-board testing for automotive vehicle emissions and holds great promise toward technology commercialization. Excellent catalytic performances of monolithic nano-array catalyst have been demonstrated using different nano-array catalysts for various important oxidation reactions in automotive emission and clean energy combustion, such as CO oxidation, NO oxidation and hydrocarbon combustion. It has also been proved the careful adjustment of nano-array size and morphology is able to achieve tunable catalytic activity, which is crucial for rational design of efficient monolithic catalyst.

Further experimental evidence of the reaction pathways and mechanism as well as how the transition metal dopants contribute to different catalytic activity have been extracted by in-situ spectroscopy investigation upon the dynamic formation and evolution of reaction intermediates on the catalyst surface. Specifically for the low temperature propane oxidation, a challenging catalytic reaction for automotive emission treatment at low temperature, the surface lattice oxygen has been identified to be the catalytic active sites and the Ni dopant is able to enhance the

oxygen activity that leads to increased reaction kinetics. The hydrocarbon oxidation has been discovered to proceed via the Mars-van Krevelen mechanism where the oxygen in the reaction feed does not participate in the reaction directly. This reaction mechanism has been further validated by isotope labeling which is very important for low temperature oxidation catalyst design and optimization.

In addition to heterogeneous catalytic reactions at the gas-solid interface, multi-functionality has been demonstrated in the nano-arrays where the nano-arrays also exhibit high performance photocatalytic water treatment and purification. High performance organic dye degradation has been successfully achieved by a recyclable koosh ball structure with photocatalytic semiconductor nano-arrays as the outer shell and magnetic oxide sphere as the core. Furthermore the monolithic TiO_2 Nano-arrays has been proved to be an effective adsorbate of dye molecules in the water due to its extremely high surface area which is promising for waste removal in water purification.

It is worth pointing out, however, that the selected metal oxide nano-arrays demonstrated here are not intended as the best options as either supports or catalytically active materials for the low temperature catalytic reactions. Instead, the selected metal oxide systems are used as the model systems for us to better understand and design the new class of nano-array based structured catalysts with better performance and functions for various energy and environmental applications. Moreover, there are several major challenges for the nano-array based monolithic catalysts. First, the current solution chemistry strategy only applies in metal oxide catalysts which usually suffer from low hydrothermal stability and sulfur poisoning. The synthetic approaches for nano-arrays of several other catalytic materials such as zeolite and perovskite, which are more stable and widely used in catalysis industry, needs to be developed. Second,

although the nano-array based monolithic catalysts demonstrate good catalytic activity toward some oxidation reactions, it is necessary to further improve the activity without increasing the catalyst usage. It thus means better understanding of the gas-solid interaction which determines the reaction kinetics in the nano-array configuration needs to be extracted. Third, the catalyst is required to perform multiple catalytic conversions since multiple gas components usually exist in industrial practice. For each specific industrial application the catalytic materials selection regarding the nano-array configuration, activity and stability is a nontrivial task. Our future research would be focused to mitigate these difficulties and provide possible solutions to address these challenges.

1. Materials selection and synthesis: design and develop effective strategies to fabricate and manufacture the nano-array morphology of more material systems including other oxides, perovskites and noble metals.

2. Catalytic reactions: apply nano-array based monolithic catalysts for complex reactions or chemical processes in industry and generate database of reaction kinetics, catalyst efficiency and potential hurdles.

3. Multifunctional catalyst design: rationally design nano-array catalysts with well-defined physical and chemical characteristics for concurrent multiple reactions.

4. Stability and sulfur tolerance: test and improve the hydrothermal, thermal and catalytic stabilities as well as the sulfur tolerance of monolithic nano-array catalyst.

We hope this dissertation can not only provide a comprehensive study of the concept, fabrication, advantages and performance of the newly invented nano-array based monolithic catalysts, but also serves as a timely and useful guidance to rational nanocatalysts design.

Appendix

Journal Publications and Book Chapters

2016

[24] W. Song, **Z. Ren**, S.Y. Chen, Y. Meng, S. Biswas, P. Nandi, H. Elsen, P. X. Gao and S. L. Suib, "Ni and Mn-Substituted Mesoporous Co_3O_4: an Ultra Stable Bifunctional Catalyst with Surface Structure Dependent Activity for Oxygen Reduction Reaction and Oxygen Evolution Reaction", 2016, submitted.

[23] S. Wang, **Z. Ren**, Y. Guo and P. X. Gao, "Nano-array Integrated Monolithic Devices: Toward Rational Materials Design and Multi-functional Performance by Scalable Nanostructures Assembly", ***CrystEngComm***, **2016**, accepted (Invited Highlight paper)

[22] C. Liu, **Z. Ren,** P. X. Gao, "High Performance UV MSM Photodetectors based on Earth-abundant Zinc Stannate Nanoparticle Films", ***J. Mater. Chem. C***, **2016**, submitted.

[21] **Z. Ren**, Z. Wu, W. Song, W. Xiao, Y. Guo, J. Ding, S. L. Suib and P. X. Gao, "Low Temperature Propane Oxidation over Co_3O_4 based Nanoarray Catalyst: Ni Dopant Effects, Reaction Mechanism and Structural Stability", ***Appl. Catal. B.***, **2016**, **180, 150-160**.

2015

[20] S. Wang, **Z. Ren**, Y. Guo, P. X. Gao, "One-dimensional Nanostructure enhanced Catalysis," Chapter, '*The Lightest Metals: Science and Technology from Lithium to Calcium*' , edited by Timothy P Hanusa, **2015**, **ISBN:978-1-118-70328-1**, **John Wiley & Sons, Ltd**.

[19] S. Wang, **Z. Ren**, W. Song, Y. Guo, M. Zhang, S. L. Suib and P. X. Gao, "ZnO/Perovskite Core-shell Nanorod Array based Monolithic Catalysts with Enhanced Material Utilization Efficiency and Propane Oxidation at Low Temperature", ***Catalysis Today***, **2015**, **258, 549-555**.

[18] **Z. Ren**, Y. Guo and P.X. Gao, "Monolithic Nano-array Catalyst: New Concept, Rational Materials Design and Tunable Catalytic Performance", ***Catalysis Today***, **2015**, **258, 441-453**.

2014

[17] Y. Guo, **Z. Ren**, W. Xiao, and P. X. Gao, "Nano-array Catalysts for Sustainable Energy and Environmental Applications," Chapter 12, *Catalysis by Materials with Well-Defined Structures* - 1st Edition, edited by Z.L. Wu, S. Overbury, **2014**, **ISBN: 978-0-128-01217-8, Elsevier**.

[16] **Z. Ren**, V. Botu, S. Wang, Y. Meng, W. Song, Y. Guo, R. Ramprasad, S. L. Suib and P. X. Gao, "Monolithically Integrated Spinel $M_xCo_{3-x}O_4$ (M=Co, Ni and Zn) Nanoarrays Catalyst: Scalable Synthesis and Cations Manipulation for Tunable Catalytic CH_4 and CO Oxidation", ***Angew. Chem. Int. Ed.***, **2014**, **53, 7223-7227**.

[15] W. Song, A. Poyraz, Y. Meng, **Z. Ren**, S. Y. Chen and S. L. Suib, "Mesoporous Co_3O_4 with Controlled

Porosity: Inverse Micelle Synthesis and High Performance Catalytic CO Oxidation at -60ºC", ***Chem. Mater.***, **2014**, **26, 4629-4639**.

[14] Y. Meng, W. Song, H. Huang, **Z. Ren**, S.Y. Chen and S. L. Suib, "Structure-Property Relationship of Bifunctional MnO_2 Nanostructures: Highly Efficient, Ultra-Stable Electrochemical Water Oxidation and Oxygen Reduction Reaction Catalysts Identified in Alkaline Media", ***J. Am. Chem. Soc.,*** **2014, 136, 11452-11464**.

[13] **Z. Ren**, P. X. Gao, "A Review of Helical Nanostructures: Growth Theories, Synthesis Strategies and Properties", ***Nanoscale*****, 2014, 6, 9366-9400** (**Feature article**)

[12] C. Liu, H. Chen, **Z. Ren**, S. Dardona, M. Piech, H. Gao and P. X. Gao, "Controlled Synthesis and Structure Tunability of Photocatalytically Active Mesoporous Metal-based Stannate Nanostructures", ***Appl. Surf. Sci.***, **2014, 296, 53-60**.

[11] C. Liu, R. Röder, L. Zhang, **Z. Ren**, H. Chen, Z. Zhang, C. Ronning and P. X. Gao, "Highly Efficient Visible-light Driven Photocatalysts: A Case on Zinc Stannate based Nanocrystal Assemblies", ***J. Mater. Chem. A.*****, 2014, 2, 4157-4167**. (**Back cover**)

2013

[10] Y. Guo, G. Liu, **Z. Ren**, A. Piyadasa and P. X. Gao, "Single Crystalline Brookite Titatium Dioxide Nanorod Arrays Rooted on Ceramic Monoliths: A Hybrid Nanocatalyst Support with Ultrahigh Surface Area and Thermal Stability", ***CrystEngComm*****., 2013, 15, 8345-8352.**

[9] W. Xiao, Y. Guo, **Z. Ren**, G. Wrobel, Z. Ren, T. Lu and P. X. Gao, "Mechanical Agitation Assisted Growth of Large Scale and Uniform ZnO Nanorod Arrays within 3D Multi-channel Monolithic Substrates", ***Cryst. Growth. Des.*****, 2013, 13, 3657-3664**.

[8] **Z. Ren**, Y. Guo, C. Liu and P. X. Gao, "Hierarchical Nanostructured Materials for Sustainable Environmental Applications", ***Front. Chem.***, **2013, 1, 18.**

[7] **Z. Ren**, Y. Guo, Z. Zhang, C. Liu and P. X. Gao, "Nonprecious catalytic honeycombs structured with three dimensional hierarchical Co_3O_4 nano-arrays for high performance nitric oxide oxidation", ***J. Mater. Chem. A.*****, 2013, 1, 9897-9906.**

[6] **Y. Guo**†, **Z. Ren**†, (†**equally contributed**) W. Xiao, C. Liu, H. Sharma, H.Gao, A. Mhadeshwar and P. X. Gao, "Robust 3D-Configurated Metal Oxide Nanoarray-based Monolithic Catalysts with Ultrahigh Materials Usage Efficiency and Catalytic Performance Tunability", ***Nano Energy*****, 2013, 2, 873-881.** (**Front cover**)

2012

[5] **Z. Ren**, Y. Guo, G. Wrobel, D. Knecht, Z. Zhang, H. Gao and P. X. Gao, "Three dimensional koosh ball nanoarchitectures with tunable magnetic core, fluorescent nanowire shell and enhanced photocatalytic property", ***J. Mater. Chem.,*** **2012, 22, 6862-6868.**

[4] Y. Guo, Z. Zhang, **Z. Ren**, H. Gao and P. X. Gao, "Synthesis, characterization and CO oxidation of

TiO_2/(La,Sr)MnO_3 composite nanorod array", ***Catalysis Today,*** **2012, 184,178-183**.

[3] P. X. Gao, P. Shimpi, H. Gao, C. Liu, Y. Guo, W. Cai, K. -T. Liao, G. Wrobel, Z. Zhang, **Z. Ren** and H. –J. Lin, "Hierarchical Assembly of Multifunctional Oxide-based Composite Nanostructures for Energy and Environmental Applications", ***Int. J. Mol. Sci.,*** **2012, 13,7393-7423**.

2011

[2] Q. Sun, **Z. Ren**, R. M. Wang, N. Wang and X. Cao, "Platinum catalyzed growth of NiPt hollow spheres with an ultrathin shell", ***J. Mater. Chem.,*** **2011, 21, 1925-1930.** (**Front cover and hot article**)

[1] Q. Sun, **Z. Ren**, R. M. Wang, W. Chen, C. P. Chen, "Magnetite hollow spheres: solution synthesis, phase formation and magnetic property", ***J. Nanopart. Res.,*** **2011, 13, 213-220**.